Using diffusion MR information to reconstruct networks of brain activations from MEG and EEG measurements

Brahim Belaoucha

UNIVERSITY OF CÔTE D'AZUR

DOCTORAL THESIS

USING DIFFUSION MR INFORMATION TO RECONSTRUCT NETWORKS OF BRAIN ACTIVATIONS FROM MEG AND EEG MEASUREMENTS

Author:
Brahim BELAOUCHA

A thesis submitted in fulfillment of the requirements for the degree of Doctor of Philosophy

in the

Athena Project-Team
University of Côte d'Azur

Jury members: **(in alphabetical order)**

Dr. Christian-George Bénar	Inserm, France	Reviewer
Dr. Rachid Deriche	Inria SAM, France	Examiner
Dr. Alexandre Gramfort	Inria, France	Examiner
Pr. Jean-Marc Lina	ETS, McGill university, Canada	Examiner
Pr. Gloria Menegaz	University of Verona, Italy	Examiner
Dr. Théodore Papadopoulo	Inria SAM, France	Supervisor
Dr. Bertrand Thirion	Inria, University of Paris-Saclay, France	Reviewer

Defended on 30 May 2017

Université Côte d'Azur

École Doctorale STIC
(Sciences et Technologies de l'Information et de la Communication)

THÈSE

pour obtenir le titre de
DOCTEUR EN SCIENCES
de l'Université Côte d'Azur
Discipline: Automatique, Traitement du Signal et des Images

présentée et soutenue par

Brahim BELAOUCHA

Utilisation de l'IRM de diffusion pour la reconstruction de réseaux d'activations cérébrales à partir de données MEG/EEG

Sountenue le 30 Mai 2017

Composition du jury: (par ordre alphabétique)

Dr. Christian-George Bénar	Inserm, France	Rapporteur
Dr. Rachid Deriche	Inria SAM, France	Examinateur
Dr. Alexandre Gramfort	Inria, France	Examinateur
Pr. Jean-Marc Lina	ETS, Université McGill, Canada	Examinateur
Pr. Gloria Menegaz	Université de Vérone, Italie	Examinateur
Dr. Théodore Papadopoulo	Inria SAM, France	Superviseur
Dr. Bertrand Thirion	Inria, Université Paris-Saclay, France	Rapporteur

UNIVERSITY OF CÔTE D'AZUR

Abstract

EDSTIC
University of Côte d'Azur

Doctor of Philosophy

USING DIFFUSION MR INFORMATION TO RECONSTRUCT NETWORKS OF BRAIN ACTIVATIONS FROM MEG AND EEG MEASUREMENTS

by Brahim BELAOUCHA

Understanding how brain regions interact to perform a given task is a very challenging task. Electroencephalography (EEG) and Magnetoencephalography (MEG) are two non-invasive functional imaging modalities used to record brain activity with high temporal resolution. As estimating brain activity from these measurements is an ill-posed problem, We thus must set a prior on the sources to obtain a unique solution. It has been shown in previous studies that structural homogeneity of brain regions could reflect their functional homogeneity. One of the main goals of this work is to use this structural information to define priors to constrain more anatomically the MEG/EEG source reconstruction problem.

This structural information is obtained using diffusion magnetic resonance imaging (dMRI), which is, as of today, the unique non-invasive structural imaging modality that provides an insight on the structural organization of white matter. This makes its use to constrain the EEG/MEG inverse problem justified. In our work, dMRI information is used to reconstruct brain activation in two ways:

- In a spatial method which uses brain parcels to constrain the sources activity. These parcels are obtained by our whole brain parcellation algorithm which computes cortical regions with the most structural homogeneity with respect to a similarity measure.
- In a spatio-temporal method that makes use of the anatomical connections computed from dMRI to constrain the sources' dynamics.

These different methods are validated using synthetic and real data.

Résumé (en français)

Comprendre comment différentes régions du cerveau interagissent afin d'exécuter une tâche, est un défi très complexe. La magnéto- et l'électro-encéphalographie (MEEG) sont deux techniques non-invasive d'imagerie fonctionnelle utilisées pour mesurer avec une bonne résolution temporelle l'activité cérébrale. Estimer cette activité à partir des mesures MEEG est un problème mal posé. Il est donc crucial de le régulariser pour obtenir une solution unique. Il a été montré que l'homogénéité structurelle des régions corticales peut reflète leur homogénéité fonctionnelle. Un des buts principaux de ce travail est d'utiliser cette information structurelle pour définir des a priori permettant de contraindre de manière plus anatomique ce problème inverse de reconstruction de sources.

L'imagerie par résonance magnétique de diffusion (IRMd) est, à ce jour, la seule technique non-invasive qui fournisse des informations sur l'organisation structurelle de la matière blanche. Cela justifie son utilisation pour contraindre notre problème inverse. Nous utilisons l'information fournie par l'IRMd de deux manière différentes pour reconstruire les activations du cerveau:

- via une méthode spatiale qui utilise une parcellisation du cerveau pour contraindre l'activité des sources. Ces parcelles sont obtenues par un algorithme qui permet d'obtenir un ensemble optimal de régions structurellement homogènes pour une mesure de similarité donnée sur tout le cerveau.

- dans une approche spatio-temporelle qui utilise les connexions anatomiques, calculées à partir des données d'IRMd, pour contraindre la dynamique des sources.

Ces méthodes sont appliquéeS à des données synthétiques et réelles.

Acknowledgements

First, I would like to express my deep gratitude to Théodore Papadopoulo for supervising my work and sharing his expertise and time during the last three and half years. I would like to thank Rachid Deriche for accepting me in his team and providing me with encouragement and advises.

I am very grateful to Christian Bénar and Bertrand Thirion for taking a significant amount of their time to review this thesis and sharing their insightful suggestions and remarks. Furthermore, I would like to thank Rachid Deriche, Jean-Marc Lina, Gloria Menegaz and Alexandre Gramfort for accepting to participate in the jury.

Special thanks to all the people that I interacted with, I want to thank them here: Sebastian Hitziger for all the discussions that we had, Marco Pizzolato and Rutger Fick for being present during my good and bad times, Guillermo Gallardo-Diez for putting up with me as an office mate, Kostiantyn Maksymenko for keeping me company during the several weekends that I spent in the office, Yousra Bekhti for her great help.

I will not forget all the amazing friends I have made during the last three unforgettable years: Kai Dang, Nathalie Gayraud, Christos Papageorgakis, Mouloud Kachouane, Patryk Filipiak, Amandine Audino, Isa Costantini, Federica Turi and Gabriel Girard.

I would also like to thank my parents for believing in me and for their prayers.

General introduction

Context

The human brain controls many voluntary and involuntary action. Understanding the brain and its functions is an ongoing challenge. The brain is a complex organ which contains around 100 billions neurons that work together to perform specific tasks. Medical imaging allows to access to structural organization and functional information of the human brain.

Electroencephalography (EEG) and Magnetoencephalography (MEG) are two non-invasive functional imagining techniques that measure, outside the brain, the human brain activity with high temporal resolution ($\approx$ 1 ms). They measure, respectively, the electrical and magnetic fields generated by the electrical communication between group of neurons which are approximated by dipole sources situated on the cortical surface. Estimating the dipoles' magnitudes and orientations is an ill-posed problem due to having fewer measurement than unknowns (sources). To obtain a unique solution, we must have a prior on the source space. This prior can be spatial, in the source space, temporal or both. Previous works show that a relation between the structural organization of brain regions and their functional homogeneity exists. That is why we used dMRI, which is the unique non-invasive imaging modality that permits us to access to the structural organization of the white matter, to constrain the source space and the sources' dynamics.

The object of this thesis is to use the dMR information to regularize the EEG/MEG inverse problem i.e. to constrain the ill-posed problem by using anatomical information obtained from dMRI. First, we used the dMR information to parcellate the cortical surface into functional regions with homogeneous structural connectivity. Then, we integrate these regions into

the EEG/MEG inverse problem by using a spatial and a spatiotemporal regularization term.

Organization

In **Chapter 1**, we describe the structural and functional organization of the cortical surface. The different white matter pathways, that relate brain regions, are presented briefly. Then , we introduced, in section 1.4 and 1.5 some of the most used structural and functional imaging techniques. We then present in section 1.4.2 how the electromagnetic field generated by the neuronal activity can be measured on the head surface (EEG) or outside the head (MEG).

Chapter 2 explains, in more details, how we can measure the brain activity by the EEG electrodes and MEG sensors. Also, we introduce in section 2.2.2 the different head models that can be used to approximate the different head's compartments. These head models are used to estimate the transformation from the source space (cortical surface) to the sensor array i.e. gain or lead-field matrix a.k.a the forward problem. Because of the low frequency of the signal measured with EEG/MEG sensor arrays, the time derivatives in the *Maxwell's* equations can be neglected. This quasi-static approximation is used then to relate the brain activity, which is approximated by electric dipoles located on the cortical surface, to either the electric potential, in the case of EEG, or to the magnetic field for MEG. In the second part of the chapter, we introduce some linear and nonlinear techniques which are used to estimate the dipoles' magnitudes and orientations from EEG/MEG measurements.

In **Chapter 3**, we introduce, in more details, one of the structural imaging techniques, diffusion magnetic resonance imaging (dMRI). The relation between the decay of the dMR signal and the diffusion direction of the water molecules in each image voxel is presented in section 3.2. In section 3.5, we list some of the scalars that are used to quantify the (an)isotropy of brain voxels. At the end of the chapter, we list the two tractography approaches,

local and global, that can be used to reconstruct the white matter pathways that connect cortical regions.

Chapter 4 contains our first contribution. It presents our parcellation algorithm to divide the whole cortical surface into regions by using a dMRI-based fingerprint (connectivity profile). It uses the mutual nearest neighbor (MNN) condition to merge cortical regions to obtain at the end the most homogeneous regions according to a similarity measure. In section 4.2 and 4.3, we present some of the techniques used to parcellate the cortical surface. Our MNN parcellation algorithm is explained in 4.3.3. We presente in section 4.4 five similarity measures that were used, in our work, to parcellate the whole cortical surface. The results of the MNN parcellation with real data can be found in section 4.6. In the same section, we show the effect of choosing a similarity measure on the resulting parcellation.

In **Chapter 5**, we present our second contribution which consists of using dMR information to solve the EEG/MEG inverse problem. The first inverse-problem is based on spatial regularization and is presented in section 5.3. It uses the homogeneity of the cortical regions to regularize the sources activations using similarity values of the connectivity profiles of cortical sources. The second proposed inverse problem uses a spatiotemporal regularization and is presented in section 5.4. We call it iterative Source and Dynamics Reconstruction (iSDR). It is, as its name indicates, an iterative approach to solve sources intensities and their interactions. Sources' dynamics are constrained by a multivariate autoregressive model.

This report ends with a conclusion which summarizes our contributions and possible future extensions of this work.

Introduction générale

Contexte

Le cerveau contrôle la plupart les actions volontaires et involontaires. Comprendre le cerveau et ses fonctions est un défi majeur. Le cerveau est un organe complexe, il contient environ 100 milliards de neurones qui travaillent ensemble pour effectuer des tâches spécifiques. L'imagerie médicale permet l'accès à l'organisation structurelle et à l'information fonctionnelle du cerveau.

L'électroencéphalographie (EEG) et la magnétoencéphalographie (MEG) sont deux techniques d'imagerie fonctionnelle non-invasive qui sont utilisées pour mesurer l'activité cérébrale avec une très grande résolution temporelle ($approx$ 1 ms). Elles mesurent, respectivement, les champs électriques et magnétiques générés par la communication électrique entre groupe des neurones modéliser par des sources dipolaires.

L'estimation des sources est un problème mal posé. Pour obtenir une solution unique, nous devons avoir un a priori sur l'espace source. Cet a priori peut être spatial, temporel ou spatio-temporel. Des travaux antérieurs montrent qu'il existe une relation entre l'organisation structurale des régions du cerveau et leurs fonctions. C'est pourquoi nous avons utilisé l'IRM de diffusion (IRMd), qui est la modalité d'imagerie non invasive unique qui nous permet d'accéder à l'organisation structurale de la matière blanche blanche, afin de contraindre l'espace source.

Le but de cette thèse est d'utiliser l'information IRMd pour régulariser le problème EEG/MEG inverse, c'est-à-dire de contraindre le problème posé en utilisant l'information anatomique obtenue à partir de l'IRMd. Dans un premier temps, nous avons utilisé l'information obtenue à partir de l'IRMd

pour segmenter la surface corticale en régions fonctionnelles avec une connectivité structurelle homogène. Ensuite, nous intégrons ces régions dans le problème inverse EEG / MEG en utilisant un terme spatial ou spatiotemporal de régularisation.

Organisation

Dans le **Chapitre 1**, nous décrivons l'organisation structurelle et fonctionnelle de la surface corticale. Les différentes voies de la matière blanche, qui relient les régions du cerveau, sont décrites brièvement. Nous introduisons certaines des modalités d'imagerie structurale et fonctionnelle les plus utilisées. En outre, nous expliquons comment le courant électrique est généré a partir d'un groupe des neurones peut être mesuré sur le cuir chevelu ou à l'extérieur de la tête en utilisant les modalités d'imagerie fonctionnelle, EEG et MEG.

Le **Chapitre 2** explique, avec plus de détails, comment nous pouvons mesurer l'activité cérébrale avec d'électrodes EEG ou capteurs MEG. Nous présentons les différents modèles de tête qui peuvent être utilisés pour approximer les différents compartiments de la tête, qui sont utilisés pour estimer la transformation entre l'espace des sources (surface corticale) vers l'espace des capteurs, c'est-à-dire la matrice de gain ou lead field.

En raison de la faible fréquence du signal mesuré avec l'EEG/MEG, les dérivées en temps dans les équations de *Maxwell* peuvent être négligées. Cette approximation quasi-statique sert alors à relier l'activité cérébrale, qui est approximée par des dipôles électriques situés sur la surface corticale, soit au potentiel électrique, dans le cas de l'EEG, soit au champ magnétique pour la MEG. Dans la deuxième partie du chapitre, nous introduisons quelques techniques qui sont utilisées pour estimer ces dipôles à partir des mesures EEG/MEG.

Dans le **Chapitre 3**, nous détaillons l'une des modalités d'imagerie structurale, IRMd (imagerie par résonance magnétique de diffusion). La relation entre la décroissance du signal IRMd et la direction de diffusion des

molécules d'eau est présentée. Certaines scalaires qui sont utilisés pour quantifier l'(an)isotropie des voxels du cerveau sont données. A la fin du chapitre, nous présentons les deux approches de tractographie, locales et globales, qui servent à reconstituer les grandes voies de la matière blanche qui relient les régions corticales.

Le **Chapitre 4** présente notre algorithme de parcellisation pour diviser la surface corticale dans sa totalité en régions en utilisant une information basée sur l'IRMd (profil de connectivité). Il utilise la condition des voisins les plus proches pour fusionner les régions corticales et obtenir les régions les plus homogènes selon une mesure de similarité. Nous étudions l'effet du choix de la mesure de similarité sur les parcelles résultantes en utilisant cinq mesures de similarité différentes. Nous avons appliqué notre algorithme à une base de donnée d'onze participants.

Dans le **Chapitre 5**, nous présentons nos méthodes pour reconstruire l'activité cérébrale à partir de la mesure EEG/MEG en utilisant l'information provenant du signal IRMd. La première méthode utilise un terme de régularisation spatiale en utilisant une matrice de pondération dont les éléments sont obtenus à partir des valeurs de similarité entre les différents profils de connectivité des sources. L'ampleur des sources est alors liée à l'homogénéité / inhomogénéité des régions du cerveau. La deuxième méthode utilise les chemins obtenus à partir du signal dMR pour contraindre dynamiquement l'évolution temporelle des sources.

Ce document se termine par une conclusion qui résume nos contributions et décrit de possibles extensions futures à ce travail.

Contents

Abstract iii

Acknowledgements v

General introduction vii

Introduction générale xi

1 Introduction 1
- 1.1 Nervous system . . . 2
- 1.2 The brain . . . 3
  - 1.2.1 Gray matter . . . 4
  - 1.2.2 White matter . . . 5
  - 1.2.3 Neurons: the building block . . . 7
- 1.3 Structural and functional organization of the brain . . . 9
- 1.4 Functional neuroimaging . . . 11
  - 1.4.1 Metabolic imaging . . . 11
    - 1.4.1.1 Positron emission tomography . . . 12
    - 1.4.1.2 Functional magnetic resonance imaging . . . 12
  - 1.4.2 Electromagnetic imaging . . . 13
    - 1.4.2.1 Electroencephalography . . . 13
    - 1.4.2.2 Magnetoencephalography . . . 15
    - 1.4.2.3 EEG versus MEG . . . 17
- 1.5 Structural neuroimaging . . . 17
- 1.6 Conclusion . . . 19

2 The MEG/EEG forward and inverse problem 21
- 2.1 Introduction . . . 22
- 2.2 Forward problem . . . 22
  - 2.2.1 The physics of EEG and MEG . . . 23
    - 2.2.1.1 Maxwell's equations . . . 23
    - 2.2.1.2 Quasi-static approximation . . . 23
    - 2.2.1.3 The electric potential equation . . . 23
    - 2.2.1.4 The magnetic field equation . . . 24
  - 2.2.2 Head Models . . . 25
    - 2.2.2.1 Spherical Model . . . 26
    - 2.2.2.2 Realistic head model . . . 26
- 2.3 Inverse problem . . . 28
  - 2.3.1 Dipole fitting approaches . . . 28
  - 2.3.2 Scanning techniques . . . 29
  - 2.3.3 Distributed source models . . . 31

2.3.3.1 Linear methods . . . 33
2.3.3.2 The choice of the regularization parameter . . 34
2.3.3.3 Non linear methods . . . 36
2.3.4 Conclusion . . . 39

3 Diffusion magnetic resonance imaging 41
3.1 Introduction . . . 42
3.2 The Principle of Diffusion . . . 42
3.3 Diffusion tensor . . . 43
3.4 Diffusion tensor estimation . . . 43
3.5 Scalar quantities . . . 45
3.5.1 Trace or mean diffusivity (MD) . . . 46
3.5.2 Fractional anisotropy (FA) and relative anisotropy (RA) 46
3.6 Multi-tensor . . . 47
3.7 Tractography . . . 48
3.7.1 Local tractography . . . 48
3.7.1.1 Deterministic tractography . . . 48
3.7.1.2 Probabilistic tractography . . . 49
3.7.2 Global tractography . . . 50
3.8 Conclusion . . . 51

4 Cortical surface parcellation 53
4.1 Introduction . . . 54
4.2 Parcellation approaches . . . 54
4.3 dMRI-based parcellation . . . 56
4.3.1 Review of dMRI-based parcellation methods . . . 56
4.3.2 Connectivity profile: a dMRI-based fingerprint . . . 58
4.3.3 dMRI-based parcellation using the mutual nearest neighbor condition . . . 59
4.4 Similarity measure . . . 62
4.4.1 Cosine coefficient . . . 62
4.4.2 Tanimoto coefficient . . . 63
4.4.3 Ruzicka coefficient . . . 64
4.4.4 Motyka coefficient . . . 65
4.4.5 Roberts coefficient . . . 65
4.5 Data acquisition . . . 65
4.6 Results of MNN parcellation . . . 66
4.6.1 Comparing parcellations . . . 67
4.6.2 Results of parcellation . . . 68
4.6.2.1 Computation time . . . 68
4.6.2.2 Number of regions . . . 68
4.6.2.3 Regions' homogeneity . . . 69
4.6.2.4 Regions' size . . . 70
4.6.2.5 Region' area . . . 70
4.6.2.6 Spatial overlap . . . 70
4.6.2.7 Best similarity measure . . . 71
4.6.2.8 Effect of perturbations on the tractograms . . 71
4.6.2.9 Comparison to atlases . . . 71

4.6.2.10 Post-processing effect . . . 73
4.7 Conclusion . . . 91

5 dMRI in the EEG/MEG inverse Problem **93**
5.1 Introduction . . . 94
5.2 State of the art . . . 94
5.3 Pure spatial regularization (sWMNE) . . . 96
5.3.1 Results . . . 99
5.3.1.1 Synthetic data . . . 99
5.3.1.2 Real data . . . 103
5.4 Spatiotemporal regularization . . . 108
5.4.1 Pruning the MAR model . . . 117
5.4.2 Magnitude bias . . . 120
5.4.3 Results . . . 121
5.4.3.1 Synthetic data . . . 121
5.4.3.2 iSDR with a higher MAR model . . . 131
5.4.3.3 Real data . . . 134
5.4.3.4 iSDR results . . . 137
5.5 Discussion . . . 155
5.6 Conclusion . . . 156

6 General conclusion **159**
6.1 Contributions . . . 160
6.1.1 Cortical surface parcellation . . . 160
6.1.2 Spatial regularization (sWMNE) . . . 160
6.1.3 Spatiotemporal regularization (iSDR) . . . 161
6.2 Other contributions . . . 161
6.3 Perspectives . . . 161

A Publication of the author **165**

References **167**

List of Figures

1.1 The central nervous system (CNS) and peripheral nervous system (PNS). (source http://activateanddominate.com) . . . 2
1.2 The three parts of the brain: *Hindbrain*, *Midbrain* and *Forebrain*. (source aslamnadeem.blogspot.com) 3
1.3 The four different lobes of human brain. (source wikipedia) . 3
1.4 White and Gray matter in a coronal slice. (adapted from best-practice.bmj.com) 5
1.5 The corpus callosum and anterior commissure. (adapted from http://www.wileyessential.com) 6
1.6 White matter fibers: (a) Ascending (blue sensory fibers) and descending (red motor fibers) projection fibers (adapted from Gray, 1918) (b) Short and long association fibers. They are pathways that connect regions of the same hemisphere (adapted from Gray, 1918) and (c) commissural fibers that connect the two hemispheres. 6
1.7 The neuron structure and its connections. (adapted from http://biology.stackexchange.com) 7
1.8 An example of Action potential (adapted from Sanei et al., 2007) 8
1.9 The six layers of the gray matter in different locations. (adapted from Kandel et al., 2000) 11
1.10 Cortical areas defined by Brodmann (Brodmann, 1909). The cortical areas are divided according to the thickness of the cortical layers. (source wikipedia) 12
1.11 PET images during rest and a motor task. (adapted from http://www.dialogues-cns.com) 13
1.12 One of the first EEG recording by H. Berger (adapted from Galán, 2013). On top, we show the actual recorded signal. On bottom, we show a sinusoidal reference signal of 10 Hz. . . 13
1.13 A diagram representation of 10-20 electrodes settings for 75 electrodes: (a) and (b) 3D representation, and (c) 2D view (Sanei et al., 2007). 14
1.14 Schematic diagrams showing the generated (a) electric and (b) magnetic fields from an equivalent current dipole. (adapted from Gramfort, 2009) 15
1.15 System of simultaneous MEG and EEG acquisition (Galán, 2013). 16
1.16 Magnetic and Electric fields generated by a brain activity. (adapted from Galán, 2013) 17

2.1 Illustration of MEG/EEG forward and inverse problem. (source http://www.childbrain.eu) 22
2.2 Spherical model with three layers: Scalp, Skull and brain. . . . 26
2.3 On the left, a slice of a CT image. On the right, the same slice obtained with MRI. We observed that the CT offers a good contrast to the skull while MRI provides a good contrast between soft tissues. (Source blog.cincinnatichildrens.org) . . 27
2.4 The different surfaces ($S_1, .., S_5$) and volumes ($\Omega_1, .., \Omega_5$) that can be extracted from MRI image. (adapted from Faugeras et al., 1999) 27
2.5 An example of dipole fitting. (source http://www.fieldtriptoolbox.org) 29
2.6 A possible shape of (a) L-curve and (b) GCV curve. The optimal λ is shown in both sub-figures by red star. (adopted from Hansen, 1992). 35
2.7 The effect of using the different norms on the estimated sources' magnitudes. Using l_2 no source is inactive (= 0), with l_1 few sources are active at each time sample, l_{21} and l_{12} allow to obtain structural activation. 38

3.1 Diffusion MRI images with three different gradient directions. Different tissue contrasts are obtained using different gradient directions. 44
3.2 Schematic of the diffusion tensor ellipsoid. The ellipsoid is the envelope where a spin -placed at its center- will diffuse with equal probability. The axes are scaled according to the square root of the eigenvalues. (modified from Johansen-Berg et al., 2009) 44
3.3 The diffusion tensor ellipsoid. Left: the ellipsoid shape in an isotropic environment. Right: the ellipsoid shape in a restricted environment. (Winston, 2012) 46
3.4 Diffusion tensor imaging. The non-diffusion weighted scan (B0) is shown on the left, followed by the fractional anisotropy (FA) image demonstrating higher values in white matter tracts then the mean diffusivity (MD) image with elevated values in the CSF. The final column shows the direction of principal eigenvector (Eig1) both in color-coded form (red = left/right, green=anterior/posterior, blue=superior/inferior) and in vector form (line segments) . (Winston, 2012) 47

3.5 Schematic illustration of deterministic tractography, (a) three adjacent voxels have a clearly directed primary diffusion direction (longitudinal diffusion) indicated by ellipsoids. A deterministic tractography analysis would result in the indicated tract. (b) week directionality of diffusion, evidenced by more spherical ellipsoids (small FA). The direction of the principal direction is, however, unchanged. This explains why deterministic tractography analysis may result in the same reconstructed tract (primary direction unchanged) although the diffusion tensor is less ellipsoidal. (Xekardaki et al., 2011) 49
3.6 Result of a probabilistic tractography. (P. Yeh et al., 2012) . . . 50

4.1 Four different view of two brain atlases: (a) Desikan-Killiany (b) Destrieux obtained from Dale et al., 1999. 55
4.2 Parcellation from (a) fMRI (500 regions, Thirion et al., 2014) and (b) MEG (174 regions, Chowdhury et al., 2013). 56
4.3 Cortical target regions a) and connectivity target-based parcellation of the Thalamus b,c,d). (reprint from (Behrens et al., 2003)). 57
4.4 The cortical surface shown in a MR image. Face is removed to maintain anonymity. 59
4.5 Representing the connectivity profiles in 2D to interpret some of the similarity measures. $\min(X_i, Y_i)$ and $\max(X_i, Y_i)$ for each i are shown in yellow and blue respectively. 64
4.6 Axial view of (a) T1 image and (b) b0 image of subject 1 in (Wakeman et al., 2015). 66
4.7 Parcellation of Subject 13 shown on the inflated brain surface. The parcellation used different similarity measures: (a) Cosine, (b) Tanimoto, (c) Motyka, (d) Ruzicka, (e) Roberts. These parcellations are obtained with $T = 100$. (f) shows the mean (over subjects) and the standard deviation of the execution time for different T values. 74
4.8 Resulting number of patches for different T values and subjects. It can be observed that the numbers of regions for each T value for the different SM are close and that there is a linear relationship between the number of regions and T. The remaining subjects show similar results. 75
4.9 Mean of similarity measures (SM) values at different T values and for the different subjects. Note that Tanimoto is almost linear with respect to T. The remaining subjects show similar results. 76
4.10 Standard of deviation (STD) of the similarity measures (SM) values at different T values and for the different subjects. The remaining subjects show similar results. 77
4.11 The coefficient of variation (CV) of the resulting parcellations for different T values and subjects. The remaining subjects show similar results. 78

4.12 The fitted distribution of the number of seeds per region for different T values and subjects. These patches are obtained using *Cosine* measure. The remaining subjects show similar results. . . . 79
4.13 The fitted distribution of the number of seeds per region for different T values and subjects. These patches are obtained using *Tanimoto* measure. The remaining subjects show similar results. . . . 80
4.14 The fitted distribution of the number of seeds per region for different T values and subjects. These patches are obtained using *Ruzicka* measure. The remaining subjects show similar results. . . . 81
4.15 The fitted distribution of the number of seeds per region for different T values and subjects. These patches are obtained using *Motyka* measure. The remaining subjects show similar results. . . . 82
4.16 The fitted distribution of the number of seeds per region for different T values and subjects. These patches are obtained using *Roberts* measure. The remaining subjects show similar results. . . . 83
4.17 The distribution of the dice coefficient of Subject 1 parcellation with different SM and (a) $T = 1000$ (b) $T = 100$. Each panel represents the distribution of dice coefficient computed between two MNN parcellations using two different similarity measure. The remaining subjects show similar results. . . . 84
4.18 The intersections of cortical areas with more than 70% spatial overlapping over the five similarity measures (Tanimoto, Cosine, Ruzicka, Motyka and Roberts with $T = 600$) of six different subjects. . . . 85
4.19 The mean and std of the similarity measures values from the simulated tractograms at five noise levels. . . . 86
4.20 Mean and std of the dice coefficient between the MNN parcellation and atlases for the different subjects and for different similarity measures (SM). . . . 86
4.21 The coefficient of variation (CV) for different subjects before and after applying *k-means* on the atlases regions (Destrieux (DX) and Desikan-Killiany (DK)). These patches are obtained using different similarity measures. . . . 87
4.22 Top panel: different views of Mindboggle atlas showed on an inflated surface. Middle panel: MNN parcellation with Tanimoto and $T = 700$ of Subject 1. Bottom panel: MNN parcellation with Tanimoto and $T = 100$ of Subject 1. MNN regions are labeled by mindboggle regions which correspond to the highest spatial overlapping computed by dice coefficient. We noticed that lobes boundaries are different between MNN parcellations and the atlas. Gray spaces are spaces between atlases' sub-regions. . . . 88

4.23 The mean and standard deviation (over subjects) of the fraction $f_{ba} = \frac{N_b - N_a}{N_b}$ for different T values and similarity measures. 90

5.1 Ground truth simulation. In (a), activation curve of one region. In (b), we show the two different activation curves used for two distinct regions. 100

5.2 An example of the mean (over 100 runs) reconstructions by the methods MNE, CP, sWMNE of the two test configurations. The left panel corresponds to the reconstruction of the first test configuration, and the right panel shows the reconstructed two active regions. From top to bottom SNR = 15, 10, 5 dB. 101

5.3 Upper panel: mean and standard deviation (over 20×100 runs) of reconstruction error E_r for different SNR levels for the two test configuration. Lower panel: focality of the reconstruction represented as the number of sources that have a total energy ($\|J_i\|_2$) greater or equal to 25% of the highest energy in the source space. The results are obtained for different noise levels 15, 10 and 5dB. MNE, CP and sWMNE results are shown, respectively, in blue, black and green colors. The ground truth GT of the number of active sources are shown in red. 102

5.4 Top panel: MEG data of Famous - Scrambled face class. Bottom panel: explained MEG data by the sWMNE reconstruction. Differences between the recorded measurements and the explained ones by sWMNE are very small. 104

5.5 The l_1-norm of source magnitudes between $t = 0$ and $t = 600$ ms obtained by sWMNE from MEG data. We show only sources that have a total l_1 norm ($\|J_i\|_1 = \sum_t |J_i(t)|$) higher than 15% of the highest l_1 norm. The results are similar with the 11 participants. 105

5.6 The average time course of a right fusiform area of (a) subject 1 and (b) subject 13 obtained by sWMNE from MEG data. . . . 106

5.7 The l_1 norm of the minimum norm estimate (MNE) and CP of MEG data (Famous-Scrambled) of Subject 1 shown on the inflated surface. Time courses are taken from the right FF region (yellow arrow). We show only sources that have an energy higher than 15% of the highest activation. 107

5.8 Left: reconstructed active regions by sWMNE from MEG data. Right: reconstructed active regions by sWMNE from EEG data. EEG and MEG data are the measurements of Subject 1. 108

5.9 Different views of the structural network of Subject 1 obtained from dMRI as explained in section 5.4.1. L and R stand, respectively, for left and right hemispheres. In red boxes, we show the uncinate fasciculus. In the yellow boxes, we show the inferior longitudinal fasciculus. Green dots represent the center of the cortical regions obtained by MNN parcellation. . 119
5.10 Histograms shows the number of structural connections that are seen by dMRI (probabilistic tractography) for the eleven participants. 120
5.11 Different view of the cortical surface used in the simulation and the location of S_1 and S_2. Edges represent the anatomical connections. 121
5.12 An example of the source estimates using MxNE, irMxNE and Lasso at SNR equal to 10 dB. In blue and green, we show the time course of S_1 and S_2. The remaining dipoles' magnitudes are shown in black. 122
5.13 The mean, over 100 runs, of the reconstruction error at different noise levels (SNR ={15, 10, 5, -5} dB). The error of the reconstruction is computed as the l_2-norm of the simulated ground truth subtracted to the reconstructed activation using iSDR, Lasso, irMxNE and MxNE. 123
5.14 The number of sources found to be active by iSDR at the four SNR levels {15, 10, 5, -5}. The total number of simulations is 400 (100 per noise level). True active set contains 2 sources. . . 125
5.15 The source reconstruction error E_r (in blue), data fit term M_r (in green) and number of detected active sources (in red) obtained from MxNE and iSDR. The regularization parameter λ that gives the true active sources are shown in black vertical lines. In the bottom panel, we show the corresponding values of the cost function for MxNE and iSDR. These results are obtained using realistic head model and a measurement at SNR level equal to 10 dB. The optimal λ for iSDR is inside the orange circle. 126
5.16 One result of simulated sources at SNR = 15 dB. We show the reconstructed sources and the number of active sources (sources with l_2-norm > 0) and the resulting MAR elements of only the detected active sources. The initial number of active sources obtained from MxNE is 149. It decreases to 2 sources in the seventh iteration. The green and red color represent, respectively, the time course of S1 and S2. We show the remaining sources in black. In the lower left corner, we show the estimated MAR for only nonzero sources at the last iteration. 128

5.17 One result of simulated sources at SNR = 10 dB. We show the reconstructed sources and the number of active sources (sources with l_2-norm > 0) and the resulting MAR elements of only the detected active sources. The initial number of active sources obtained from MxNE is 186. It decreases to 2 sources in the seventh iteration. The green and red color represent, respectively, the time course of S1 and S2. We show the remaining sources in black. In the lower left corner, we show the estimated MAR for only nonzero sources at the last iteration. 129
5.18 One result of simulated sources at SNR = 5 dB. We show the reconstructed sources and the number of active sources (sources with l_2-norm > 0) and the resulting MAR elements of only the detected active sources. The initial number of active sources obtained from MxNE is 261. It decreases to 5 sources in the 7^{th} iteration. The green and red color represent, respectively, the time course of S1 and S2. We show the remaining sources in black. In the lower left corner, we show the estimated MAR (5×5 matrix) for the 5 nonzero sources at the last iteration. 130
5.19 The mean of reconstruction error of mixed norm estimates and iSDR (with $p = 2$) for the synthetic simulation when considering MAR model of order 2 for different initialization of MAR matrices at three different noise levels. 131
5.20 The values of the reconstructed initial source estimate of S_1 and S_2 (with $p = 2$) for the synthetic simulation when considering MAR model of order 2 at three different noise levels and initialization of iSDR. The ground truth values are shown in black. 132
5.21 An example of the time course from iSDR by considering initial values (a) (α, β) = (1.0, 0.0) (b) (α, β) = (0.75, 0.25) and (c) (α, β) = (0.5, 0.5) at SNR equal to 5dB. 133
5.22 The values of the reconstructed eigenvalues of the MAR model from iSDR (with $p = 2$) at three different noise levels and initialization of iSDR. The ground truth values are shown in black. From left to right: iSDR with $(\alpha, \beta) = (0.5, 0.5)$, $(\alpha, \beta) = (0.75, 0.25)$, $(\alpha, \beta) = (1.0, 0.0)$. The estimated eigenvalues with positive real part are superposed with the ground truth. 134
5.23 Sub-figure (a) and (b) show, respectively, where faces produced greater BOLD response than scrambled faces using a statistical test on fMRI data (p<0.001 uncorrected) and famous vs scrambled faces (Wakeman et al., 2015). In (c), we show the group-averaged fMRI t-value maps with a contrast of face stimulus conditions against the baseline (Fukushima et al., 2015). 135

5.24 The effective network obtained from real data (Wakeman et al., 2015) using dhVB (Fukushima et al., 2015) for the 11 subjects. 136
5.25 Different views of the functionally relevant structural network that predicts fMRI signal for face recognition task. Nodes reflect parcels and edges are anatomical connections that are significant predictors of fMRI data. The node's size are scaled with its task selectivity, large spheres represent parcels with higher face selectivity. (adopted from Osher et al., 2016) 136
5.26 Activation strength, after bias correction, of the obtained regions using (a) iSDR with $p = 1$ and (b) MxNE for subject 1. There are 70 active regions in both reconstructions. Some of the noticeable differences between iSDR and MxNE reconstructions are shown in circles. 138
5.27 The activation strength, after bias correction, of the obtained regions using (a) iSDR with $p = 1$ and (b) MxNE for subject 2. 69 and 70 regions for iSDR and MxNE respectively. Some of the noticeable differences between iSDR and MxNE reconstructions are shown in circles. 139
5.28 Effective network of subject 1 during face recognition and perception. Each node represents a parcel. The size of each uni/bi-directed edge represents the mean of the absolute value of the effective connectivity of one or both directions. 70 regions were found to be active. 140
5.29 Effective network of subject 2 during face recognition and perception. Each node represents a parcel. The size of each directed edge represents the mean of the absolute value of the effective connectivity of both directions. 69 regions were found to be active after 7 iterations. 141
5.30 Effective network of subject 3 during face recognition and perception. Each node represents a parcel. The size of each directed edge represents the mean of the absolute value of the effective connectivity of both directions. 71 regions were found to be active after 5 iterations. 142
5.31 Effective network of subject 12 during face recognition and perception. Each node represents a parcel. The size of each directed edge represents the mean of the absolute value of the effective connectivity of both directions. 69 regions were found to be activated after 8 iterations. 143
5.32 Effective network of subject 13 during face recognition and perception. Each node represents a parcel. The size of each directed edge represents the mean of the absolute value of the effective connectivity of both directions. 72 regions were found to be active after 4 iterations. 144

5.33 Effective network of subject 15 during face recognition and perception. Each node represents a parcel. The size of each directed edge represents the mean of the absolute value of the effective connectivity of both directions. 71 regions were found to be active after 4 iterations. 145
5.34 The active regions of participant 1 using iSDR of order 2 shown on the inflated surface. We show three-time courses of medial occipital (MO) (in blue), right fusiform area (RFF) (in black), and a region in the orbitofrontal area (OF) (in red). . 147
5.35 The effective connectivity between the different active regions (55 patches) of subject 1 obtained by iSDR with order 2 from MEG data. The highest eigenvalue of the companion matrix is 1 which means that there are nonstationary source signals. 148
5.36 The active regions of participant 1 using iSDR of order 2 shown on the inflated surface obtained from EEG data. We observe a negative peak around 200 ms in RFF. 149
5.37 The effective connectivity between the different active regions (53 patches) of subject 1 obtained by iSDR with order 2 from EEG data. The highest eigenvalue of the companion matrix is 1 which means that there are nonstationary source signals. 150
5.38 The temporal course obtained by iSDR ($p = 2$) from MEG of a right FF area (a) and a left FF (b). In (c) and (d), we show the temporal course of a right FF and left FF region respectively. Each curve is normalized with its l_2-norm for comparison between the 9 subjects. In (d), we show the average, over subjects, of temporal courses of the left and right FF. 153
5.39 Acquired EEG and MEG data and the explained data, computed as $G_d J_v$, with iSDR(p = 2) of subject 15. We show the reconstructed MEG after magnitude debiasing. No magnitude debiasing is applied for reconstructed EEG. Our initialization favors small activations at the beginning, but could explain accurately the remaining time samples. 154

6.1 Source reconstruction of synthetic data using MEM solver with three parcellations (MSP, Ransom and dMRI-based parcellation) 162

List of Tables

4.1 The number of seeds for each subject after removing the thalamus. 66
4.2 Mean and standard deviation (std) of the parameters of the linear relationship between N_r and T (Eq 4.14) when using a mesh of size 10^4. 68
4.3 Mean and standard deviation (std) of the parameters of the linear relationship between N_r and T (Eq 4.14) when using high a resolution mesh (3×10^4). 69
4.4 Mean $\pm$ standard deviation (in cm^2) of MNN parcellation regions area using Tanimoto similarity measure and different T values. 89

5.1 The mean and standard deviation (std), over 100 runs, of the initial values of the reconstructed active sources S_1 and S_2 error over 100 runs at different noise levels (SNR ={15, 10, 5} dB). 124

List of Abbreviations

AP	**A**ction **P**otential
CNS	**C**entral **N**ervous **S**ystem
CSF	**C**erebro**S**pinal **F**luid
CT	**C**omputed **T**omography
CV	**C**oefficient of **V**ariation
CP	**C**onnectivity **P**rofile
dMRI	**D**iffusion **M**agnetic **R**esonance **I**maging
DTI	**D**iffusion **T**ensor **I**maging
EEG	**E**lectro**E**ncephalo**G**raphy
FOCUSS	**FOC**al **U**nderdetermined **S**ystem **S**olution
fMRI	**F**unctional **M**agnetic **R**esonance **I**maging
FF	**F**usi**F**orm
TP	**T**emporal **P**ole
GCV	**G**eneralized **C**ross **V**alidation
iSDR	**i**terative **S**ource and **D**ynamics **R**econstruction
IRLS	**I**terative **R**eweighted **L**east **S**quares
IOG	**I**nferior **O**ccipital **G**yrus
LFF	**L**eft **F**usi**F**orm
LCMV	**L**inearly **C**onstrained **M**inimum **V**ariance
LORETA	**LO**w **RE**solution brain electromagnetic **T**omogr**A**phy
LASSO	**L**east **A**bsolute **S**hrinkage and **S**election **O**perator
MNE	**M**minimum **N**orm **E**stimates
MNN	**M**utual **N**earest **N**eighbor
MEG	**M**agneto**E**ncephalo**G**raphy
MEM	**M**aximum **E**ntropy on the **M**ean
MUSIC	**MU**ltiple **SI**gnal **C**lassification
OF	**O**rbito**F**rontal
PET	**P**ositron **E**mission **T**omography
PSP	**P**ost-**S**ynaptic **P**otential
RAP MUSIC	**R**ecursively **AP**plied **MUSIC**
RFF	**R**ight **F**usi**F**orm
sWMNE	structural **Weighted** **M**minimum **N**orm **E**stimates
SVD	**S**ingular **V**alue **D**ecomposition
SSS	**S**ignal **S**pace **S**eparation
SQUID	**S**uperconducting **QU**antum **I**nterference **D**evice
WMNE	**Weighted** **M**minimum **N**orm **E**stimates

Dedicated to my parents…

Chapter 1

Introduction

Contents

1.1 Nervous system 2
1.2 The brain 3
1.2.1 Gray matter 4
1.2.2 White matter 5
1.2.3 Neurons: the building block 7
1.3 Structural and functional organization of the brain 9
1.4 Functional neuroimaging 11
1.4.1 Metabolic imaging 11
1.4.2 Electromagnetic imaging 13
1.5 Structural neuroimaging 17
1.6 Conclusion 19

The human nervous system (NS) is a complex system that allows and controls interactions between the different organs and the external environment. Also, it manages the communication between the different body parts. The brain is the core part of the NS. It is estimated to have around 100 billion neurons which exchange information through interneuronal connections. This exchange is driven by an electrochemical phenomenon which can be measured directly or indirectly using several imaging modalities.

In this chapter, we review the basic anatomy of the NS and the functions of its different parts. We also introduce briefly, some functional and structural imaging modalities which give insight into the brain activity and underlying structure.

1.1 Nervous system

The role of the nervous system, as stated before, is to coordinate body's deliberate and unconscious functions. It gathers and receives information, coming from the internal and external environment, and determines the appropriate action(s) to be conducted by different body parts. The communication is done through electrical and chemical signals that will be explained later in this chapter.

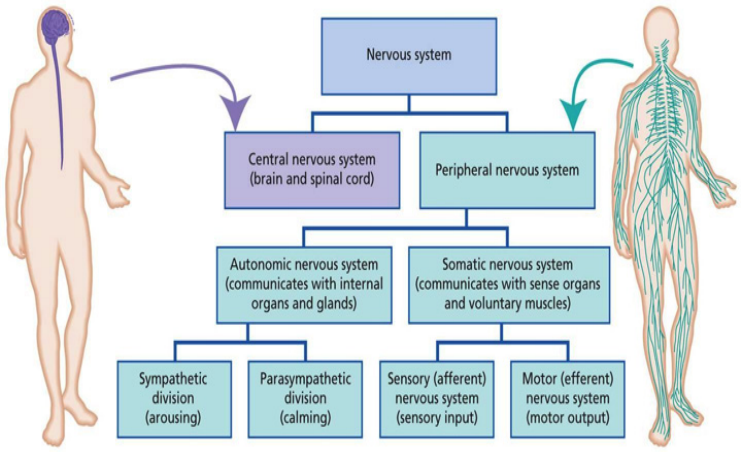

Figure 1.1: ***The central nervous system (CNS) and peripheral nervous system (PNS). (source http://activateanddominate.com)***

The NS consists of several parts that are task specific, see Figure 1.1. The nervous system can be decomposed into: *central nervous system* (CNS) and *peripheral nervous system* (PNS). CNS consists of the brain and spinal cord. It is responsible for all central processing. The PNS is an extension of the CNS and consists of cranial and spinal nerves emerging from the brain and spinal cord respectively. It delivers the sensory and motor impulses between the CNS and the body surfaces, skeletal muscles, and internal organs. The *PNS* is decomposed functionally into two parts: *somatic nervous system* (SNS) and

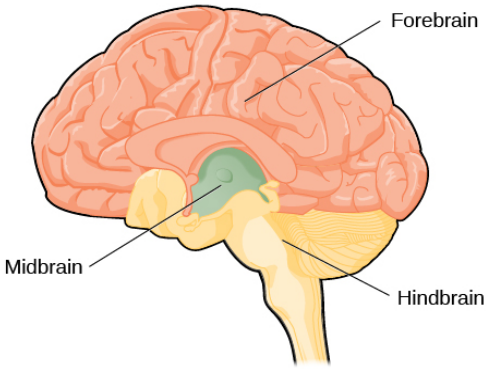

Figure 1.2: ***The three parts of the brain: Hindbrain, Midbrain and Forebrain. (source aslamnadeem.blogspot.com)***

autonomic nervous system (ANS). ANS is responsible for controlling the internal organs without any consciousness. SNS is responsible for transmitting the sensation information from the sensory organs to the CNS. Also, it is responsible for transmitting motor commands from CNS to the body (Rogers, 2010; Ghosh, 2011).

In this work, we focus on the brain because of its importance in gathering and processing information.

1.2 The brain

The brain is the primary unit of the nervous system. It works as the body's information processing and decision-making center. The adult human brain weighs, on average, 1.5 Kg (Rogers, 2010). It is enclosed by the thick bones of the cranium and wrapped in three layers of membranes known as the *meninges*. It floats in the *cerebrospinal fluid* (CSF) which fills the open chambers in the brain and the ventricular system, and spaces around the brain. CSF protects the brain tissue from injury when jolted or hit i.e it works as a shock absorber.

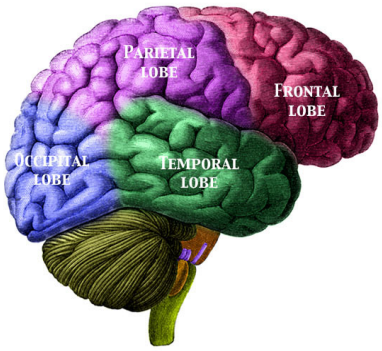

Figure 1.3: ***The four different lobes of human brain. (source wikipedia)***

The brain is divided into three parts. The *Hindbrain*, *Midbrain* and *Forebrain* (see Figure 1.2). The Hindbrain consists of the Medulla, Cerebellum and the Pons (brainstem + cerebellum). Medulla is located deep in the head just above the spinal cord. Pons is located above the Medulla. The cerebellum is located in the bottom rear of the brain. They are involved in regulating body maintenance, dreaming, movement control and coordination.

The Midbrain represents the uppermost portion of the brainstem. It contains numerous important nuclei and white matter tracts, most of which are involved in motor control, as well as auditory and visual pathways. Notable midbrain nuclei include the superior and inferior colliculus nuclei (Ruchalski et al., 2012).

The last part, Forebrain, consists of the cerebral cortex and subcortical structures: thalamus (a gate between the spinal cord and the cerebral cortex), hypothalamus (emotions control) and hippocampus (a storage facility for long-term memory).

The Forebrain is further decomposed into two hemispheres that are connected by the corpus callosum and Diencephalon (a part of the forebrain that contains the epithalamus, thalamus, hypothalamus). The two hemispheres are divided into 4 lobes: Frontal, Parietal, Temporal, and Occipital lobes (see Figure 1.3). Each lobe contains regions responsible for processing information coming from different sources, internal and external. This processing is made by the neurons situated in the Forebrain.

- Frontal lobe is associated with reasoning, planning, parts of speech, movements, emotions and problem-solving.
- Parietal lobe is associated with movements, orientation, recognition and speech.
- Occipital lobe is associated with visual processing.
- Temporal lobe is associated with perception and recognition of auditory stimuli, memory and speech.

The Forebrain volume consists of two distinct volumes: gray and white matter (Figure 1.4). They play important role in information processing and action decisions.

1.2.1 Gray matter

Gray matter is made up of the neuronal cell bodies, dendrites, synapses and glial cells. Because it mainly consists of neurons and their supporting cells, it is considered to be the processing unit of the brain and handles the complex and high-level processing of information. Its surface is topographically highly folded (in humans) or wrinkled and is marked by the formation of slit-like fissures or valleys known as sulci and raised ridges between these fissures known as gyri. Neurons in the gray matter are connected via horizontal fibers which unfortunately are not detected by non-invasive imaging modality.

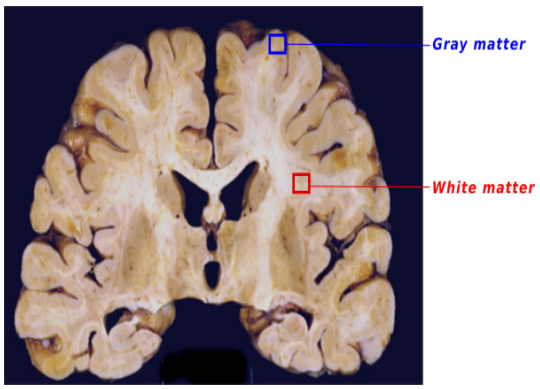

Figure 1.4: ***White and Gray matter in a coronal slice. (adapted from bestpractice.bmj.com)***

1.2.2 White matter

As stated before, gray matter consists of cell bodies of neurons and glial cells. Because glial cells play a supporting role, we are interested only by neurons. The myelinated axons, originating from neurons, constitute white matter. These axons connect several regions of the gray matter to other regions of gray matter and to the spinal cord through organized pathways. Depending on the endpoints of these pathways (axons/fibers), they can be divided into three categories:

- **Commissural fibers**, also known as transverse fibers: They connect different sites of the two hemispheres. *Corpus Callosum (CC)* is the largest and the most important commissural structure. Another important commissural structure is the *anterior commissure*, see Figure 1.5. An example of these pathways can be seen in Figure 1.6c.

- **Association fibers:** they are fibers that connect cortical regions within the same hemisphere. They are divided into two groups. *U-shape* fibers are short fibers that connect adjacent sites/regions. They lie immediately under the gray matter. Long association bundles are pathways that connect distant sites/regions.

  An example of an association fiber, that can be seen in Figure 1.6b, is the uncinate fasciculus that connects frontal and temporal lobe or the superior longitudinal fasciculus that connects frontal and occipital lobes. The temporal and occipital are connected through inferior longitudinal fasciculus.

- **Projection fibers:** these are the ascending or the descending pathways connecting some cortical region to cerebellum, spinal cord and subcortical areas such as thalamus. Functionally, the main descending pathways are motor fibers, whereas the ascending fibers are mainly sensory.

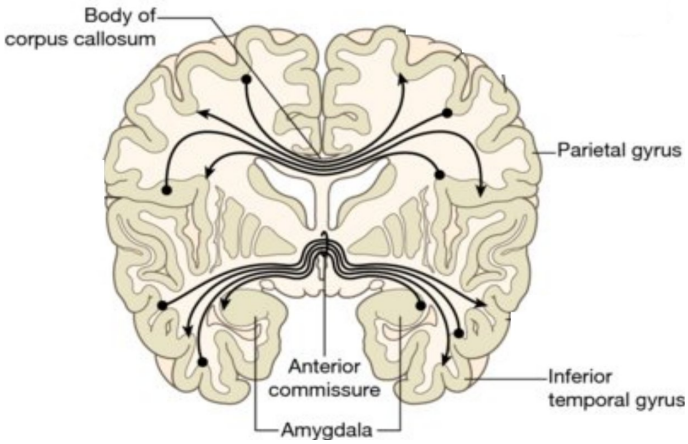

Figure 1.5: ***The corpus callosum and anterior commissure. (adapted from http://www.wileyessential.com)***

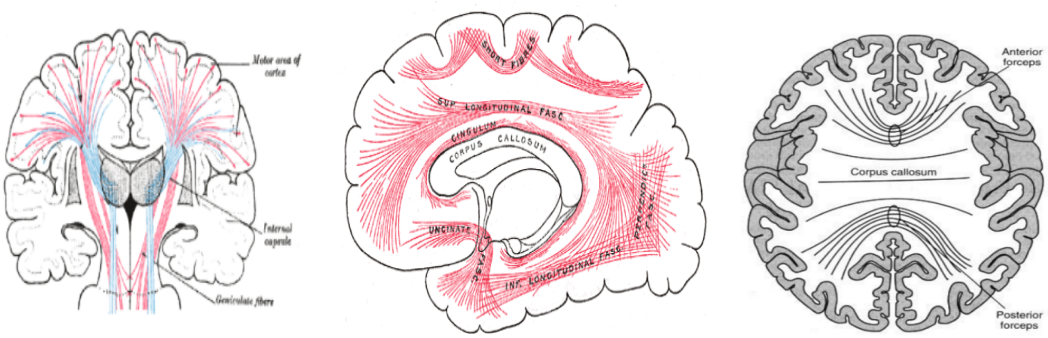

(a) (b) (c)

Figure 1.6: ***White matter fibers: (a) Ascending (blue sensory fibers) and descending (red motor fibers) projection fibers (adapted from Gray, 1918) (b) Short and long association fibers. They are pathways that connect regions of the same hemisphere (adapted from Gray, 1918) and (c) commissural fibers that connect the two hemispheres.***

Like in all body parts, water is present in the white matter. The fibrous structure of the white matter constrains the motion of the water molecules. Water molecules move less easily in a direction perpendicularly to the fibers because they are restricted inside or outside the axons. But, they move freely parallel to the fibers. Diffusion magnetic resonance imaging (dMRI) is an imaging modality that is sensitive to the motion of water molecules. It can be used to perceive the microstructure and pathways of the white matter but it fails to detect horizontal fibers located in the gray matter. More details about dMRI can be found in Chapter 3.1.

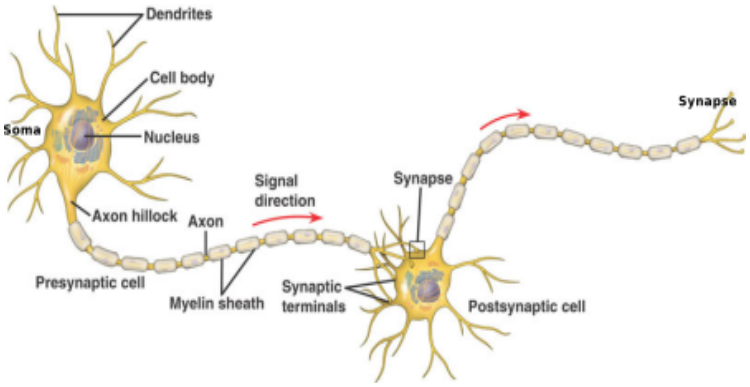

Figure 1.7: ***The neuron structure and its connections. (adapted from http://biology.stackexchange.com)***

1.2.3 Neurons: the building block

Gray matter contains the processing units which are neurons. A neuron is an electrically excitable cell which is capable of processing and transmitting information. Because information can not travel forever, we also find inhibitory neurons which work as information blockers. Neuron consists of four parts: dendrites, soma, axon and synapses (see Figure 1.7). Dendrites are short filaments attached to the cell body forming a tree-like shape. They collect information from other neurons and pass it to the soma. The soma is the part of neuron that processes the information coming from the dendrites. The axon is responsible for transmitting information from the soma to the other neurons via synapses.

There are special cells in the CNS to serve, protect, and support neurons. They are called neuroglia cells. They form myelin which wraps around neuronal axons. They improve both the efficiency and speed of the neuronal transmission. Neuroglia cells also provide oxygen, destroy pathogens and provide a general support structure to neurons. Axons have a diameter of few microns and can extend to a meter in the human brain. Unmyelinated axons are poor transmitters of the electrochemical signals due to leakage of ions.

Oligodendrocyte is a type of glial cell that creates myelin sheaths around the axons in the CNS which help to improve the efficiency and transmission speed (Baumann et al., 2001). *Astrocytes* is a star-shaped glial cell. It works as a bridge between blood vessels and neurons. They provide nutrients for neurons and protects them from unwanted substances. Also, they work as modulation to cell-to-cell communication by releasing and/or absorbing ions and neurotransmitters (Santello et al., 2009).

As stated before, the axons work as transmitters between the soma and synapses. They transmit signals that are called Action Potentials (AP), see Figure1.8. A neuron receives several input signals (postsynaptic potentials (PSPs)) through its dendrites from the different neurons that it is connected to. Then, the neuron will spike or not i.e. transmit an AP to other neurons

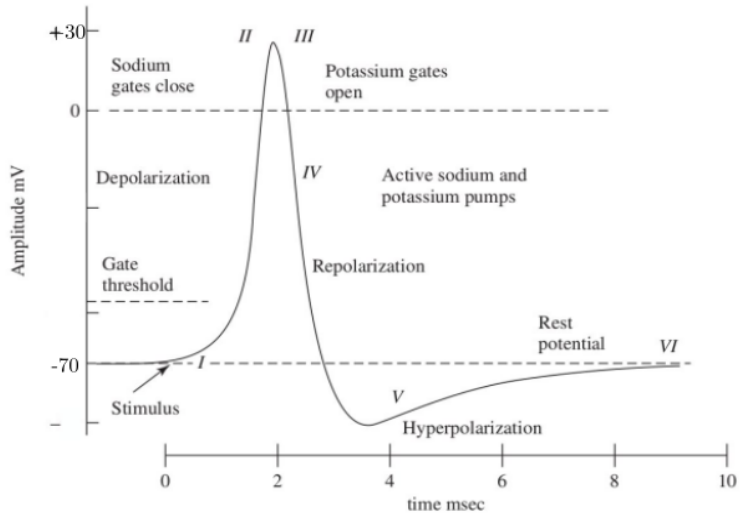

Figure 1.8: ***An example of Action potential (adapted from Sanei et al., 2007)***

through its synapses.

How do neurons transmit and receive information?

The signals in the dendrites are called postsynaptic potentials (PSPs) i.e. received information. The signal emitted, moving along the axon of a neuron, is called action potential (AP) i.e transmitted information.

The junction between axon terminal of a neuron and a dendrite or a soma of another neuron can be chemical or electrical, but synapses are mostly chemical. When an AP arrives at the end of an axon terminal, it leads to the release of neurotransmitters. These neurotransmitters reach other neurons and affect their membrane permeability so that specific ions (Sodium (Na) and Potassium (K)) penetrate inside the neuron (Gramfort, 2009).

Figure 1.8 shows an example of an action potential. APs are triggered if the sum of the received information (PSPs) is above a certain threshold through cell body and axon. This threshold is a change of 20 mV from the resting membrane potential which is around -70 mV. This results to opening of ions channels which yields to a change in the membrane potential.

When the threshold is reached, Na^+ gates opens which result to gradients of Na^+. Na^+ ions concentration is higher outside the cell. The gradients allow the Na^+ ions to enter the cell through Na^+ gates. This makes the membrane's potential positive (depolarization), see Figure 1.8. For human being, the AP amplitude ranges between approximately -70 mV and +30 mV (Sanei et al., 2007). The steps of AP can be summarized by the following (Sanei et al., 2007):

I When the Dendrites of the cell receive the stimulus, Na^+ gates open. This allows the Na^+ to enter the cell making the membrane's potential positive. If the membrane's potential is higher than a threshold, the process continues. If not, the membrane's potential will come back to rest potential.

II More Na^+ ions enter the cell. This results in an increase of the membrane's potential. It is called depolarization.

III Na^+ ions' gates close and K^+ ions' gates open.

IV With the K^+ ions' gates open, the membrane potential begins to repolarized back towards its rest potential because K^+ ions get out from the axons.

V The repolarization results to overshoot in the membrane's potential. This is called hyperpolarization.

VI Finally, the membrane's potential comes back to its rest value.

When Na^+ and K^+ penetrate the cell body, a potential difference is created. This results in a current flowing through the axon. The current flowing from the soma to the dendrites is called the intracellular (**primary**) current. Since the electric charges need to be conserved, extracellular (**secondary**) currents are generated. Both currents, primary and secondary, contribute to creating an electric and magnetic field that can be measured outside the head or on the scalp under some conditions, see section 1.4.2.1.

The current generated by a single neuron is too small and its electromagnetic field decays proportionally with the inverse of the distance to the field's origin. Hence, the currents of several neurons located in a small region must be synchronized to be picked up by sensors outside the brain. Because the duration of an action potential is too short (1 ms) to allow synchronization and it deceases faster than PSP, postsynaptic potential (last for several tens of millisecond) are likely the main contributors to the measured electromagnetic field. Another condition to measure the brain activity is that postsynaptic potentials (PSP) must have the same direction to add up. Contrary to the stellate neurons whose dendrites are oriented in all directions, pyramidal cells, which constitute about 70%-80% of the neocortex (Gramfort, 2009), are orthogonal to the cortical surface and thus well designed to generate PSPs in the aligned directions.

1.3 Structural and functional organization of the brain

The first work that reported a localized functional region was done by Broca in 1861. He performed an autopsy on a patient who suffered from what is known now by Broca's aphasia. The patient could understand what was being said to him but he failed to generate meaningful sentences. Broca concluded that the illness due to a large defect in a region that called Broca's area (Johansen-Berg et al., 2009).

Gray matter is composed mainly of neurons and their supporting cells. It has been shown that neurons in the gray matter have a vertical organization (Sanei et al., 2007). There are mainly six layers in the cortex, numbered from

the outer surface of the cortex to the white matter, Figure 1.9 (Kandel et al., 2000).

- Layer I: consists mainly of dendrites of the cells located deeper in the cortex and horizontal axons.
- Layer II: external granular layer consists of small pyramidal and stellate neurons.
- Layer III: external pyramidal layer contains moderate size pyramidal cells.
- Layer IV: internal granular layer contains different types of stellate and pyramidal neurons.
- Layer V: internal pyramidal layer consists of large pyramidal cells.
- Layer VI: polymorphic (or multiform layer) consists of pyramidal and multiform cells.

Every layer is defined primarily by the presence or the absence of neuronal cell bodies, each layer also contains additional elements. Thus, layer $I - III$ contain the apical dendrites of neuron that have their cell bodies in layer V and VI, while layer V and VI contain the basal dendrites of neurons with cell bodies in layer III and IV (Kandel et al., 2000).

Figure 1.9 shows the six different layers at four different brain locations. The primary motor cortex has a thin layer IV but a prominent layer III. Primary visual cortex has a prominent layer IV. As can be seen, the gray matter layers differ in thickness, cell composition and also between cortical regions (Sanei et al., 2007; Vallaghé, 2008). Based on these cytological differences, the cortex can be subdivided into 52 Brodmann's regions (Kandel et al., 2000).

The work of Brodmann (Brodmann, 1909) was the basis of several other works that define regions as having dissimilar microstructures. Brodmann separated regions that differ in cell density, size and layering i.e histology (Sporns, 2011), see Figure 1.10. With the introduction of functional imaging modalities (see section 1.4), some Brodmann's regions appear to coincide in part/total with specific functional tasks (Binder et al., 1997; Hoenig et al., 2005).

In (Passingham et al., 2002; Sporns et al., 2004; Tomassini et al., 2007), authors show that the structural connectivity (connections between neurons through the white matter) can be another indicator for the functional homogeneity of cortical regions. Diffusion magnetic resonance imaging (dMRI) is a non-invasive modality that allows the access to this structural connectivity. More information about dMRI and structural connectivity can be found in Chapters 3.1 and 4.1, respectively.

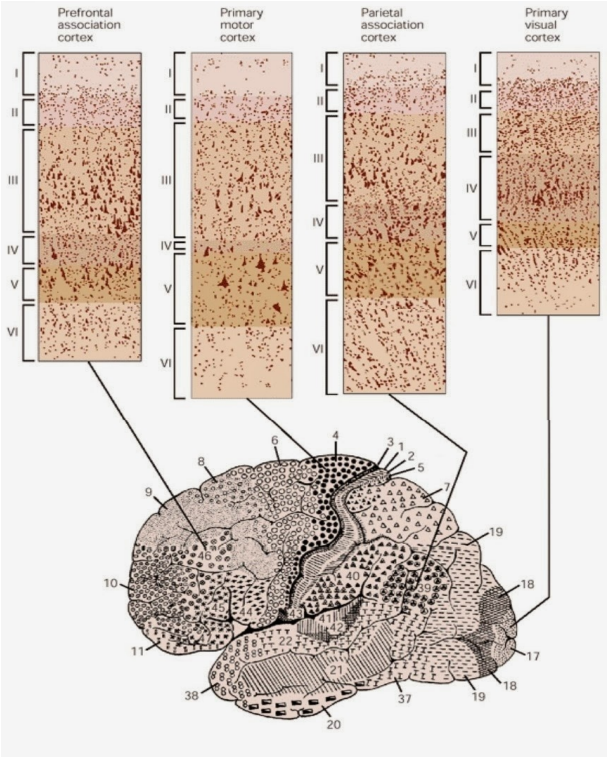

Figure 1.9: ***The six layers of the gray matter in different locations. (adapted from Kandel et al., 2000)***

1.4 Functional neuroimaging

Functional neuroimaging is the use of an imaging modality to measure the brain activity of a specific mental or physical function i.e. a reaction to an external stimulus. It can be also used to measure the resting state of the brain. It can be divided into two groups: metabolic and electromagnetic imaging. Positron emission tomography (PET) and functional magnetic resonance imaging (fMRI) are considered as Metabolic imaging techniques. In electromagnetic imaging, we can find Electroencephalography (EEG) and Magnetoencephalography (MEG). The advantage of electromagnetic over metabolic imaging is that in the former we measure directly the brain activity, whereas, in the latter we measure an indirect metabolic response to an activity: the variation of oxygen's quantity for fMRI or radioactivity emitted by tracer in PET.

In the following sections, we introduce briefly these two types of functional neuroimaging.

1.4.1 Metabolic imaging

As stated before, the metabolic imaging modalities measure indirectly the brain activity. In this chapter, we describe briefly two imaging modalities that lie under this category.

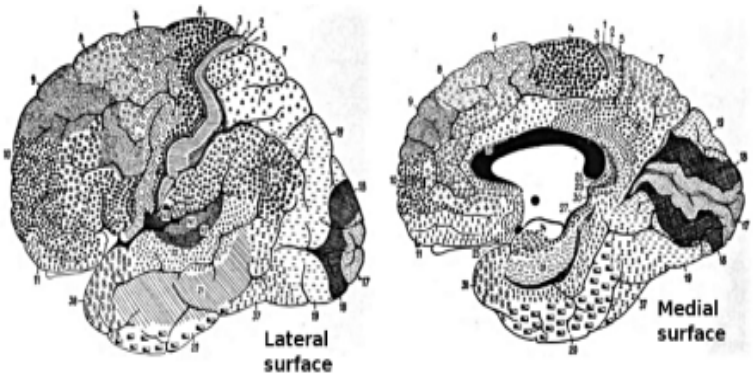

Figure 1.10: ***Cortical areas defined by Brodmann (Brodmann, 1909). The cortical areas are divided according to the thickness of the cortical layers. (source wikipedia)***

1.4.1.1 Positron emission tomography

Positron emission tomography (PET) is an invasive functional imaging modality that is used to observe metabolic processes of the body, including the brain. It consists of injecting a radioactive tracer substance, generally fludeoxyglucose (FDG) an analogue of glucose, in the bloodstream which then travels to the brain. PET is based on the assumption that the areas of high radioactivity (areas with high blood flow) are associated with brain activity i.e the tracer is metabolized by active cells (Dendy, 2006).

Radiation is emitted where the blood is located. We observe higher concentration of radiations in brain regions that use higher amount of blood i.e. active regions. PET can localize different radioactive concentrations in the brain, which allows us to have an idea about the blood flow hence the brain activity.

During a task or rest, the brain needs blood. To obtain the task related map using PET imaging, we need to subtract it to the image obtained from PET during rest. This can be seeing in Figure 1.11. It shows a slice of PET images during rest and a motor task. The brain region responsible for the motor task (indicated by an arrow) is then obtained by subtracting the two images.

PET imaging suffers from several drawbacks. It is an expensive modality. Because it is an invasive modality, its use is undesirable by patients. But it is still be used because of its ability to study body functions and to detect early stages of neurological illnesses such as epilepsy, and also, because of its very good spatial resolution.

1.4.1.2 Functional magnetic resonance imaging

On the contrary to PET, functional magnetic resonance imaging (fMRI) is a non-invasive imaging modality. It works by detecting the changes in the blood oxygenation and flow that occur after neural activity. An active region consumes more oxygen than usual. This increases the blood flow to that region. Oxygen is transported to neurons via haemoglobin carried by red

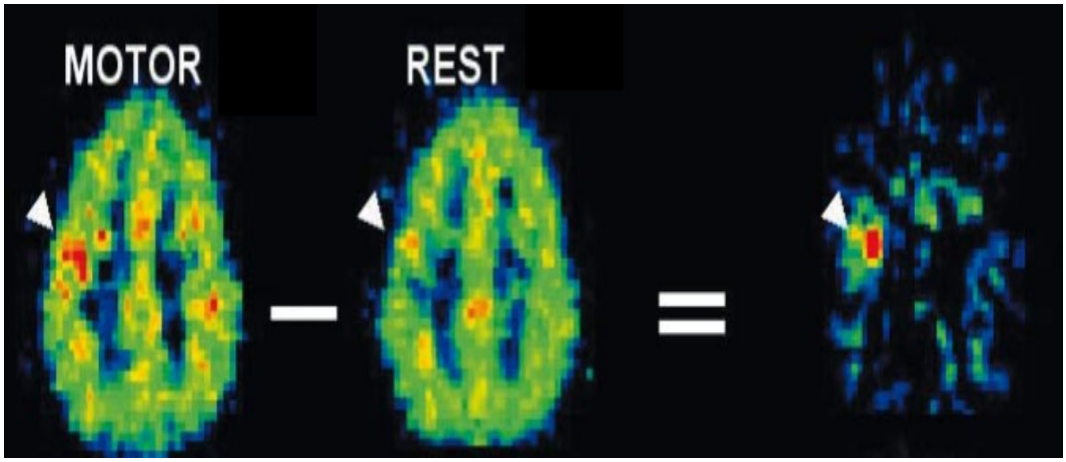

Figure 1.11: ***PET images during rest and a motor task. (adapted from http://www.dialogues-cns.com)***

blood cells. When oxygenated, it is diamagnetic and paramagnetic when the hemoglobin is deoxygenated. This difference in the magnetic properties leads to a small difference in the MR signal. This type of MRI is known as blood oxygenation level dependent (BOLD) signal. It is worth mentioning that the blood oxygenation increases after a neural activation with a delay of few seconds.

fMRI has high spatial resolution (few mm) but low temporal resolution (time scale of hemodynamic processes i.e. few seconds). Like PET, fMRI needs to be compared to a resting state fMRI (rfMRI) to have an idea about active regions during a specific task.

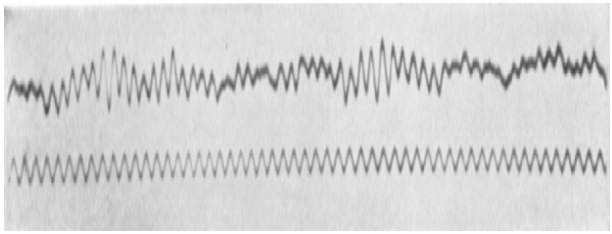

Figure 1.12: ***One of the first EEG recording by H. Berger (adapted from Galán, 2013). On top, we show the actual recorded signal. On bottom, we show a sinusoidal reference signal of 10 Hz.***

1.4.2 Electromagnetic imaging

1.4.2.1 Electroencephalography

Electroencephalography (EEG) is the recording of time-varying voltages on the human scalp generated by the electrical activity of the brain (Nunez, 2005). Hans Berger was the first to measure the time traces of human brain electrical activity (Figure 1.12) in 1924/1929. He gave the name of ***electroencephalogram*** to the measured signal (Schomer et al., 2012).

- Electro refers to the registration of brain electrical activities.
- Encephalo refers to signals coming from the head.
- Graphy or gram which means drawing or writing.

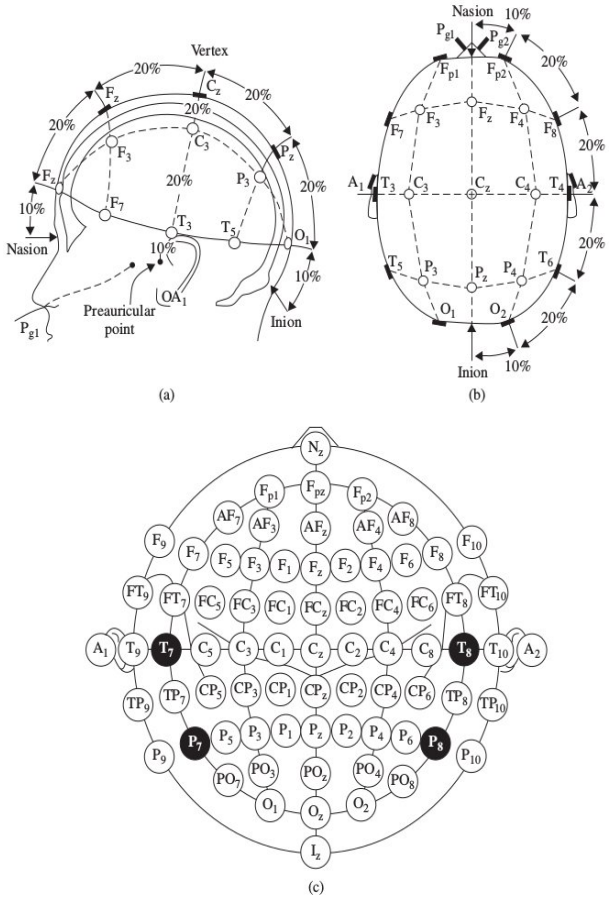

Figure 1.13: ***A diagram representation of 10-20 electrodes settings for 75 electrodes: (a) and (b) 3D representation, and (c) 2D view (Sanei et al., 2007).***

They are combined so that the acronym EEG is used to denote electrical neural activity of the brain (Sanei et al., 2007). To be more specific, it measures the electric field generated by the postsynaptic activity that flows along the dendrites of the pyramidal nerve cells, see Figure 1.14a. The current dipole of a cortical pyramidal cell is around 0.2 pA which can not be measured outside the brain. The weakest measurable cortical signal are when you have a current of around 10 nA which corresponds to about 50000 synchronous cells. This number of cells can be found in a cortical area of around 0.63 mm^2 which corresponds to a circular patch with diameter 0.9 mm (Schomer et al., 2012). However, an experimental study showed that the minimal detectable activity spreads over an area of about 100 mm^2 (Hämäläinen et al., 1993a).

While Berger originally only used a single pair of electrodes to record the potential difference between two locations on the scalp, modern EEG

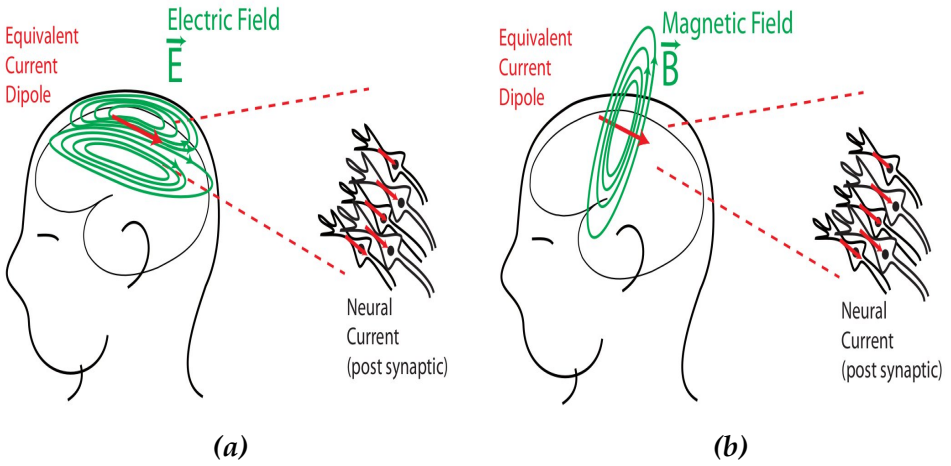

Figure 1.14: ***Schematic diagrams showing the generated (a) electric and (b) magnetic fields from an equivalent current dipole. (adapted from Gramfort, 2009)***

uses several electrodes that are usually glued to the skin or located in an elastic cap with uniform coverage of the entire scalp to measure the brain activity. Figure 1.13 shows an example of the EEG sensors (75 electrodes) position following the 10-20 electrodes setting. EEG is recorded in very high temporal resolution (order of 1 ms) which gives a detailed temporal view of the brain activity.

EEG is inexpensive with respect to other imaging modalities. It requires only a set of electrodes, an amplifier and a computer. That is why, with its high temporal resolution, it is used even if it has poor spatial resolution (1 cm).

1.4.2.2 Magnetoencephalography

Magnetoencephalography (MEG) was first measured by David Cohen in 1968, using a copper induction coil as detector (Galán, 2013). MEG is the recording of the magnetic field produced by the same activity as EEG (almost, the difference will be explained in the next section), see Figure 1.14b. They are generated by current flowing in neurons. There is a small contribution to the MEG from the current flow in the volume-conducting medium around the neurons. Typically, it ranges from 10 to 100 fT ($1fT = 10^{-15}T$, where T stands for Teslas). The Earth's static magnetic field is about billion times bigger than the typically measured MEG.

MEG is very sensitive to noise due to the range of magnitude of the magnetic field generated by brain activity. To reduce interference, the MEG system is placed inside a shielded room (see Figure 1.15) and noise cancellation techniques are used. Measuring such extremely small magnetic fields requires a specific sensor. It is called Superconducting Quantum Interference Device.

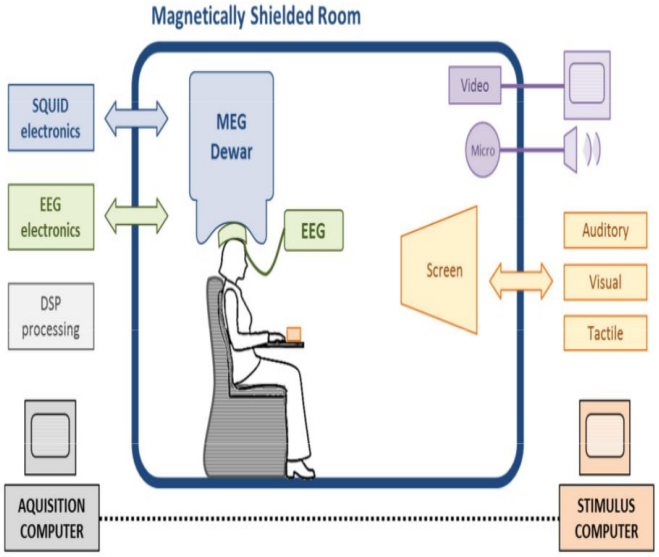

Figure 1.15: ***System of simultaneous MEG and EEG acquisition (Galán, 2013).***

The most important part of the MEG system is the dewar that contains Superconducting Quantum Interference Device (SQUID). The SQUIDs work in low temperature. That is why they are cooled down using liquid helium (Schomer et al., 2012). Modern MEG systems consist of a helmet-shaped dewar that contains hundreds of sensors and that fits the subject's head.

The use of liquid helium to cool the SQUIDS makes MEG expensive compared to EEG. But it has a better spatial resolution (few mm). This makes it a very attractive imaging modality.

EEG/MEG rythms

Neuroelectrical recording can produce signals with different characteristics depending on the activity. In the first EEG recording by Hans Berges, a strong oscillation activity at 10 Hz was observed, see Figure 1.12. Other oscillations of different frequencies can be observed by both EEG/MEG and divided into distinct frequency bands (Schomer et al., 2012; LopesÂădaÂăSilva, 2013):

- Delta band: <4 Hz e.g deep sleep.
- Theta band: 4-7 Hz e.g drowsiness.
- Alpha band: 8-13 Hz e.g focusing, relaxation.
- Beta band: 14-30 e.g for logical thinking.
- Gamma band: > 30 Hz e.g. information processing and sudden sensory stimuli.

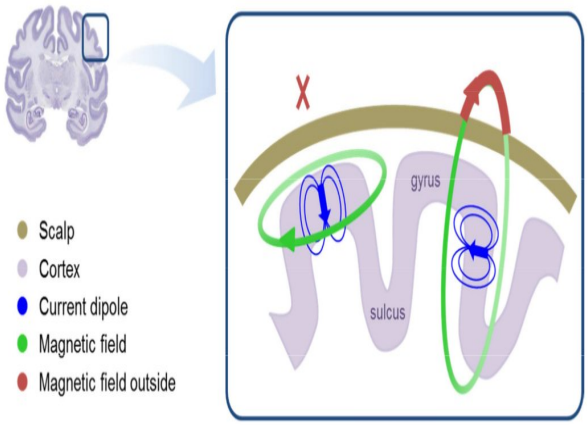

Figure 1.16: ***Magnetic and Electric fields generated by a brain activity. (adapted from Galán, 2013)***

1.4.2.3 EEG versus MEG

Both EEG and MEG modalities measure the brain activity and record it in real time with very high temporal resolution. The acquisition of MEG signals must be inside a shielded room and the use of liquid helium makes it a very expensive imaging modality compared to EEG. Another disadvantage of MEG over EEG is that it can not be used in long-term acquisition because the subject must be immobilized during the acquisition. But it is used because of its better spatial resolution.

The magnetic field is tangential to circles around the line of the current flow. Because of this, MEG is insensitive to radial dipoles, Figure 1.16. Whereas EEG is more sensitive to both tangential and radial dipoles. The most important advantage of MEG over EEG is that MEG is not affected by the smearing effects of the volume-conducting medium because all tissues between the source dipoles and the MEG sensors are transparent to magnetic fields (Schomer et al., 2012).

This means that MEG is better when we want to detect tangential dipoles and EEG is better in detecting radial sources. MEG and EEG can be viewed as complementary rather than competing imaging modalities. That is why several MEG facilities are equipped with simultaneous EEG acquisition, Figure 1.15. Artifacts originated from muscles movements, pulsating blood vessels, eye movements and blinks (occur in the delta range) and noise coming from the AC electrical line current must be eliminated before reconstructing the brain activity.

1.5 Structural neuroimaging

Structural (anatomical) neuroimaging allows to distinguish between different tissues as it shows a contrast between them. It is mostly used by clinicians to detect the presence of tumours or malformations. Computerized tomography (CT) and Structural magnetic resonance imaging (MRI) are two

of the most used structural imaging techniques. The former is based on X-ray which means that the subject is exposed to radiation during CT scan. CT is more suited to detect bones, whereas MRI is more suited for finding the contrast between soft tissues. The later relies on the magnetic properties of a hydrogen atoms to produce images and uses the concept of nuclear magnetic resonance (NMR). The hydrogen atom consists of nucleus with a single proton (positive charge) and an electron. The spinning proton produces a magnetic field that is called magnetic moment. Because hydrogen protons are oriented randomly, the net magnetic field is zero. A NMR scan is composed of a primary magnet, gradient magnets (used to select a specific slice) and a radio-frequency (RF) coils. It starts by first, applying a strong external magnetic field to a volume, called the primary magnetic field $B0$, which consequently aligns all the magnetic moments of nucleus of hydrogen atoms parallel or antiparallel to $B0$. More magnetic moments are aligned parallel to the $B0$ resulting to a net magnetic vector M. Then, it excites the nuclei with a 90 degree RF pulse that tilts the magnetic moment into the plane whose normal is along the main magnetic field $B0$. The spins subsequently start to precess around the magnetic field. The angular frequency of the precession is given by (Johansen-Berg et al., 2009)

$$\omega = \rho B_0 \tag{1.1}$$

where ρ is the gyromagnetic ratio. For the hydrogen nucleus, it is equal to 2.68×10^8 rad/s/Tesla. Spins, that are initially in-phase, dephase due to magnetic field inhomogeneity and dipolar interactions leading to a decay in the acquired signal at the NMR scan receivers (Johansen-Berg et al., 2009). The magnetic field inhomogeneity can be reversed through another 180 degrees RF pulse and the signal is reproduced (echo). This is called the *Spin-echo* experiment. The generated signal (echo) is measured by RF coils. Hydrogen protons resume their normal state, in the primary magnetic field, prior to the RF pulse (relaxation). The relaxation, time to reach the equilibrium state, can be measured in two directions

- Longitudinal magnetisation (T1): measured parallel to $B0$ and increases over time.
- Transverse (T2): measured perpendicular to $B0$ and decreases over time.

The T1 and T2 relaxation times depend on the tissue's type. This results in contrast between tissues, for example between the white and gray matter. The change in the net magnetic field induces an electrical signal which is measured by the RF coils. The MR image is then obtained by applying an inverse Fourier transform to the acquired signal.

Other acquisition sequences can be used with MR machine. The most innovated method is dMRI which can be used to perceive the microstructure and pathways of the white matter. Hence, it is an imaging modality that allows us to understand the structural organization of white matter. dMRI is explained in more details in section 3.1

1.6 Conclusion

The brain is the central unit of the nervous system. It gathers information coming from the different sensors, processes it and decides on the different actions that must be done by the different body parts. That is why understanding the brain is an important task. At a macroscopic scale, the brain is primarily constituted of grey and white matter. The grey matter consists mainly of cell bodies: neurons and supporting cells. The axons of these neurons constitute the white matter which interconnects several gray matter sites through pathways.

Metabolic imaging measures the brain activity indirectly. Active brain regions use more blood than usual. PET maps the concentration of a radioactive tracer that was injected into the bloodstream. FMRI, a non-invasive modality, quantifies the change in the blood oxygenation. Both modalities have high spatial resolution but poor temporal resolution. EEG/MEG allows measuring electrical brain activity in real time. The structural connectivity of the brain can give an insight about the functional regions, as shown in several studies. This structural connectivity can be perceived non-invasively by dMRI modality.

In our work, we use both modalities: dMRI and EEG/MEG. We try to use both informations to investigate the functional activity and homogeneity of the brain regions. It is challenging to fuse information coming from these imaging modalities because they have a quite different nature.

Chapter 2

The MEG/EEG forward and inverse problem

Contents

2.1 Introduction 22
2.2 Forward problem 22
2.2.1 The physics of EEG and MEG 23
2.2.2 Head Models 25
2.3 Inverse problem 28
2.3.1 Dipole fitting approaches 28
2.3.2 Scanning techniques 29
2.3.3 Distributed source models 31
2.3.4 Conclusion 39

2.1 Introduction

In this chapter, we introduce the physics behind the EEG and MEG measurements. The problem that consists in modelling the head in order to compute the electric potential or the magnetic field that are produced by a certain configuration of sources in the brain (measured by the MEG/EEG sensors) is called the forward problem. The MEG/EEG inverse problem is the estimation of the sources configuration from measurements. The source estimation or reconstruction is an ill-posed problem due to the small number of sensors used to measure the brain activity. Some approaches used to estimate the brain activity are presented in this chapter. These source reconstruction approaches have to assume priors on the sources to obtain a unique solution because of the ill-posedness.

First, we review the equations and the methods for solving the forward problem. Also, we list the models used to estimate the geometry of the head. Then, the inverse problem in MEG/EEG is introduced briefly.

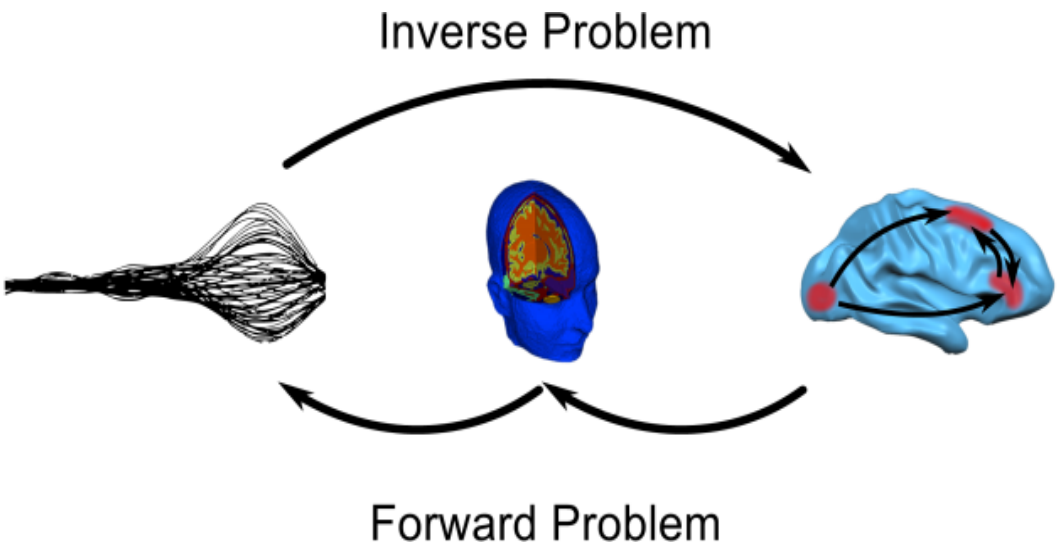

Figure 2.1: ***Illustration of MEG/EEG forward and inverse problem. (source http://www.childbrain.eu)***

2.2 Forward problem

The EEG/MEG forward model is understanding how the activation in the brain is mapped onto the EEG/MEG sensors. In other words, we want to find the contribution of each source to the measurement acquired at each sensor. But first, we need to understand how EEG/MEG measures the brain activity.

2.2.1 The physics of EEG and MEG

Understanding how the current generator located on the cortical surface can produce a distribution of potential on the scalp (EEG) or a magnetic field (MEG) outside the head is called the forward problem. The measurements depend on the generators and also on the head model. The first step to estimate the generators is the modeling of the electromagnetic properties of the head tissues and of the sensors array i.e Forward model.

2.2.1.1 Maxwell's equations

Maxwell's equations relate the electromagnetic field to charge and current density. We denote by E the electric field, B the magnetic field, ρ and J the charge and current density respectively. Maxwell's equations are a set of four equations:

$$\nabla \cdot E = \frac{\rho}{\epsilon} \tag{2.1a}$$

$$\nabla \times E = -\frac{\partial B}{\partial t} \tag{2.1b}$$

$$\nabla \cdot B = 0 \tag{2.1c}$$

$$\nabla \times B = \mu(J + \epsilon\frac{\partial E}{\partial t}) \tag{2.1d}$$

where μ is the magnetic permeability and ϵ is the electric permittivity of the medium. For human tissues, the electric permittivity $\epsilon_r = \frac{\epsilon}{\epsilon_0}$ varies a lot depending on tissue and frequency whereas the magnetic permeability μ is the same as for vacuum (μ_0). At a frequency of 100 Hz, ϵ_r is around 4×10^6 for gray matter, 5×10^5 for fat and 6×10^3 for compact bone (Gabriel et al., 1996; Gramfort, 2009). The solution of the forward problem does not depend on ϵ, because it is multiplied in Equation 2.1d by $\frac{\partial E}{\partial t}$ which will be neglected due to the Quasi-static approximation.

2.2.1.2 Quasi-static approximation

The post-synaptic potentials have a time duration of about 10 ms. As a consequence, it is commonly accepted that the time frequencies of the brain electromagnetic field that can be measured outside the head can rarely exceed 100 Hz. For such a low frequency, the time derivatives in Maxwell's equations can be neglected. This is called the quasi-static approximation.

Justification of the quasi-static approximation can be found in (Hämäläinen et al., 1993b).

2.2.1.3 The electric potential equation

In the quasi-static approximation, we neglect all the time derivatives. From Equation 2.1b, we can write:

$$E = -\nabla V \tag{2.2}$$

where V is the electric potential.

As stated in section 1.2.3, the total current generators, J, can be decomposed into two parts. The *primary current*, J^p, is a current that flows within neurons and across their membranes. The *volume current* J^v (or return/extracellular current) follows a path that depends on the tissue conductivity.

$$\begin{aligned} J &= J^p + J^v \\ &= J^p + \sigma E \\ &= J^p - \sigma \nabla V \end{aligned} \tag{2.3}$$

Neglecting the time derivative in Maxwell equations (Equation 2.1d) leads to:

$$\begin{aligned} \nabla \times B &= \mu_0 J \\ \Rightarrow \nabla \cdot \nabla \times B &= \nabla \cdot (\mu_0 J) \\ 0 &= \nabla \cdot J \end{aligned} \tag{2.4}$$

which leads to the Poisson's equation relating potential, conductivity and primary current:

$$\nabla \cdot (\sigma \nabla V) = \nabla \cdot J^p \tag{2.5}$$

with the boundary condition (head boundary):

$$(\sigma \nabla V) \cdot n = 0$$

which means that there is no current flowing outside the head, which is mostly true.

2.2.1.4 The magnetic field equation

Because $\nabla \cdot B = 0$, B is derived from a vector potential A:

$$B = \nabla \times A \tag{2.6}$$

This leads to:

$$\nabla \times B = \nabla \times \nabla \times A = \nabla(\nabla \cdot A) - \Delta A = -\Delta A \tag{2.7}$$

because of an added gauge condition ($\nabla(\nabla \cdot A) = 0$). The Maxwell's equation $\nabla \times B = \mu_0 J$ becomes $\Delta A = -\mu_0 J$ which is a Poisson equation. It has the general solution in $\mathbb{R}^3$

$$A(r) = \frac{\mu_0}{4\pi} \int_{\mathbb{R}^3} \frac{J(r')}{\|r - r'\|} dr'$$

when assuming that the magnetic field decreases to zero at infinity. The magnetic field can be obtained by applying the curl to the solution:

$$B(r) = \frac{\mu_0}{4\pi} \int_{\mathbb{R}^3} J(r') \times \frac{r - r'}{\|r - r'\|^3} dr'$$

from Eq. 2.3, the previous equation can be rewritten as:

$$B(r) = B_0(r) - \frac{\mu_0}{4\pi} \int_{\mathbb{R}^3} \sigma \nabla V(r') \times \frac{r - r'}{\|r - r'\|^3} dr', \tag{2.8}$$

with

$$B_0(r) = \frac{\mu_0}{4\pi} \int_{\mathbb{R}^3} J^p(r') \times \frac{r - r'}{\|r - r'\|^3} \tag{2.9}$$

It is worth noticing that B_0, the primary magnetic field, does not depend on the environment i.e. the value of the conductivity. This makes the magnetic field less affected by the choice of the conductivity values.

The forward problem consists in first finding the potential V given the conductivity σ and the primary current J^p using Eq. 2.5. The magnetic field is then computed using Eq. 2.8 given the conductivity, primary current and the corresponding potential.

We used OpenMEEG (Kybic et al., 2005; Gramfort et al., 2010) which uses the Boundary Element Method (BEM) to solve the forward problem from the different surfaces obtained from an anatomical image and the position and orientation of the generators and sensors. BEM is a numerical method used to solve the linear partial differential equations by transforming them into integral equations defined over the boundaries of the different tissues/domains. BEM assumes that the domains have homogeneous and isotropic conductivity.

This estimation yields to what we call the Gain (lead field) matrix, G of size $N_c \times N_s$ (number of sensors $\times$ number of sources (generators)). Each column corresponds to the contribution of a source to the sensors array. The linear relation between J^p, modeled by dipoles at discrete locations of magnitudes J, and EEG/MEG measurement (M) is:

$$M = GJ \tag{2.10}$$

It is worth mentioning that it is possible to work in volume not on a cortical surface. This can be achieved using Finite element method (FEM) (Wolters et al., 2004). Its advantage over BEM is that it could assign different conductivity values to voxels of the same tissue type.

2.2.2 Head Models

The human head is a bounded conductor and no electric current flows outside the head (except at the neck). The head has different electrical conductivities σ that depend on the tissue types. The skull is between 20 and 100

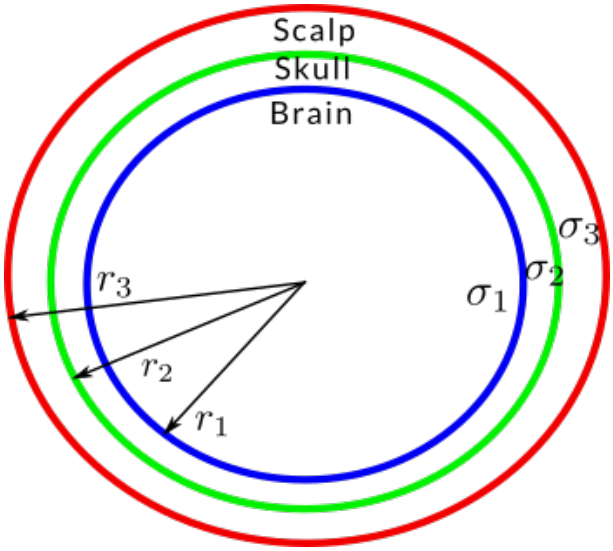

Figure 2.2: ***Spherical model with three layers: Scalp, Skull and brain.***

times less conductive than the other head tissues. Conductivity must be included in the head model for accurate approximations of the potential and magnetic field generated from the brain activity (Gramfort et al., 2010).

2.2.2.1 Spherical Model

This modeling consists in approximating the head by a set of nested concentric spheres. Each volume enclosed between consecutive spheres represents a head tissue with constant electrical conductivity. This simple approximation allows an analytic solution for the electric potential and magnetic field generated by the brain activity. This approximation can be extended to non-concentric spheres (Meijs et al., 1987) or ellipsoidal geometries (Dassios et al., 2003). In this case, the primary magnetic field does not depend at all on head conductivities. This makes head modeling less "important" in MEG studies. On the contrary to MEG, EEG depends on electrical conductivities of the head. This makes it very crucial to consider realistic head models with more complex geometries.

2.2.2.2 Realistic head model

It is clear that the brain geometry is not spherical. Since the late 1980's, realistically shaped models were gradually introduced and applied (Meijs et al., 1988; Hämäläinen et al., 1989; Yvert et al., 1995) to improve the accuracy of the forward model estimation. These more accurate head models can be obtained using different imaging techniques like computed tomography (CT) and anatomical magnetic resonance imaging (MRI).

Figure 2.3 shows CT and MR images of the same subject at the same slice. You can notice that the CT imaging is more appropriate for bones than MRI because of the absence of water molecules in the skull. But because the

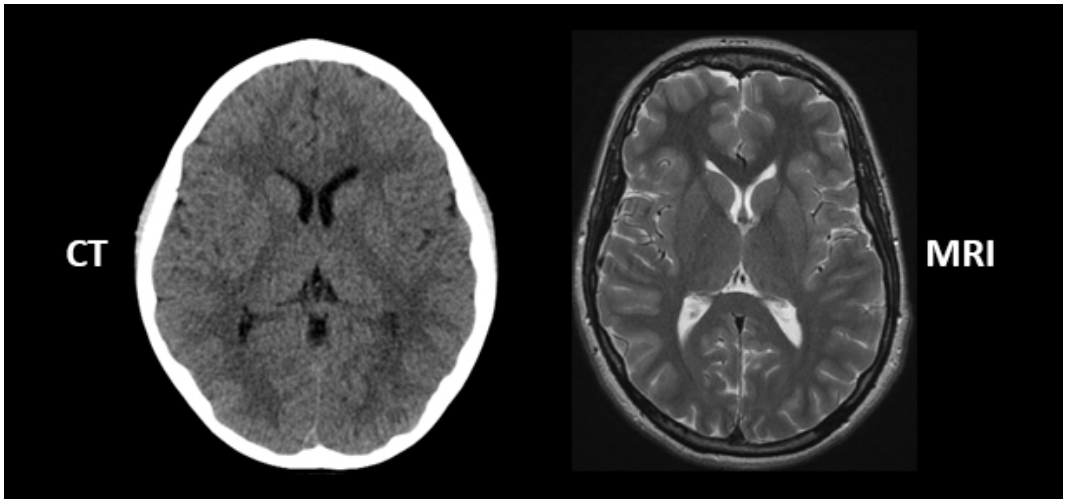

Figure 2.3: ***On the left, a slice of a CT image. On the right, the same slice obtained with MRI. We observed that the CT offers a good contrast to the skull while MRI provides a good contrast between soft tissues. (Source blog.cincinnatichildrens.org)***

patients are exposed to the hazards of ionizing radiation in CT, MRI is most commonly used in the head modeling.

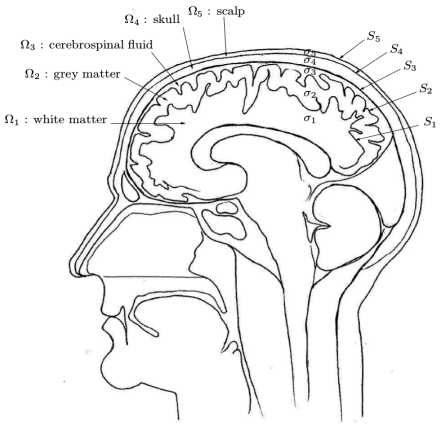

Figure 2.4: ***The different surfaces ($S_1, .., S_5$) and volumes ($\Omega_1, .., \Omega_5$) that can be extracted from MRI image. (adapted from Faugeras et al., 1999)***

Figure 2.4 shows the surfaces and volumes that can be extracted from MR images. Each volume, Ω_i, corresponds to a head tissue with homogeneous and isotropic conductivity σ_i (in BEM).

It has been shown that if the head is modeled as a simple spherical model, the error in localizing the active sources can reach $3cm$ when using EEG data (Sutherling et al., 1988; Vallaghé, 2008). This is why the use of the realistic head model is crucial to get more accurate results. Usually in EEG and MEG studies, the head in divided into three homogeneous compartments which are: scalp, skull, grey matter.

2.3 Inverse problem

As mentioned earlier, hundreds of thousands of pyramidal cells must fire synchronously so that we could detect it using EEG and MEG. The EEG/MEG inverse problem consists of localizing active sources from the functional imaging EEG and/or MEG. Brain activity generates electric and magnetic field that can be measured by EEG and MEG respectively. In section 2.1, we introduced the forward model, in which the linear relation between the measurements and the neural activity is computed. In this section, we explain how we can estimate the neural activity from the measurements i.e. the inverse problem. There are three types of approaches that can be used to solve the inverse problem

- Parametric models a.k.a dipole fitting approaches.
- Scanning techniques.
- Distributed source models a.k.a image-based methods.

Through this section, we briefly explain the first two approaches. In our work, we focus on the third approach which allows to set priors on the brain activity.

2.3.1 Dipole fitting approaches

Parametric models or dipole fitting approaches assume that the measured EEG/MEG signals are generated by one or a small number of sources. Each source, small cortical region of few mm^2, is modeled by a dipole. The number of dipoles, K, is fixed a priori. The dipole i is situated in the position r_i and has a moment q_i. The dipole strength is given by $x_i = \|q_i\|_2$. The dipole orientation is defined by $\theta_i = \frac{q_i}{x}$.

Let $g_i(r_i, \theta_i)x_i$ be the forward field produced by the dipole i and m is the measured M/EEG.

$$\min_{(r_i,q_i)i=1,..,K} \left\| M - \sum_{i=1}^{K} g_i(r_i, \theta_i)x_i \right\|_2^2 \tag{2.11}$$

where M is EEG/MEG measurement at a specific time. If the dipoles are allowed to move (we do not fix dipoles' locations), the method is called *moving dipole* (6 parameters are estimated), if they can only rotate it is referred as *rotating dipole* (3 parameters are estimated). Only one parameter is estimated (x_i) when working with *fixed dipole* in which the position and orientation are fixed. Dipole fitting approaches seem to be more reasonable for a small number of sources. But in reality, brain activity is widespread and a big number of neurons may contribute to the generation of EEG/MEG signals. This is solved by assuming that sources in cortical regions are equivalent dipoles.

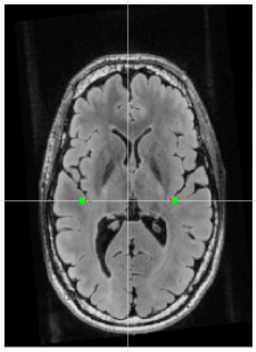

Figure 2.5: ***An example of dipole fitting. (source http://www.fieldtriptoolbox.org)***

The limitation of this type of inverse problem solvers is that the number of dipoles must be fixed a priori and the optimization problem is nonlinear and non-convex.

2.3.2 Scanning techniques

Scanning methods avoid the convexity issue which is present in equivalent dipoles approach by scanning through regions of interest. They were first introduced in the radar and sonar community. All of the scanning methods estimate a spatial filter. The spatial filter is a vector (in the case of constrained fixed dipoles) or a matrix (3 columns) that provides an estimate of the source intensity at a given location by suppressing the remaining sources. We need first to divide the brain volume or cortical into n grid points. Each grid point is assumed to represent a dipole.

Beamforming

The sources are assumed be uncorrelated with each other and with noise. Let's denotes by M, the EEG/MEG measurement during a time window. Equation 2.10 can be rewritten as:

$$M = g_1 J_1 + \cdots + g_n J_n$$

where g_i is the i^{th} column of G and J_i is the i^{th} dipole magnitude (location is fixed). The previous equation can be rewritten as:

$$M = g_r J_r + N$$

where N is the contribution to measurement of all sources except source r. A perfect spatial filter, of source r, blocks out the interference of all sources except source r on the measurement M. Let's denotes by ω_r, the spatial filter of source J_r.

$$\begin{aligned} \omega_r^T M &= \omega_r^T g_r J_r + \omega_r^T N \\ \omega_r^T M &= \omega_r^T g_r J_r \end{aligned} \tag{2.12}$$

with the constraint of unity passband i.e. $\omega_r^T g_r = 1$ (we want to fully see the r^{th} source). $()^T$ is the transpose operator.

$$J_r = w_r^T M \tag{2.13}$$

A simple spatial filter can be obtained by normalizing the lead field (gain matrix obtained from the forward problem) columns, i.e.:

$$w_r = \frac{g_r}{\|g_r\|_2}$$

where g_r is the column that corresponds to the dipole at the location r. In reality, the use of matched filter is limited because of the correlation of the gain matrix columns'. If g_r and g_k are correlated, $w_r g_k \neq 0$. So the assumption in Equation 2.12 is not fulfilled i.e. $\omega_r N \neq 0$.

Rather than making $w_r g_k = 0$, we want to make it as small as possible. In other words, we want to compute a filter that minimizes the variance of sources. This approach is called Linearly Constrained Minimum Variance (LCMV) beamformer (Van Veen et al., 1997). Let v_r be the source variance. If the sources are centered at zero, v_r is defined as follows:

$$v_r = J_r J_r^T \tag{2.14}$$

With centered measurement and by replacing Equation 2.13 in 2.14, we obtain:

$$\begin{aligned} v_r &= w_r^T M M^T w_r \\ v_r &= w_r^T C w_r \end{aligned} \tag{2.15}$$

where $C = MM^T$ is the covariance matrix of the measurement. When minimizing the variance subjected to unit bandpass ($w_r g_r = 1$) and by using the Lagrange multiplier the filter for each source can be found to be:

$$w_r^T = (g_r^T C^{-1} g_r)^{-1} g_r^T C^{-1} \tag{2.16}$$

The LCMV beamformer is widely used because it does not need any prior on the number of active sources. Also, it allows to scan through all sources or a region of interest and can be applied in the frequency domain. But it fails to reconstruct strongly correlated sources. Several brain regions are activated simultaneously with possible correlated activations. Also, It relies on a good estimation of the data covariance matrix (C) which implies that we need to have sufficient amount of data (big time window).

An alternative to LCMV is Synthetic aperture magnetometry (SAM) (Robinson et al., 1998) and Dynamics imaging of coherence (DICS) (Gross et al., 2001). The former works on statistical quantities based on the difference between the measurement acquired in resting state and when performing a task. The latter is used for localization of coherent Sources.

MUSIC

An alternative to spatial filtering is based on signal classification between signal and noise by using signal subspace. The most commonly used method is MUltiple SIgnal Classification (MUSIC) (Mosher et al., 1992). In MUSIC, the measurements M is divided with Singular Value Decomposition (SVD) into a signal space and a noise space. The signal space is estimated from the data by finding the the SVD of M.

$$M = USV^T$$

The signal space, U_r, is spanned by the r first left singular vectors of U. r can be chosen to be the the number of U's columns corresponding to the highest drop in the eigenvalues after sorting their values in deceasing order. The MUSIC algorithm then scans a single dipole model through the brain volume or cortical surface and computes projections onto the signal space. The cost function associated with MUSIC is given by (Mosher et al., 1992):

$$e_i = \frac{\left\|(I - U_r U_r^T) g_i\right\|}{\|g_i\|}$$

where I is the identity matrix. The linear operator $(I - U_r U_r^t)$ is the orthogonal projection onto the noise space. The smaller e_i, the more the i^{th} dipole contributes to the measurements (Mosher et al., 1988). It is clear that this approach could detect one dipole that has the minimum e_i. For multiple activation configurations, a variant of MUSIC that is called recursively applied MUSIC (RAP MUSIC) (Mosher et al., 1999) can be used. As its name implies, it applies the MUSIC successively after removing the contribution of the previously identified dipole.

Estimating the subset size, r, in MUSIC can be an issue when there is no sharp drop after the r^{th} singular value. Also, MUSIC fails to detect dipoles with dependent time series.

2.3.3 Distributed source models

An alternative to dipole fitting and scanning methods is called distributed source models a.k.a image-based approaches. It uses a significantly large number of dipoles (from thousands to hundreds of thousands). In this method, dipoles are sampled or distributed over the source space. The source space can be either a volume or a surface. The distributed source model estimates the magnitude of the activations and it can be displayed on the volume or surface hence the comparison with images.

Each dipole has a fixed position and its orientation is fixed, a unit vector normal to the cortical surface, or to be estimated with the source magnitude. The former is used in this thesis. This means that the positions and orientations of dipoles are not part of the solution to be found. We estimate only the strength of the dipoles.

We denote the number of sensors by N_c, the number of sources by N_s and the number of time samples by T. The gain matrix (lead field) G of size $\in \mathbb{R}^{N_c \times N_s}$, obtained by solving the forward problem, allows us to relate cortical activations ($J \in \mathbb{R}^{N_s \times T}$) and the MEG/EEG measurements ($M \in \mathbb{R}^{N_c \times T}$):

$$M = GJ + E \tag{2.17}$$

where $E \in \mathbb{R}^{N_c \times T}$ is the measurement noise.

The number of sensors, N_c, can be between few tens, for low EEG studies, and few hundred for simultaneous EEG/MEG acquisition. The number of time samples, T, depends on the sampling rate that can be around 1 kHz.

In practice, the number of distributed sources, N_s, can be of the order 10^4. Because the number of sources' parameters is much higher than the number of sensors, we have an infinite number of solutions to the inverse problem. Inverting G to obtain J from M ($J = G^{-1}M$) is not possible because the problem is underdetermined. Constraining the sources is needed to obtain a unique source estimate.

Setting a prior consists in assuming that the source estimates is small for a given norm $P(J)$. A good estimate of brain activity J^* is then obtained according to the following minimization:

$$J^* = \underset{J}{\operatorname{argmin}}\, D(M, J) \quad \text{subject to } P(J) \leq \alpha \tag{2.18}$$

where α is a parameter that controls the regularity of the solution and $D(M, J)$ is a data fidelity term.

In practice Equation 2.18 is more presented in the Lagrangian formulation:

$$J^* = \underset{J}{\operatorname{argmin}}\, U(J) = \underset{J}{\operatorname{argmin}}\, D(M, J) + \lambda P(J) \tag{2.19}$$

with λ a positive number that controls the trade-off between the data fit term $D(M, J)$ and the regularity of the estimate. The cost function U is composed of two terms:

- A data fit term, D, that quantify how well the estimated sources magnitudes' match the measured data. It takes into account the characteristic of the measurement noise, E.
- A regularization term P, a.k.a penalty term or prior, which is used to introduce a priori knowledge on sources. Because the MEG/EEG is ill-posed problem, this term is mandatory to obtain a sound solution.

In the context of EEG/MEG, D, is usually the squared l_2-norm of the residual $R = M - GJ$:

$$D(M, J) = \|M - GJ\|_2^2 = \|R\|_2^2 = \sum_{i=1}^{N_c} \sum_{t=1}^{T} R(i, t)^2 \tag{2.20}$$

In a more general way, the inverse problem techniques for distributed source models can be written as (Gavit et al., 2001):

$$U(J) = D(M, J) + \lambda U_s(J) + \mu U_t(J) \tag{2.21}$$

where D is the data fit term, U_s is the spatial prior term (prior on the source space), U_t is the temporal prior term and λ and μ are two positive numbers used to balance their respective contributions to the data fit term. They can have one or multiple terms. The source activation is obtained by optimizing the functional U, equation 2.21. The regularization terms used to reconstruct the brain activity can be divided into: spatial ($\mu = 0$) or temporal ($\lambda = 0$) or spatiotemporal in which the two terms are present in the functional. According to the definition of the regularization terms (U_s and U_t), the reconstruction algorithm can lead to linear or nonlinear methods.

2.3.3.1 Linear methods

The resolution of the inverse problem in the case of distributed dipoles leads to the optimization of the data fit error $D(M, J)$ balanced by a penalization term $U_s(J)$ or $U_t(J)$. Although both of them can be used to regularize the inverse problem, we find in the literature only the spatial term when using only one prior maybe because they are interested to reconstruct one-time sample at a time. The functional D and U_s are often linearly related to J. The linear approaches assume that sources have centered Gaussian distribution and that sources are independent. The inverse problem is then solved by optimizing the following:

$$U(J) = \|M - GJ\|_F^2 + \lambda \|WJ\|_F^2 \tag{2.22}$$

where λ is a positive number used to balance D and U_s. This method is also known as Tikhonov regularization or Ridge Regression (Tikhonov, 1943). Several methods can be found in the literature. They differ only by the choice/definition of the weighting matrix W.

The solution of equation 2.22 is obtained by setting the derivative of U with respect to J to 0:

$$\begin{aligned} \frac{dU}{dJ} &= 0 \\ -G^T(M - GJ) + \lambda W^T W J &= 0 \\ (G^T G + \lambda W^T W)J &= G^T M \\ J &= (G^T G + \lambda W^T W)^{-1} G^T M \end{aligned} \tag{2.23}$$

The minimum norm estimates (MNE) sets W to the identity matrix. The drawback of the MNE is that it overestimates the extent of the activity regions due to underestimating the magnitude of active sources resulting from the use of l_2 norm. But, due to the simple solution, which is a matrix multiplication, this approach is attractive.

The low resolution brain electromagnetic tomography (LORETA) method corresponds to the case, $W = L^T L$ (Pascual-Marqui et al., 1994). L is the 3D-discretized Laplacian matrix. The i^{th} row of L acts like a discrete differentiating operator by computing differences between the i^{th} voxel and its direct neighbors. This method provides the solution with the maximum spatial smoothness.

In the general case, where W is different from the identity, we need to invert a big matrix of size $N_s \times N_s$. This is solved in the case of MNE by using the Woodbury matrix identity in which instead of inverting $N_s \times N_s$, we invert a smaller matrix of size $N_c \times N_c$.

$$J_\lambda = G^T(GG^T + \lambda I)^{-1}M \tag{2.24}$$

The solution is smooth because of the assumption that the sources follow a Gaussian distribution which penalises the sources with higher activation i.e it underestimates the true activation. The regularization parameter plays a central role, λ, because the reconstruction depends on its value. This makes the choice of the optimal value of λ crucial.

2.3.3.2 The choice of the regularization parameter

L-curve

This method was proposed by Hansen in (Hansen, 1992). It is based on creating a curve that relates the norm of the solution ($\|J_\lambda\|$), or the semi-norm $\|WJ_\lambda\|$, to the norm of the data fit term ($\|M - GJ_\lambda\|$) for different values of λ. This permits us to get an idea of the compromise between the data fit term and the prior.

The curve is plotted in *loglog* scale. Figure 2.6a is an illustration of the curve shape. The curve has the shape of the letter "**L**", hence the name of the algorithm. The optimal λ corresponds to the point with the highest curvature value which corresponds to a good balance between a small residual norm $\|M - GJ_\lambda\|$ and small solution norm/semi-norm $\|WJ_\lambda\|$.

Hansen argues that for values of λ smaller than this optimal value, a part of the noise is reconstructed. And if the measurement is buried in noise, the corner of the L-curve becomes harder to see.

Generalized cross-validation (GCV)

Another alternative to estimate the optimal λ is the Generalized cross validation (GCV). It was proposed by G. Golub (Golub et al., 1979). It is based on statistical considerations, namely, that a good value of the regularization parameter should predict missing information from a sensor i using the measurement from the remaining sensors.

Let us denote by $M_{|i}$ to be the measurement of all electrodes except sensor i. The source reconstruction obtained by not considering measurement in electrode i (i.e. only $M_{|i}$) and $G_{|i}$ (i.e. we remove the i^{th} row of G that

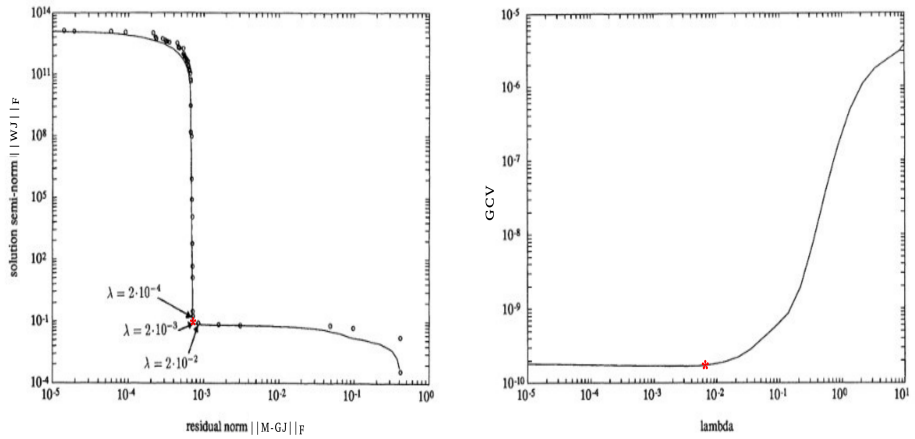

(a) *(b)*

Figure 2.6: ***A possible shape of (a) L-curve and (b) GCV curve. The optimal λ is shown in both sub-figures by red star. (adopted from Hansen, 1992).***

corresponds to the i^{th} sensor) is called $J_{|i}$.

$$J_{|i} = G_{|i}^T (G_{|i} G_{|i}^T + \lambda I)^{-1} M_{|i}$$

The generalized cross-validation error is defined as:

$$GCV(\lambda) = \sum_i \left\| M_i - G_i J_{|i} \right\|^2$$

Golub et al., 1979 showed that this value can be computed with the following formula:

$$GCV(\lambda) = \frac{\|M - GJ\|_F^2}{(\text{Trace}(I - GG^T(GG^T + \lambda I)^{-1}))^2} \tag{2.25}$$

Or in a more general way (weighted minimum norm):

$$GCV(\lambda) = \frac{\|(I - A(\lambda))M\|_F^2}{(\text{Trace}(I - A(\lambda))^2}$$

with $J = A(\lambda)M$ e.g. for MNE $A(\lambda) = GG^T(GG^T + \lambda I)^{-1}$.

Finding the best λ consists in minimizing GCV with respect to λ. Equation 2.25 is obtained by assuming that noise is independent and identically distributed across sensors. This hypothesis can be done by prewhitening the data. An example of the shape of the GCV curve can be seen in Figure 2.6b.

Bayesian interpretation

Up to now, priors have been presented without giving much attention to their underlying assumptions. In order to understand those, we have to relate the functional in equation 2.19 to Bayesian estimation.

Let us assume that M and J are random variables. According to Bayes' rule, we can write:

$$P(J|M) = \frac{P(M|J)P(J)}{P(M)}$$

where $P(X|Y)$ is the probability of X given Y, $P(J)$ is the probability that we assume on sources. The optimal J^* is obtained by estimating a maximum a posteriori (MAP):

$$\begin{aligned} J^* &= \underset{J}{\operatorname{argmax}}\, P(J|M) \\ &= \underset{J}{\operatorname{argmax}}\, P(M|J)P(J) \\ &= \underset{J}{\operatorname{argmax}}\, \ln(P(M|J)) + \ln(P(J)) \end{aligned} \tag{2.26}$$

where ln is the natural logarithm. If measurement noise and source amplitudes are assumed to be Gaussian variables with zero mean and covariance Σ_M and Σ_J respectively, we can write:

$$\begin{aligned} J^* &= \underset{J}{\operatorname{argmin}}(M - GJ)^T\Sigma_M^{-1}(M - GJ) + J^T\Sigma_J^{-1}J \\ &= \underset{J}{\operatorname{argmin}}(J^TG^T\Sigma_M^{-1}GJ - J^TG^T\Sigma_M^{-1}M - M^T\Sigma_M^{-1}GJ \\ &\quad + M^T\Sigma_M^{-1}M + J^T\Sigma_J^{-1}J) \end{aligned}$$

By taking the derivative with respect to J and setting it to zero, we obtain the MAP estimate' sources:

$$J^* = (G^T\Sigma_M^{-1}G + \Sigma_J^{-1})^{-1}G^T\Sigma_M^{-1}M \tag{2.27}$$

Note that equation 2.27 is equivalent to the minimum norm estimate in the case where $\Sigma_J^{-1} = \lambda I$ (λW^TW for WMNE) and $\Sigma_M^{-1} = I$.

In practice, the MEG/EEG noise is not white but one can estimate the measurement noise covariance matrix, Σ_M, either from measurement before the stimuli or empty-room recording. This matrix then can be used to whiten the data.

2.3.3.3 Non linear methods

With non-linear approaches, more complex statistical models can be assumed not only gaussianity like in linear approaches. Several non-linear source reconstruction approaches are used to favor a specific source configuration. Sparse prior was introduced to address the problem of the MNE in which the estimated cortical activity is smeared leading to widely extended activations. We can set the sparsity priors by using the quasi-norm l_p with $p < 2$.

Let $x \in \mathbb{R}^n$. The l_p norm for $1 \leq p < \infty$ and the quasi-norm for $0 \leq p < 1$ of the vector x is defined by:

$$\|x\|_p = (\sum_i^n |x_i|^p)^{\frac{1}{p}}.$$

When $p = 0$, $\|x\|_0$ is the number of nonzero elements of the vector x. When $p = 1$, the minimization using $\|x\|_1$ is convex. Finally, when $0 \leq p < 1$, the minimization is no more convex. l_0 norm can be solved by testing all source configurations which is computationally impractical. An approximation of l_0 can be obtained iteratively by using focal underdetermined system solution (FOCUSS) (Gorodnitsky et al., 1995).

With l_1-norm (LASSO or Minimum Current Estimate) (Matsuura et al., 1995), few sources are active. This is done by adding l_1 prior as regularizer. It consists in solving the following functional for each time instant (Matsuura et al., 1995; Gramfort, 2009):

$$J_\lambda = \underset{J}{\operatorname{argmin}} \frac{1}{2} \|M - GJ\|_2^2 + \lambda \|J\|_1 \ , \lambda > 0. \tag{2.28}$$

This results in non-continuous source activations, see Figure 2.7. l_1 prior promotes spatial sparsity which was proven to be relevant for clinical applications (Huppertz et al., 2001). This method suffers from significant limitations. As it promotes spatial sparsity independently at each time instant, it fails to recover time courses of cortical sources. In order to go beyond this limitation, there has been a growing interest in approaches that allows a structured sparsity (Gramfort et al., 2012).

In the Mixed Norm Estimate (MxNE), a temporal smoothness of sources term is added to spatial sparsity. It uses the mixed norm l_{21} instead of l_1 norm. $l_{21}-$norm is defined as:

$$\|J\|_{21} = \sum_i \sqrt{\sum_j J_i(j)^2} \, , \tag{2.29}$$

where the sum over i is over sources (spatial position) and the sum over j is the sum over the time-course of the source i i.e. the l_{21}-norm corresponds to the sum of the l_2-norm of individual source time courses. The solution of this method can be found in (Gramfort, 2009; Gramfort et al., 2012). MxNE results in few active sources in a time window, see Figure 2.7. Its drawback is that it underestimates the source activity due to the use of the l_2 norm over the time courses. More details on how to obtain mixed norm estimates can be seen in Chapter 5.1.

It is possible to obtain another structured sparsity by using the l_{12} norm, in which the sparsity is applied temporally. This means that it favors activation at some time samples the rest of time all sources are inactive, see Figure2.7. This norm is defined as:

$$\|J\|_{12} = \sum_j \sqrt{\sum_i J_i(j)^2}$$

The assumption behind this norm is far from the truth because even in resting state there are some defaults regions that are active in the brain.

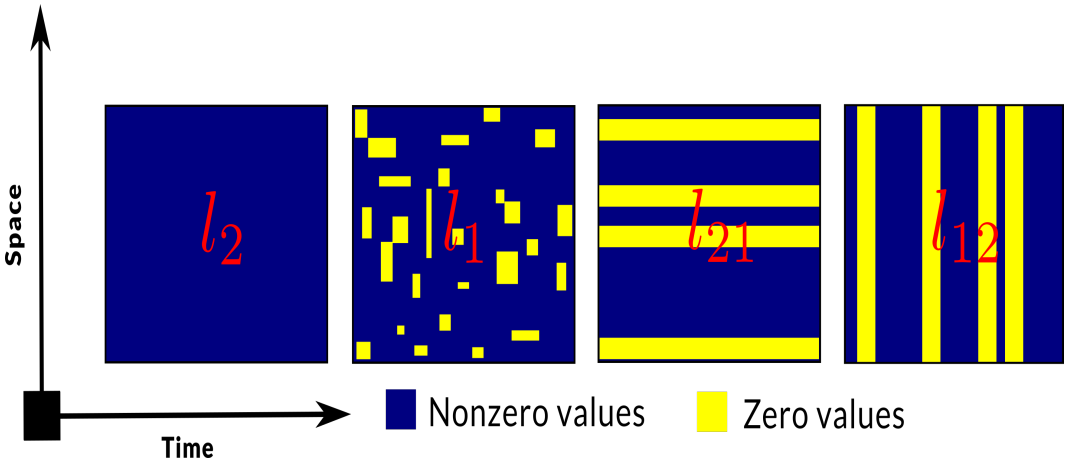

Figure 2.7: ***The effect of using the different norms on the estimated sources' magnitudes. Using l_2 no source is inactive (= 0), with l_1 few sources are active at each time sample, l_{21} and l_{12} allow to obtain structural activation.***

When using l_2-norm to regularize the inverse problem, the cost function is differentiable and strictly convex. The solution can be obtained by differentiating the cost function with respect to J and set it to zero. The use of the above norms (l_1, l_{21} and l_{12}) do not have this advantage.

Iterative reweighted least squares (IRLS) is a solver that was proposed to estimate the brain activity with sparsity prior (Daubechies et al., 2008). It is similar to FOCUSS in which the source estimate is obtained by computing, iteratively, weighted MN solution (re-estimated at each iteration). The only difference between the two solvers is the value of weights used at each iteration. Least-angle regression (LARS) - Least Absolute Shrinkage and Selection Operator (LASSO) is another solver with sparsity prior (Efron et al., 2004). It is considered to be a powerful method because the optimum solution is given for all the regularization parameter values at the same time. Coordinate descent (Friedman et al., 2007), block coordinate relaxation (Sardy et al., 2000) or proximal operators (Beck et al., 2009; Gramfort et al., 2012) are possible methods to solve EEG/MEG with structured sparsity prior.

The proximal (proximity) operator (Moreau, 1965) is defined as follows:

Let $\phi : \mathbb{R}^p \to \mathbb{R}$ be a proper convex function. The proximity operator associated to Φ and $\lambda > 0$, denoted by $\text{prox}_{\lambda\phi}$: $\mathbb{R}^p \to \mathbb{R}^p$ reads:

$$prox_{\lambda\phi} = \underset{x \in \mathbb{R}^p}{\text{argmin}} \, \|y - x\|_2^2 + \lambda\phi(y) \tag{2.30}$$

The proximal operator associated to the l_{21} norm is given by $x = \text{prox}_{\lambda\|\cdot\|_{21}}(y)$ where x reads for each coordinate (source) (Gramfort et al., 2012):

$$x_{i,t} = y_{i,t}\left(1 - \frac{\lambda}{\|y_i\|_2}\right)^+, \tag{2.31}$$

where $(\cdot)^+$ is defined as $(a)^+ = \max(a, 0)$ with the convention $(0/0 = 0)$.

Other nonlinear approaches are based on entropy. Entropy can be seen

as the distance between the probability density of the sources to a reference density. In (Amblard et al., 2004), the authors proposed a method based on the entropy called Maximum Entropy on the Mean (MEM). It tries to maximize the information coming from measurements to correct the reference probability density of sources.

The main drawback of nonlinear methods is that they are time-consuming and a solution is obtained iteratively which may lead to computational instability (multiple solutions).

2.3.4 Conclusion

MEG and EEG are two imaging modalities that measure the brain activity in real time. The forward problem needs to be solved first to know the contribution of each source to the sensors. The accuracy of the source estimate depends on the head model assumed for the forward model. It has been shown that a realistic head model gives more accurate source reconstructions. The inverse problem uses the result of the forward model, the gain matrix, to estimate the brain activity. There are three main approaches to estimate brain activity from EEG/MEG measurements. The dipole fitting approaches which assume that the measurement is obtained from few dipoles. The scanning approaches scan through the source space to chose sources which explain the best the measurements. Finally, the imaging-based approaches which do not fix a priori a number of sources. In these approaches, the number of sensors is less than the number of sources. That is why we need to set prior on the source space to have a unique solution. Depending on the priors, we can divide the image-based approaches into two categories: linear and nonlinear. Linear approaches are easy to implement and give faster and above all unique reconstructions, while non-linear approaches are time-consuming and there is no guarantee that the "best solution" is obtained.

Chapter 3

Diffusion magnetic resonance imaging

Contents

3.1 Introduction **42**
3.2 The Principle of Diffusion **42**
3.3 Diffusion tensor **43**
3.4 Diffusion tensor estimation **43**
3.5 Scalar quantities **45**
3.5.1 Trace or mean diffusivity (MD) 46
3.5.2 Fractional anisotropy (FA) and relative anisotropy (RA) 46
3.6 Multi-tensor **47**
3.7 Tractography **48**
3.7.1 Local tractography 48
3.7.2 Global tractography 50
3.8 Conclusion **51**

3.1 Introduction

Diffusion MRI (dMRI) was first developed in the 1980s. It is based on the assumption that water molecules do not freely diffuse in a constrained environment. Membranes obstruct the motion of the water molecules i.e. water molecules moves freely parallel to axons and they are blocked when moving across them. Water diffusion can thus give an insight into the microscopic properties and structure of the brain tissues.

3.2 The Principle of Diffusion

MRI uses a physical phenomena called nuclear magnetic resonance (NMR), explained briefly in section 1.5, in order to detect the motion of nuclei of atoms in a body placed within the NMR scanner. When applying the primary magnetic field $B0$ (see section 1.5 for more details) moving hydrogen protons result into lower MRI signal. When the hydrogen atoms are free to move parallel to $B0$, the MR signal is lower because of the translation motion "diffusion" of hydrogen atoms. This is the bases of dMRI. Over 65 years ago, Erwin Hahn showed that the molecular translational motion can be measured using the spin echoes in NMR.

Ludwig Boltzmann proposed that temperature was a measure of thermal energy and the laws of thermodynamics could be understood from the mechanics of the molecular motion by using statistical average. Molecules move randomly, in a Brownian motion, in the medium. Einstein (Einstein, 1905; Einstein, 1956) formulated the average distance that water molecules travel in a constant time, τ, as:

$$r^2 = 6D\tau \tag{3.1}$$

where D is the characteristic of the environment that depends on the environment in which the molecules are diffusing and r^2 is the mean-squared displacement of molecules during the diffusion time τ.

dMRI applies constant diffusion gradients higher in magnitude with respect to the primary magnetic field ($B0$) to encode the diffusion in the transverse plane i.e. the decay of the signal due only to the diffusion. First, a diffusion gradient, of strength g, orientation q and duration δ, is applied and it dephases the spins. The dephasing is undone by applying a second identical gradient, after the 180 degrees RF, with the same duration δ. The time between these two gradients is Δ. If the spins move during the period Δ, the second gradient can not correct the dephasing which results in reducing the transverse magnetization, implying a loss in the echo signal.

The diffusion signal decay can be formulated as (Stejskal et al., 1965; Basser et al., 1994b):

$$S = S_0 \exp(-bq^t Dq) \tag{3.2}$$

where b (b-value) is defined by $b = \tau g\ s/mm^2$ and S_0 is the signal with no diffusion gradients applied (b=0).

3.3 Diffusion tensor

Diffusion tensor is a first model to represent diffusion anisotropy of the water molecules inside voxels (Basser et al., 2000; Basser et al., 2002; Arsigny et al., 2006). This model is based on the assumption that the water's diffusion follows a 3D Gaussian distribution which is characterized by a 3×3 symmetric positive definite matrix, D. It is generally represented by an ellipsoid whose main axes are the eigenvectors, v_i, of D and whose size is the eigenvalues, λ_i, of D.

$$D = \begin{bmatrix} D_{xx} & D_{xy} & D_{xz} \\ D_{xy} & D_{yy} & D_{yz} \\ D_{xz} & D_{yz} & D_{zz} \end{bmatrix} \tag{3.3}$$

D is a 3×3 symmetric and positive definite matrix. This implies that there are six unknowns to be estimated from the diffusion signal. Therefore, we need at least six DWIs, acquired at different gradient directions, in addition to the S_0 image to estimate the elements of D.

In an anisotropic environment, the movement of molecules depends on the obstacles present in the environment. The probability of molecules to move is (Basser et al., 1994b):

$$p(r,\tau) = \frac{1}{\sqrt{(4\pi\tau)^3|D|}} \exp(-\frac{r^t D^{-1} r}{4\tau}) \tag{3.4}$$

where $|D|$ is the determinant of D, r is the displacement. D must be positive definite because the above equation must tend to zero for large displacement. The signal decay S depends on the strength and direction of the applied gradient (g) i.e. different contrasts is obtained with different gradient directions, see in Figure 3.1. These dMRI images are called diffusion weighted images (DWI).

The diffusion tensor, whose size, shape and orientation are embedded in the diffusion matrix, can be described by a three-dimensional ellipsoid. It gives an insight about the preferred diffusion direction of the water molecules. The shape of the ellipsoid is controlled by the eigenvalues (λ_1, λ_2, λ_3) of D. The three orientations of the ellipsoid are the three eigenvectors (v_1, v_2, v_3) of D (see Figure 3.2 and 3.3).

3.4 Diffusion tensor estimation

Equation 3.2 can be rewritten as (Basser et al., 1994b, Basser et al., 1994a, Johansen-Berg et al., 2009) under narrow gradient pulse assumption:

$$S = S_0 \exp(-b_{xx}D_{xx} - b_{yy}D_{yy} - b_{zz}D_{zz} - 2(b_{xy}D_{xy} + b_{xz}D_{xz} + b_{yz}D_{yz})) \tag{3.5}$$

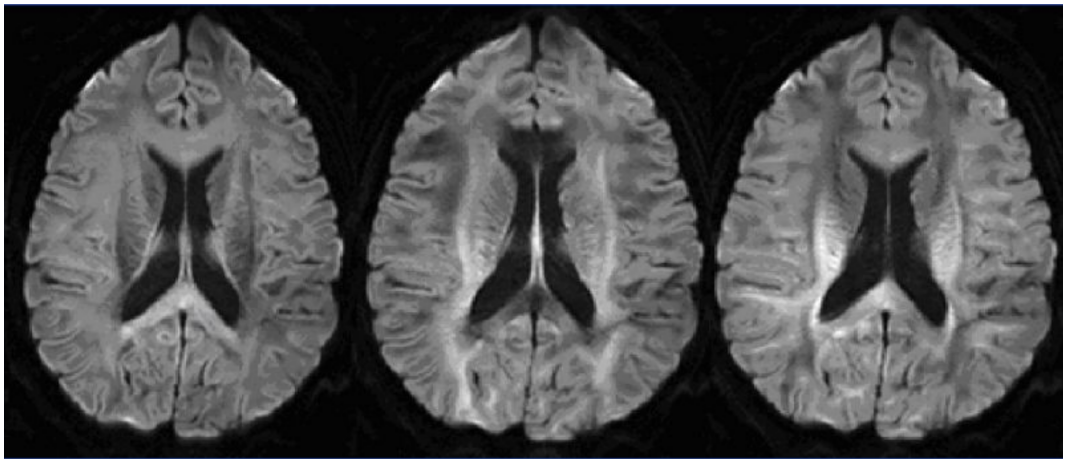

Figure 3.1: ***Diffusion MRI images with three different gradient directions. Different tissue contrasts are obtained using different gradient directions.***

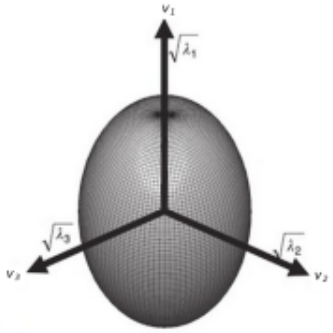

Figure 3.2: ***Schematic of the diffusion tensor ellipsoid. The ellipsoid is the envelope where a spin -placed at its center- will diffuse with equal probability. The axes are scaled according to the square root of the eigenvalues. (modified from Johansen-Berg et al., 2009)***

where:

- b_{xx} = b-value G_xG_x
- b_{yy} = b-value G_yG_y
- b_{zz} = b-value G_zG_z
- b_{xy} = b-value G_xG_y
- b_{xz} = b-value G_xG_z
- b_{yz} = b-value G_yG_z

where (G_x, G_y, G_z) are the coordinates of the applied gradient. If X is a vector of the log-transformed signal intensities ($X = [-\ln(\frac{S_1}{S_0}), -\ln(\frac{S_2}{S_0}), \cdots, -\ln(\frac{S_N}{S_0})]^T$), we introduced B as a $N \times 6$

matrix (N number of measurements).

$$B = \begin{bmatrix} b_{xx}^1 & b_{xy}^1 & b_{xz}^1 & b_{yy}^1 & b_{yz}^1 & b_{zz}^1 \\ b_{xx}^2 & b_{xy}^2 & b_{xz}^2 & b_{yy}^2 & b_{yz}^2 & b_{zz}^2 \\ \vdots & \vdots & \vdots & \vdots & \vdots & \vdots \\ b_{xx}^N & b_{xy}^N & b_{xz}^N & b_{yy}^N & b_{yz}^N & b_{zz}^N \end{bmatrix} \tag{3.6}$$

and d as the vector containing the elements of the diffusion tensor, i.e.: $d = [D_{xx}, D_{xy}, D_{xz}, D_{yy}, D_{yz}, D_{zz}]^T$. Then, we can write:

$$X = Bd \tag{3.7}$$

When having a square matrix, B, i.e. six measurements, the solution can be obtained by directly inverting B, i.e. $d = B^{-1}X$. This method does not fit the data alone but also perturbations due to noise. A better approach is to use a high number of measurements. In this case B is no longer square and thus pseudo-inverse is used to estimate the diffusion tensor (Ordinary least square (OLS)).

$$d = (B^T B)^{-1} B^T X \tag{3.8}$$

OLS assumes that variance of noise is constant over the measurement which is, in general, not true. Voxels with low diffusion signal have high variance and vice versa. Consequently, a weighting linear least square (WLS) scheme weights the measurements by their corrected error estimates, i.e., (Basser et al., 1994a; Johansen-Berg et al., 2009).

$$d = (B^T \Sigma^{-1} B)^{-1} B^T \Sigma^{-1} X \tag{3.9}$$

where Σ^{-1} contains the reciprocal errors of the log-transformed signal intensities (Basser et al., 1994a).

Another approach is to fit the data directly to the diffusion signal not to its log-transformation. Due to the exponential term, non-linear regression techniques are needed to estimate the diffusion tensor which needs initialization. Non-linear approaches are called also non-linear least squares (NLLS).

3.5 Scalar quantities

Several scalars can be derived from the diffusion tensor. They can be divided into two categories: *diffusion magnitude* and *anisotropy measures* (O'Donnell et al., 2011). They give insights about the ellipsoid shape and direction. They are rotationally and translationally invariant and measure parameters intrinsic to the tissue.

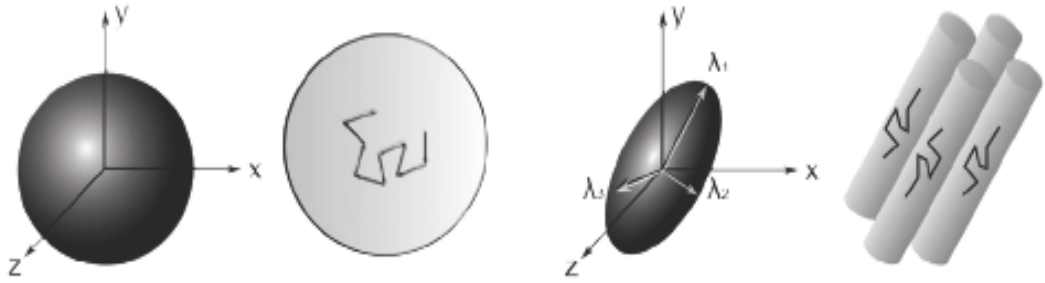

Figure 3.3: ***The diffusion tensor ellipsoid. Left: the ellipsoid shape in an isotropic environment. Right: the ellipsoid shape in a restricted environment. (Winston, 2012)***

3.5.1 Trace or mean diffusivity (MD)

The *mean diffusivity* or *trace* are the most clinically useful measures. The trace is proportional to the MD. They are defined as:

$$\begin{aligned} Tr(D) &= \sum_{i=1}^{3} \lambda_i \\ MD(D) &= \frac{1}{3} Tr(D) \end{aligned} \tag{3.10}$$

The values of MD are remarkably similar across grey and white matter, between different subjects and across mammalian species (Winston, 2012) (see Figure 3.4).

3.5.2 Fractional anisotropy (FA) and relative anisotropy (RA)

Relative anisotropy compares the magnitude of the anisotropic part to the isotropic part by looking at the ratio of the variance of the eigenvalues to their mean (Winston, 2012)(see Figure 3.4).

$$RA(D) = \sqrt{\frac{1}{3}} \frac{\sqrt{\sum_i (\lambda_i - \tilde{\lambda})}}{\tilde{\lambda}} \tag{3.11}$$

$$FA(D) = \sqrt{\frac{3}{2}} \sqrt{\frac{\sum_i (\lambda_i - \tilde{\lambda})^2}{\sum_i \lambda_i^2}} \tag{3.12}$$

where $\tilde{\lambda} = MD(D)$. FA and RA are scalar values between 0 and 1 that describe the degree of anisotropy. A value of one means that the diffusion occurs only along one direction. And a value of zero means that there is no preferred direction i.e. unrestricted diffusion (isotropic environment).

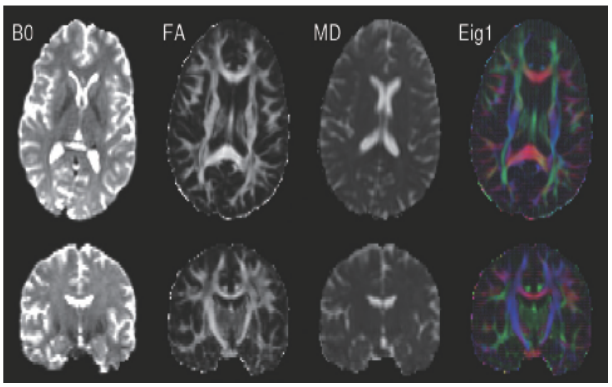

Figure 3.4: ***Diffusion tensor imaging. The non-diffusion weighted scan (B0) is shown on the left, followed by the fractional anisotropy (FA) image demonstrating higher values in white matter tracts then the mean diffusivity (MD) image with elevated values in the CSF. The final column shows the direction of principal eigenvector (Eig1) both in color-coded form (red = left/right, green=anterior/posterior, blue=superior/inferior) and in vector form (line segments) . (Winston, 2012)***

Even though DTI could measure the degree of anisotropy in the white matter, it fails to characterize more complex structures e.g. crossing fibers. How can we explain more complex structures?.

3.6 Multi-tensor

The single tensor model characterizes the Gaussian process of the water diffusion in simple tissues. It fails to characterize tissues with complex fiber architectures. The single tensor model gives a voxel-average diffusion tensor. This makes it a key limitation when trying to characterize complex fiber architectures i.e it can not model e.g. fiber crossing. Several studies showed that there are two or more fibers per voxel in two third of the white matter (Descoteaux, 2008; Jeurissen et al., 2010). The multi-tensor model a.k.a multi-compartment model was introduced by Tuch et al., 2002. It assumes that the diffusion signal is a sum of free diffusion Gaussian processes (Alexander, 2005):

$$S(b, \mathrm{g}) = S_0 \sum_{i=1}^{n} a_i \exp(-b \mathrm{q}^T D_i \mathrm{q}) \tag{3.13}$$

where D_i is the i^{th} diffusion tensor, n is the number of fibers, q is the gradient direction and a_i is the i^{th} volume fraction of the i^{th} fiber population that verifies $\sum_{i=0}^{n} a_i = 1$.

The multi-tensor model has several drawbacks. The number of fiber per voxel must be predefined. Unlike the diffusion tensor model, the diffusion signal in the case of the multi-tensor model cannot be linearized in the elements of the tensor matrices (3.7). Therefore, non-linear approaches must be used to estimate the n diffusion tensors. The n fiber direction at each

voxel is the eigenvector which corresponds to the highest eigenvalue of D_i, $i = 1 \cdots n$. In all the work that follows, we used 2^{nd} order multi-tensor model i.e. two fiber directions per voxel. This is driven by the results of several studies that found that the two-fiber model to be sufficient (Tuch et al., 2002; Kreher et al., 2005; Peled et al., 2006; Behrens et al., 2007; Guo et al., 2006; Zhan et al., 2006).

Other more complex models can be used. Diffusion Spectrum (DS) estimates the full distribution with respect to orientation and magnitude. Q-ball estimates only the probability over orientations. Ball-and-stick estimates the orientation and magnitude of an n anisotropic compartments. For more details about these methods, we refer to (Johansen-Berg et al., 2009). The problem with these methods is that the acquisition time is high because they need a high number of images at several gradient directions.

The fiber orientation, at each voxel, is obtained from the eigenvalues of D. But the question now is how to reconstcut the anatomical connections between brain regions?

3.7 Tractography

The algorithms that reconstruct the fiber pathways by estimating their trajectories are called *tractography algorithms*. These pathways are called *tractograms*. Tractography is also a modern tool that allows us to visualize the brain structural connectivity without dissection or the use of radiations. The tractography algorithms can be divided into two categories: local and global.

3.7.1 Local tractography

It is local because the tractograms are computed separately at each voxel. The direction of the pathways are determined locally and not using the whole image space. We can distinguish two groups of methods: *deterministic* and *probabilistic* tractographies.

3.7.1.1 Deterministic tractography

It is the first method proposed to reconstruct white matter pathways. It consists in following iteratively the maxima of the ellipsoids at each voxel until a stopping criterion is reached (Basser et al., 2000). It begins from a point in the cortex called a seed and traces along the dominant fiber direction. The direction of the fiber at each voxel is the eigenvector that corresponds to the highest eigenvalue (λ_1) of the diffusion tensor model.

With more general models, if there are more than one direction, the closest eigenvector to the previous fiber orientation is chosen. Deterministic tractography tries to estimate the most likely single path from a chosen starting point based on the streamline concept which is that the curve is always tangential/parallel to the principal direction of the fiber.

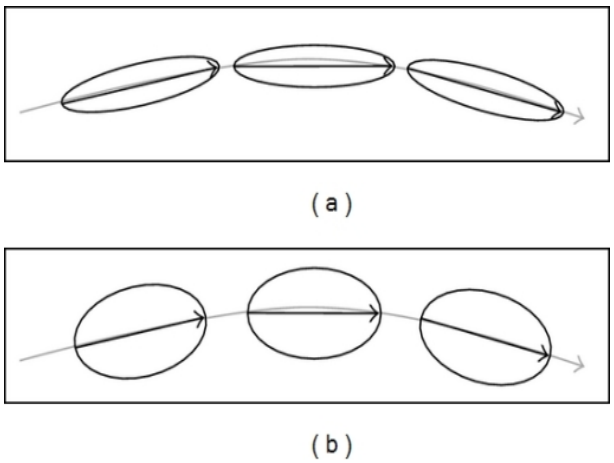

Figure 3.5: ***Schematic illustration of deterministic tractography, (a) three adjacent voxels have a clearly directed primary diffusion direction (longitudinal diffusion) indicated by ellipsoids. A deterministic tractography analysis would result in the indicated tract. (b) week directionality of diffusion, evidenced by more spherical ellipsoids (small FA). The direction of the principal direction is, however, unchanged. This explains why deterministic tractography analysis may result in the same reconstructed tract (primary direction unchanged) although the diffusion tensor is less ellipsoidal. (Xekardaki et al., 2011)***

A drawback of this approach is that the tensor information beyond the first eigenvector is neglected. In other words, an almost round tensor with very weak directionality has the same impact as a very pointed one (Knösche et al., 2015; Xekardaki et al., 2011), see Figure 3.5.

The error in streamlines can occur due to several factors (Johansen-Berg et al., 2009): (1) noise causing poor estimation of the fiber directions, (2) modelling error of the voxels, as the tensor model can not model the complexity of the white matter and (3) accumulated error in the tractography.

Due to these origins of error and because the deterministic tractography follows the fiber direction blindly, a stopping criterion must be used to reduce the effect of this error. The two most used stopping criteria are FA and curvature k threshold. Regions with low FA tend to have high uncertainty in the principal diffusion direction. The curvature k is defined as the angle between two successive steps. It is unusual to find white matter pathways that bend and have radii of curvature on the scale of the voxel (few millimeters) (Johansen-Berg et al., 2009). This means that the pathways must have small curvature.

3.7.1.2 Probabilistic tractography

Probabilistic tractography was proposed to address the limitation of deterministic tractography. Its output differs from the one of the deterministic tractography. With probabilistic tractography, we get the likelihood/uncertainty of two regions to be connected. Whereas in deterministic

Figure 3.6: ***Result of a probabilistic tractography. (P. Yeh et al., 2012)***

tractography, we attempt to get the connectivity between these two regions (binary value).

Unlike the deterministic tractography, probabilistic tractography takes into account the uncertainty of the local fiber directions (preferred diffusion directions) (Smith et al., 2004; Behrens et al., 2007). The probabilistic tractography follows the following procedure:

- Drop a set of particles at the seed point.
- Draw a sample orientation from the uncertainty fiber direction.
- Move the particle by a step along the previous direction.
- Repeat for all particles until a stopping criterion.

This procedure is repeated for each seed point. It gives at the end an image that contains a probability that two regions are connected (see Figure 3.6).

The advantage of probabilistic over deterministic tractography is that unlike in later, the probabilistic tractography can progress in several directions. The second advantage of probabilistic tractography is that is robust to noise. It has been shown that paths that have taken errant routes tend to disperse quickly, which gives low probability values (Johansen-Berg et al., 2009).

3.7.2 Global tractography

In global tractography, the tracking is not done through local orientations like in the previous two tracking methods but it is done in a global manner (Jbabdi et al., 2007). This approach tries to find the fiber configurations between two regions that best explains the diffusion signal. Each segment of the fiber is a parameter to be optimized in the global tractography (P. Yeh et al., 2012). Some algorithms can be found in (Jbabdi et al., 2007; Fillard et al., 2009; Kreher et al., 2008; Reisert et al., 2011).

The advantage of global over local tractography is that it fits the entire pathway between source and target regions. It is more suited to reconstruct known white-matter pathways. Unlike local tractography, global tractography results in symmetric paths between the seed and target regions and it accepts many solutions. The main problem of global tractography is the computation time and it is sensitive to initialization.

3.8 Conclusion

In this chapter, we explained briefly how the diffusion signal is related to the microstructure of the white matter. We also introduced some scalars which give insight about the anisotropy of tissues. We talked briefly about the three tractography methods used to reconstruct the white matter pathways. Deterministic tractography is faster than probabilistic approach, but it can not characterize crossing fibers or more complex fiber arrangements. Probabilistic tractography can reconstruct pathways with fiber-crossing. On the other hand, global approaches are computationally expensive because they search through a larger solution space of all possible connections between two regions. Because of this, we decided to use probabilistic tractography to reconstruct white matter pathways that will be included in the EEG/MEG inverse problem.

Chapter 4

Cortical surface parcellation

Contents

4.1 Introduction 54
4.2 Parcellation approaches 54
4.3 dMRI-based parcellation 56
4.3.1 Review of dMRI-based parcellation methods 56
4.3.2 Connectivity profile: a dMRI-based fingerprint . . . 58
4.3.3 dMRI-based parcellation using the mutual nearest neighbor condition 59
4.4 Similarity measure 62
4.4.1 Cosine coefficient 62
4.4.2 Tanimoto coefficient 63
4.4.3 Ruzicka coefficient 64
4.4.4 Motyka coefficient 65
4.4.5 Roberts coefficient 65
4.5 Data acquisition 65
4.6 Results of MNN parcellation 66
4.6.1 Comparing parcellations 67
4.6.2 Results of parcellation 68
4.7 Conclusion 91

4.1 Introduction

Several studies show that the functional and structural organization of neurons are not random and follow specific arrangements (Brodmann, 1909; Toga et al., 2006; Beeck et al., 2008). Subdividing the cortical surfaces into areas of specific features is called parcellation. Parcellation of the cortical surface can be done through three different methods. First, it can done postmortem like in cytoarchitecture (Brodmann, 1909), in which regions are defined to be patches with similar neurons' types and densities. Functional data can be also used to parcellate the cortical surface. The most used functional measurements are fMRI (Bellec et al., 2006; Cottereau et al., 2012; Thirion et al., 2014) and MEG/EEG (Mattout et al., 2005; Cottereau, 2008; Blumensath et al., 2012; Chowdhury et al., 2013). Lastly, dMRI can be used to get regions with similar anatomical connectivities. Atlases can be also used to label brain regions. In this chapter, we explain briefly the advantages and disadvantage of parcellations from each of these imaging modalities. We then introduce our proposed parcellation algorithm and provide some evaluation.

4.2 Parcellation approaches

Brodmann defined region on the cortical substrate based on the cytoarchitecture organization of neurons (see Figure 1.10). Despite that some studies show correlation between some of the Brodmann's regions and diverse cortical functions (Mohr, 1976; Mohr et al., 1978; Picard et al., 1996; Binder et al., 1997; Geyer et al., 2012), cytoarchitecture is a destructive method and because Brodmann' areas are big some of the areas show functional inhomogeneity.

Labeling the cortical regions can be done by registering the cortical surface into an Atlas defined from a training data set. Brain atlases provide sets of predefined regions that cover the whole brain's surface/volume. Some of the atlases that can be found in literature are: Destrieux (Fischl et al., 2004), Desikan-Killiany (Desikan et al., 2006), and Mindboggle (Klein et al., 2005). They are obtained by using surface information e.g. curvature to parcellate cortical surface. Desikan-Killiany and Mindboggle atlases show similar regions. This is why, we compare our parcellation to only Desikan-Killiany and Destrieux atlases.

Despite their obvious usefulness, atlases are limited:

- Several atlases are mutually inconsistent. This raises the question of which atlas represents the most the "modules" of the brain (Fodor, 1983; Sporns, 2011). These modules are defined by network analysis.
- Atlases are created from a training set of subjects. We are not sure that atlases can fit new data (subject) due to the lack of representation of the different populations.

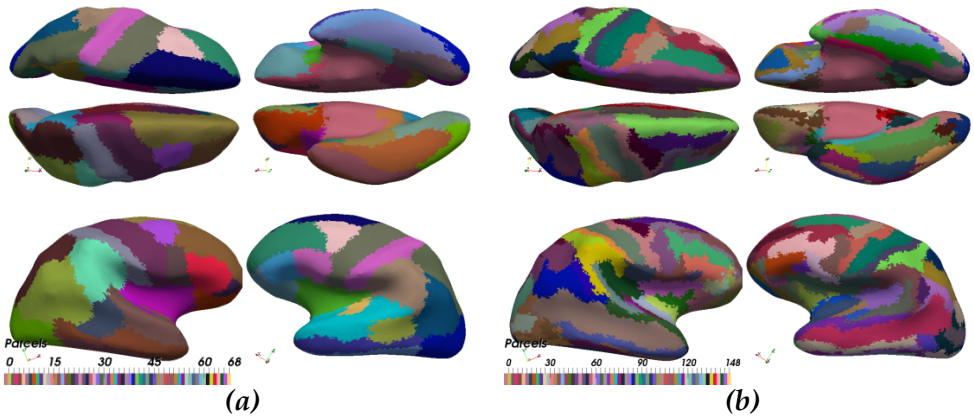

Figure 4.1: ***Four different view of two brain atlases: (a) Desikan-Killiany (b) Destrieux obtained from Dale et al., 1999.***

Atlas mislabeling can be due to image characteristics and processing strategies that have evolved since the atlas creation, because a given study deals with a population that is not well represented by the subjects used to construct the atlas, or because the information of interest is simply not mapped properly in the given atlas. Brodmann's parcellation was based on a single brain. This raises the question of how well do these atlases agree with other brains in which other borders are known.

Figure 4.1 shows four different views of two atlases, Desikan-Killiany (Desikan et al., 2006) and Destrieux (Fischl et al., 2004). In both atlases, we have large regions. This do not agree with the assumption of small functional localized regions. Subdividing these large regions must be done to obtain smaller regions with more precise functional roles (Thirion et al., 2014).

Functional data-driven parcellations use functional imaging like fMRI, EEG and MEG to parcellate the brain (Mattout et al., 2005; Bellec et al., 2006; Cottereau, 2008; Blumensath et al., 2012; Cottereau et al., 2012; Chowdhury et al., 2013; Thirion et al., 2014). They use the time courses of every voxel on the cortical surface (or brain volumes) to define regions with similar activations. The drawback of using functional measurements to parcellate the cortical surface is that only the activated areas can be mapped (e.g. Multivariate source prelocalization (MSP) (Mattout et al., 2005)). This means that these parcellations are task-specific. Resting state fMRI can also be used to divide the brain into cortical regions (Varoquaux et al., 2011).

The work of (Brodmann, 1909) was the base of several other works that assume that regions with dissimilar microstructure have different functions. The works of (Passingham et al., 2002; Sporns et al., 2004; Tomassini et al., 2007) show that the structural connectivity of a cortical region is the principle indication of its function. That is why dMRI seems attractive to parcellate the cortical surface. The dMRI-based parcellation is subject-specific and not task-specific.

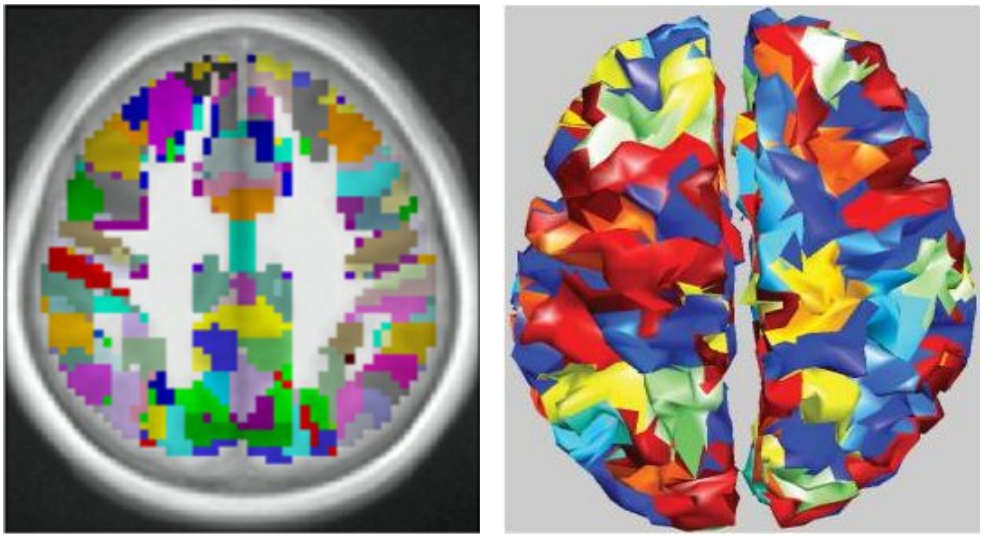

(a) *(b)*

Figure 4.2: ***Parcellation from (a) fMRI (500 regions, Thirion et al., 2014) and (b) MEG (174 regions, Chowdhury et al., 2013).***

4.3 dMRI-based parcellation

dMRI is a non-invasive imaging modality and allows to access the short and long brain connectivity (see Chapter 3.1). Producing the pathways between regions is challenging due to the limitation of dMRI (see Chapter 3.7). The dMRI connectivity-based parcellation algorithm uses connectivity information to subdivide the cortical surface. It involves three steps:

- The computation of connectivity properties of points or patches situated on the cortical surface. These are called connectivity fingerprints or profiles.
- Comparing the connectivity profiles of the different points or patches. This is done by using a similarity metric.
- A clustering algorithm that groups the points/patches with the closest connectivity fingerprints.

4.3.1 Review of dMRI-based parcellation methods

The term connectivity fingerprint was first used in (Hudspeth et al., 1976) to describe the properties of points in the cortical layer. In (Passingham et al., 2002) connectional fingerprint referred to the unique pattern of cortico-cortical connections: the strength of the connection is coded with a number between 0 (unconnected) to 4 (strong connection), the fingerprint is represented in vectorial form so that a vector-based similarity measure such as Euclidean distance or a correlation coefficient can be used to compare the fingerprints of the different points/patches (Passingham et al., 2002).

The work of (Passingham et al., 2002) opened the door to anatomical connectivity-based parcellation. (Behrens et al., 2003) were the first to use

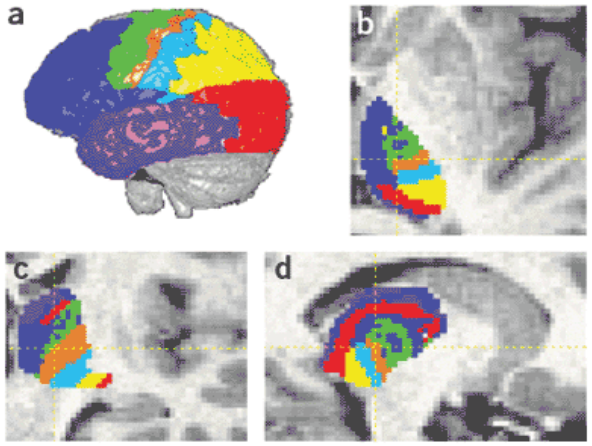

Figure 4.3: ***Cortical target regions a) and connectivity target-based parcellation of the Thalamus b,c,d). (reprint from (Behrens et al., 2003)).***

diffusion generated tracts to parcellate points in the brain. In their work, they generated probabilistic tractograms (see Chapter 3.7), for each point of the thalamus (see Figure 4.3). Then, they assigned each of the thalamus points to one of the cortical patches based on the connection strength between the thalamus point and each of the cortical regions (Figure 4.3 (a)). They then parcellate the thalamus according to the strength of the target regions. In (Johansen-Berg et al., 2004), the fingerprint is defined by the strength of the connectivity at each white matter voxel instead of only the end points i.e. target regions. This is less sensitive to noise and incorporate structural organization of white matter in the fingerprint.

(Anwander et al., 2007) used an unsupervised method to define boundaries of subregions of the Broca's region. They used the *k-means* algorithm to divide the Broca's region into subregions with similar fingerprints. They also constructed the fingerprint from all of the white matter voxels and used correlation as a similarity metric to compare each fingerprint-pair.

k-means is one of the popular clustering algorithms. It has been used in several works; (Anwander et al., 2007; Tomassini et al., 2007; Mars et al., 2011; Philippe et al., 2013; Belaoucha et al., 2014; Belaoucha et al., 2015a). Although *k-means* is used in the dMRI-based parcellations due to its simplicity of interpretation, it suffers from the limitation of needing the number of regions/sub-regions as a parameter. To solve this limitation, several approaches have been proposed (Jbabdi et al., 2009; Philippe et al., 2013; Belaoucha et al., 2015a; Belaoucha et al., 2016) in which the number of regions was obtained from the data itself.

In (Jbabdi et al., 2009), it is assumed that the fingerprints originate from a mixture of Gaussian distributions. The number of clusters is therefore the number of Gaussian distributions that generate the data observed. In (Philippe et al., 2012; Philippe et al., 2013), the number of clusters/regions is the number of the n highest eigenvalues (λ_i) of the cross-correlation matrix computed using dMRI fingerprints. The value of n validates the following criterion:

$$n = \min_k \frac{\sum_{i=1}^{k} \lambda_i}{\sum_{i=1}^{p} \lambda_j} \geq c_{th} \tag{4.1}$$

where p is the total number of fingerprints and $c_{th} \in [0, 1]$ ($c_{th} = 1 \implies n = p$ and $c_{th} = 0 \implies n = 1$). Different c_{th} values will result to different parcellations. In (Belaoucha et al., 2016), we used the eigen-gap method (Von Luxburg, 2007) to choose the number of subregions per atlas patch (see Von Luxburg, 2007; Belaoucha et al., 2016 for more details). The number of subregions is chosen automatically to be the indices of the highest drop in the eigenvalues, ordered in deceasing order, of the cross-correlation matrix. In this approach, no parameter is needed to parcellate the whole cortical surface.

k-means has been shown to be unstable when working in high dimensional data and to dependent strongly on the initialization of the regions' centers (Bubeck et al., 2012). Hierarchical clustering was proposed to overcome the limitation of the methods previously explained i.e. sensitivity to the initialization of the regions' centers and knowing a priori the number of regions. Hierarchical clustering approaches can be divided into two categories: divisive (Top-down) and agglomerative (Bottom-up) clustering.

Divisive clustering starts by assuming that brain is one region. Then, it subdivided into several regions. The Agglomerative clustering assumes that each voxel in the brain volumes is a region. Then, it merges regions according to a criterion. Like divisive clustering, agglomerative approaches suffers from the high dimentiality of connectivity profile.

Some works used agglomerative clustering to parcellate the brain (Thirion et al., 2014; Bonmati et al., 2015). The Agglomerative methods can compare only the neighboring seed pairs, which yields lower execution times. Our approach uses the advantage of the agglomerative approaches to obtain connected-regions, by merging only neighboring regions, with the highest structural homogeneity.

4.3.2 Connectivity profile: a dMRI-based fingerprint

Connectivity profile is defined in this work as a vector in which each element corresponds to the strength of connectivity between a seed (starting point) and a voxel of the white matter. To estimate the strength of structural connectivity, we applied the probabilistic tractography (see section 3.7.1.2) implemented in FSL (Smith et al., 2004) to all of the cortical surface points i.e. seeds.

These dMRI-based fingerprints obtained from FSL are high in dimension. They have the dimension of the diffusion image space. We reduce this space by only considering brain's voxels i.e. we neglect the voxels outside the brain because they do not have any structural connectivity to the cortical surface (voxels with 0 values). This uses less memory and decreases the computation time without affecting the computation accuracy. It is worth mentioning that the dMRI-based fingerprint is a vector of positive values.

4.3.3 dMRI-based parcellation using the mutual nearest neighbor condition

Few works were done to parcellate the whole cortical surface at a time due to the high dimensionality of the problem (Perrin et al., 2008; Roca, 2011; Philippe et al., 2013; Moreno-Dominguez, 2014).

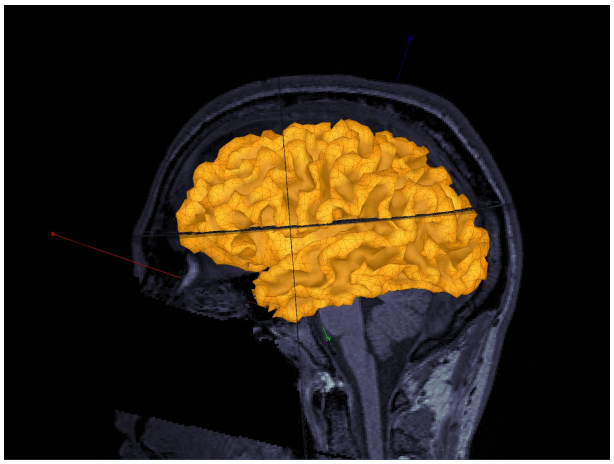

Figure 4.4: ***The cortical surface shown in a MR image. Face is removed to maintain anonymity.***

Our proposed dMRI-based parcellation algorithm uses a hierarchical method based on the Mutual Nearest Neighbor (MNN) condition (Bellec et al., 2006) to merge regions with the highest similar connectivity profiles.

This algorithm uses the fact that close seeds in the same region should have close connectivity profiles. Initially, all seeds are considered to be singleton regions. Then, we test the neighbors of each region. The merging candidate is the region with the highest similarity measure value.

The cortical surface is considered as a mesh (see Figure 4.4). Each vertex in the mesh is considered as a seed. We generated the connectivity profile of every seed as explained in section 4.3.2.

- CP is a matrix that contains the connectivity profiles of all seeds. $CP(i)$ is the connectivity profile of seed i.
- MC is a $NS \times NS$ (NS is the number of seeds) binary matrix whose elements reflects the mesh connectivity.
- K is the maximum number of iterations.
- T is a parameter used to stop merging big regions.
- SM is the similarity measure used to compare the connectivity profiles of two seeds or two pair of regions (0 for total dissimilarity and 1 for equal connectivity profiles).
- C is a vector of length equal to the number of regions.

- Label is an NS vector that contains the label of each seed of the cortical mesh.

Algorithm 1 Cortical parcellation algorithm

1: **procedure** PARCELLATION(CP, MC, T, K)
2: **Initialize:**
$s \leftarrow \frac{NS}{T}$, Label=1:$NS$
3: **while** $K > 0$ **do**
4: **for** each region r **do**
5: $N_r \leftarrow$ *Neighbors*(MC, r)
6: C(r)$\leftarrow \arg\max_{r_k \in N_r} SM(r, r_k)$
7: **end for**
8: **for** each region r **do**
9: **if** $|r| < s$ and MNN$(r, C(r))$ and $|C(r)| < s$ **then**
10: Label$(C(r)) \leftarrow$ Label(r)
11: **end if**
12: **end for**
13: Relabel Label with values between 1 and |unique(Label)|
14: **if** Label unchanged **then**
15: $N_s \leftarrow$ Regions smaller than s
16: **while** $N_s \neq \emptyset$ **do**
17: **for** each region r in N_s **do**
18: $N_r \leftarrow$ *Neighbors*(MC, r)
19: Label(r) $\leftarrow \arg\max_{r_k \in N_r} SM(r, r_k)$
20: **end for**
21: $N_s \leftarrow$ Regions smaller than s
22: **end while**
23: **return** Label
24: **end if**
25: $K \leftarrow K - 1$
26: **end while**
27: **return** Label
28: **end procedure**

We tested our algorithm with five different similarity measures (see section 4.4). Algorithm 1 can be summarized by the following steps:

- Initialization (line 2).
- Computing of merging candidates (line 4-7).
- Merge best candidates (line 8-12).
- Stop when no merging occurs after post-processing small regions (line 13-21) or after K iterations.

At line 2, we initialize the *Label* vector of length NS by considering each seed as a region of one point and the threshold $s = \frac{NS}{T}$ which controls the size of the resulting regions. The size of a region r ($|r|$) is defined as the

number of seeds in that region. Regions that have more or equal than s seeds are validated. Then, for each region, r, we find the set of its neighbors N_r, using the function *Neighbors* (line 5).

At line 6, we compute similarity values between a region r and its neighbors in the set N_r. The similarity between two region r and r_k is defined as:

$$SM(r, r_k) = \frac{1}{|r_k||r|} \sum_{(v,u)\in(r\times r_k)} S(CP(v), CP(u)) \tag{4.2}$$

where S is the similarity measure used to quantify the similarity between the connectivity profile of seed v ($CP(v)$) and u ($CP(u)$). The definition of the similarity measure can be seen in the next section.

The candidate region for merging with r is the region with the highest similarity measure value (see line 6). The result is saved in the merging candidate vector C. The length of C is equal to the number of regions in the previous iteration. After finding the candidates for merging (line 4-7), we merge only regions that validate the MNN condition and have size less than s (line 9):

$$MNN(r, C(r)) = \begin{cases} 1 & C(C(r)) = r \\ 0 & \text{otherwise} \end{cases} \tag{4.3}$$

This means that r is merged with $C(r)$ if r is the neighbor of $C(r)$ with the highest similarity measure value **and** $C(r)$ is the neighbor of r with the highest similarity value i.e. $r = C(C(r))$. Before merging, we test whether the regions' sizes are smaller than s (see line. 9). A region, r, is merged if $|r|$ is smaller than s. This is done to have relatively consistent regions. After merging, the label of the region $C(r)$ is changed to r (line 10) for clarity.

The algorithm stops iterating if:

- There are no pairs validating the MNN condition.
- The algorithm reaches the total number of iterations, K.

The regions before the post-processing, before line 14, have size between 1 and $2(s-1)$. This is because we merge regions with size smaller than s i.e. the biggest merging candidate can have size $(s-1)$. In the extreme case, r and $C(r)$ can both have size $s-1$ which results to a region of size $2(s-1)$ after the merging. The minimum size is 1 seed, because a region could not validate the MNN condition with its neighboring regions.

It is worth mentioning that we do not neglect the invalidated regions like in (Bellec et al., 2006) but we apply a post-processing step (see line 14-24) to obtain regions of relatively consistent size because we will be working in reconstructing sources inside regions of certain size. In the algorithm, lines 4-12 give regions with the highest homogeneity due to the MNN condition. But this is reduced by the post-processing (line 13-21) due to merging small regions that do not validate the MNN condition. A small region r ($|r| < s$) is merged with a valid neighboring region r_k ($r_k \geq s$) if $SM(r, r_k)$ gives the highest similarity value among the neighboring of r. The effect of the

post-processing stage on the resulting parcellation is investigated in Chapter 4.6.2. This post-processing is a good compromise between the structural homogeneity and regions' size. This algorithm gives regions of size between s and $3(s-1)$ after the post-processing

4.4 Similarity measure

As explained in section 4.3, to parcellate the cortical surface we need a similarity measure to compare the different connectivity fingerprints/profiles. This similarity must satisfy the property of symmetry and nonnegativity. It must be also bounded i.e. the similarity measure between the fingerprint X and Y is smaller or equal to a finite number d. These properties make it easier to interpret and compare the results. In our work, similarity measure is used but it is worth mentioning that this algorithm can easily use the concept of distance instead of similarity ($distance = d - similarity$) with some small modifications.

While the Euclidean distance is one of the most commonly used when working with low-dimensional data, it does not score well in high dimensionality (Aggarwal et al., 2001; Terada, 2013). We tested several similarity measures described in the next sections.

4.4.1 Cosine coefficient

The idea of Cosine coefficient comes from correlation. The correlation coefficient measures the linear dependencies between two variables (X and Y). It has been used to quantify the similarity between tractograms (connectivity profiles) in several works (Anwander et al., 2007; Philippe et al., 2013; Belaoucha et al., 2015a). Let n be the length of X and Y i.e. $n = |X| = |Y|$.

$$\begin{aligned} S(X,Y) &= \frac{\sum_{i=1}^{n}(X_i - \overline{X})(Y_i - \overline{Y})}{\sqrt{\sum_{i=1}^{n}(X_i - \overline{X})^2 \sum_{i=1}^{n}(Y_i - \overline{Y})^2}} \\ &= \frac{(X - \overline{X}) \cdot (Y - \overline{Y})}{\left\|X - \overline{X}\right\| \left\|Y - \overline{Y}\right\|} \end{aligned} \tag{4.4}$$

where X_i and Y_i are the i^{th} element of the vector X and Y respectively, $\overline{X}_i$ and $\overline{Y}_i$ are the mean of X and Y respectively. This quantity can produces negative values which is hard to interpret. That is why (Moreno-Dominguez, 2014) modified S by removing the centering resulting into the

normalized dot product of the fingerprints:

$$
\begin{aligned}
S_c(X,Y) &= \frac{\sum_{i=1}^{n} X_i Y_i}{\sqrt{\sum_{i=1}^{n} X_i^2 \sum_{i=1}^{n} Y_i^2}} \\
&= \frac{X \cdot Y}{\|X\| \, \|Y\|}
\end{aligned}
\tag{4.5}
$$

which is known as the *Cosine* coefficient. S_n varies between 0 and 1. One when X is equal to Y and zero if they are perpendicular i.e. $X^T Y = 0$. It is based on the normalized inner product measure i.e it only considers voxels that are non-zero in both vectors.

Another similarity measure that can be used to cluster the cortical surface is the mutual information (Moreno-Dominguez, 2014). This measure has the advantage over S_c and S_n that it does not only capture the linear dependencies but also higher order dependencies. But it is also computationally more expensive than the previous two, which is a big drawback if we want to parcellate the whole cortical surface.

The values of both measures are close because the fingerprints/profiles contain many zeros which result to very small mean. In consequence, the differences between S_n and the classical Pearson's correlation, S_c, are minimal (Moreno-Dominguez, 2014).

4.4.2 Tanimoto coefficient

In (Bajusz et al., 2015), the Tanimoto measure was used also to quantify the similarity between molecular fingerprints. It is defined as (Kristensen et al., 2010; Bajusz et al., 2015; Strehl et al., 2000; Todeschini et al., 2012):

$$
\begin{aligned}
S_t(X,Y) &= \frac{\sum_{i=1}^{n} X_i Y_i}{\sum_{i=1}^{n} X_i^2 + \sum_{i=1}^{n} Y_i^2 - \sum_{i=1}^{n} X_i Y_i} \\
&= \frac{X \cdot Y}{\|X - Y\|^2 + X \cdot Y} \\
&= \frac{X \cdot Y}{\|X\|^2 + \|Y\|^2 - X \cdot Y}
\end{aligned}
\tag{4.6}
$$

The dMRI-based fingerprints X and Y contain positive values (see 4.3.2 for more details). This leads S_t to vary between 0 and 1. Zero in the case of total dissimilarity ($X^T Y = 0$) and one when X is identical to Y (.i.e $\|X - Y\|^2 = 0$). *Tanimoto* is reduced to the *Jaccard* index if X and Y are binary vectors. Like *Cosine* measure, *Tanimoto* is a normalized inner product.

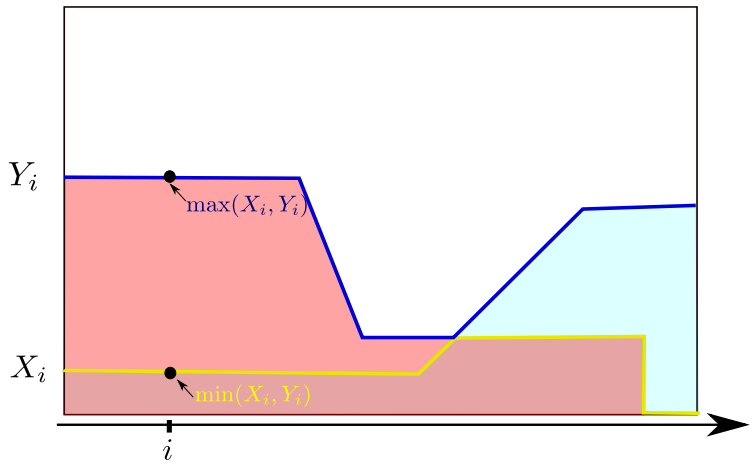

Figure 4.5: ***Representing the connectivity profiles in 2D to interpret some of the similarity measures. min(X_i, Y_i) and max(X_i, Y_i) for each i are shown in yellow and blue respectively.***

4.4.3 Ruzicka coefficient

The Ruzicka measure is defined as (Mukherjee, 1956; Cha, 2008):

$$S_r(X, Y) = \frac{\sum_{i=1}^{n} \min(X_i, Y_i)}{\sum_{i=1}^{n} \max(X_i, Y_i)} \tag{4.7}$$

This measure was used to quantify the similarity between images and between molecules (Weken et al., 2002; Cha, 2008). If $X^T Y = 0$, the numerator of Eq 4.7 is equal to zero because $\forall i \ \min(X_i, Y_i) = 0$ (X and Y contain positive values). This makes 0 the lower bound of S_r. If $X = Y$, $\forall i$ $\min(X_i, Y_i) = \max(X_i, Y_i)$. One is the upper bound of S_r.

If you plot X and Y in 2D (versus elements' indices), this measure can be seen as the fraction between the area of intersection and area of union between X and Y (see Figure 4.5). The values of $\sum_{i=1}^{n} \min(X_i, Y_i)$ and $\sum_{i=1}^{n} \max(X_i, Y_i)$ correspond to the area under the yellow and blue curves, respectively. You can see that the S_r is the fraction between the area under the yellow curve and the one under the blue curve.

4.4.4 Motyka coefficient

The *Motyka* coefficient, derived from *Czekanowski distance*, is defined as (Motyka et al., 1951; Mukherjee, 1956):

$$S_m(X,Y) = 2\frac{\sum_{i=1}^{n}\min(X_i,Y_i)}{\sum_{i=1}^{n}(X_i+Y_i)} \tag{4.8}$$

It was used in divisive and agglomerative clustering algorithms (Shirkhorshidi et al., 2015). This measure can be seen as the fraction between the lower area ($\sum_{i=1}^{n}\min(X_i,Y_i)$) and the two areas $\sum_{i=1}^{n}X_i$ and $\sum_{i=1}^{n}Y_i$.

4.4.5 Roberts coefficient

The *Roberts* coefficient is defined as (Murty et al., 2016):

$$\begin{aligned} S_{ro}(X,Y) &= \frac{\sum_{i=1}^{n}(X_i+Y_i)\frac{\min(X_i,Y_i)}{\max(X_i,X_j)}}{\sum_{i=1}^{n}(X_i+Y_i)} \\ &= \frac{\sum_{i=1}^{n}\min(X_i,Y_i)(1+\frac{\min(X_i,Y_i)}{\max(X_i,Y_i)})}{\sum_{i=1}^{n}(X_i+Y_i)} \end{aligned} \tag{4.9}$$

It is also a measure that ranges between zero and one. The sum of the fingerprints values is weighted by fraction between the minimum and the maximum values. *Roberts* measure is similar to *Motyka*. It is computed as a fraction between the minimum area (weighted at each vector element by $1 \leq (1+\frac{\min(X_i,Y_i)}{\max(X_i,Y_i)}) \leq 2$) and the total area under the curves X_i and Y_i. This means that for the same X and Y, S_{ro} will always give equal or smaller SM values compared to S_m.

4.5 Data acquisition

Structural and diffusion MRI data were taken from 16 healthy subjects (Wakeman et al., 2015), 9 males and 7 females with an average age of 26.37 years. T1-weighted structural images of size $256\times256\times192$ were acquired by a Siemens 3T Trio scanner with a GRAPPA 3D MPRAGE sequence (TR = 2250 ms; TE = 2.98 ms; flip-angle = 9°; acceleration factor = 2; 190 Hz/pixel) at 1 mm isotropic resolution. The diffusion weighted images of size $96\times96\times68$ were collected by the same scanner at 2 mm isotropic resolution (64 gradient directions and *b-value* =1000 s/mm^2), with one b0 image.

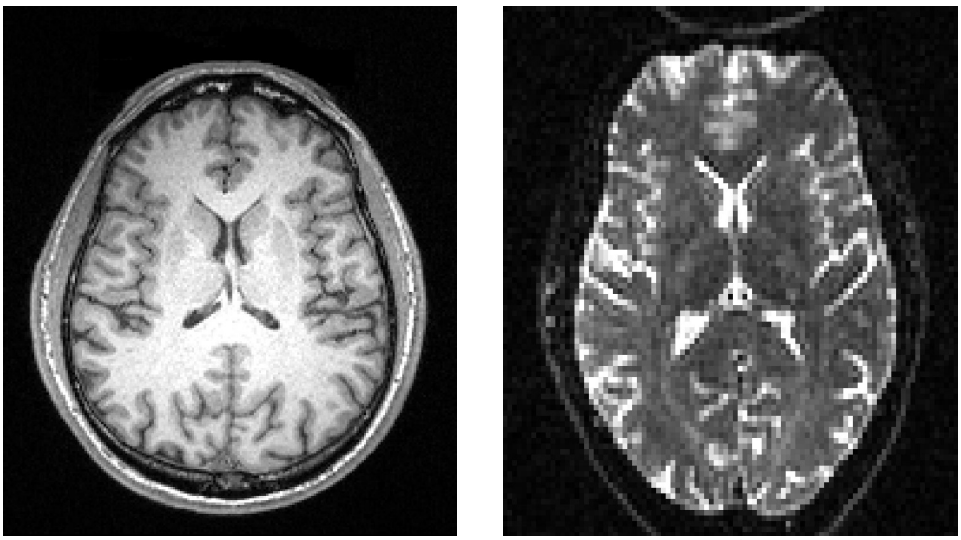

(a) *(b)*

Figure 4.6: ***Axial view of (a) T1 image and (b) b0 image of subject 1 in (Wakeman et al., 2015).***

The face of the participant in the T1 image was subsequently manually removed to help maintain anonymity (Wakeman et al., 2015). An example of T1 and b0 image can be seen in Figure 4.6

The cortical surfaces were extracted using Freesurfer (Dale et al., 1999) from T1 images and remeshed to 10^4 vertices using CGAL (Project, 2016) which provides meshes with relatively equal triangles.

Subject N	1	2	3	4	5	6
N of seeds	9347	9324	9395	9382	9341	9384
Subject N	9	12	13	14	15	-
N of seeds	9365	9359	9405	9398	9252	-

TABLE 4.1: The number of seeds for each subject after removing the thalamus.

It is worth mentioning that the thalamus was removed from the cortical surface using the labeling of Freesurfer atlas because EEG/MEG can hardly measure activation located there. This result to the number of seeds (vertices) shown in Table 4.1. The whole subjects cortical surfaces contain around 10^4 vertices. We used only the data from subjects [1, 2, 3, 4, 5, 6, 9, 12, 13, 14, 15] because they are only the subjects who have dMRI data.

4.6 Results of MNN parcellation

Only the subjects that have dMRI, in the dataset (Wakeman et al., 2015), were used to obtain parcellations at different levels. The average age of the remaining subjects is 26.63 years, with a standard deviation (STD) of ± 2.70.

The cortical surfaces are extracted from the T1 images then projected into the diffusion space images of their corresponding subjects using linear registration (Smith et al., 2004). Each vertex in the cortical mesh is considered as a seed. The probabilistic tractography implemented in FSL (Smith et al., 2004) is run to obtain connectivity image (profile) for each seed.

4.6.1 Comparing parcellations

We obtained parcellations with different similarity measures (see section 4.4) and atlases. Results are compared in spatial domain with spatial overlapping and structural homogeneity.

Spatial overlapping between two regions was measured using Dice coefficient (Dice, 1945). Let $A = (A_i), i \in \{1, .., n\}$ and $B = (B_j), j \in \{1, .., m\}$ be two parcellations of the same subject in n and m regions respectively. Then, the *Dice coefficient vector*, $D \in \mathbb{R}^n$, between A and B is defined as (Belaoucha et al., 2016):

$$D(i) = \max \frac{2|A_i \cap B_j|}{|A_i| + |B_j|}, \quad \text{for} j \in \{1, .., m\} \tag{4.10}$$

D contains the Dice coefficient of two regions with the highest spatial overlapping. The Dice coefficient value ranges is between 0 and 1. Zero when the two regions are non-overlapping and one when total spatial overlapping. D has a different length when comparing A to B and B to A because n and m can be different.

The MNN can give a matrix, R, that contains the similarity measures between all of the seeds pairs inside all of the regions i.e. R is a block matrix. Let SM_p be the vector that contains the values of these block matrices (one block per region). To compare the structural homogeneity of the obtained regions, we used the mean of the SM values of all pairs. It is defined as follows:

$$smv = \frac{1}{|SM_p|} \sum_{i}^{|SM_p|} SM_p(i) \tag{4.11}$$

Let STD be the standard deviation of the SM values, computed as follows:

$$STD = \sqrt{\frac{1}{|SM_p|} \sum_{i}^{|SM_p|} (SM_p(i) - smv)^2} \tag{4.12}$$

Coefficient of variation (CV) measures the dispersion of the similarity values. It is defined as follows:

$$CV = \frac{STD}{smv} \tag{4.13}$$

Smaller CV value means that the SM values are close to the mean value smv i.e. homogeneous regions. The higher the CV, the greater the dispersion in SM_p.

4.6.2 Results of parcellation

First, we apply the MNN parcellation algorithm to all the eleven subjects with different T values (parameter used to stop merging big regions, see section 4.3.3 for more details) and similarity measures. Figure 4.7 (a)-(e) shows the resulting parcellation of Subject 1 with different similarity measures and $T = 100$.

4.6.2.1 Computation time

Figure 4.7 (f) shows the mean and the standard deviation of the computation time over subjects for the different T values and SMs. In our implementation, *Cosine* and *Tanimoto* are the fastest and have close execution times. These values are obtained when using Intel(R) Core(TM) i7-3840QM CPU @ 2.80GHz. They are followed, in increasing order, by: *Motyka*, *Ruzicka* and *Roberts*. When $T = 100$, the execution time of *Tanimoto* for a cortical surface of 10^4 vertices is around 5 min which is seven times faster than when using MNN with *Roberts* similarity measure of the same mesh.

4.6.2.2 Number of regions

As can be seeing in Figure 4.8, the resulting number of patches is proportional to the value of the parameter T of the MNN parcellation algorithm. This parameter controls the size of regions (and hence the number of regions). With the MNN parcellation algorithm, the number of regions does not depend much on the similarity measure. This can also be seeing in Figure 4.7 (a)-(e), in which the number of regions was between 67 and 72 for the five similarity measures with the same T value. Let's assume the following relation between the resulted number of patches, N_r, and T:

$$N_r = aT + b \tag{4.14}$$

The mean and standard deviation (std) of the parameters a and b over subjects and SMs are shown in Table 4.2.

		SM				
		Tanimoto	Cosine	Ruzicka	Roberts	Motyka
a	mean	0.763	0.761	0.764	0.763	0.765
	std	0.013	0.015	0.012	0.012	0.013
b	mean	-12.5	-11.6	-14.0	-13.4	-13.7
	std	3.08	4.00	3.58	4.49	3.59

TABLE 4.2: Mean and standard deviation (std) of the parameters of the linear relationship between N_r and T (Eq 4.14) when using a mesh of size 10^4.

We can observe, from Table 4.2, that the mean values of a over similarity measures are very close to each other (≈ 0.760). The standard deviation, over subjects, of a is very low compared to its mean value. The mean value over subjects of the b value is close between the different similarity measures ($b \approx 12$). The relationship can be approximated to $N_r \approx 0.76T - 12$.

Does this equation hold when using higher mesh resolution ?

We parcellated the high-resolution meshes of the eleven subjects. The number of vertices of the meshes is around 3 $\times 10^4$. The relationship between N_r and T for these high resolution meshes is shown in Table 4.3. The correlation between N_r and T decreases (≈ 0.72).

The MNN parcellation algorithm results to a number of regions proportional to the value of T. The factor can be considered as a constant over subject and similarity measures because the standard deviation is very small. This results to close values of the number of parcels over similarity measures and per subject.

But do the different similarity measures give parcellations with close structural homogeneity and high spatial overlapping?.

This question can be answered from Figure 4.9, 4.10, 4.11.

		SM				
		Tanimoto	Cosine	Ruzicka	Roberts	Motyka
a	mean	0.721	0.727	0.720	0.710	0.721
	std	0.006	0.008	0.006	0.024	0.006
b	mean	-7.41	-8.35	-7.6	-5.18	-7.89
	std	2.90	2.98	3.23	5.69	2.96

TABLE 4.3: Mean and standard deviation (std) of the parameters of the linear relationship between N_r and T (Eq 4.14) when using high a resolution mesh (3 $\times 10^4$).

4.6.2.3 Regions' homogeneity

Figures 4.9 and 4.10 show the mean, smv, and the standard deviation of SM values of the resulting parcellation with the different similarity measures and subjects, respectively. Higher smv was obtained with Motyka and lower values with Tanimoto similarity measure. Higher STD value are obtained with Cosine and lower values with Ruzicka similarity measure. Figure 4.11 shows the CV values for the different subjects, T values and similarity measures. The mean and STD of SM value is proportional to T. This is true for all similarity measures. Higher CV value is obtained using Tanimoto and lower value with Motyka, this is true for all subjects.

For all the eleven subjects, the order in decreasing order with respect to the mean of the SM values is: *Motyka*, *Roberts*, *Cosine*, *Ruzicka* and *Tanimoto* for high values of T. For low T, *Ruzicka* gives higher mean compared to *Cosine* but otherwise the order remains the same. The STD values increase with T. This is because when decreasing the T, the resulting number of regions is decreased which results to bigger regions resulting in including dissimilar seeds. This makes the mean similarity values low and the standard deviation high.

CV is a relative measure of dispersion around the mean value. For all subjects and SMs (Figure 4.11), CV is mostly decreasing with T. For high T, CV is small which means that there is a low dispersion of the SM values

i.e. more homogeneous regions. Low homogeneity is observed for low T values which are translated by high CV values.

The question now is which SM is the best? Do they give better results than atlases?.

These questions are answered with the help of the following studies.

4.6.2.4 Regions' size

The fitted distribution of the number of seeds per regions for the different SM can be found in Figures 4.12, 4.13, 4.14, 4.15, 4.16. For all subjects and similarity measure, the number of seeds per region increases when decreasing the T parameter. The standard deviation of the number of seeds distribution is inversely proportional to T. This is expected because when decreasing T, the merging threshold s increases hence making regions bigger.

4.6.2.5 Region' area

In Table 4.4, we show the mean and standard deviation of the region's' area for the eleven different subjects. The parcels are obtained using the *Tanimoto* similarity measures. Like the number of seeds per region (see section 4.6.2.4), the area of regions is inversely proportional to the parameter T. When increasing the number T, this result to fewer seeds/sources inside each region, which result to getting small areas.

4.6.2.6 Spatial overlap

Figure 4.17 shows the distribution of the Dice coefficient between the resulting parcellations with the five similarity measures of Subject 1 for $Y \in \{100, 1000\}$. For $T = 1000$, regions are small which results to high spatial overlapping. For $T = 100$, even though the obtained regions are bigger, we can see high spatial overlapping between some of the regions of the different parcellations. This can be seeing clearly between *Tanimoto-Cosine* and *Motyka-Ruzicka* and *Motyka-Roberts*, Figure 4.17 (b). This is true for all subjects.

What are the regions that are insensitive to the choice of the SM?

It is clear that the spatial overlapping as defined in this work (Dice coefficient) depends on the number of regions. For a high number of regions, we obtained small regions and this results to high spatial overlapping. For a small number of regions, the resulting regions are big which also results in relatively big spatial overlapping coefficient.

In the limit, when the number of regions is equal to the number of seeds (singleton regions), the Dice coefficient vector of two parcellations is equal to $\mathbb{1}$. This is also true when having only two regions, one per hemisphere. The dice coefficient starts high, then decreases when the number of regions decreases. After a certain number, the Dice coefficient starts increasing while the number of regions is decreasing to reach total overlapping when the number of regions is equal to two (one region per hemisphere). This is

why we decided to compare the MNN parcellation with $T = 600$ and with the different similarity measures.

Cortical areas that have more than 70% spatial overlapping over the five similarity measures with $T = 600$ (areas in red color). The results are shown in Figure 4.18. We observed that some areas on the medial and lateral parietal lobe and also in the inferior temporal lobe. Also, some regions of the inferior and medial frontal lobe were observed to be less affected by the choice of the similarity measure.

4.6.2.7 Best similarity measure

We still did not answer the question of which SM is better. *Motyka*, *Roberts* and *Ruzicka* give low SM values dispersion, CV, which means higher homogeneity. *Tanimoto* and *Cosine* have more dispersed SM values. But if you observe Figure 4.11 that *Motyka*, *Roberts* and *Ruzicka* have small change of the CV values with respect to the decrease of the T value which implies that for these SM, the dispersion of the SM values does have low change between high and low T. *Tanimoto* and *Cosine* give high variation between the CV in high and low T values.

Regions in the cortical surface are localized and not extended. Having big regions (i.e. small T) should result in high CV values. This is observed only with *Tanimoto* and *Cosine*. Because the difference between the CV values with high and low T is lower when using *Cosine*, we decide to use *Tanimoto* similarity measure for the rest of the work. In Figure 4.11, at $T = 600$ a significant change in CV is observed. That is why, we suggest using the MNN with *Tanimoto* similarity and for T values greater than 600.

4.6.2.8 Effect of perturbations on the tractograms

In this part, we investigate the effect of noise on the similarity measures used in this work by using 100 seeds. To do so, we generate a random tractogram of length 10^4 with elements greater or equal to 0 that we consider to be the mean connectivity vector t_m. Each of the connectivity profiles, t_i, is deviated from the mean tractogram by an additive noise (ϵ) i.e.:

$$t_i = t_m + \epsilon$$

The mean similarity measure values of the five similarity measures are presented in Figure 4.19. We noticed that *Cosine* and *Tanimoto* are less affected by noise compared to the remaining three similarity measures. They are followed by Motyka, Roberts and Ruzicka. Ruzicka coefficient is found to be the most affected by noise level, this is due the increase of the distance between the minimum and the maximum value between the two connectivity profiles which results in lower similarity value.

4.6.2.9 Comparison to atlases

Figure 4.1 shows the atlases, Destrieux and Desikan-Killiany, that we used to compare to our parcellations. Figure 4.20 shows the spatial overlapping

between the atlases and the MNN parcellations for the different atlases and SM. T is chosen so that the MNN parcellation results in a close number of regions with respect to the number of regions in the corresponding atlases. The Dice coefficient between the MNN parcellation and atlases has a mean of $\simeq 0.4$. This means that on average, the regions have 40 % of a spatial intersection. This is due to the big size of the atlases' regions.

But what will happen if we have smaller regions (subdivide the atlases' regions)? Will this increase the homogeneity of the parcellated atlases and make it better than the MNN parcellation?.

Figure 4.21 shows the coefficient of variation (CV) of the SM values of the atlases before and after subdividing their regions using *k-means* for all subjects and SMs. The number of sub-regions is obtained by using the eigen-gap (Belaoucha et al., 2016). The number of sub-regions is decided by the index of the highest drop in the eigenvalues of the similarity matrix of each atlas' region. We obtained a mean, over subjects, of 181 and 396 regions for Desikan-Killiany and Destrieux atlases, respectively (Belaoucha et al., 2016).

As expected, the homogeneity of the regions is increased after subdividing the atlases' regions. This is translated to a decrease in the CV value. This is true for all subject, atlases, and SM. But when compared to the CV of the MNN parcellation (see Figure 4.11), they have higher values (Belaoucha et al., 2016). This means that the MNN gives more homogeneous regions than the atlases even after subdividing atlases' regions. This suggests that the atlases boundaries do not respect the structural connectivity of the seeds and that atlas based approaches are limited by their initialization (Philippe et al., 2013).

We assigned the obtained regions by MNN to the different brain lobes, defined by an atlas, with the highest dice coefficient. We compared the MNN parcellation, with $T \in \{700, 100\}$ and *Tanimoto*, to Mindboggle atlas which is similar to Desikan-Killiany (see Figure 4.22). We used Mindboggle instead of Desikan-Killiany because the former has the lowest number of regions (62). In the top panel, we show different views of mindboggle atlas on an inflated surface. Each color corresponds to a lobe e.g. green for temporal lobe. In the middle and bottom panels, we show the parcellation result of MNN of Subject 1 with T equal to 700 and 100, respectively. As can be observed in Figure 4.22, the brain lobes (frontal, prefrontal, temporal and occipital lobes) can be obtained from MNN parcellation. Even thought with $T = 700$ we obtain small regions, boundaries of the obtained lobes are different from the atlases. This is more clear when MNN results in bigger regions ($T = 100$). With $T = 100$, parts of Limbic region are detected as parietal regions. We notice that boundaries occipital lobe is the less affected by MNN. This suggest that the connectivity profiles of seeds inside occipital lobe are very different compared to their direct neighbors (temporal and parietal). The lobes' boundaries which are strongly affected by T are the central and temporal regions.

It is clear that the boundaries between the brain regions can not be considered as true lobes' boundaries. To get more accurate frontiers we suggest

to use functional imaging, see section 1.4, during several mental and physical tasks to draw more accurate lobes' boundaries.

4.6.2.10 Post-processing effect

Let's define the fraction:

$$f_{ba} = \frac{N_b - N_a}{N_b}$$

where N_b and N_a are, respectively, the number of regions before and after the post-processing defined earlier in section 4.3.3. This fraction gives us an idea about the number of regions that have a size, before post-processing, less than s (see Algorithm 1).

In Figure 4.23, we show the mean and standard deviation (over the eleven subjects) of the fraction f_{ba}. We observed that f_{ba} is inversely proportional to the parameter T. Another interesting result is that the similarity measures do not have a high impact on the number of invalid regions that were post processed. The number of regions that were merged after the MNN parcellation with the nearest region that gives highest SM values ranges between 25% ($T = 1000$) and 52% ($T = 100$), slightly more for Roberts, Ruzicka and Motyka than for Cosine and Tanimoto.

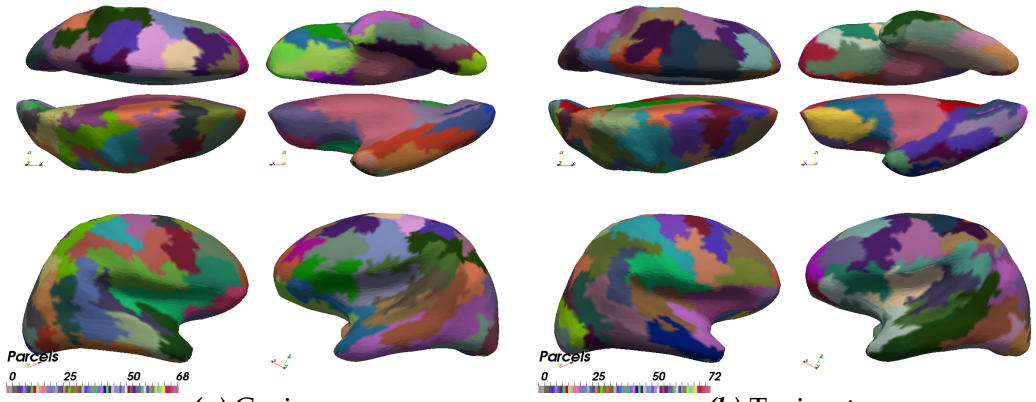

(a) Cosine

(b) Tanimoto

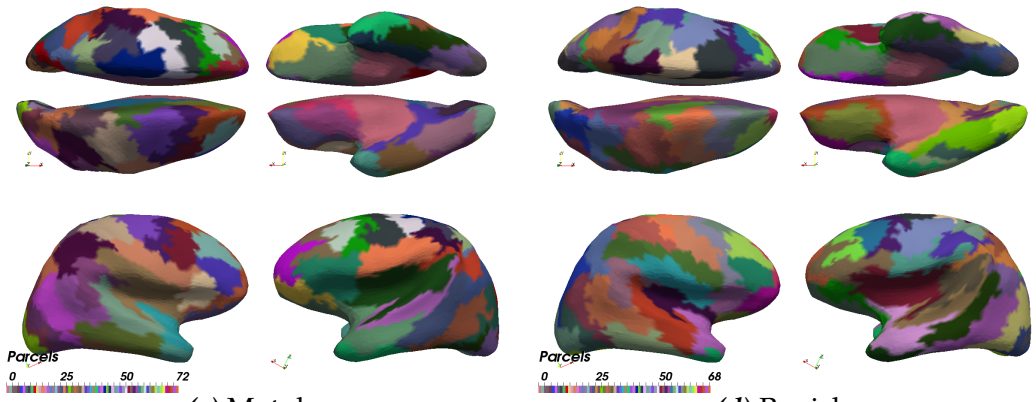

(c) Motyka

(d) Ruzicka

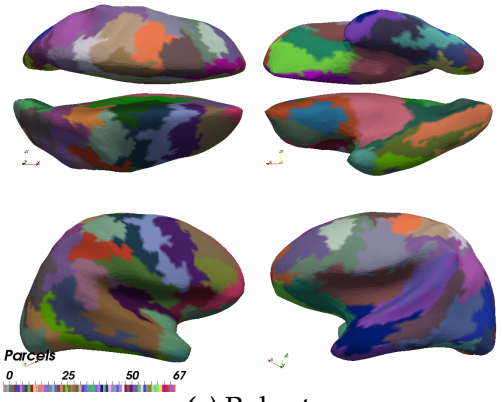

(e) Roberts

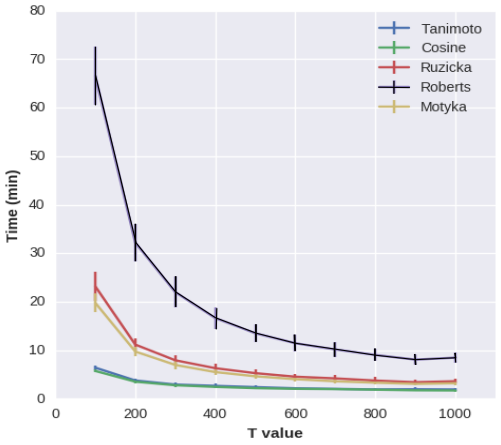

(f)

Figure 4.7: ***Parcellation of Subject 13 shown on the inflated brain surface. The parcellation used different similarity measures: (a) Cosine, (b) Tanimoto, (c) Motyka, (d) Ruzicka, (e) Roberts. These parcellations are obtained with*** $T = 100$. ***(f) shows the mean (over subjects) and the standard deviation of the execution time for different*** T ***values.***

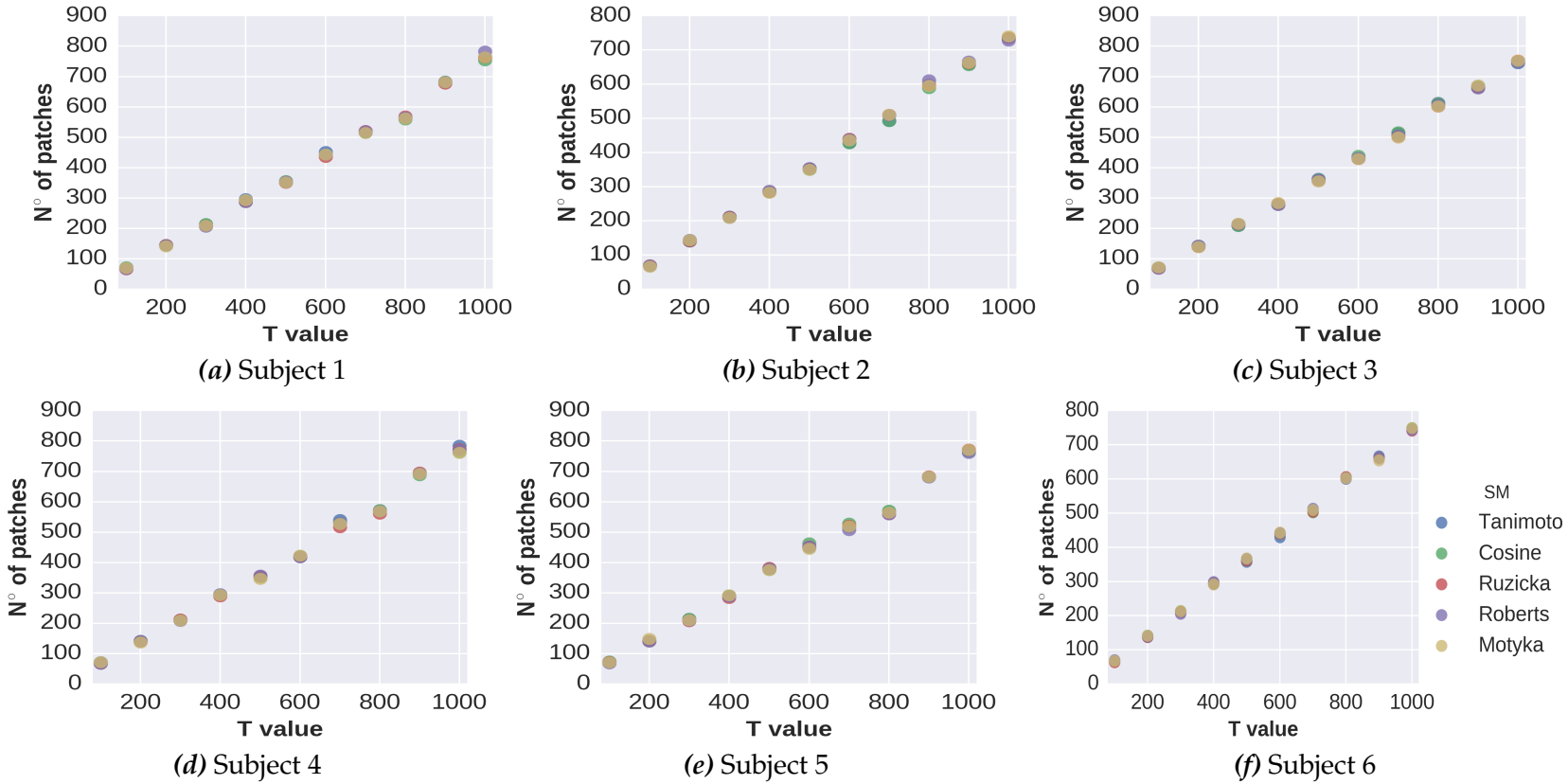

(a) Subject 1 *(b)* Subject 2 *(c)* Subject 3

(d) Subject 4 *(e)* Subject 5 *(f)* Subject 6

Figure 4.8: ***Resulting number of patches for different T values and subjects. It can be observed that the numbers of regions for each T value for the different SM are close and that there is a linear relationship between the number of regions and T. The remaining subjects show similar results.***

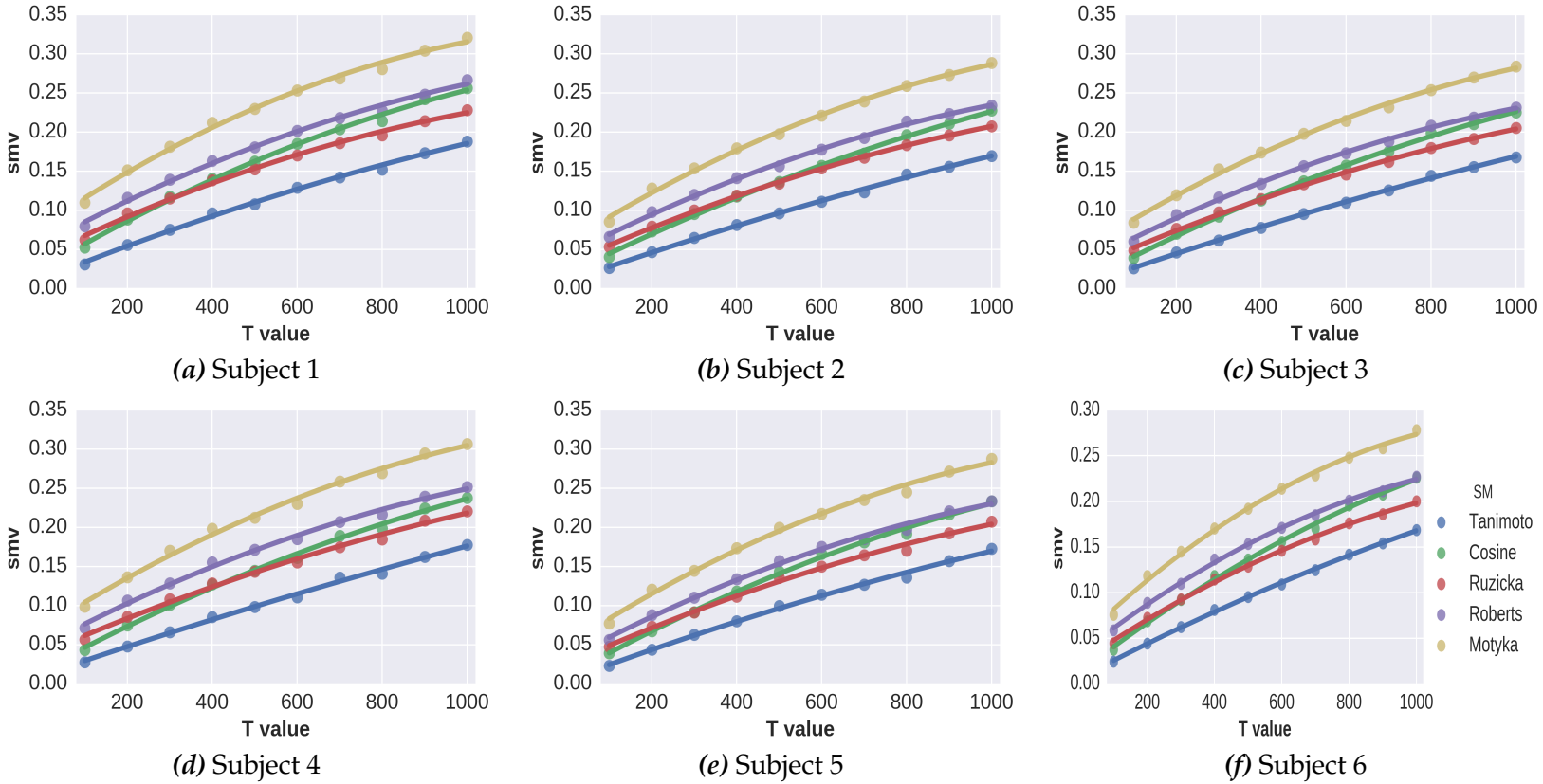

(a) Subject 1 *(b)* Subject 2 *(c)* Subject 3

(d) Subject 4 *(e)* Subject 5 *(f)* Subject 6

Figure 4.9: ***Mean of similarity measures (SM) values at different T values and for the different subjects. Note that Tanimoto is almost linear with respect to T. The remaining subjects show similar results.***

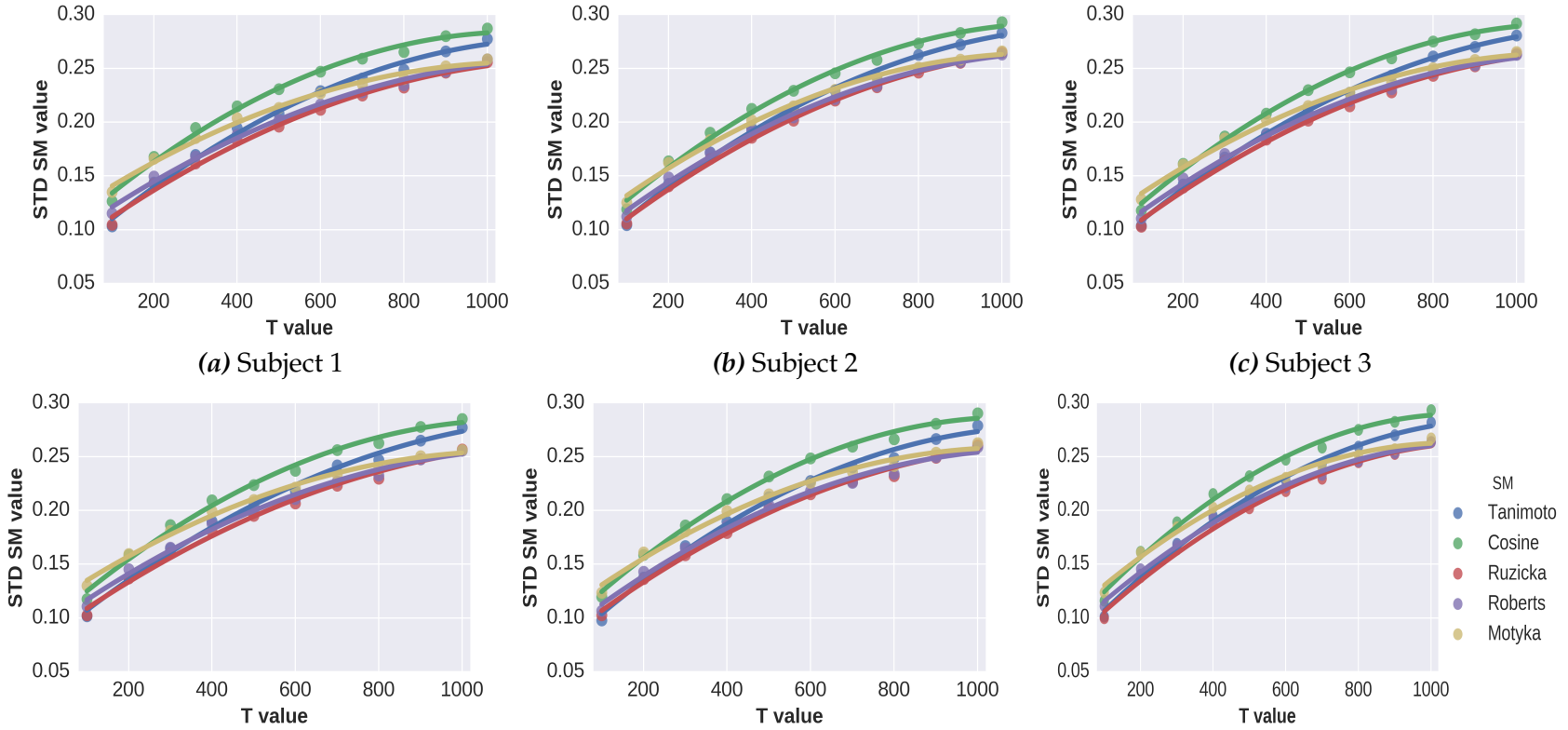

(a) Subject 1 *(b)* Subject 2 *(c)* Subject 3

(j) Subject 4 *(k)* Subject 5 *(l)* Subject 6

Figure 4.10: ***Standard of deviation (STD) of the similarity measures (SM) values at different T values and for the different subjects. The remaining subjects show similar results.***

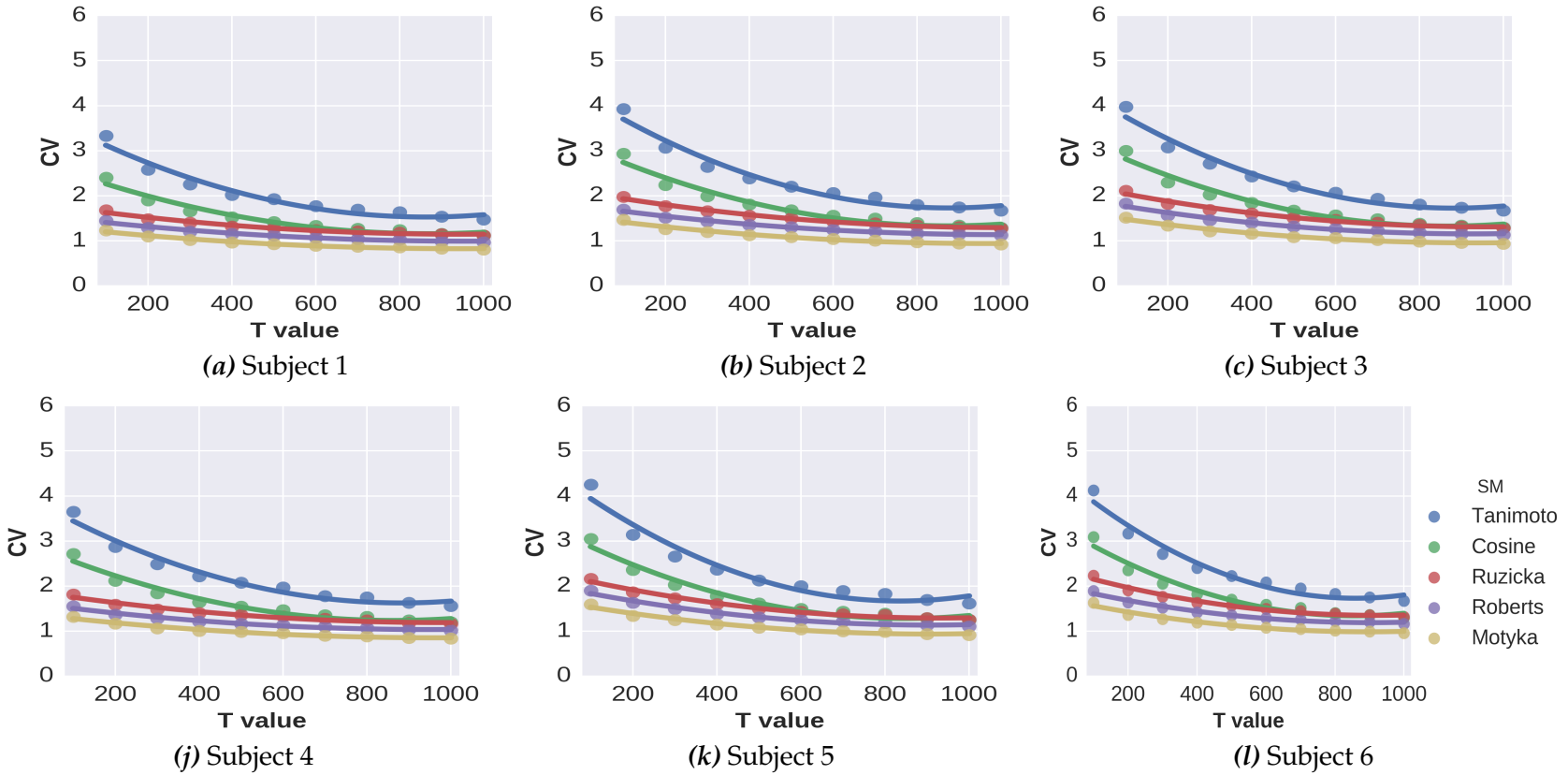

(a) Subject 1 *(b)* Subject 2 *(c)* Subject 3

(j) Subject 4 *(k)* Subject 5 *(l)* Subject 6

Figure 4.11: ***The coefficient of variation (CV) of the resulting parcellations for different T values and subjects. The remaining subjects show similar results.***

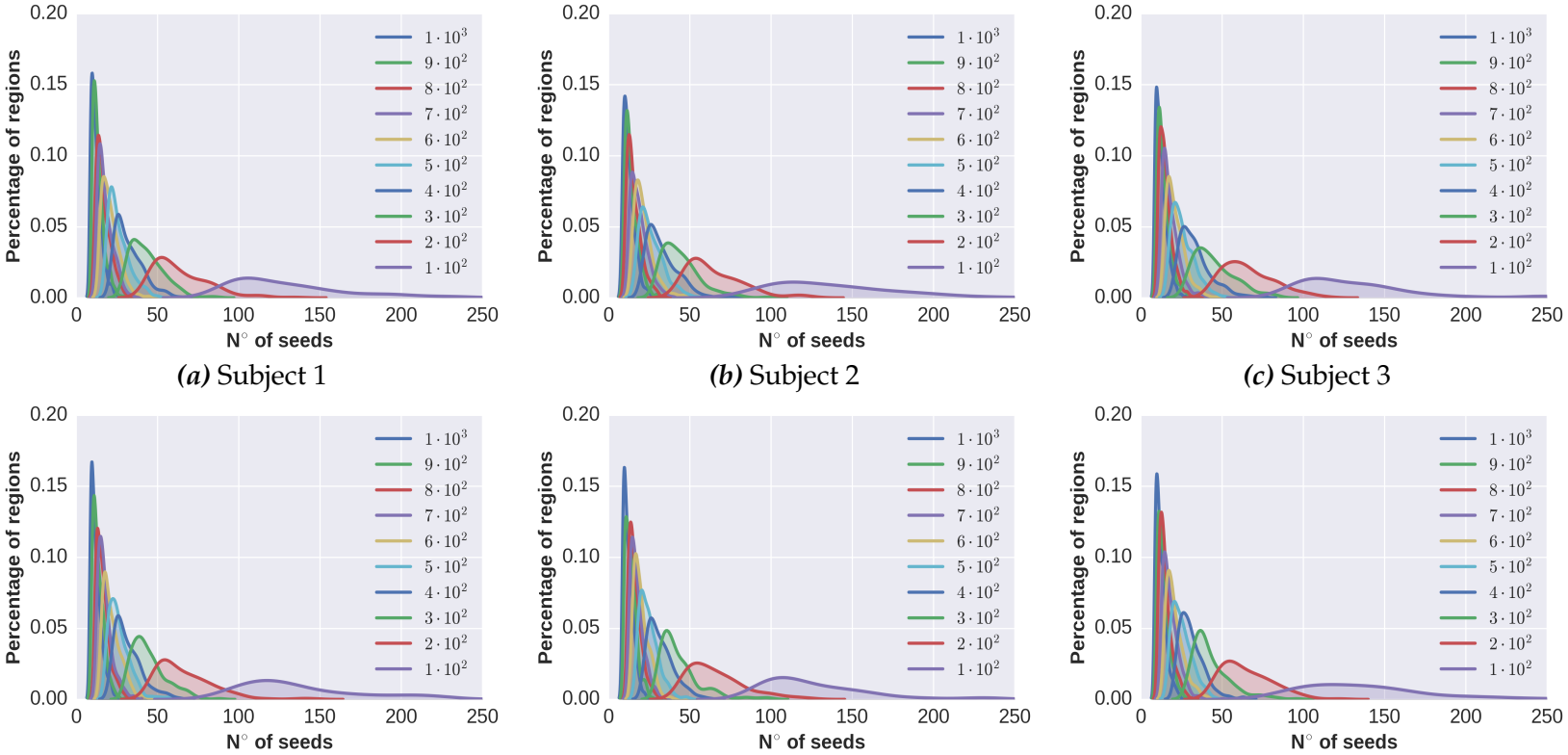

(a) Subject 1 *(b)* Subject 2 *(c)* Subject 3

(d) Subject 4 *(e)* Subject 5 *(f)* Subject 6

Figure 4.12: ***The fitted distribution of the number of seeds per region for different T values and subjects. These patches are obtained using Cosine measure. The remaining subjects show similar results.***

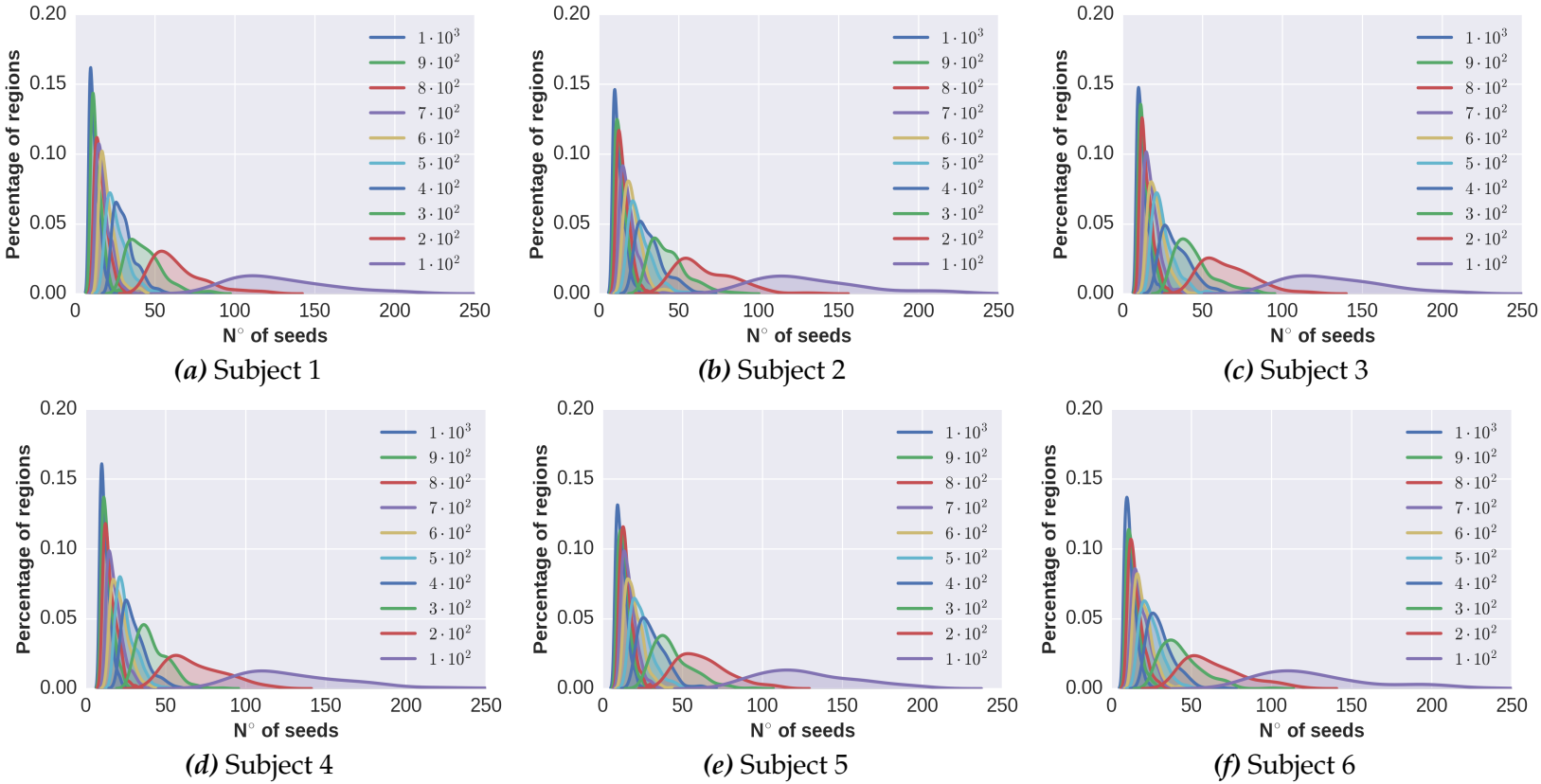

(a) Subject 1 *(b)* Subject 2 *(c)* Subject 3

(d) Subject 4 *(e)* Subject 5 *(f)* Subject 6

Figure 4.13: ***The fitted distribution of the number of seeds per region for different T values and subjects. These patches are obtained using Tanimoto measure. The remaining subjects show similar results.***

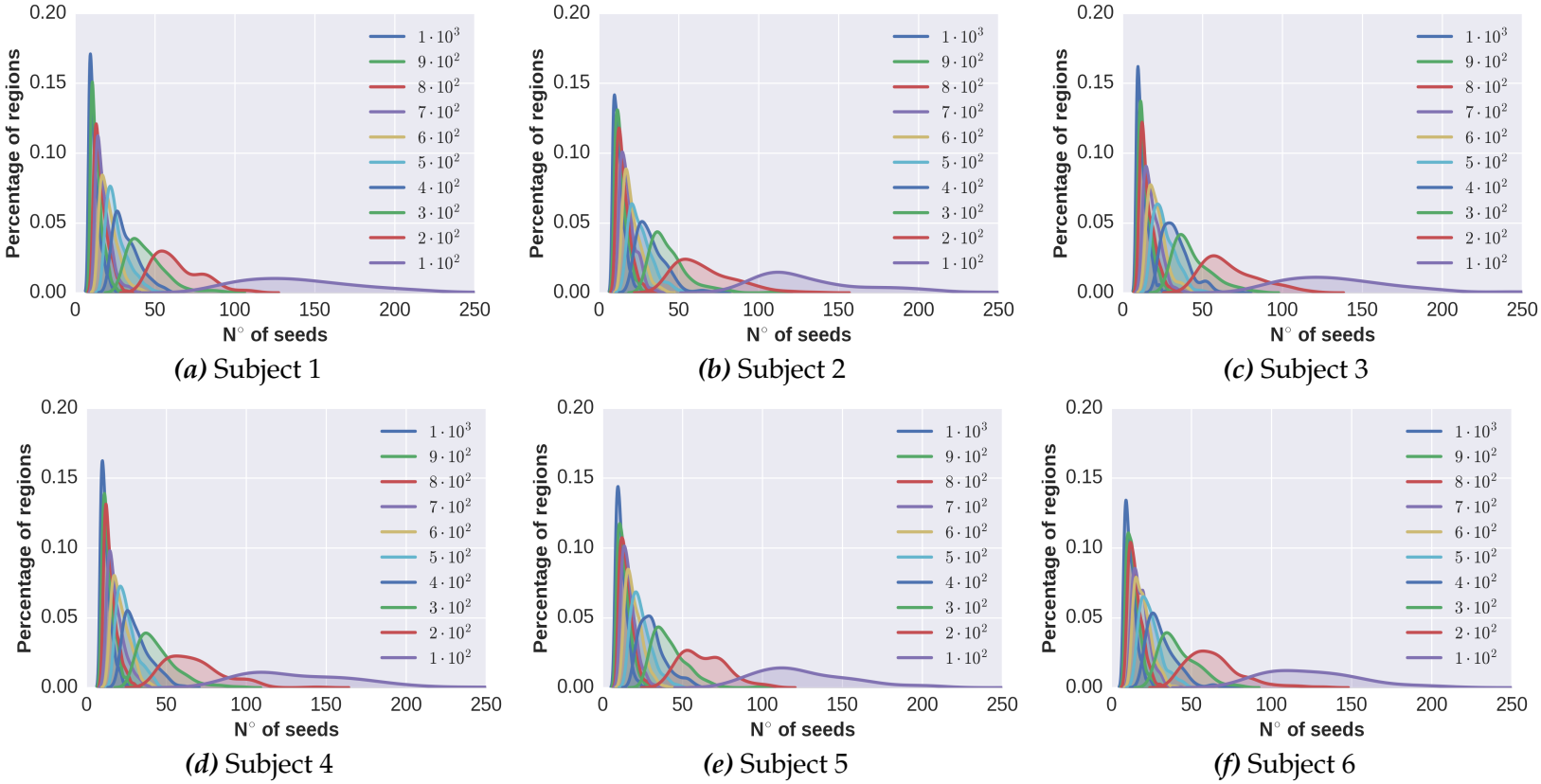

(a) Subject 1 *(b)* Subject 2 *(c)* Subject 3

(d) Subject 4 *(e)* Subject 5 *(f)* Subject 6

Figure 4.14: ***The fitted distribution of the number of seeds per region for different T values and subjects. These patches are obtained using Ruzicka measure. The remaining subjects show similar results.***

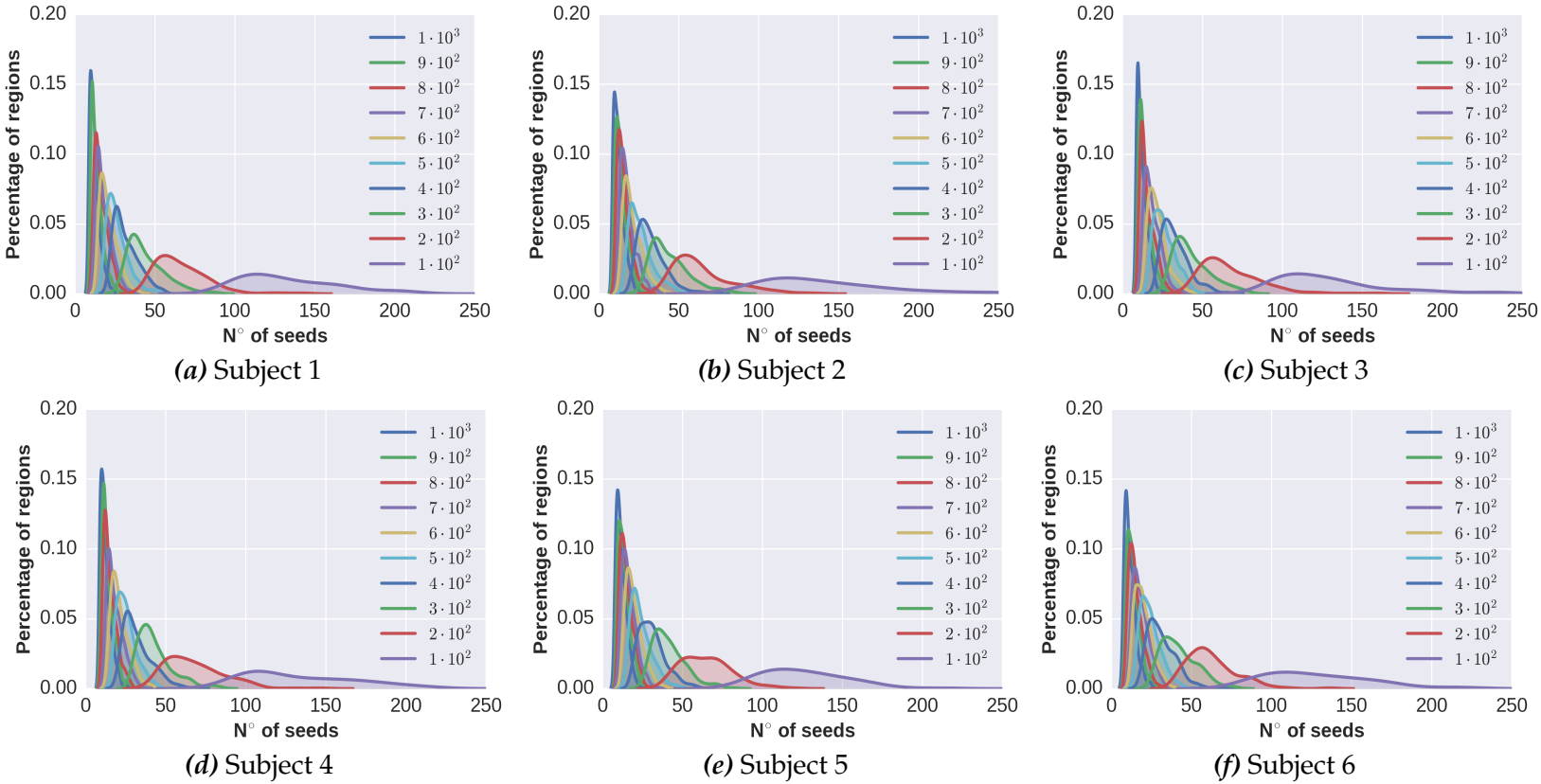

(a) Subject 1 *(b)* Subject 2 *(c)* Subject 3

(d) Subject 4 *(e)* Subject 5 *(f)* Subject 6

Figure 4.15: ***The fitted distribution of the number of seeds per region for different T values and subjects. These patches are obtained using Motyka measure. The remaining subjects show similar results.***

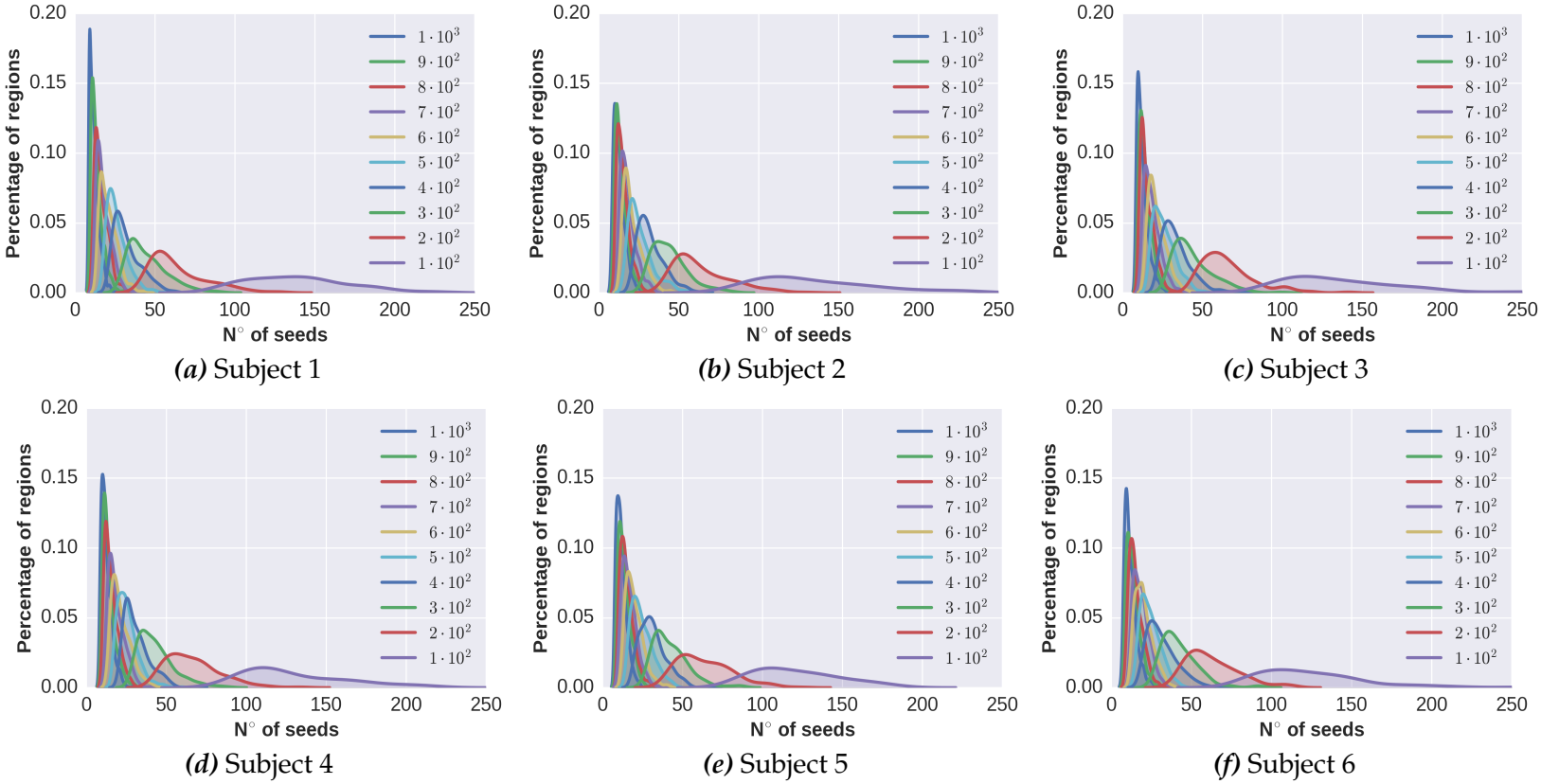

(a) Subject 1 *(b)* Subject 2 *(c)* Subject 3

(d) Subject 4 *(e)* Subject 5 *(f)* Subject 6

Figure 4.16: ***The fitted distribution of the number of seeds per region for different T values and subjects. These patches are obtained using Roberts measure. The remaining subjects show similar results.***

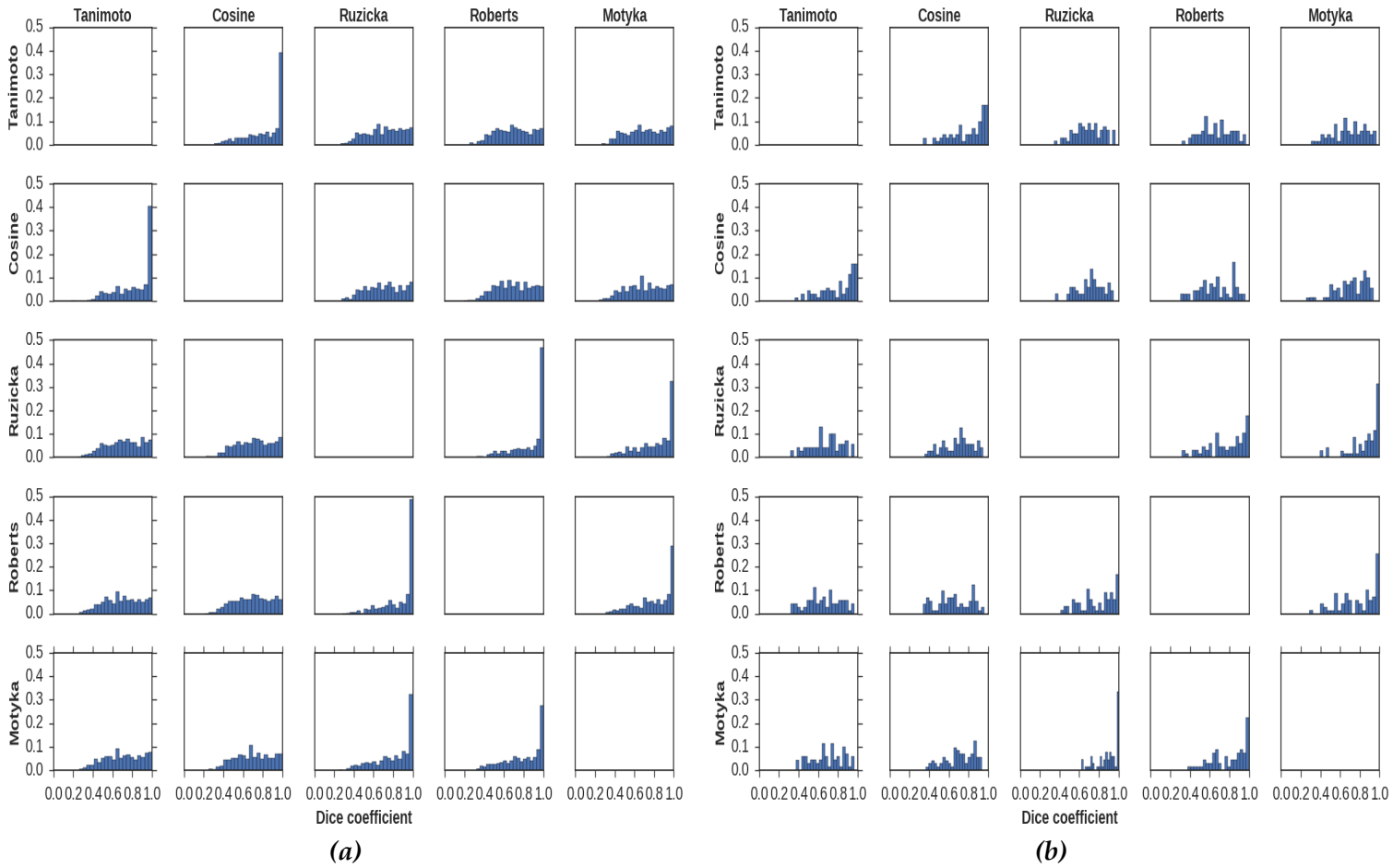

Figure 4.17: ***The distribution of the dice coefficient of Subject 1 parcellation with different SM and (a)*** $T = 1000$ ***(b)*** $T = 100$***. Each panel represents the distribution of dice coefficient computed between two MNN parcellations using two different similarity measure. The remaining subjects show similar results.***

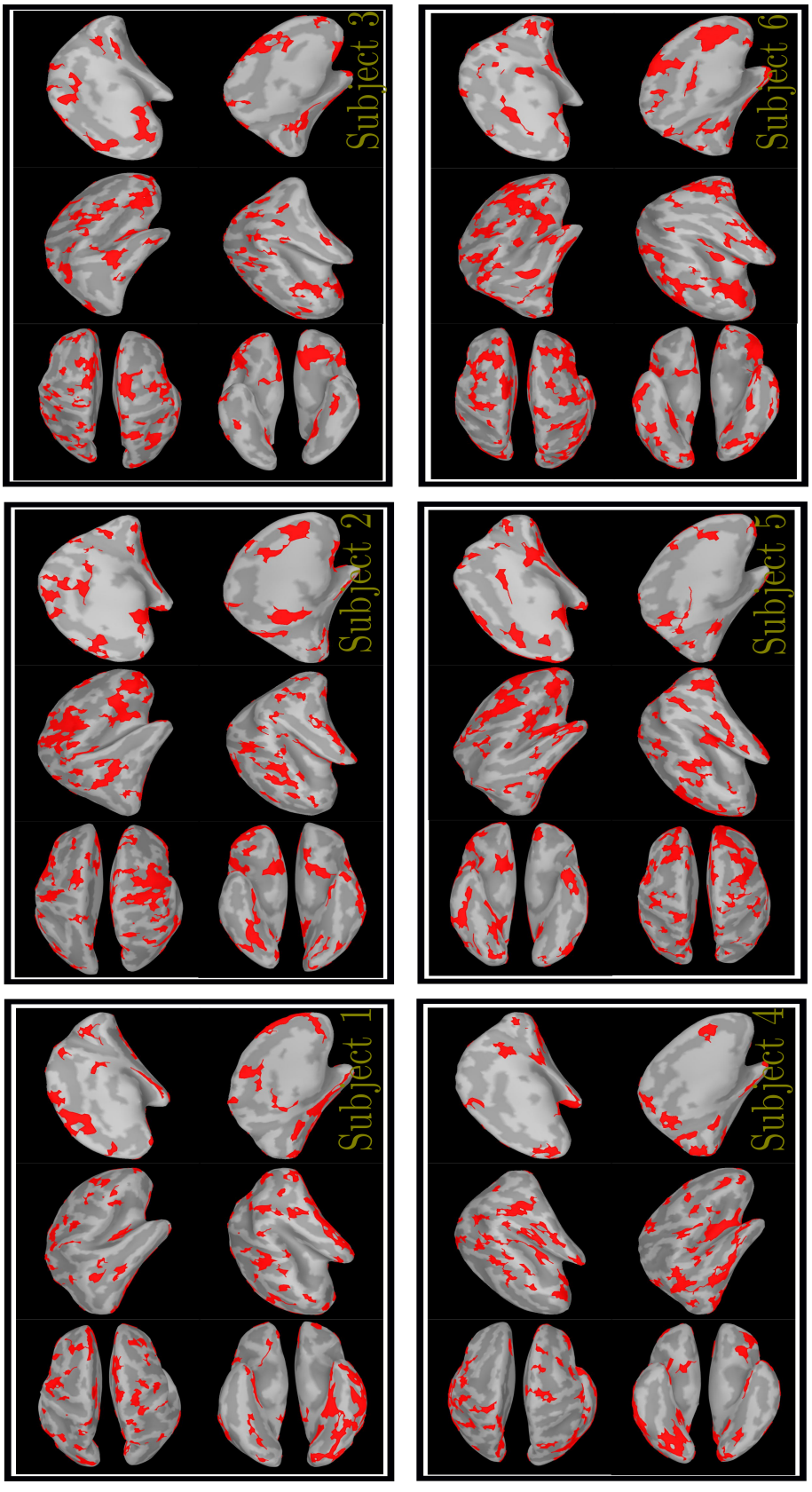

Figure 4.18: The intersections of cortical areas with more than 70% spatial overlapping over the five similarity measures (Tanimoto, Cosine, Ruzicka, Motyka and Roberts with $T = 600$) of six different subjects.

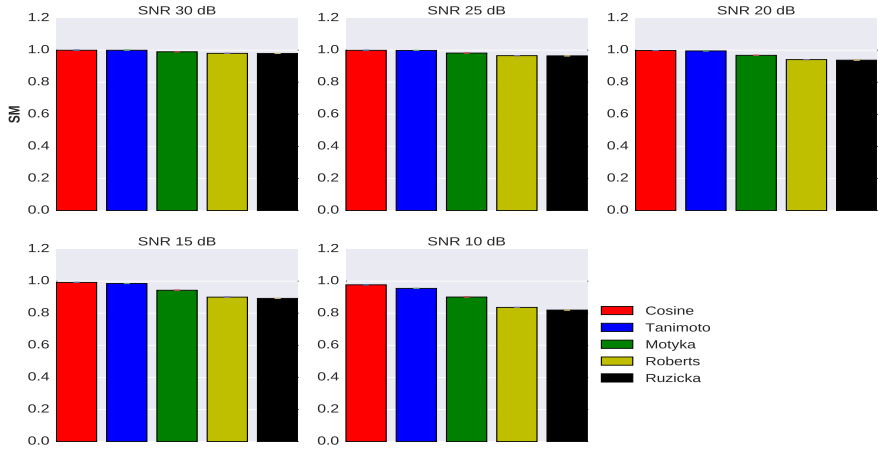

Figure 4.19: ***The mean and std of the similarity measures values from the simulated tractograms at five noise levels.***

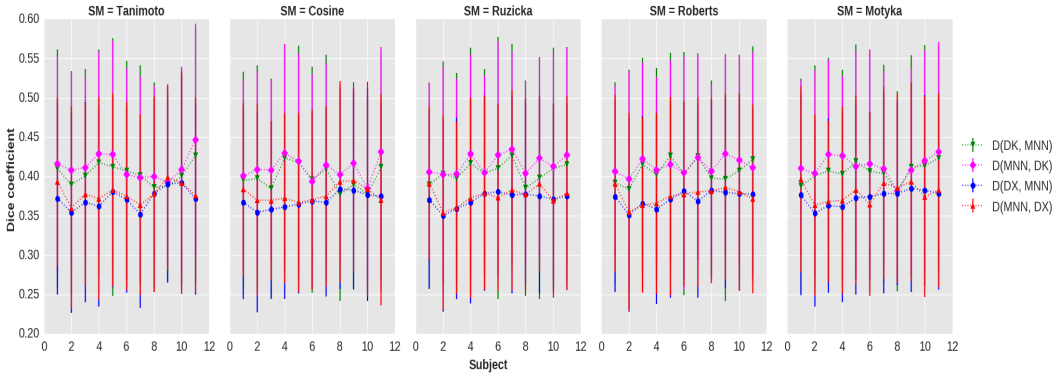

Figure 4.20: ***Mean and std of the dice coefficient between the MNN parcellation and atlases for the different subjects and for different similarity measures (SM).***

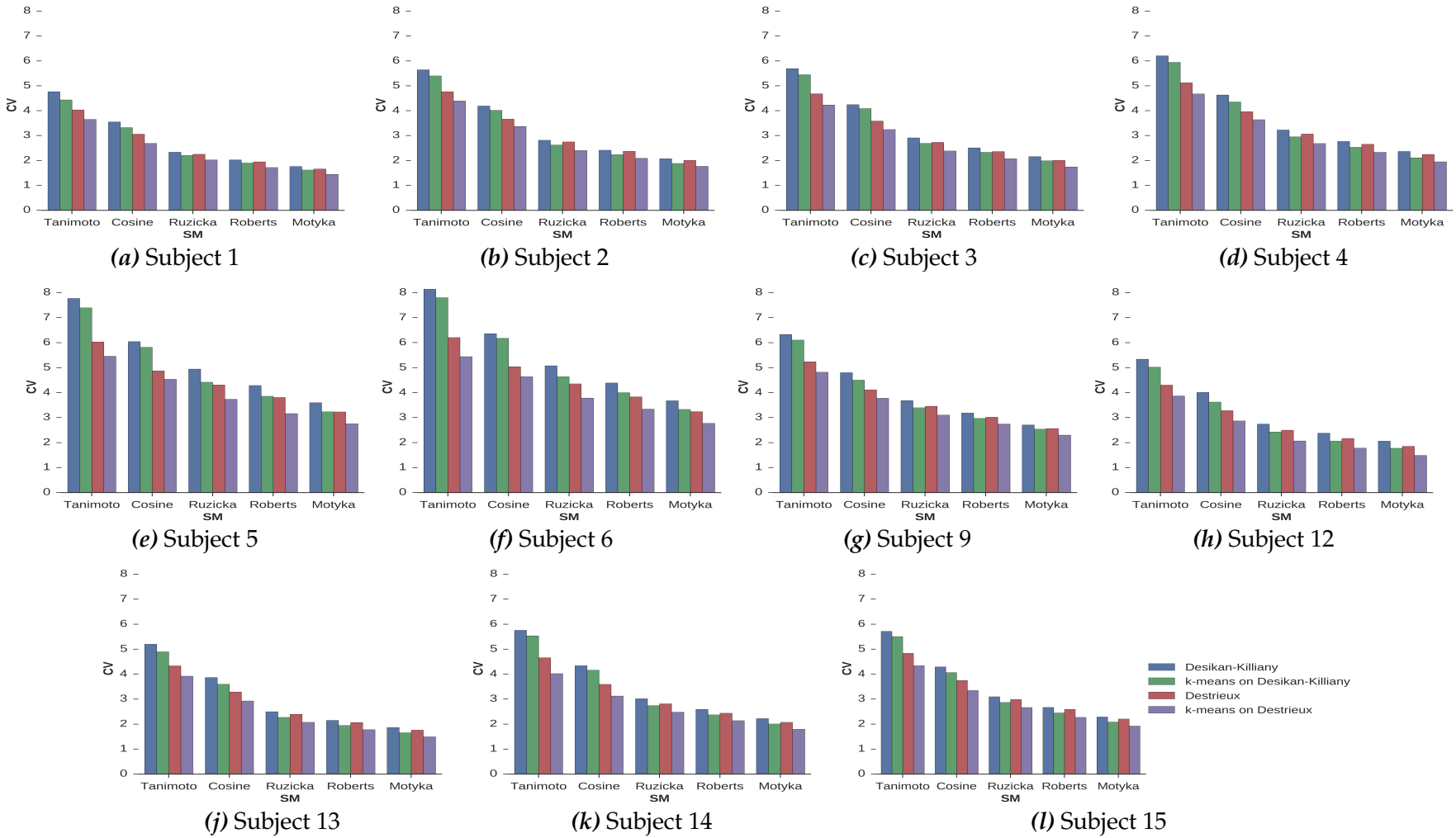

Figure 4.21: ***The coefficient of variation (CV) for different subjects before and after applying k-means on the atlases regions (Destrieux (DX) and Desikan-Killiany (DK)). These patches are obtained using different similarity measures.***

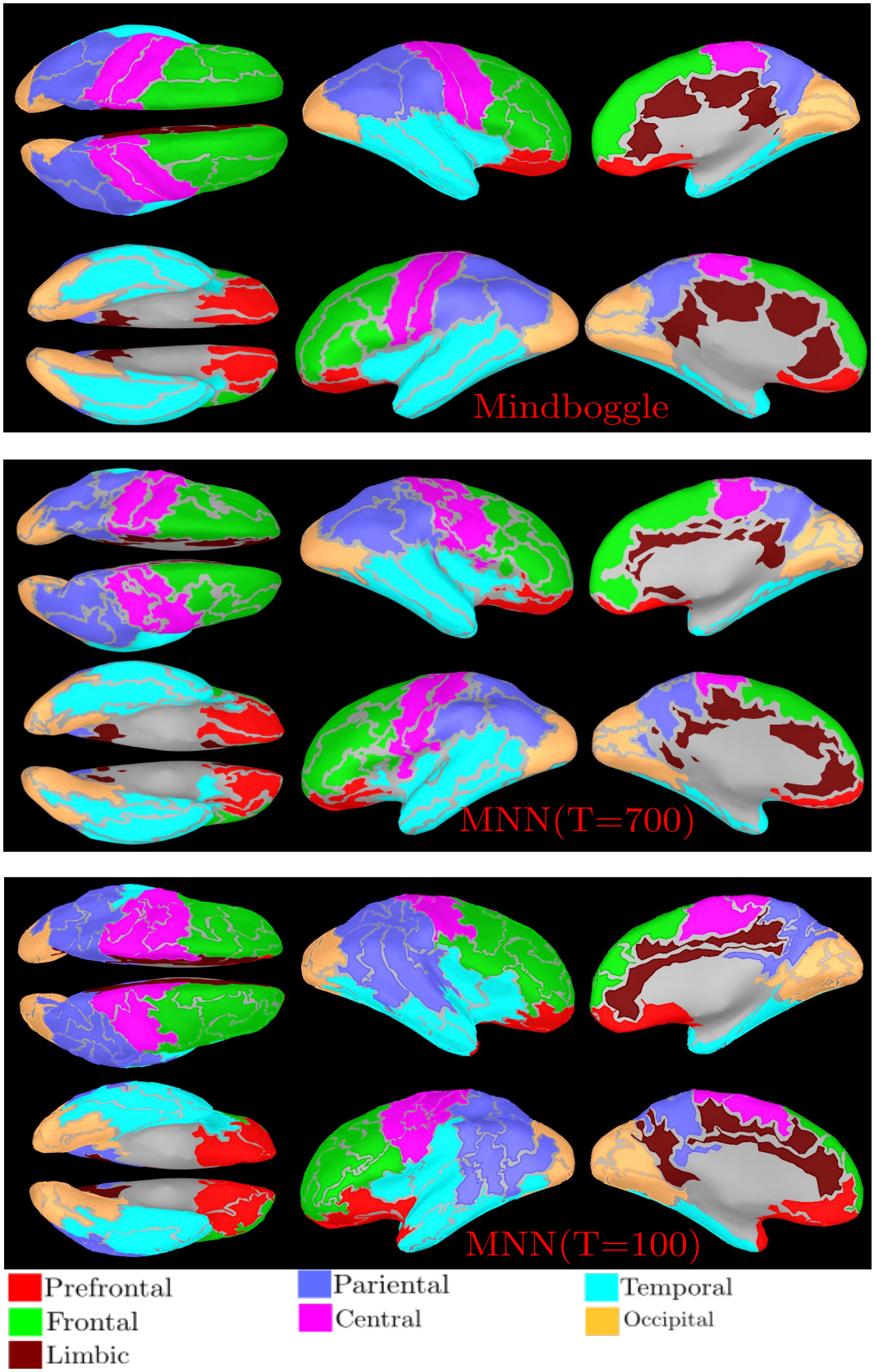

Figure 4.22: ***Top panel: different views of Mindboggle atlas showed on an inflated surface. Middle panel: MNN parcellation with Tanimoto and $T = 700$ of Subject 1. Bottom panel: MNN parcellation with Tanimoto and $T = 100$ of Subject 1. MNN regions are labeled by mindboggle regions which correspond to the highest spatial overlapping computed by dice coefficient. We noticed that lobes boundaries are different between MNN parcellations and the atlas. Gray spaces are spaces between atlases' sub-regions.***

		T values								
		100	**200**	**300**	**400**	**500**	**600**	**700**	**800**	**900**
Subjects	1	13.59±4.76	5.72±2.05	3.52±1.22	2.2851±0.90	1.80±0.75	1.24±0.58	1.03±0.48	0.90±0.42	0.66±0.36
	2	14.53±4.34	6.45±2.22	3.81±1.42	2.66±1.09	1.96±0.91	1.51±0.72	1.24±0.64	0.93±0.46	0.79±0.43
	3	14.32±3.87	6.22±1.89	3.87±1.51	2.66±1.07	1.86±0.79	1.46±0.65	1.13±0.53	0.87±0.45	0.75±0.38
	4	14.76±4.76	6.82±2.25	3.72±1.21	2.42±0.93	1.85±0.73	1.51±0.68	1.21±0.58	0.94±0.48	0.78±0.41
	5	13.05±3.51	5.75±1.88	3.61±1.39	2.31±0.91	1.70±0.76	1.24±0.56	0.98±0.48	0.84±0.41	0.71±0.37
	6	14.73±4.90	6.51±2.45	4.00±1.58	2.56±1.02	1.92±0.83	1.41±0.67	1.27±0.60	0.94±0.52	0.79±0.43
	9	14.05±4.23	6.21±1.97	3.87±1.38	2.52±1.01	1.85±0.73	1.44±0.65	1.16±0.58	0.89±0.44	0.77±0.42
	12	14.12±4.52	5.87±1.80	3.49±1.26	2.2684±0.84	1.74±0.69	1.24±0.50	1.01±0.46	0.90±0.41	0.64±0.33
	13	13.44±3.80	6.09±2.07	3.70±1.26	2.36±0.90	1.85±0.79	1.48±0.65	1.01±0.47	0.93±0.45	0.68±0.37
	14	14.13±5.01	6.06±1.87	3.56±1.25	2.40±0.86	1.65±0.62	1.29±0.54	1.05±0.47	0.91±0.43	0.69±0.36
	15	13.38±4.13	5.73±1.84	3.34±1.22	2.18±0.79	1.65±0.62	1.28±0.56	1.01±0.46	0.79±0.39	0.67±0.35

TABLE 4.4: Mean ± standard deviation (in cm^2) of MNN parcellation regions area using Tanimoto similarity measure and different T values.

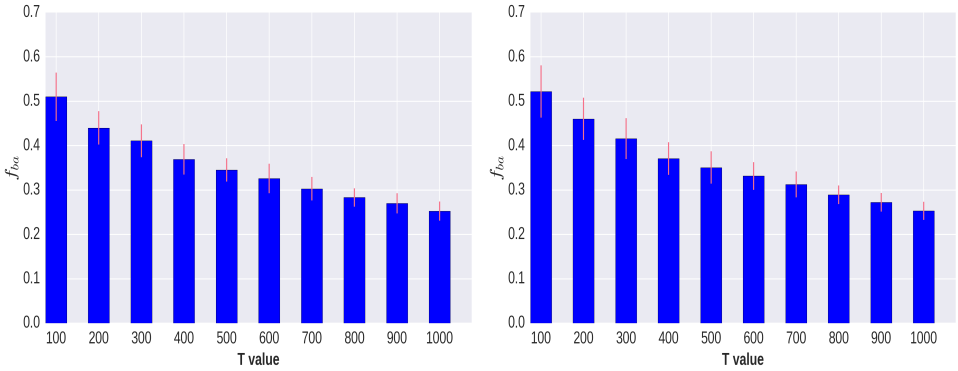

(a) Cosine

(a) Tanimoto

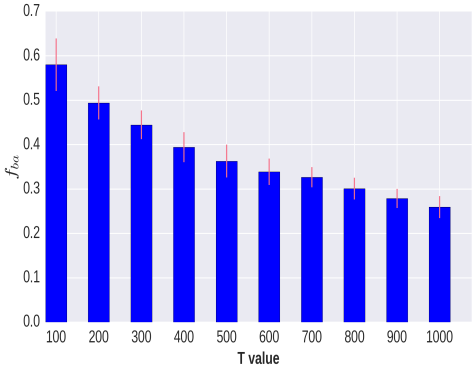

(a) Roberts

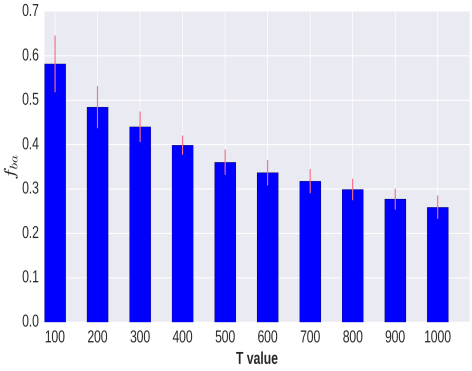

(a) Ruzicka

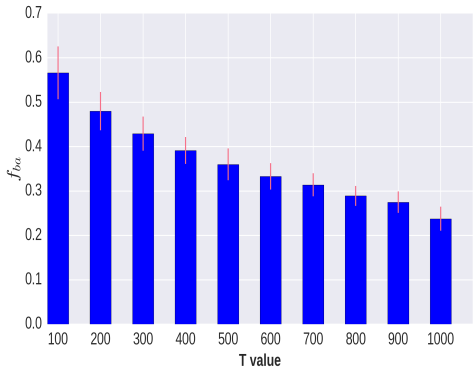

(a) Motyka

Figure 4.23: ***The mean and standard deviation (over subjects) of the fraction*** $f_{ba} = \frac{N_b - N_a}{N_b}$ ***for different T values and similarity measures.***

Related work

Brahim Belaoucha, Maureen Clerc, Théodore Papadopoulo. Cortical surface parcellation via dMRI using mutual nearest neighbor condition. *ISBI - 13th IEEE International Symposium on Biomedical Imaging*, April 2016, Prague, Czech Republic.

Brahim Belaoucha, Jean-Marc Lina, Maureen Clerc, Théodore Papadopoulo. MEM-diffusion MRI framework to solve MEEG inverse

problem. *European Signal Processing Conference (EUSIPCO 2015)*, 2015, Nice, France.

Brahim Belaoucha, Anne-Charlotte Philippe, Maureen Clerc, Théodore Papadopoulo. Diffusion Magnetic Resonance information as a regularization term for MEG/EEG inverse problem, *Biomag - 19th International Conference On Biomagnetism*, 2014, Halifax, Canada.

4.7 Conclusion

Few studies parcellated the whole cortical surface into regions due to computational cost, in our case dMRI. To overcome this problem, atlases can be used as pre-parcellations. This can reduce the computation time, but rises the problem of the accuracy of these atlases in terms of the dividing line between atlases' regions. We proposed to use an agglomerative approach to subdividing the cortex into regions with the highest structural homogeneity, defined by the connectivity profiles, according to a similarity measure.

The MNN parcellation algorithm is based on the mutual nearest neighbor condition. This algorithm depends only on one parameter, T, which controls the resulting number of regions, N_r. We have shown that there is a linear relationship between N_r and T. This can help to choose the parameter T so that you obtain a specific number of regions.

The algorithm was tested with different subjects and several similarity measures that can be found in the literature. Also, it was compared to three atlases: Destrieux, Desikan-Killiany and Mindboggle. The algorithm gives regions with more homogeneity than the atlases' regions even after subdividing the atlases' regions. *Tanimoto* and *Cosine* are the only SMs that present the bigger difference between the dispersion values of SM_p between low and high T values. Pure MNN can give singleton regions, that is why a post-processing step was added to the MNN algorithm. The fraction of regions corrected by this post-processing (regions with size less than s) was found to be inversely proportional to T. This is true for all the similarity measures. The number of corrected regions was found to be lower when using *Tanimoto* and *Cosine*.

For these reasons, we decided to use *Tanimoto* coefficient. A big increase of CV was observed when $T \leq 600$, that is why we suggest using MNN parcellations with $T > 600$. It is worth mentioning that there are some areas located in the four brain lobes (temporal, occipital, frontal and parietal) that are less sensitive to the choice of the similarity measure. This was observed with different subjects. Another study with more subjects and different similarity measure should be conducted to define regions that are less affected by the choice of the similarity measure.

In our work, we compared five different similarity measures. Other methods can be used in the MNN parcellation algorithm e.g. mutual information. Group studies must be conducted to investigate the possibility of structural based atlas using the MNN parcellation algorithm. Functional data (e.g. fMRI) can be used to validate some/all regions obtained by MNN

parcellation. Also, it could be used to tune the MNN's parameter T in order to to obtain regions close to functional parcellation.

Chapter 5

dMRI in the EEG/MEG inverse Problem

Contents

5.1 Introduction 94
5.2 State of the art 94
5.3 Pure spatial regularization (sWMNE) 96
5.3.1 Results 99
5.4 Spatiotemporal regularization 108
5.4.1 Pruning the MAR model 117
5.4.2 Magnitude bias 120
5.4.3 Results 121
5.5 Discussion 155
5.6 Conclusion 156

5.1 Introduction

Problems that are underdetermined need to be regularized to obtain a unique solution. This is also true for EEG/MEG inverse problem. Few methods used dMR information to regularize the inverse problem, probably due to the different nature of the diffusion signal compared to EEG/MEG. On the other hand, several works relate the structural organization of white matter to functional homogeneity of cortical regions. For example, it has been used to predict functional connectivity from functional MRI (Finger et al., 2016; Osher et al., 2016). This makes the use of dMRI in the EEG/MEG regularization justified. In this chapter, we first introduce some works on how the diffusion MRI information was used to solve the EEG/MEG problem. We then present our work to reconstruct both the brain activity and interactions between brain regions/sources.

5.2 State of the art

There are few works that use the diffusion MRI with the EEG/MEG measurements to reconstruct the brain activity. dMRI was used as a pure spatial prior in the MEG/EEG inverse problem. In (Hammond et al., 2012; Hammond et al., 2013), the authors used the dMRI to parcellate the cortical patches and to retrieve the anatomical connections between brain regions. They assume that connected regions have similar activity. In (Philippe, 2013), the authors built a weighting matrix whose elements depend on the size of cortical regions (obtained from dMRI) to favor similar activity inside each patch. In (Knosche et al., 2013), the authors used regions defined by dMRI to define LORETA patch-based algorithm i.e. smooth sources inside patches. The structural connectivity between brain regions was used also to reconstruct brain activity by imposing stronger penalty for regions with weak anatomical connections (Pineda-Pardo et al., 2014).

dMRI was also used in spatiotemporal framework (Fukushima et al., 2012; Fukushima et al., 2013; Fukushima et al., 2015). In addition to parcellating the cortical surface, they used dMRI to constrain temporally the sources dynamics by assuming a multivariate autoregressive model (MAR) whose elements are constrained by anatomical connections obtained from dMRI. To the best of our knowledge, dMRI was not used to set pure temporal prior.

As explained in section 1.3, sources that have similar connectivity profiles have similar function. Because dMRI is a non-invasive modality which allows us to access the anatomical connectivity of the white matter, we decided to use it to define these functional regions. The first step is to subdivide the cortical into regions with homogeneous structural connectivity, see Chapter 4.1. Then with these regions, we reconstruct the brain activity using two solvers.

In (Philippe, 2013) (more details about the method can be found in section 5.3), the authors followed the same steps but their algorithm suffers from the following:

- The parcellation is based on atlases. This raises the question of the regions' boundaries accuracy because public atlases are based on the surface curvature and not the structural organization of the white matter. The drawback of using atlases is discussed in more details in section 4.3.

- It is a linear algorithm which fails to detect focal sources. No temporal information was included in the cost function.

Several studies were conducted to include spatiotemporal/temporal regularization term in the EEG/MEG inverse problem based on the multivariate autoregressive models (MAR) (Galka et al., 2004; Long et al., 2006; Giraldo et al., 2010; Lamus et al., 2012). In the first, the authors modeled the brain activity at each source location i by the following:

$$J_t(i) = a_i J_{t-1}(i) + b_i \sum_{j \neq i} J_{t-1}(j) + \varepsilon_t$$

where ε_i is noise at the source location i and the sum is over the direct neighbors of i. In their method, there is only two parameters per source (a_i, b_i) to be estimated which reduce the dynamics that can be explained by their model. The degree of freedom of this model was reduced in (Long et al., 2006), in which they set $a_i = 1$ and $b_i = \frac{1}{n_i}$ (n_i number of neighbors of i). In (Lamus et al., 2012), also two parameters need to be estimated but the activity of neighboring sources are weighted by their distances to source i.

A nonlinear model is considered in (Giraldo et al., 2010). They modeled the brain activity as follows:

$$J_t = (a_1 + b_1 L) J_{t-1} + a_2 J_{t-1}^2 + a_3 J_{t-1}^3 + a_4 J_{t-2} + \varepsilon_t$$

where L is a Laplacian operator applied to neighboring sources. Although this nonlinear model could explain more complex dynamics compared to the previous mentioned work, it uses only 5 parameters to explain source dynamics. Only few works used dMRI to constrain sources' dynamics using MAR (Fukushima et al., 2015).

In (Fukushima et al., 2013; Fukushima et al., 2015), the authors constrained the dynamics of sources by a multivariate autoregressive model (MAR) and used a dynamic hierarchical variational Bayesian (dhVB) method to estimate both the sources magnitudes and their interactions. The only possible nonzero elements of the MAR matrix are the elements corresponding to anatomical connections between pair of sources/regions. The time-lag, in their method, for each pair of sources/regions is fixed by the length of the pathways between them. This method reduces the degree of freedom of the MAR model by assuming that nonzero MAR coefficients never overlap (Fukushima et al., 2015) which restricts the source signals

that can be explained by the MAR model. Their method is time-consuming (days for realistic head models).

In this chapter, we propose two source reconstruction methods based on dMRI information:

- The first one uses a spatial regularization which can be used to detect extended activation.
- The second method uses a spatiotemporal regularization, a variant of MxNE, which can be used to reconstruct focal activation and effective connectivity between cortical sources/regions.

Both of these methods use the resulting parcellation of the whole cortical surface using the MNN parcellation algorithm explained in Chapter 4.3.3.

5.3 Pure spatial regularization (sWMNE)

As explained earlier in section 2.3.3.1, linear reconstruction methods can be written, by replacing the penalty term $P(J)$ by two terms, as:

$$U(J) = \|M - GJ\|_2^2 + \lambda \|WJ\|_2^2 + \mu \|J\|_2^2 \tag{5.1}$$

where λ and μ are two positive regularization parameters, G is the lead field matrix, M and J are, respectively, the EEG/MEG measurement and sources' magnitudes. They, both, control the regularization of the source estimate. If μ is very small compared to λ, sources signals tend toward the solution favored by the source configuration in the weighting matrix W. In the inverse situation, the sources tend to have small norm i.e. minimum norm estimate.

Different methods correspond to different definition of the weighting matrix W. Generally, the connectivity profile is used in the construction of cortical regions with homogeneous connectivity profiles. But possible structural inhomogeneity inside regions are neglected in the EEG/MEG inverse problem. In (Philippe et al., 2013; Philippe, 2013), the authors defined the elements of W as:

$$J_i \in R_p \rightarrow W_{CP}(i,j) = \begin{cases} 1 - \frac{1}{|R_p|} & \text{if } i = j \\ -\frac{1}{|R_p|} & \text{if } S_j \in R_p \\ 0 & \text{if} S_j \notin R_p \end{cases} \tag{5.2}$$

where R_p is the p^{th} region. The l_2-norm $\|WJ\|_2^2$ is minimum if J belongs to the nullspace of W:

$$J_i = J_j \quad \forall i,j \in R_p, p = 1...P,$$

where P is the total number of regions. The optimization of the functional $U(J) = \|W_{cp}J\|_2^2$ leads to the solution that we call CP. This estimate assumes that all sources inside a region have the same contribution. When minimizing only the prior, excluding $\|J\|_2^2$, this results to equal sources in

each region. The weights in the method depend only on the size of the regions. They neglected the variation of the connectivity profiles (see section 4.3.2) inside the cortical regions. In (Tian et al., 2013), authors regularized the EEG/MEG inverse problem with a Laplacian matrix whose elements depend on the euclidean distances between sources. Close sources, in the euclidean sense, will have close magnitudes.

In this part, we assume that changes of sources inside the cortical regions are due to the their structural inhomogeneity. To incorporate the structural information, we built a weighting matrix based on the homogeneity of the similarity values of the connectivity profiles of sources. We denote by $d_{i,j}$ the similarity measure value (see section 4.4 for more details) between the connectivity profile of source i and j which belong to the same region R_p. d_i is the sum of similarity values between source i and the remaining sources in the region or:

$$d_i = \sum_{j=1}^{|R_p|} d_{i,j} \tag{5.3}$$

The elements of our weighting matrix are defined as:

$$J_i \in R_p \rightarrow W_s(i,j) = \begin{cases} 1 - \frac{1}{d_i} & \text{if } i = j \\ -\frac{d_{i,j}}{\sqrt{d_i d_j}} & \text{if } S_j \in R_p \\ 0 & \text{if} S_j \notin R_p \end{cases} \tag{5.4}$$

It is worth mentioning that the symmetrical similarity measure value $d_{i,j}$ is between 0 (dissimilar connectivity profiles) and 1 (if the connectivity profile of i and j are the same). We denote by $sWMNE$ (structural weighted minimum norm estimate) the source estimate obtained by minimizing Equation 5.1 using the weighing matrix W_s. If in all regions, the connectivity profiles of the sources are equal ($d_{i,j} = 1 \; \forall i, \forall j$), sWMNE is equivalent to CP solver i.e. $W_s = W_{cp}$.

To have an idea about the effect of this new weighting matrix, let's assume that we have five sources. $P = [1, 1, 1, 2, 2]$ is a vector containing the region label of each source. Three sources are in the first region and the remaining ones are in the second region. The weighing matrix, W_s, for this particular case is:

$$W_s = \begin{pmatrix} 1 - \frac{1}{d_1} & \frac{-d_{1,2}}{\sqrt{d_1 d_2}} & \frac{-d_{1,3}}{\sqrt{d_1 d_3}} & 0 & 0 \\ \frac{-d_{1,2}}{\sqrt{d_1 d_2}} & 1 - \frac{1}{d_2} & \frac{-d_{2,3}}{\sqrt{d_2 d_3}} & 0 & 0 \\ \frac{-d_{1,3}}{\sqrt{d_1 d_3}} & \frac{-d_{2,3}}{\sqrt{d_2 d_3}} & 1 - \frac{1}{d_3} & 0 & 0 \\ 0 & 0 & 0 & 1 - \frac{1}{d_4} & \frac{-d_{4,5}}{\sqrt{d_4 d_5}} \\ 0 & 0 & 0 & \frac{-d_{4,5}}{\sqrt{d_4 d_5}} & 1 - \frac{1}{d_5} \end{pmatrix} \tag{5.5}$$

this results in:

$$W_s J = \begin{pmatrix} (1-\frac{1}{d_1})J_1 - \frac{d_{1,2}}{\sqrt{d_1 d_2}}J_2 - \frac{d_{1,3}}{\sqrt{d_1 d_3}}J_3 \\ -\frac{d_{1,2}}{\sqrt{d_1 d_2}}J_1 + (1-\frac{1}{d_2})J_2 - \frac{d_{2,3}}{\sqrt{d_2 d_3}}J_3 \\ -\frac{d_{1,3}}{\sqrt{d_1 d_3}}J_1 - \frac{d_{2,3}}{\sqrt{d_2 d_3}}J_2 + (1-\frac{1}{d_3})J_3 \\ (1-\frac{1}{d_4})J_4 - \frac{d_{4,5}}{\sqrt{d_4 d_5}}J_5 \\ -\frac{d_{4,5}}{\sqrt{d_4 d_5}}J_4 + (1-\frac{1}{d_5})J_5 \end{pmatrix} \tag{5.6}$$

the norm $\|W_s J\|_2$ is minimum when J belongs to the nullspace of W_s:

$$\begin{cases} (1-\frac{1}{d_1})J_1 - \frac{d_{1,2}}{\sqrt{d_1 d_2}}J_2 - \frac{d_{1,3}}{\sqrt{d_1 d_3}}J_3 = 0 \\ -\frac{d_{1,2}}{\sqrt{d_1 d_2}}J_1 + (1-\frac{1}{d_2})J_2 - \frac{d_{2,3}}{\sqrt{d_2 d_3}}J_3 = 0 \\ -\frac{d_{1,3}}{\sqrt{d_1 d_3}}J_1 - \frac{d_{2,3}}{\sqrt{d_2 d_3}}J_2 + (1-\frac{1}{d_3})J_3 = 0 \\ (1-\frac{1}{d_4})J_4 - \frac{d_{4,5}}{\sqrt{d_4 d_5}}J_5 = 0 \\ -\frac{d_{4,5}}{\sqrt{d_4 d_5}}J_4 + (1-\frac{1}{d_5})J_5 = 0 \end{cases} \tag{5.7}$$

this set of equations has the following solution:

$$\begin{cases} J_1 = \sqrt{d_1}J_{R1} \\ J_2 = \sqrt{d_2}J_{R1} \\ J_3 = \sqrt{d_3}J_{R1} \end{cases} \quad \begin{cases} J_4 = \sqrt{d_4}J_{R2} \\ J_5 = \sqrt{d_5}J_{R2} \end{cases}, \tag{5.8}$$

where J_{R1} and J_{R2} are the cortical activations of regions R_1 and R_2, respectively. The term $\|W_s J\|_2^2$, when minimized, tends to constrain the source activation by their similarity values which allows us to incorporate the structural inhomogeneity of regions in the EEG/MEG inverse problem. Sources with close connectivity profile have close activation, and vice versa. If J_i and J_j are two sources which belongs to the same region:

$$\sqrt{d_i}J_j \approx \sqrt{d_j}J_i \tag{5.9}$$

The solution of Equation 5.1 is given by the unique solution:

$$J_\lambda = (G^T G + \lambda W_s^T W_s + \mu I)^{-1} G^T M \tag{5.10}$$

The matrix $(G^T G + \lambda W_s^T W_s + \mu I)$ is always invertible for $\mu \neq 0$. It is worth mentioning that μ should not be zero because $W^T W$ is singular and its kernel with the nullspace of $G^T G$ may have a nonzero intersection which makes the matrix inversion computationally unstable. The regularization parameters μ and λ can be fixed by cross-validation (Arlot et al., 2010). In our work, we used 3-fold cross-validation to set λ and μ.

5.3.1 Results

The section is dedicated to the sWMNE algorithm and is divided into two subsections. In the first subsection, we use synthetic simulation to test the accuracy and focality of the structural weighted minimum norm estimate. In the second subsection, we use EEG/MEG real data acquired when performing face a recognition task. We compare the results to what can be found in the literature about the regions that contribute to the face perception and recognition.

5.3.1.1 Synthetic data

For a reasonably fast and realistic comparison between sWMNE, MNE and CP, we simulated a data set with 20 sensors and a source space containing 500 points distributed equally into 50 regions i.e. 10 points per region. Each region is associated to a connectivity profile r_i^*, of length 10^3, which is drawn from a normal distribution $\mathcal{N}(100,\, 200)$. We give to a source point j, that belongs to R_i, the following connectivity profile vector:

$$r_j = r_i^* + \epsilon_j, \tag{5.11}$$

where the elements of the vector ϵ_j are drawn randomly from a normal distribution $\mathcal{N}(50,\, 100)$, values lower than 100 were set to zero to mimic the results of probabilistic tractography in which the values of the connectivity profiles are positive. The elements of the weighting matrix $d_{i,j}$ (see Equation 5.4) are obtained by computing the *Tanimoto* similarity measure between the sources' connectivity vectors that belong to the same regions. The forward model G, gain matrix, is drawn from a normal distribution $\mathcal{N}(0,\, 1)$. Its columns are normalized to be of norm 1.

We consider two testing configurations of activation:

- One active region.
- Two active regions.

In each case, we simulate 100 data sets (see Figure 5.1 for time courses). The measurements, obtained by applying the forward model G to the simulated sources, are corrupted by an additive Gaussian noise $\mathcal{N}(0,\, \alpha I)$. We considered three noise levels (Signal-to-Noise ratio (SNR) = $15,\, 10\,, 5$ dB). The SNR used in this work is defined here as $\|M_{gt}\|_2^2 / \|M_{noise}\|_2^2$, where M_{gt} and M_{noise} are, respectively, the noiseless and noisy measurements. To test the accuracy of the reconstructions, we compute the source reconstruction error:

$$E_r(J_{gt}, J_r) = \|J_{gt} - J_r\|_2 \tag{5.12}$$

where J_{gt} and J_r are the simulated (ground truth) and reconstructed sources. To test the focality of the solution, we compute the number of sources that have a total activation higher than 25% of the source with the highest activation.

One extended active region

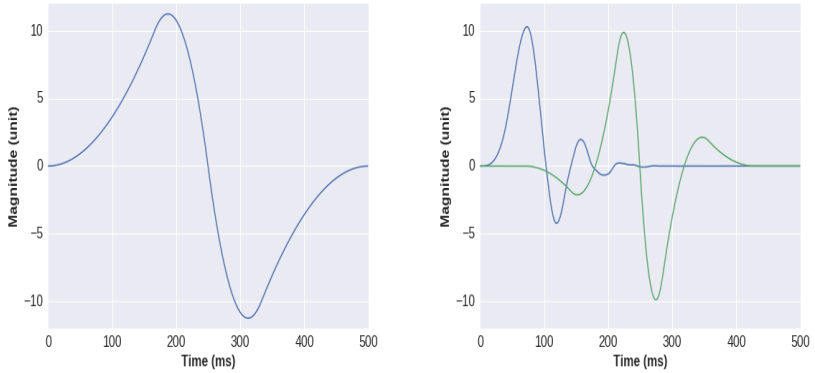

Figure 5.1: ***Ground truth simulation. In (a), activation curve of one region. In (b), we show the two different activation curves used for two distinct regions.***

We activate one random region, R, among the 50 regions, see Figure 5.1 (a). We activate one random source (J_c) in a region (R), and we used it as a reference to set the magnitude of the other sources that are located in the same region using the following equality:

$$J_i = \sqrt{\frac{d_i}{d_c}} J_c \text{ for all } i \in R$$

where d_i (respectively d_c) is the sum of the similarity measure values between the tractogram of source i and the other sources (see Equation 5.3 for more details). We simulate the measurements for these sources and do a reconstruction from the noisy measurement. We compared the sWMNE reconstruction to both MNE and CP source estimates. It is worth mentioning that the simulations follow our assumption that the magnitudes of sources inside cortical regions differ according to structural inhomogeneity.

We do this at the same noise level 100 times and repeat this for 20 different regions. The results are presented in Figure 5.2.

The mean, over 20×100 simulations, of the reconstructed source signals of the activated region, which contains 10 sources, are shown in blue panel (see the left panel) of Figure 5.2. In terms of magnitude bias, CP and sWMNE show a better reconstruction of the magnitude of the true positive sources. This is translated by lower E_τ. MNE smears activations which makes it hard to distinguish true from false activations. This can be seen clearly in the MNE reconstruction panel in Figure 5.2. CP favors the sources to have the same activation per region, whereas sWMNE favors activations to vary according to the structural connectivities of sources in each region. This can be seen in the panels that correspond to CP and sWMNE reconstructions in Figure 5.2.

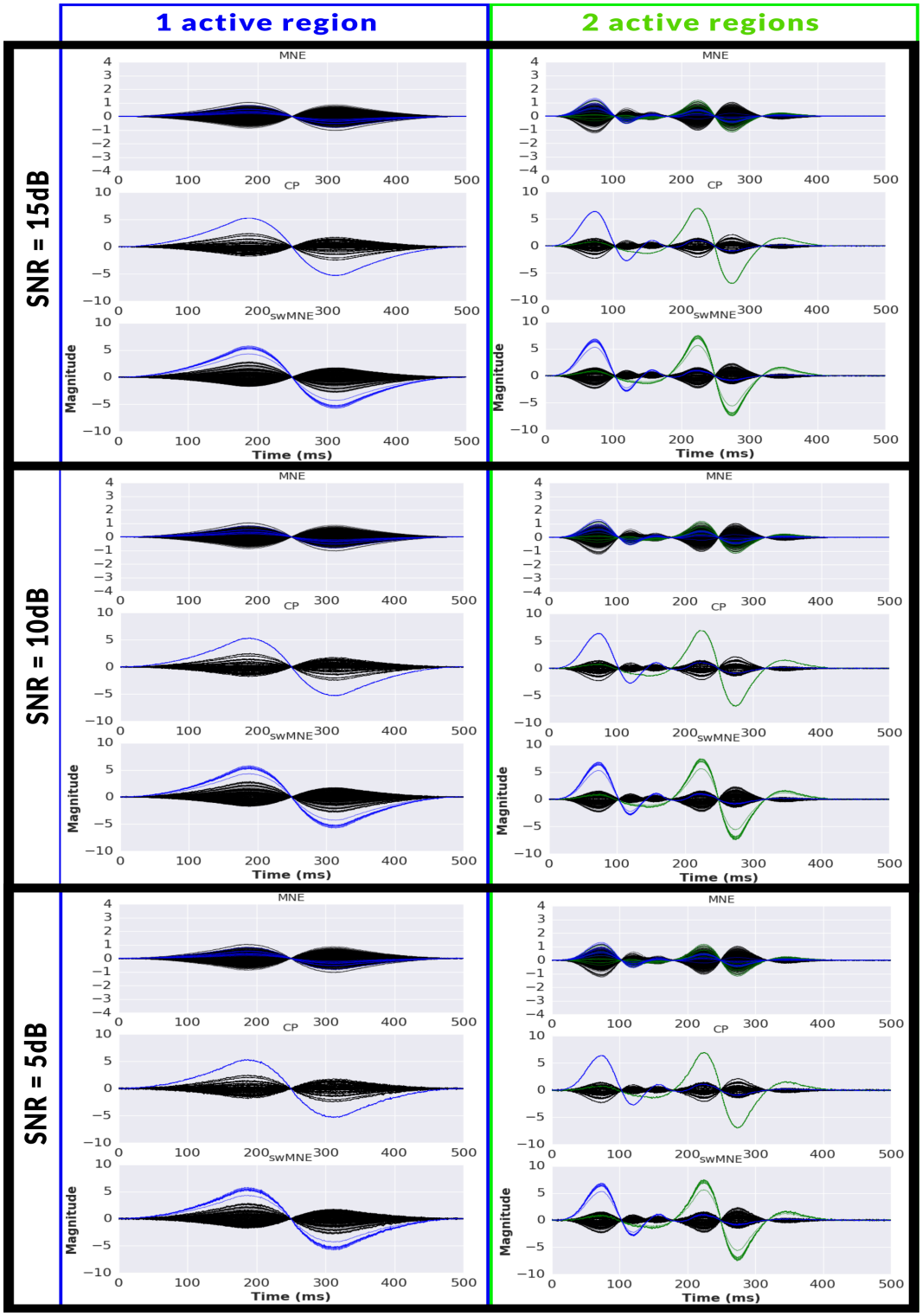

Figure 5.2: ***An example of the mean (over 100 runs) reconstructions by the methods MNE, CP, sWMNE of the two test configurations. The left panel corresponds to the reconstruction of the first test configuration, and the right panel shows the reconstructed two active regions. From top to bottom SNR = 15, 10, 5 dB.***

Two extended active regions

We follow the same steps as explained in the first test configuration, but now we activate two random regions using the signals that are shown in Figure 5.1 (b). Like in the previous test configuration, we activate 20 different pairs of regions for 100 repetitions at the three different noise levels mentioned earlier. The results can be found in the right panel of Figure 5.2.

Like in the first test configuration, CP and sWMNE give better approximation of the source signals when compared to the minimum norm estimate.

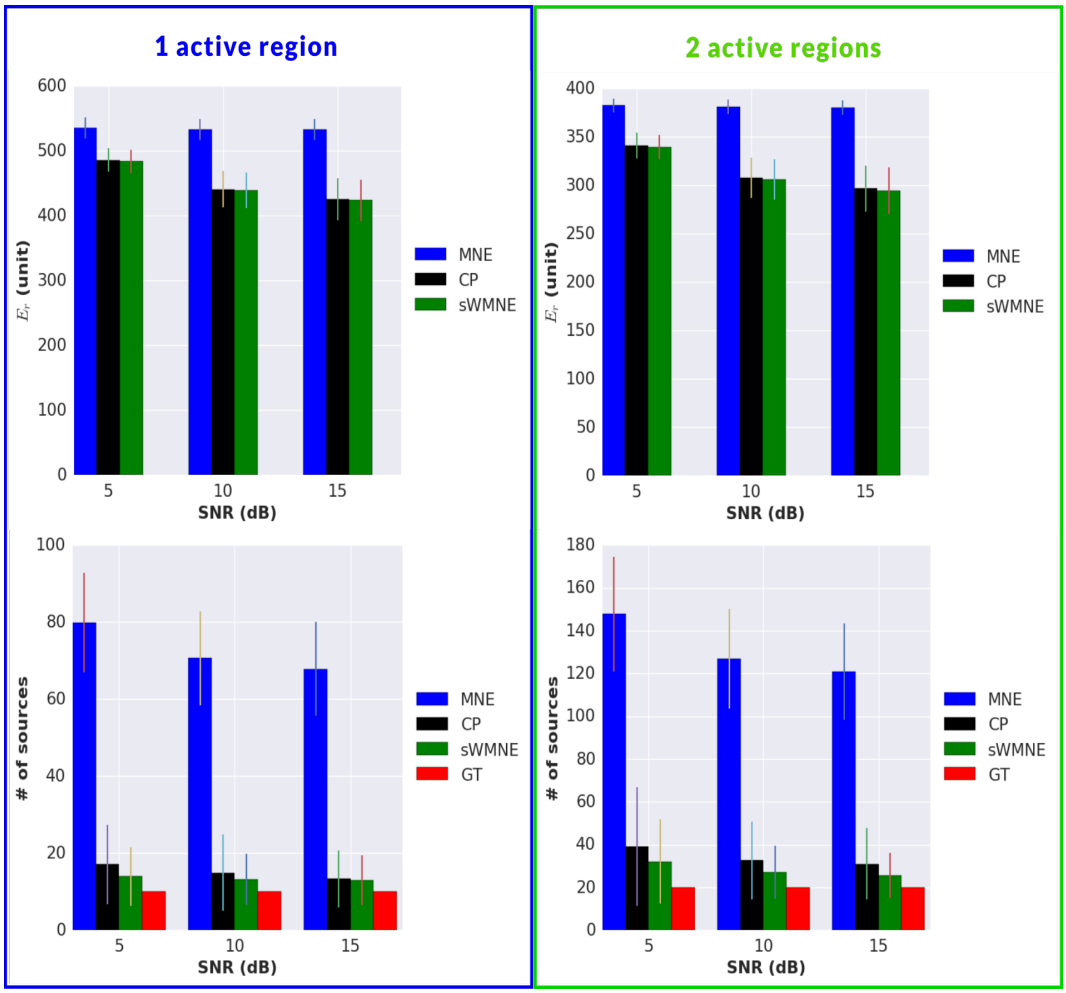

Figure 5.3: ***Upper panel: mean and standard deviation (over 20×100 runs) of reconstruction error E_r for different SNR levels for the two test configuration. Lower panel: focality of the reconstruction represented as the number of sources that have a total energy ($\|J_i\|_2$) greater or equal to 25% of the highest energy in the source space. The results are obtained for different noise levels 15, 10 and 5dB. MNE, CP and sWMNE results are shown, respectively, in blue, black and green colors. The ground truth GT of the number of active sources are shown in red.***

In the bottom of Figure 5.3, we show the number of sources that have

l_2-norm more than 25% of the highest source energy. The ground truth values (GT) are shown in red, 10 sources in the first test configuration and 20 sources when activating two regions. The blue bars represent the number of sources, obtained by MNE, that are found to have activation higher than 25% of the maximum activation. The number of active sources found by CP and sWMNE are shown, respectively, in black and green color.

Both CP and sWMNE give better reconstruction when compared to MNE in terms of focality and error of reconstruction. These results are true for all noise levels. sWMNE provides more focal reconstructions compared to CP despite the small difference in the reconstruction error between them.

In this synthetic simulation activating one or two regions corresponding to a given parcellation, CP and sWMNE are closer to the synthetic activation than MNE. We also observed that the solution of sWMNE provides more focal reconstructions compared to both MNE and CP. The smearing effect of MNE was reduced using CP and sWMNE. This is due to the use of regions in constraining brain activity.

5.3.1.2 Real data

Stimuli

We now use real data obtained from Wakeman et al. (Wakeman et al., 2015). This database contains eleven subjects with dMRI, T1, EEG and MEG data. The details of dMRI and T1 were presented earlier in section 4.5. The MEG/EEG were simultaneously recorded during a face recognition task. Three sets of grayscale photographs were used:

- 150 photos of famous people (known to the participants). Half of the faces were male, half female.
- 150 photos of unknown people. Half of the faces were male, half female
- 150 photos of scrambled faces obtained by applying 2D-Fourier transform, permuting the phase information, and then applying 2D-inverse Fourier transform to reconstruct scrambled photos.

For more details about the stimuli, refer to (Wakeman et al., 2015).

Experimental design

The stimuli (photos) were projected into a screen (black background with a white fixation cross in the center) approximately 1.3 m in front of the participants. The start of the trial was indicated by the appearance of the fixation cross for a random duration. The grayscale photograph were projected, for a random duration between 800 and 1000 ms, into the screen. The interval between two successive face projections is 1700 ms. Participants were asked not to blink during the stimulus period (Wakeman et al., 2015).

Both MEG (Elekta Neuromag Vectorview 306 system, 102 magnetometer and 204 gradiometer) and EEG (70 electrodes conforming to the extended

10-10 system) were measured in a light magnetically shielded room. The data was presented to public in six runs of 7.5 min each.

Data pre-processing

Environmental noise was removed using Signal Space Separation (SSS) (Taulu et al., 2005). The EEG and MEG data were filtered using a low-pass filter with a cutoff frequency of 35 Hz. This frequency was chosen because some studies reported the presence of gamma-band in complex visual stimuli (Lachaux et al., 2005). We averaged the data of each condition (Familiar, Unfamiliar, Scrambled). We showed in this work the result with the eleven different subjects (all subjects that have T1 and dMRI images). We focus on the brain regions responsible for face perception and recognition. To do so, we subtracted the average MEG with famous pictures of scrambled faces.

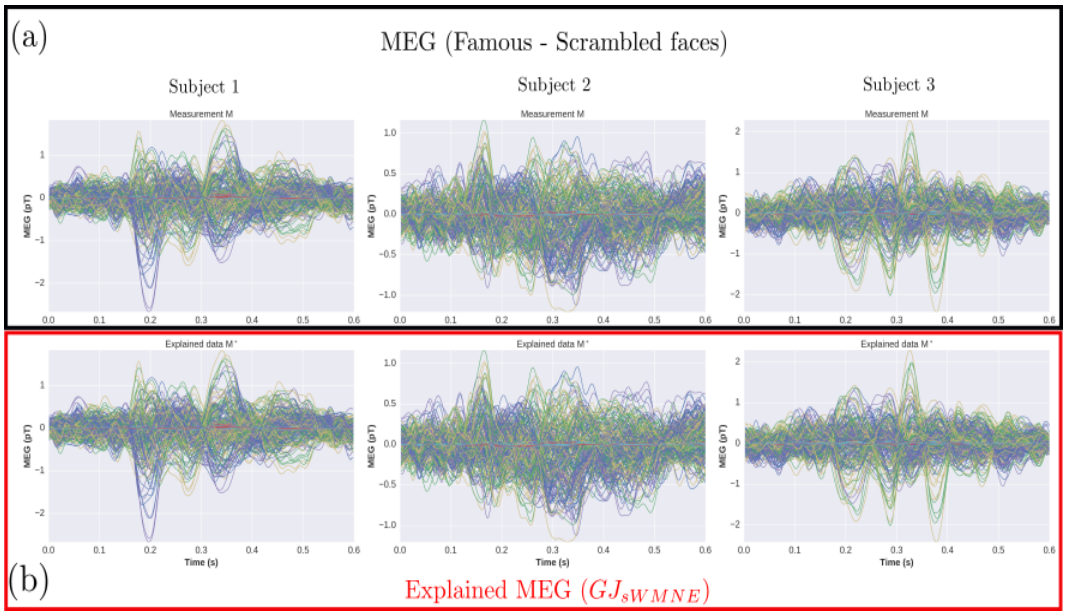

Figure 5.4: ***Top panel: MEG data of Famous - Scrambled face class. Bottom panel: explained MEG data by the sWMNE reconstruction. Differences between the recorded measurements and the explained ones by sWMNE are very small.***

Downsampling

In (Horowitz et al., 2015), the authors show a correlation between the axon diameter and conduction velocity in the human brain. They have found the ratio between axon diameter and the axon conduction velocity to be 8.75 m/s for each μm, which coincide with what was obtained before in the work of (Aboitiz et al., 1992). This results in a speed between 10 and 40 m/s for the majority of fibers. The average in this case is 25 m/s. The length of bundles can range between $50mm$ for U-shape connections to 100 mm for long connections. Thus the time needed to travel from the source to the target region is between 2 to 4 ms. This is why we decided to downsample the measurements to 367 Hz (i.e 1 sample about every 3 ms). An

example of MEG measurements of three different subjects can be found in Figure 5.4 (a).

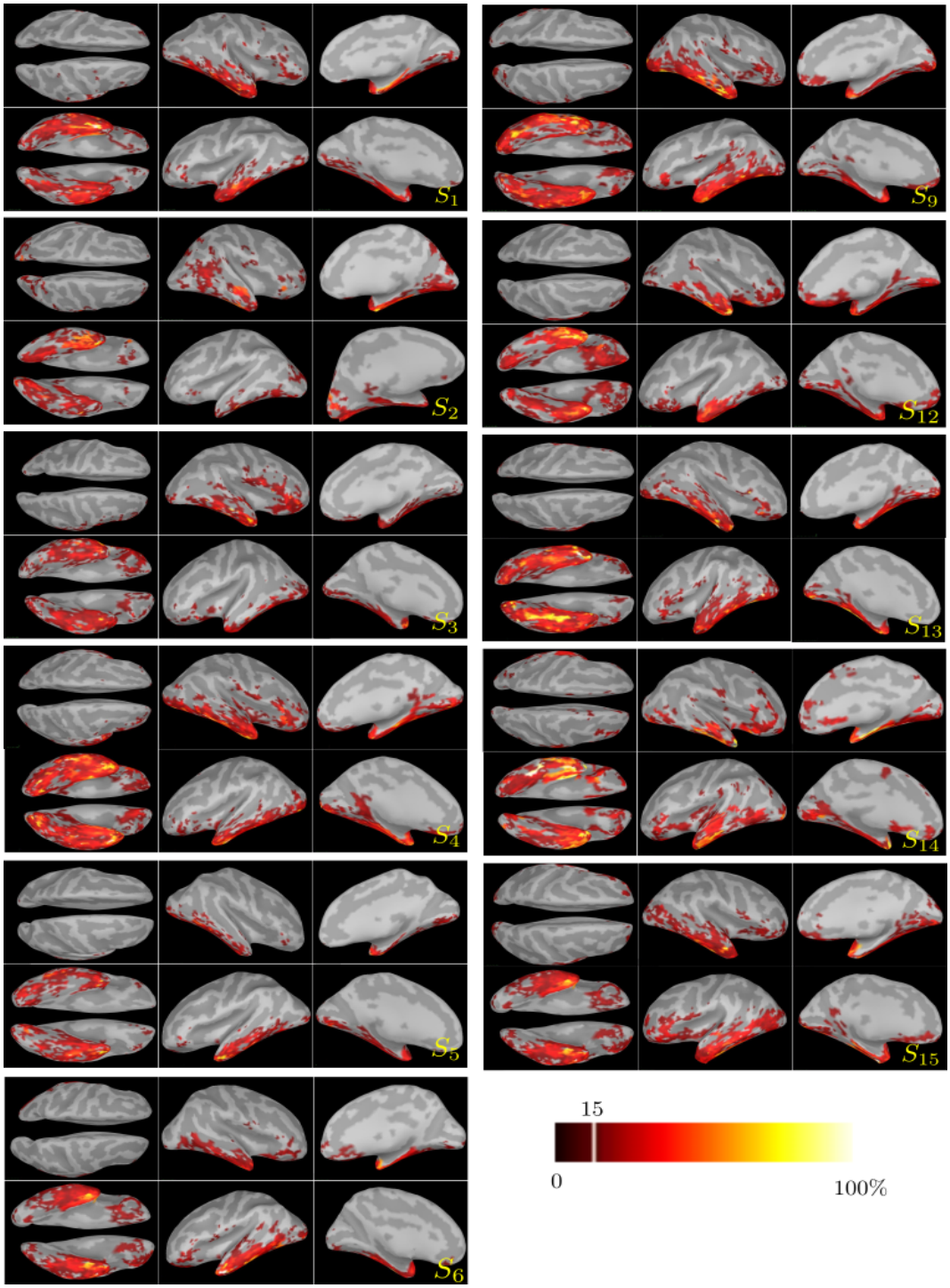

Figure 5.5: ***The l_1-norm of source magnitudes between $t = 0$ and $t = 600$ ms obtained by sWMNE from MEG data. We show only sources that have a total l_1 norm ($\|J_i\|_1 = \sum_t |J_i(t)|$) higher than 15% of the highest l_1 norm. The results are similar with the 11 participants.***

Cortical surface parcellation

The cortical surfaces of all participants were parcellated into regions using the MNN approach and *Tanimoto* similarity measure with $T = 800$. Then, the weighting matrix W_s for each subject is constructed.

Source reconstruction

In (Wakeman et al., 2015), the authors performed fMRI group-analysis during the same tasks. They noticed the presence of fusiform (FFA) and occipital (OFA), which are located in the ventral occipital-temporal gyrus, activations in both hemispheres. Further fMRI clusters in anterior medial temporal lobes, right posterior superior temporal cortex and orbitofrontal cortex are found to be active. Also, bilateral temporal pole clusters, extending to inferior prefrontal cortex on left, and bilateral medial parietal cortex as expected are found to be active from previous fMRI and neuropsychological studies (Henson et al., 2003; Wakeman et al., 2015).

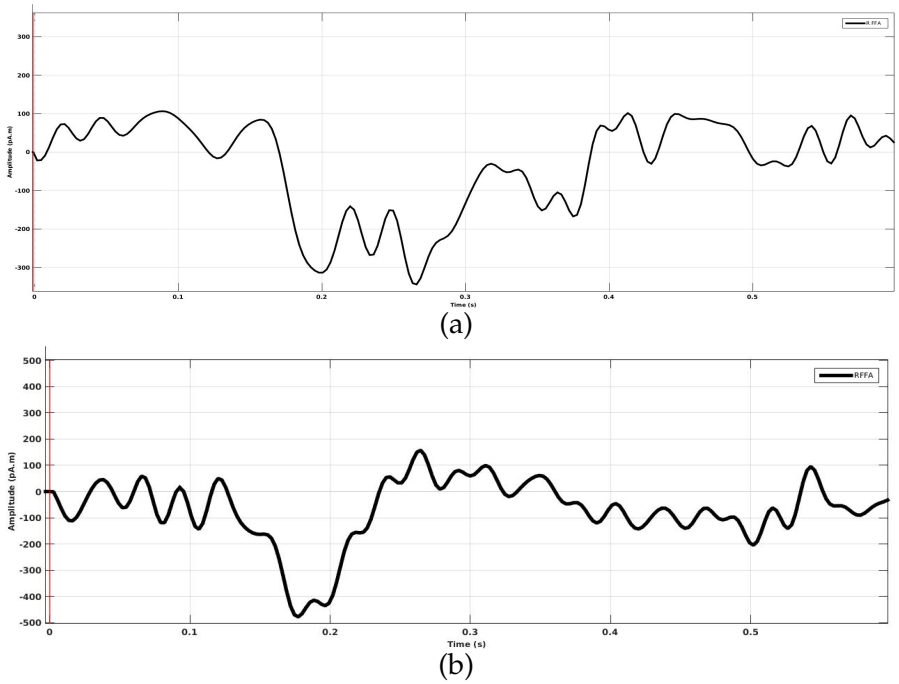

Figure 5.6: ***The average time course of a right fusiform area of (a) subject 1 and (b) subject 13 obtained by sWMNE from MEG data.***

Results of the sWMNE can be seen in Figure 5.5. An example of the time course of the right FFA of subjects 1 and 13 can be seen in Figure 5.6. As reported in previous studies, the right FFA shows a high activation between 170 and 200 ms when using familiar faces stimuli. Figure 5.7 shows the active regions obtained by the minimum norm estimate and CP of the first participant computed from MEG data and the mean time course of the RFF region. The temporal characteristic of RFF was preserved in the three reconstruction algorithms (see Figure 5.6 (a) and 5.7). But sWMNE provides

more focal activation like in synthetic data (see Figure 5.5 S1 and 5.6 (a)). This is more pronounced in the right and left frontal lobe, and in the lateral temporal lobe.

Also, we applied the sWMNE algorithm to the EEG data. In Figure 5.8, we show the detected active regions from the EEG data of Subject 1 using sWMNE.

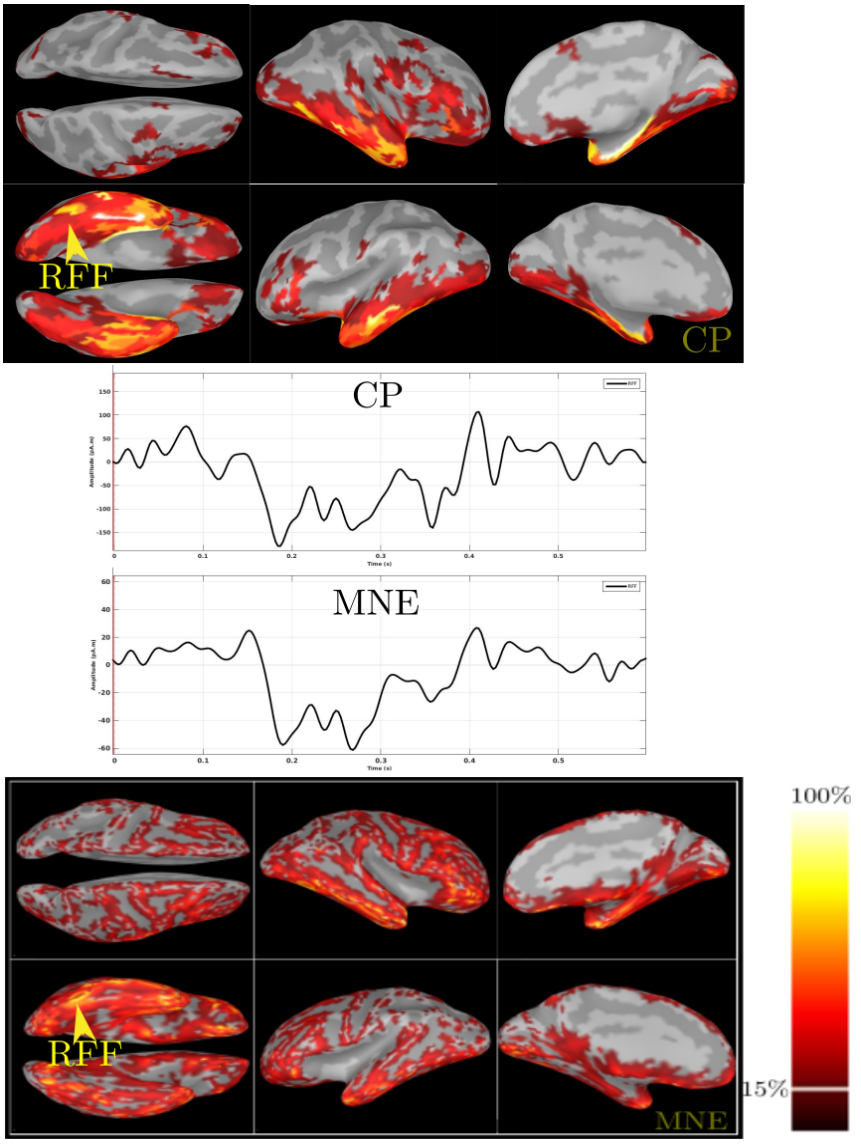

Figure 5.7: ***The l_1 norm of the minimum norm estimate (MNE) and CP of MEG data (Famous-Scrambled) of Subject 1 shown on the inflated surface. Time courses are taken from the right FF region (yellow arrow). We show only sources that have an energy higher than 15% of the highest activation.***

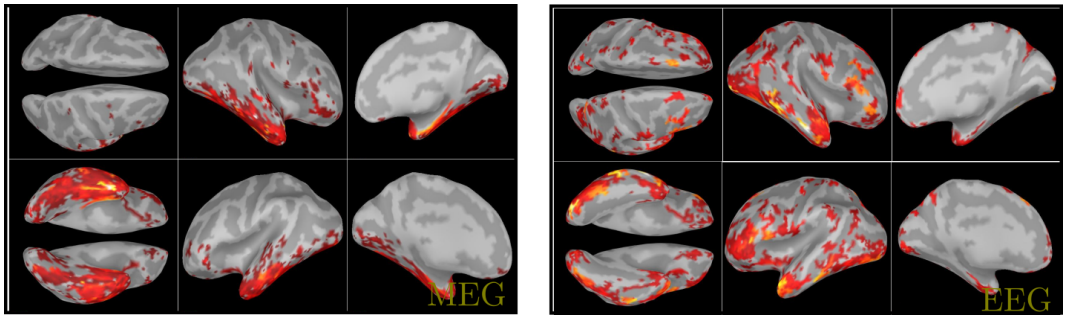

Figure 5.8: ***Left: reconstructed active regions by sWMNE from MEG data. Right: reconstructed active regions by sWMNE from EEG data. EEG and MEG data are the measurements of Subject 1.***

In the sWMNE reconstruction, the majority of subjects show activations in the right posterior superior temporal lobes and in the orbitofrontal area. Like in (Wakeman et al., 2015), all of the participants show activations in both temporal poles, ventral occipital-temporal gyrus, and anterior medial temporal lobes. Unlike in (Wakeman et al., 2015), few participants show activation in the medial parietal cortex. In MNE reconstruction, broad areas were found to be active which makes it hard to distinguish the cortical areas responsible of face perception and recognition.

The sWMNE reconstruction from MEG is more focal than the reconstruction from EEG data, see Figure 5.8. This focality is more pronounced in the parietal and frontal lobes. This difference is due to the difference in spatial resolution between MEG and EEG, see section 1.4.2.3 for more details.

Because we do not know the ground truth of brain activity when using real measurements, to have an idea about the accuracy of the reconstruction, we can only compare the actual measurement to the explained ones by the source reconstruction. In Figure 5.4 (b), we show only the results of three subjects. The black panel contains the acquired MEG data, after pre-processing, of class Famous subtracted to class Scrambled faces. In the red panel, we show the explained MEG data obtained by multiplying the reconstructed sources, S_{sWMNE}, by the lead field matrix. As can be noticed in Figure 5.4 (b), sWMNE explains well the MEG measurements for all the three participants (no significant difference between the measured and reconstructed EEG/MEG data).

5.4 Spatiotemporal regularization

Several works show that source estimates can be improved by using spatiotemporal constraints (Haufe et al., 2010; Lamus et al., 2012; Fukushima et al., 2012; Tian et al., 2013). They consist in assuming special behaviors in the source (spatial) space and time courses. Mixed norm estimate algorithm also uses spatiotemporal regularization to estimate brain activity by assuming structurally sparse on the spatial domain over a time window.

In (Schmitt et al., 2001; Schmitt et al., 2002), the authors assumed that the electrical sources do behave temporally in a smooth manner. This is was achieved, in their work, by adding a derivative term of the source temporal courses $\left\| \frac{d}{dt} J(t) \right\|$ in the cost function. This derivative is approximated by a simple difference between consecutive time samples of sources signals. This forbids big changes in the source temporal courses.

Functional connectivity analysis is often computed at the sensor level (Thirion, 2003; Michalareas et al., 2009; Sekihara et al., 2015). But, lately, number of studies have begun to use source-space analysis. Although a certain degree of inaccuracy exists in the source estimation step, source space analysis has the potential of providing more accurate information regarding which regions are interacting functionally (Sekihara et al., 2015).

There are several ways to find functional connectivity between different brain areas. Some of these connectivity measures are based on correlation like Coherence (absolute, real and imaginary). Coherence is defined as the cross-spectrum normalized by the square root of auto-spectrum and its range is between zero and one (Sekihara et al., 2015). Other measures are based on synchronization. The phase difference and time delay between two brain regions can be estimated from the imaginary and real part of the cross-spectrum (Sekihara et al., 2015). These measures are symmetric (or of opposite signs) so do not provide information about the direction of interaction. Also, some quantities can be derived from multivariate autoregressive models (MVAR or MAR) which is a common basis for coupling analysis. Directed Transfer Function (DTF) and Partial Directed Coherence (PDC) are two measurements derived from the frequency representations of the signals, which have the potential of providing directed interactions. All of these quantities rely on a good estimation of the sources' time courses and provide an insight into the strength of interactions between regions.

Previous works relate the dynamics to either the neighboring sources or to an anatomical network (Long et al., 2006; Giraldo et al., 2010; Fukushima et al., 2012). In our work, we included both of them in the dynamics of sources. Let's define a dynamical model for the sources by the multivariate autoregressive model:

$$J_t = \sum_{i=1}^{p} A_i J_{t-i} + \omega_t \tag{5.13}$$

where ω_t is a zero-mean white Gaussian noise in the source space, p is a positive integer that defines the order of the MAR model, A_i is a $N_s \times N_s$ matrix that defines the contribution of sources at time $t - i$ to sources at time t. We assume that the A_i matrices are constant for a time window of length T. This model is purely temporal if sources depend only on their past values i.e. the nonzero elements of A_i are located on the diagonal. Our model assumptions are based on some recent works (Fukushima et al., 2013; Fukushima et al., 2015), in which the authors assumed that the dynamics are based on MAR model. In (Osher et al., 2016), the authors also used a simple linear model to predict the fMRI signals from brain structural connectivity of individual subjects. This suggests that it is possible to estimate the brain

functional activity using the structural connectivity matrix.

Using the Z-transform (Ragazzini et al., 1952), the reverse characteristic matrix of a MAR model can be written as (Lütkepohl, 2007):

$$C(z) = I - \sum_{i=1}^{p} A_i z^i \tag{5.14}$$

$$\text{with } C(z^{-1})J(z) = \omega(z)$$

The condition for stability (stationarity) is that the roots of $C(z)$ must lie outside the unit circle i.e.

$$\det(C(z)) \neq 0 \text{ for } |z| \leq 1$$

MAR is more than a combination of purely temporal and purely spatial correlation, it also takes into account the time-lagged correlation between sources which is modeled by A_i. To have an insight about the dynamics of the MAR model, another matrix, called the companion matrix which has the same eigen-polynomial as of $det(C(z)) = 0$, is formed as follows:

$$\mathbf{\Phi} = \begin{bmatrix} A_1 & A_2 & \cdots & A_{p-1} & A_p \\ I & & & & \\ & \ddots & & & \\ & & & I & \end{bmatrix} \tag{5.15}$$

It can be seen as an autoregressive model of order one. Depending on the eigenvalues of Φ, we can distinguish three cases:

- If the eigenvalues of Φ are all inside the unit circle, the process is stationary (stable).
- If one or more eigenvalues of Φ are on the unit circle, the process is nonstationary. In this case, the process can be stable or unstable depending on the sources' initial values.
- If at least one eigenvalues of Φ is outside the unit circle, the process is generally explosive (unstable) depending on the initial sources' values.

In our work, we do not consider the last case in which the eigenvalues of Φ are outside the unit circle or unstable nonstationary processes because unstable processes are not of interest in our work. By substituting Equation 5.13 in 2.17, we obtain:

$$M_t = \begin{cases} GJ_t + \varepsilon_t & \text{if } t \leq \text{p} \\ G\sum_{i=1}^{p} A_i J_{t-i} + \tilde{\varepsilon}_t & \text{if } t > \text{p} \end{cases} \tag{5.16}$$

where ε_t is the measurement noise at time t, $\tilde{\varepsilon}_t = \varepsilon_t + G\omega_t$, G $(N_c \times N_s)$ is the lead field matrix obtained by solving EEG/MEG forward problem. This

equation can be rewritten as:

$$M_t = \begin{cases} GJ_t + \varepsilon_t & \text{if } t \leq \text{p} \\ \sum_{i=1}^{p} G_i J_{t-i} + \tilde{\varepsilon}_t & \text{if } t > \text{p} \end{cases} \tag{5.17}$$

where $G_i = GA_i$. It is a matrix of the same size as G.

Our solver reconstructs the brain activity and the interaction between the active brain regions by iterating between two steps. The first is called the S-step in which source signals are reconstructed using a variant of mixed norm estimate. The second is called the A-step in which the elements of the MAR model are estimated from the reconstructed source signals. In the following section, we explain in more details how the mixed norm estimate is obtained.

Mixed norm estimate

The mixed norm estimate (MxNE) is obtained by optimizing the following functional (Gramfort et al., 2012):

$$U(J) = \frac{1}{2} \|M - GJ\|_2^2 + \lambda \|J\|_{21}, \tag{5.18}$$

where $\|\cdot\|_{21}$ is an l_2-norm over time and l_1-norm over space, see Equation 2.29. The MxNE solver boils down to two updates. First, the gradient step in which the source estimate is updated according to the gradient of the data fit term and a gradient step μ. The second step is the soft thresholding arising from the proximal operator of $\|\cdot\|_{21}$. The two steps combined are called iterative shrinkage-thresholding algorithm (ISTA) or the forward-backward iterations. This ISTA algorithm uses the Lipschitz constant (L) to set the gradient's step (μ, set as the inverse of L, used in both gradient step and soft thresholding step). However, this makes the solver slow when using one gradient step μ for the whole problem. Block coordinate descent (BCD) solves the problem for each source, where the Lipschitz constant is restricted to each source, iteratively. This makes the convergence faster because the gradient step, when solving source by sources, is bigger than L^{-1}.

BCD for MxNE can be given as follows (Strohmeier et al., 2016):

$$\begin{aligned} J_s^k &= J_s^{k-1} + \mu_s G_s^T (M - GJ^{k-1}) \\ J_s^k &= J_s^k \text{max}(1 - \frac{\mu_s \lambda}{\text{max}(\|J_s^k\|_2, \mu_s \lambda)}, 0) \end{aligned} \tag{5.19}$$

where J_s^k is the signal of the source s at the iteration k. The step length μ_s for each BCD sub-problem is determined by $\mu_s = L_s^{-1}$ with $L_s = \left\|G_s^T G_s\right\|$ (spectral norm) being the Lipschitz constant of the data fit restricted to the s^{th} source.

Unfortunately, the gradient of the functional U with respect to J can not be computed because U is non-differentiable. Because MxNE is a convex problem, we can use duality gap η (Gramfort et al., 2012) to obtain an

optimal source estimate. It is defined as $\eta = \mathcal{F}_p(J) - \mathcal{F}_d(Y) \geq 0$, where $\mathcal{F}_p = U(J)$ is called *primal* cost function and $\mathcal{F}_d(Y)$ is the *dual* cost function. Y is the mapping of J to the dual space. The mapping function will defined later.

Due to Slater's conditions, strong duality holds ($\eta = 0$) for the mixed norm estimate (Boyd et al., 2004; Gramfort et al., 2012) for an optimal J^* and a good choice of the mapping function. Using the Fenchel-Rockafellar duality theorem (Rockafellar, 1970), the dual objective function associated to the primal objective function (MxNE)

$$\begin{aligned} \mathcal{F}_p(J) = & \quad \frac{1}{2}\left\|M - GJ\right\|_2^2 + \lambda\Omega(J) \\ = & \quad \frac{1}{2}\left\|M - GJ\right\|_2^2 + \lambda\left\|J\right\|_{21}, \\ = & \; U(J) \end{aligned} \tag{5.20}$$

is:

$$\mathcal{F}_d(Y) = -\frac{1}{2}\left\|Y\right\|_2^2 + \text{Trace}\left(Y^T M\right) - \lambda\Omega^*\left(\frac{G^T Y}{\lambda}\right) \tag{5.21}$$

where Ω^* is the Fenchel conjugate of Ω (Gramfort et al., 2012).

$$\Omega^*\left(\frac{G^T Y}{\lambda}\right) = \sup_{J \in \mathbb{R}^{N_s \times T}} \frac{1}{\lambda}\text{Trace}\left(Y^T GJ\right) - \Omega(J),$$

where sup is the supremum. Karush-Kuhn-Tucker (KKT) conditions (Kuhn et al., 1951) provide a mapping between the primal and dual space by setting Y to measurement residual i.e. $Y = M - GJ$. Y needs to be scaled to satisfy the constraint Ω^* ($\Omega^* = 0$) (Gramfort et al., 2012):

$$Y = Y\min\left(\frac{\lambda}{\left\|G^T Y\right\|_{2\infty}}, 1\right) \tag{5.22}$$

Algorithm 2 Dual gap η

1: **procedure** COMPUTE_DUAL_GAP(G, M, J^k)
2: $R^k = M - GJ^k$
3: $Y^k = R^k \min(1, \frac{\lambda}{\left\|G^T r^k\right\|_{2\infty}})$
4: $\eta^k = \frac{1}{2}\left\|r^k\right\|_2^2 + \lambda\left\|J^k\right\|_{21} + \frac{1}{2}\left\|Y^k\right\|_2^2 - \text{Trace}((Y^{(k)})^T M)$
5: **return** η^k
6: **end procedure**

Algorithm 2 shows how to compute the dual gap η (Gramfort et al., 2012). J^k represents the estimated sources' magnitudes at iteration k. The duality gap, the output of algorithm 2, depends on the scaled residual (hence it depends also on the data M). In (Gramfort et al., 2012), the authors

show, experimentally, that there is no significant change in the reconstruction for $\eta \leq 10^{-5}$.

MxNE suffers from amplitude bias due to the use of the l_1-norm in the spatial domain. This is due to the soft-thresholding. It also often suboptimal in terms of active source detection due to high correlations in the columns of the lead field matrix. The iterative reweighted mixed norm estimate (irMxNE), which is a variant of MxNE, was developed to tackle these limitations. It could provide better results in terms of magnitude bias and source active set by removing the contribution of small active sources on the measurements. The irMxNE is obtained from the following:

$$\tilde{J} = \underset{J}{\operatorname{argmin}} \left\{ \frac{1}{2} \|M - GJ\| + \lambda \sum_s \sqrt{\|J_s\|_2} \right\} \tag{5.23}$$

where the sum is over the sources. This non-convex optimization is solved by iterative reweighted convex surrogate optimization problems (Strohmeier et al., 2016). The solution is formulated as follows:

$$\begin{cases} J^k = \underset{J}{\operatorname{argmin}} \frac{1}{2} \left\|M - GW^k J\right\|_2^2 + \lambda \|J\|_{21} \\ \tilde{J} = W^k J^k \\ W^k = \operatorname{diag}(w^{(k)}) \\ w^k(s) = 2\sqrt{\left\|\tilde{J}_s^{(k-1)}\right\|_2} \end{cases} \tag{5.24}$$

where $W^{(k)}$ is a diagonal weighting matrix at iteration k, computed from the previous estimates ($\tilde{J}^{(k-1)}$). If a source was detected to be with small activation at iteration k, its l_2-norm is low which reduces its contribution to the measurement by multiplying its corresponding column in the gain matrix by $2\sqrt{\left\|\tilde{J}_s^{(k-1)}\right\|_2}$. If the l_2-norm of a source is high, it means that the source is important and favored in the next iterations. This makes the irMxNE procedure similar to FOCUSS (Gorodnitsky et al., 1995).

irMxNE provides better temporal and magnitude reconstruction, but it does not use source interactions to recover the brain activity. In the next section, we present our spatiotemporal source reconstruction with a constrained sources' dynamics.

Iterative Source and Dynamics Reconstruction (iSDR)

In this method, we assume that sources' dynamics follow a stable MAR model whose elements are constrained by neighboring and anatomical connected regions. Also, we consider regions to be spatially sparse in a time window T. We decided to use only the measurements from time $[p+1, T]$ for some reasons that will be listed later in this section.

We rewrite Equation 5.18 by considering only the EEG/MEG measurements from the sample $p+1$ to T and relating them to sources magnitudes

from the first sample till $T-1$. Let's now define the following functional:

$$U(J) = \|M_v - \mathbf{G_d} J_v\|_2^2 + \lambda \|J\|_{21} \tag{5.25}$$

where

- N_c and N_s are the number of sensors and sources, respectively.
- $M_v = \text{vec}(M)$, $M \in \mathbb{R}^{N_c \times (T-p)}$, represents the measurements between $p+1$ and T.
- $J \in \mathbb{R}^{N_s \times T-1}$ contains the sources' activity between the first time sample and $T-1$.
- $J_v = \text{vec}(J)$.
- $\mathbf{G_d} \in \mathbb{R}^{N_c(T-p) \times N_s(T-1)}$

$$\mathbf{G_d} = \begin{bmatrix} G_1 & G_2 & \cdots & G_p & & \\ & G_1 & \cdots & G_{p-1} & G_p & \\ & & \ddots & \ddots & \ddots & \ddots \\ & & & G_1 & \cdots & G_{p-1} & G_p \end{bmatrix} \tag{5.26}$$

The data fidelity term includes errors coming both from the MAR model and source reconstruction.

This functional can be seen as an extension to the problem defined in (Gramfort et al., 2012; Strohmeier et al., 2016). The major improvement of our method with compared to both MxNE and irMxNE is that the interactions between sources are included in the functional. In our work, the weights are not only in the diagonals of A_i matrices like in irMxNE but also contains nonzero elements that correspond to the neighbors or anatomical connections. These weights are estimated from the following functional:

$$V(A_v) = \|J_v^* - SA_v\|_2^2 + \gamma Q(A_v) \tag{5.27}$$

where A_v is the vectorial form of $A = [A_1, \cdots, A_p]$ and Q is a prior on the MAR model elements. J_v^* is the vectorial form of sources' magnitudes between the 2^{nd} sample and $T-1$. S is a $N_s(T-p) \times pN_s^2$ matrix:

$$S = \begin{bmatrix} \text{D}(J_1) & \text{D}(J_2) & \cdots & \text{D}(J_p) \\ \text{D}(J_2) & \text{D}(J_3) & \cdots & \text{D}(J_{p+1}) \\ \vdots & \vdots & \ddots & \vdots \\ \text{D}(J_{T-p-1}) & \text{D}(J_{T-p}) & \cdots & \text{D}(J_{T-1}) \end{bmatrix} \tag{5.28}$$

where $\text{D}(J_k)$ is a $N_s \times N_s^2$ matrix:

$$\text{D}(J_k) = \begin{bmatrix} J_k^T & 0 & \cdots & 0 \\ 0 & J_k^T & \cdots & 0 \\ \vdots & \vdots & \ddots & \vdots \\ 0 & 0 & \cdots & J_k^T \end{bmatrix} \tag{5.29}$$

The non-convex optimization problem is solved by iteratively solving a sequence of weighted MxNE (Equation 5.25) and estimating the MAR model elements by minimizing Equation 5.27.

It is possible, in our method, to have some other priors on the coefficient values which can be included in $Q(A_v)$. In our work, we do not include extra prior i.e. $\gamma = 0$. The Maximum Likelihood (ML) solution for the MAR coefficients is (Weisberg, 2005) (Ordinary Least Square solution):

$$A_v = (S^T S)^{-1} S^T J_v^* \tag{5.30}$$

In section 2.3.3.3, we showed briefly how MxNE is computed. Our method iSDR is non-convex but can be solved by solving a sequence of weighted convex optimization problem (MxNE) with weights being defined based on the previous sources' estimates by minimizing the functional V.

$$\begin{cases} U(J^k) = \left\| M_v - {\mathbf{G_d}}^{k-1} J_v \right\|_2^2 + \lambda \left\| J \right\|_{21} \\ V(A_v^k) = \left\| J_v^* - S^k A_v^k \right\|_2^2 \end{cases} \tag{5.31}$$

where ${\mathbf{G_d}}^k$ is $\mathbf{G_d}$ (Equation 5.26) obtained from the k^{th} estimate of the MAR model elements and S^k is obtained from the k^{th} iteration of the sources magnitudes using Equation 5.28. iSDR consists in iterating between two steps. We call S-step (MxNE) the part of iSDR that consists in optimization U. The A-step consists in estimating the MAR elements from the result of S-step.

The pseudo code of iSDR is provided in Algorithm 3. The algorithm needs the following inputs:

- G: lead field matrix.
- M: EEG and/or MEG data.
- A: initialization of MAR model.
- λ: the value of the regularization parameter.
- L: number of iterations between the S-step and A-step. It is equal to 12 in this work.
- I: number of iterations for BCD optimization. It is equal to 6×10^3.

iSDR returns both the sources estimates J, obtained from the S-step, and the sources effective connectivity matrix A.

The algorithm starts by initializing the residual vector R by M_v i.e. assuming no source activations (line 3), before iterating between the S-step and A-step, and the number of active sources n^0 to N_s.

S-step: It consists in computing the gradient step μ_s for each source s (line 5) then constructing the big matrix G_d (line 6) defined by Equation 5.26 for each iSDR iteration k. lines 7-17 represent the pseudo-code of BCD (MxNE). In each iteration, a source is set to zero if its l_2-norm is lower than its $\mu_s \lambda$. Otherwise, its activation is multiplied by $(1 - \frac{\mu_s \lambda}{\|J_s\|_2})$. This is done at line 10. Note that $G_{d,s}^k$ is the columns of ${\mathbf{G_d}}^k$ that correspond to the source s

at iteration k. Also the the dual gap η^i is computed (line 13) in each BCD iteration i. The ϵ-optimal solution is obtained when $\eta^i < \epsilon = 10^{-6}$. When the optimal solution at iteration i, J^i, is obtained, the iSDR algorithm exits the S-step and enters the A-step.

A-step: It consists first in constructing the matrix S^k and the vector J_v^* (line 18) from the output of the S-step i.e. J^k. Then, it estimates the MAR elements using Equation 5.30 (line 19). The MAR elements are saved in the vector A_v^k.

Improving the convergence speed

If a source s, at a given iteration k, is found to be inactive (0 at each time sample of the window size), there exists no causality between this source and the remaining sources. The A-step sets the corresponding elements of this source in the MAR model to zero. This is why this source will remain inactive for all the remaining iterations. To reduce the computation time, we remove the contribution of inactive sources into the measurement i.e. we remove the columns that correspond to inactive sources.

Stopping criteria

iSDR includes three stopping criteria. The first is when k is equal L (maximum number of iSDR iterations). The second tests if there is no significant change in the iSDR estimates between iteration k and $k-1$ i.e. $\left\|J_v^{k-1} - J_v^k\right\|_2 < \tau$ for small τ. In this work, we set $\tau = 10^{-6}\left\|J\right\|_{2\infty}$. The last stopping criterion compares the size of active sources obtained in iteration k and $k-1$. If they are the same, the algorithm stops. The last stopping criterion is achieved when no more sources validate $\mu_s\lambda > \left\|J_s\right\|_2$. This means that the active source set found at iteration k is the same as the one found in the next iterations. This results to $G_d^k J_v^k \approx G_d^{k+1} J_v^{k+1}$.

The formulation of iSDR functional U does not include the first p measurements. It is possible to include them by adding p blocks of G in $\mathbf{G_d}$. But this makes the gradient step μ_s smaller. Hence increasing the convergence time. It is worth mentioning that the first p source values are still predicted from the future MEG/EEG measurements ($t > p$).

Algorithm 3 iterative Source and Dynamics Reconstruction (iSDR)

procedure iSDR(G, M, A, λ, L, I)
  M_v =vec(M)
  $R = M_v$, $n^0 = N_s$
  for $k = 1 : L$ **do**
    Compute μ_s for $s \in [1, N_s]$
    $G_d \overset{\text{def}}{=}$ Equation 5.26
    for $i = 1 : I$ **do**
      for j=1:N_s **do** ▷ Update J
        $J_s^i = J_s^{i-1} + \mu_s (G_{d,s}^k)^T R$
        $J_s^i = J_s^i \max(1 - \frac{\mu_s \lambda}{\max(\|J_s^i\|_2, \mu_s \lambda)}, 0)$ ▷ Soft thresholding
        $R = R - G_{d,s}^k (J_s^i - J_s^{i-1})$
      end for
      η^i=COMPUTE_DUAL_GAP(G, M, J^k)
      if $\eta^i < \varepsilon$ **then**
        break
      end if
    end for
    Construct S and J_v^*
    $A_v^k = ((S^k)^T S^k)^{-1} (S^k)^T J_v^*$ ▷ Update A
    if $\left\| J_v^{k-1} - J_v^k \right\|_2 < \tau$ or $n^k = n^{k-1}$ **then**
      break
    end if
  end for
  return J^k, A_v^k
end procedure

5.4.1 Pruning the MAR model

The total number of MAR model to be estimated is pN_s^2 which is a huge number to be estimated from limited data. We need to consider fewer MAR elements because we expect that brain does not have random functional network but few brain regions interact to perform a mental task. First, we parcellate the cortical surface into functional regions with homogeneous structural connectivity. The parcellation is explained in more details in chapter 4.1. This allows us to reduce the number of MAR elements to be estimated, and the complexity of the EEG/MEG inverse problem from trying to estimate N_s sources to only estimating the activation of P regions without losing the generality of iSDR. Other assumptions on sources inside the same region can be used. A possible one is to use the structural homogeneity to set the relation between sources, see Equation 5.9.

We can also remove elements from MAR models by creating masks. These masks can be obtained by

- Inferring connections from dMRI (B).
- Neighbors connections undetected by dMRI (N).

- Connections from other modalities (e.g. fMRI) (O).

The nonzero elements of the MAR model A_i are:

$$\text{mask}(A_i) = B \text{ OR } N \text{ OR } O \tag{5.32}$$

where OR is the logic "or" applied element by element i.e. $A_i(i,j)$ is nonzero if $B(i,j)+N(i,j)+O(i,j) \neq 0$. B is a matrix with the nonzero elements correspond to dMRI structural connections. The edges of the surface mesh are used to define the neighboring regions (N). The matrix O can be constructed differently. For example, it can be used to add connections, undetected by dMRI, between regions that are known to be connected from other imaging modalities, e.g. fMRI.

In this work, we consider only the B and N matrix.

dMRI connections (B)

B elements correspond to the strength of structural connectivity between brain regions. The connectivity strength, c, between two regions, target t and s source, is defined by the fractions of the particles (thrown by the probabilistic tractography) that started from s and arrived to t i.e.:

$$C_p(s,t) = \frac{\frac{n_t}{|t|}}{\frac{n_s}{|s|}}, \tag{5.33}$$

where

- $|s|$ is the number of voxels in s.
- n_s is the number of particles thrown in s.
- n_t is the number of particles thrown from s that arrived to t.

In this work, we used in the probabilistic tractography 6000 particles per seed, this makes $\frac{n_s}{|s|} = 6000$. The elements of B are defined by: $B(s,t) = \max(C_p(s,t), C_p(t,s))$. We prune the MAR matrix and consider only connections that have connectivity strength value higher than 10^{-3}. This means that an anatomical connection is validated if at least, on average, 0.1% of the seeds (equivalent to 6 seeds in our study) that are drawn from s arrived at t. The value is found to be a good compromise to obtain long anatomical connections (see Figure 5.9). By choosing a small threshold, we increased the number of potential connections, to not miss any true anatomical connection, and thus the number of MAR coefficients to be estimated.

In Figure 5.9, we show an example of structural connectivity obtained from dMRI information of Subject 1 (Wakeman et al., 2015). Each green dot represents a center of a cortical region obtained by using the MNN parcellation algorithm. Each edge corresponds to an anatomical connection between two regions. In the superior view, we can see some of the anatomical connections between the two hemispheres (through the corpus callosum). Some of the association fibers can be seen in the left and the right lateral views. For example, the uncinate fasciculus, is a white matter bundle that connects the anterior regions of the temporal lobe with the inferior frontal

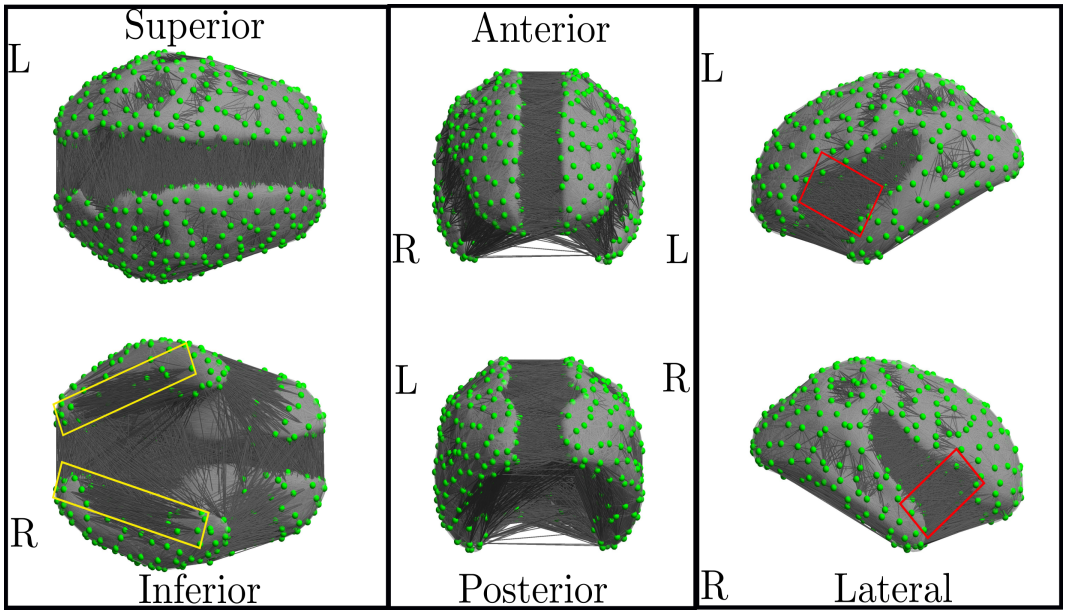

Figure 5.9: ***Different views of the structural network of Subject 1 obtained from dMRI as explained in section 5.4.1. L and R stand, respectively, for left and right hemispheres. In red boxes, we show the uncinate fasciculus. In the yellow boxes, we show the inferior longitudinal fasciculus. Green dots represent the center of the cortical regions obtained by MNN parcellation.***

gyrus and the lower surfaces of the frontal lobe (see the red boxes in Figure 5.9). The inferior longitudinal fasciculus, which is another association fibers, connects the temporal and occipital lobes which can be seen in the inferior view of Figure 5.9 (yellow boxes). Both inferior longitudinal and uncinate fasciculus are considered to be long bundles.

Figure 5.10 shows the histogram of the structural connections that are detected by the probabilistic tractography (see section 3.7.1.2). We can distinguish two groups of subjects. The first one, left part of Figure 5.10, shows fewer structural connections when comparing to the second group, right part of Figure 5.10. Obtaining few connections means that the probabilistic tractography failed to connect some cortical regions. This is probably due to the values of FA and curvature, which are used to stop the probabilistic tractography, or noise presents in the DW images.

Because our algorithm is based on the structural connections, we preferred to use the second group, which shows a higher number of connections (not to miss any true anatomical connections) when using iSDR to reconstruct brain activity. The participants in this group are 1, 2, 3, 4, 12, 13, 14 and 15.

Neighbor connections (N)

Usually, sources interact with their neighbors. Sometimes, these functional interactions are not reflected by detectable structural connections with dMRI e.g. horizontal fibers. Thus, we assume that the MAR model

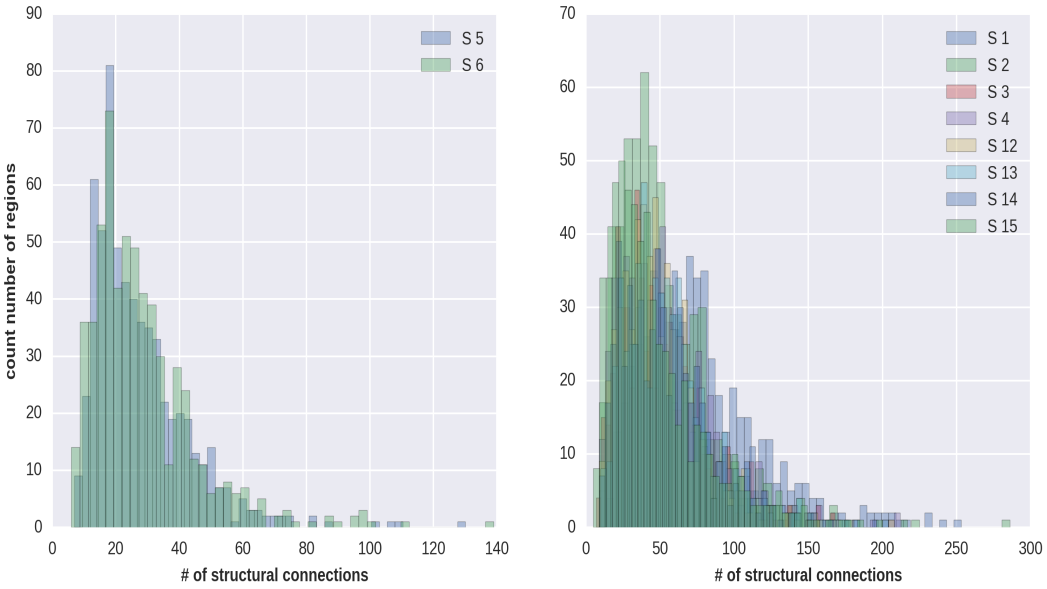

Figure 5.10: ***Histograms shows the number of structural connections that are seen by dMRI (probabilistic tractography) for the eleven participants.***

matrices, A_i, are obtained from two matrices. First, the structural connectivity between the sources/regions (B). Secondly, the direct neighboring regions/sources (N). In another word:

$$\text{mask}(A_i) = OR(B, N) \tag{5.34}$$

Solving Equation 5.27 is memory consuming because of the big size of the matrix S. But because of the sparsity of A_v, we can reduce the size of S by removing all the columns of S that correspond to the indices of zero elements in A_v. For example, if the set of active sources is X, we keep only the columns in S indexed by:

$$X + iN_s \text{ for } i \in [0, N_s p[$$

5.4.2 Magnitude bias

Like all the reconstruction methods that uses the l_1-norm, iSDR suffers from magnitude bias i.e. the estimated magnitude is lower than the real one. The standard practice for magnitude compensation consists in computing the least squares fit (Belaoucha et al., 2015b) after restricting the source space to the active source set obtained from iSDR which is typically an overdetermined optimization problem. By including the MAR model in the least squares fit term, we can preserve the sources' dynamics estimated by the A-step.

Another debiasing method that preserves the sources temporal courses was proposed in (Gramfort et al., 2013; Strohmeier et al., 2016). It consists of estimating one constant, over time, scalar (≥ 1) per sources by optimizing

the following functional:

$$\tilde{D} = \underset{D}{\operatorname{argmin}} \left\| M - GD\tilde{J} \right\|_2^2 \text{ s.t. } \begin{cases} D(i,j) \geq 1 & \text{if } i = j \\ D(i,j) = 0 & \text{if } i \neq j \end{cases} \tag{5.35}$$

then the bias corrected sources magnitudes is computed as $J = \tilde{D}\tilde{J}$.

Both debiasing approaches can be used in our framework. But for $p > 1$, the second approach becomes computationally expensive. The debiasing is applied only when working with real data because it is considered as a post-processing step and we want to compare MxNE and iSDR without any post-processing. This is why we used both of the debiasing only when working with real data. The second approach is used when working with MAR model of order 1 and the first for higher order MAR models.

5.4.3 Results

The section is dedicated to the iSDR algorithm and is divided into two subsections. In the first subsection, we use synthetic simulation to test the accuracy and focality of iSDR. In the second subsection, we use the same EEG/MEG data mentioned in section 5.3.1.2. We compare the results to what can be found in the literature about the regions that contribute to the face perception and recognition.

5.4.3.1 Synthetic data

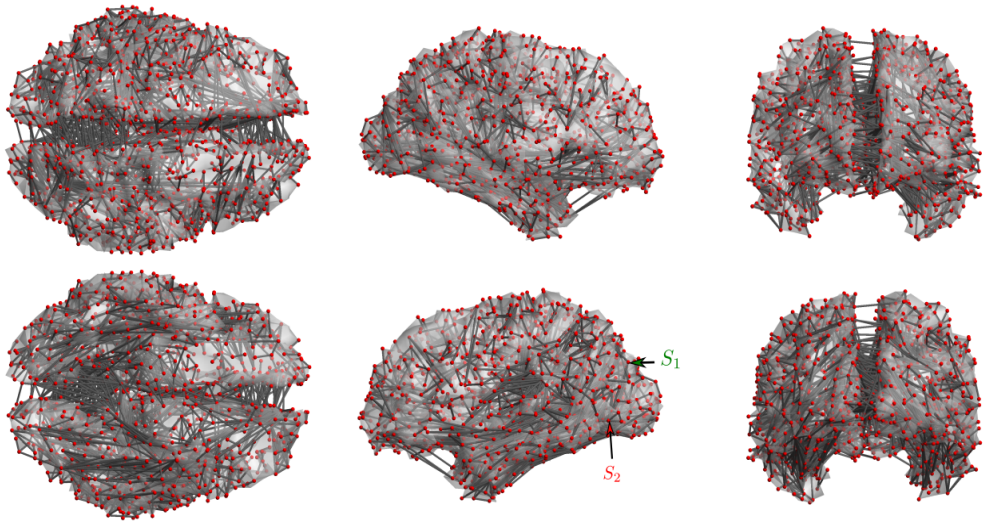

Figure 5.11: ***Different view of the cortical surface used in the simulation and the location of S_1 and S_2. Edges represent the anatomical connections.***

We consider the regions' dynamics to follow a multivariate autoregressive model of order one ($p = 1$). We investigate the accuracy of the proposed framework by using simulated data generated from this simple MAR

model. We compared iSDR($p = 1$) to the one obtained from MxNE, Lasso and irMxNE.

We simulate two regions according to a simple MAR model. The simulation is done at different SNR values. We used the head model of participant 1 (MEG lead field) of (Wakeman et al., 2015) to test the accuracy of the iSDR method. We reduce the source space from 10^4 to 2×10^3 regions, using random parcellation in Brainstorm (Tadel et al., 2011), for fast comparison. Then, we estimate the anatomical connections as described in section 5.4.1. This results to around 7×10^3 anatomical connections. Two sources, S1 and S2, are located in the left occipital lobe and connected anatomically, see Figure 5.11. We activated S1 and S2 while the other areas are inactive. S1 is connected anatomically to three areas, whereas S2 is linked to five areas.

$$\begin{cases} J_t(S1) &= 0.96J_{t-1}(S1) + 0.25J_{t-1}(S2) \\ J_t(S2) &= -0.25J_{t-1}(S1) + 0.95J_{t-1}(S2) \end{cases}$$

with $J_0(S1) = -J_0(S2) =$5 nA. The MAR matrix has two nonzero eigenvalues $0.955 \pm 0.25j$ (module <1). Because of the presence of imaginary part in the eigenvalues, the sources oscillate.

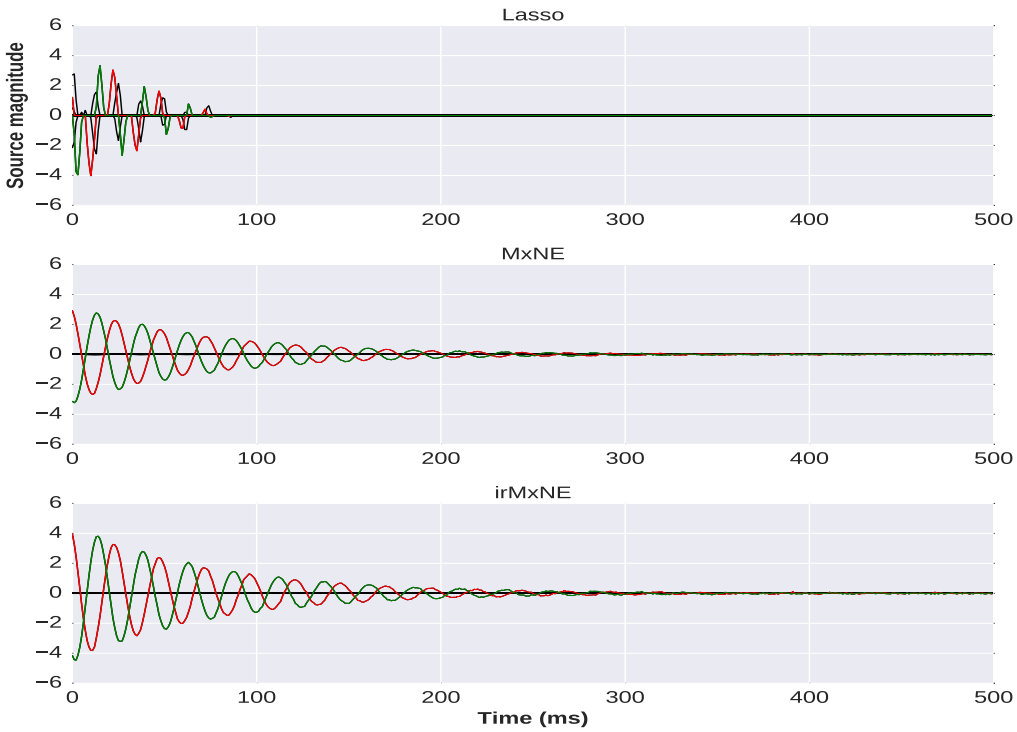

Figure 5.12: ***An example of the source estimates using MxNE, irMxNE and Lasso at SNR equal to 10 dB. In blue and green, we show the time course of S_1 and S_2. The remaining dipoles' magnitudes are shown in black.***

Reconstruction accuracy

The regularization parameter for each reconstruction algorithm was fixed by 3-fold cross-validation, except irMxNE in which λ was fixed to 20%

of the lowest λ that results to empty active set i.e. all regions are inactive. The MAR model for iSDR is simply taken as the identity matrix. This makes iSDR at least as sparse as MxNE.

In Figure 5.12, we show an example of the reconstructed sources using Lasso, MxNE and irMxNE. Example of iSDR reconstructions at different noise levels will be given latter. Lasso algorithm underestimates the simulated source magnitudes. It sets small source magnitudes to zero without taking into account the activation temporal smoothness. Also, it may gives wrong active source set, see top panel in Figure 5.12. MxNE gives better reconstruction compared to Lasso, but there is a magnitude bias. irMxNE reconstruction magnitude is more accurate compared to Lasso and MxNE, but it still smaller than the ground truth.

We compared the accuracy of iSDR estimate to MxNE, irMxNE and Lasso at three different noise levels (SNR $\in \{15, 10, 5, -5\}$ dB) by computing the reconstruction error between the ground truth and the source estimate. The result can be seen in Figure 5.13.

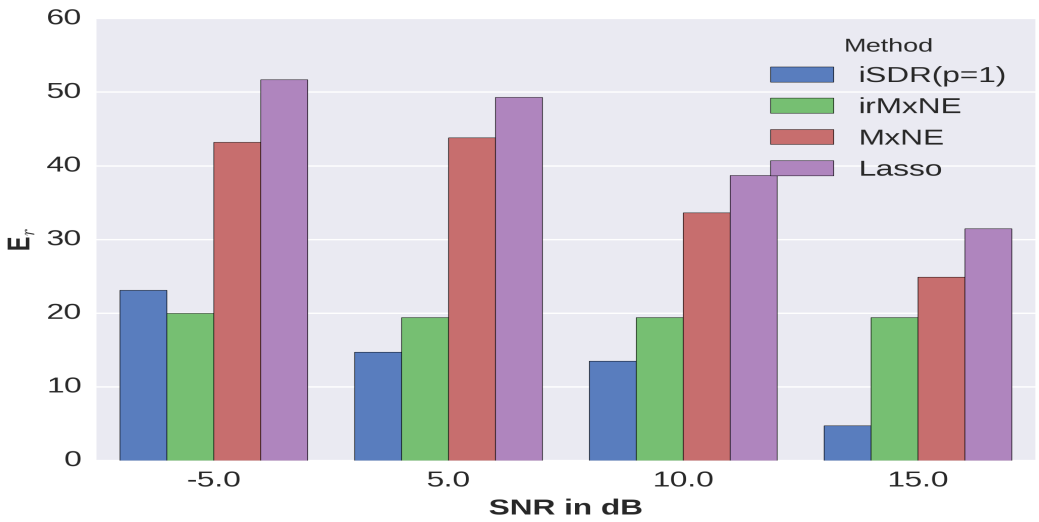

Figure 5.13: ***The mean, over 100 runs, of the reconstruction error at different noise levels (SNR ={15, 10, 5, -5} dB). The error of the reconstruction is computed as the l_2-norm of the simulated ground truth subtracted to the reconstructed activation using iSDR, Lasso, irMxNE and MxNE.***

iSDR shows better reconstruction compared to MxNE, irMxNE and Lasso for an SNR higher than 5 dB. For low SNR, -5 dB, irMxNE gives better reconstruction compared to iSDR but iSDR is still more accurate than the remaining two reconstruction algorithms. irMxNE shows stable solution over SNR levels, as was reported in (Strohmeier et al., 2016).

We also compare the accuracy of the reconstructed initial values of the simulated sources $S_1(t = 0)$ and $S_2(t = 0)$ because all the time courses of sources depend quite a lot on their initial values ($S(t = n) = A^n S(t = 0)$), see Table 5.1.

		Estimated $S_1(t=0)$ & $S_2(t=0)$			
		mean	std	mean	std
MxNE	15 dB	4.23	0.06	-4.69	0.07
	10 dB	3.26	0.13	-3.31	0.10
	5 dB	2.54	0.20	-2.93	0.26
	-5 dB	1.47	0.37	-1.36	0.27
iSDR	15 dB	4.98	0.03	-4.98	0.03
	10 dB	4.98	0.05	-4.97	0.06
	5 dB	4.96	0.08	-4.95	0.12
	-5 dB	5.28	0.71	-4.36	0.95
irMxNE	15 dB	3.95	0.015	-4.15	0.016
	10 dB	3.95	0.023	-4.16	0.025
	5 dB	3.96	0.044	-4.15	0.045
	-5 dB	3.9	0.3	-4.02	0.4
Lasso	15 dB	2.52	0.41	-2.95	0.49
	10 dB	1.10	0.87	-2.17	0.85
	5 dB	0.97	1.40	-1.80	1.13
	-5 dB	0.48	1.51	-0.91	1.21

TABLE 5.1: The mean and standard deviation (std), over 100 runs, of the initial values of the reconstructed active sources S_1 and S_2 error over 100 runs at different noise levels (SNR ={15, 10, 5} dB).

irMxNE shows a stable estimation of the initial source magnitude over SNR levels. iSDR gives values, on average, that are the closest to the ground truth even in low SNR (-5 dB). It is worth mentioning that the initial values estimated by iSDR are not using the measurement at time $t = 0$. The accuracy of the remaining methods, Lasso and MxNE, decreases with SNR level which is predictable since they need higher value of λ to distinguish between true and false active sources.

In conclusion, iSDR provides more accurate results in terms of sources signals magnitude retrieval compared to MxNE, Lasso and irMxNE. This is mostly because it predicts better initialization of the sources magnitudes (magnitudes at $t = 0$), which is important for the MAR model, even though the measurements at $t < p$ were not used in the iSDR model.

Spatial extent of the reconstruction

In Figure 5.14, we show the histogram of the size of the active source set, defined as the number of sources with nonzero l_2-norm, obtained from iSDR(p = 1), MxNE, irMxNE and Lasso algorithms for all noise levels. iSDR

has the highest percentage of true active set detection. It is followed, in decreasing order, by irMxNE, MxNE and Lasso. iSDR detected higher number of active sources compared to irMxNE when working in low SNR. This is due to noise and the initialization of iSDR's parameters i.e. (λ, A).

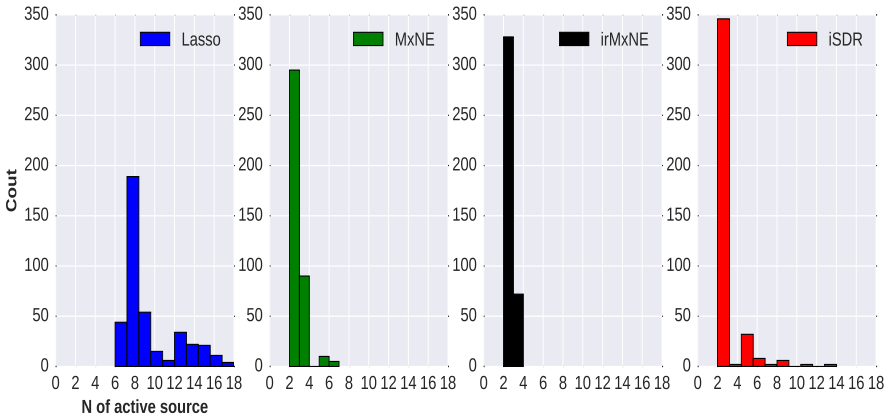

Figure 5.14: ***The number of sources found to be active by iSDR at the four SNR levels $\{$15, 10, 5, -5$\}$. The total number of simulations is 400 (100 per noise level). True active set contains 2 sources.***

Influence of regularization parameter

In Figure 5.15 (a), we show an example of the source reconstruction error E_r in blue, see equation 5.12, the measurement error M_r in green, equal to the data fit term, and the number of estimated active sources in red (right y-axis) for different regularization parameters. As expected for MxNE, the number of active sources decreases while increasing λ, this is due to the soft-thresholding function in which more sources will have l_2-norm lower than λ which result to a multiplication of time courses with zero i.e. deactivating sources. The optimal λ, that results to small M_r, is around 5×10^{-4} for MxNE. For iSDR, several values of λ result to the true active set (S_1 and S_2) which resulted in a decrease in both E_r and M_r curves. The optimal λ is smaller than the one found for MxNE. This explains why iSDR provided a less magnitude biased solution. iSDR reduces the size of active set from around 350 sources, in the first iteration i.e MxNE solution, to 12 sources after 6 iterations.

Figure 5.15 (b) shows the cost function U of MxNE (in black) and iSDR (in blue). Contrary to MxNE, the cost function of the iSDR estimate is non-convex. The source estimate depends on MVAR model estimated in the previous iteration. This shows the importance of choosing the "right" values interval of the regularization parameter λ.

iSDR is better in terms of magnitude bias with respect to MxNE due to the choice of the regularization parameter λ. Both mixed norm and iSDR estimates scale the magnitudes of the sources by $s = (1 - \frac{\mu\lambda}{\max(\|J\|_2, \mu\lambda)})^+$. In MxNE, a high λ is used to set weak active sources to zero which leads s to

be much less than 1. In iSDR, a relatively lower value for λ can be used to converge to the true active source. This makes s bigger.

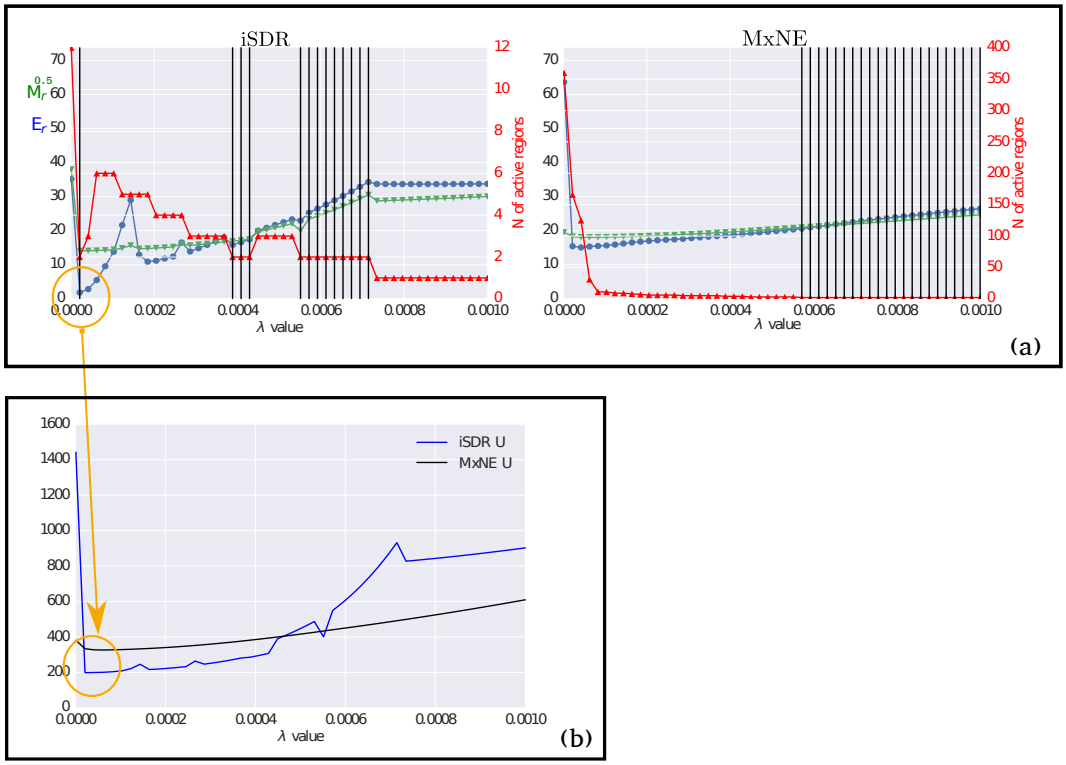

Figure 5.15: ***The source reconstruction error E_r (in blue), data fit term M_r (in green) and number of detected active sources (in red) obtained from MxNE and iSDR. The regularization parameter λ that gives the true active sources are shown in black vertical lines. In the bottom panel, we show the corresponding values of the cost function for MxNE and iSDR. These results are obtained using realistic head model and a measurement at SNR level equal to 10 dB. The optimal λ for iSDR is inside the orange circle.***

Estimated MAR model

In Figure 5.16, 5.17 and 5.18, we show, respectively, an example of sources reconstruction estimated by iSDR at SNR equal to 15, 10 and 5 dB at various iterations (from left to right and from upper to lower panel). The reconstructed time course of S_1 and S_2 are shown, respectively, in green and red. The remaining time courses are shown in black. The left upper panel represents the initial sources' time courses obtained by setting A to the identity matrix i.e. MxNE solution.

We also show, in the lower left corner, the estimated MAR matrix of only the remaining active sources at convergence, i.e. sources with an l_2-norm greater than zero. Its elements ranges between -1 (dark blue) and +1 (red).

In the case of Figure 5.18, it was reduced from 237 to only 5 sources. Two among those sources, S_1 and S_2, are more active than the others. The estimated MAR matrix is sparse. Only S_1 and S_2 have effective connectivity

between each other. The remaining sources have small diagonal MAR elements. It is worth mentioning that we noticed that the false active sources are not the ones connected to true active sources.

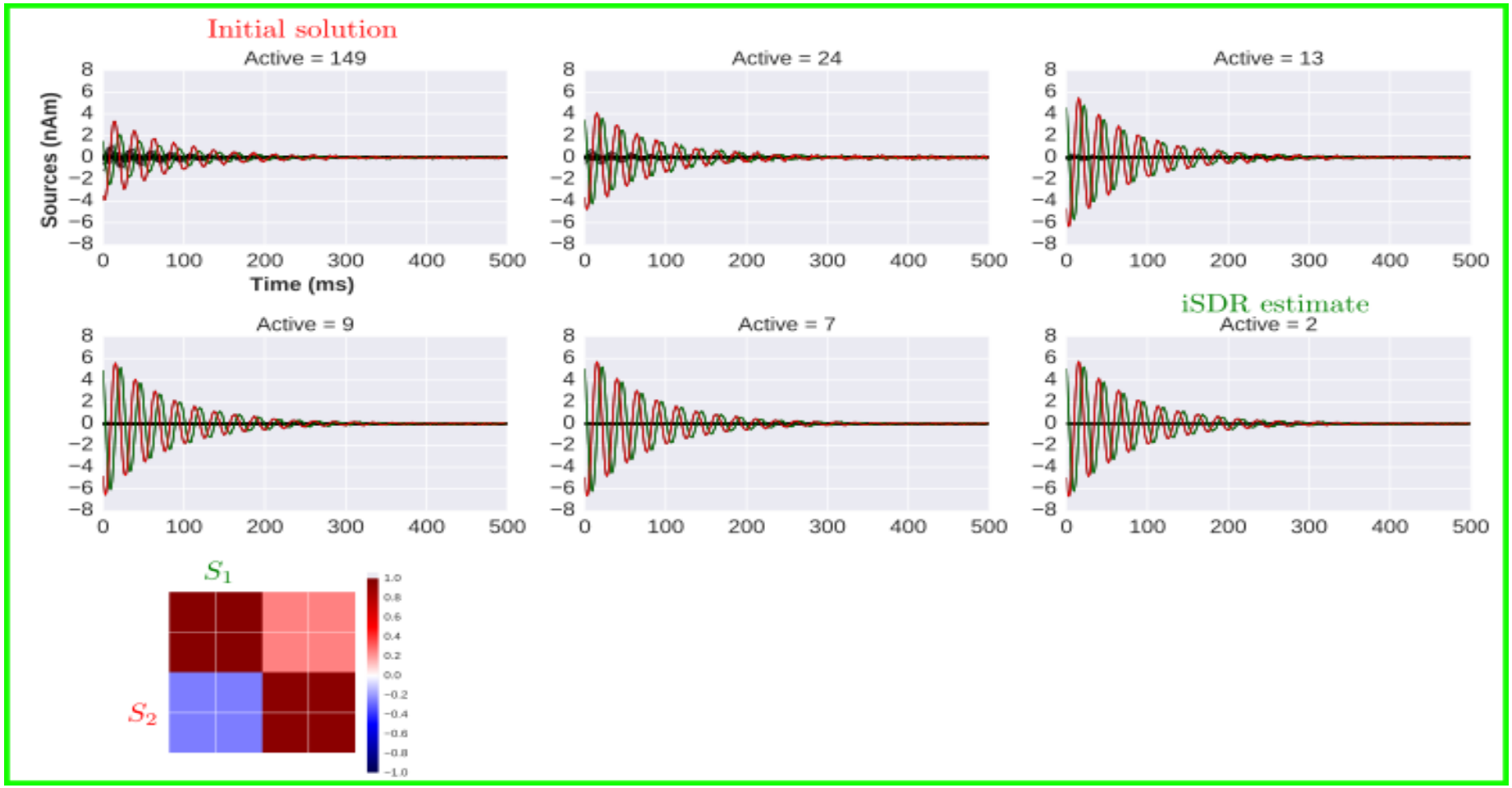

Figure 5.16: ***One result of simulated sources at SNR = 15 dB. We show the reconstructed sources and the number of active sources (sources with l_2-norm > 0) and the resulting MAR elements of only the detected active sources. The initial number of active sources obtained from MxNE is 149. It decreases to 2 sources in the seventh iteration. The green and red color represent, respectively, the time course of S1 and S2. We show the remaining sources in black. In the lower left corner, we show the estimated MAR for only nonzero sources at the last iteration.***

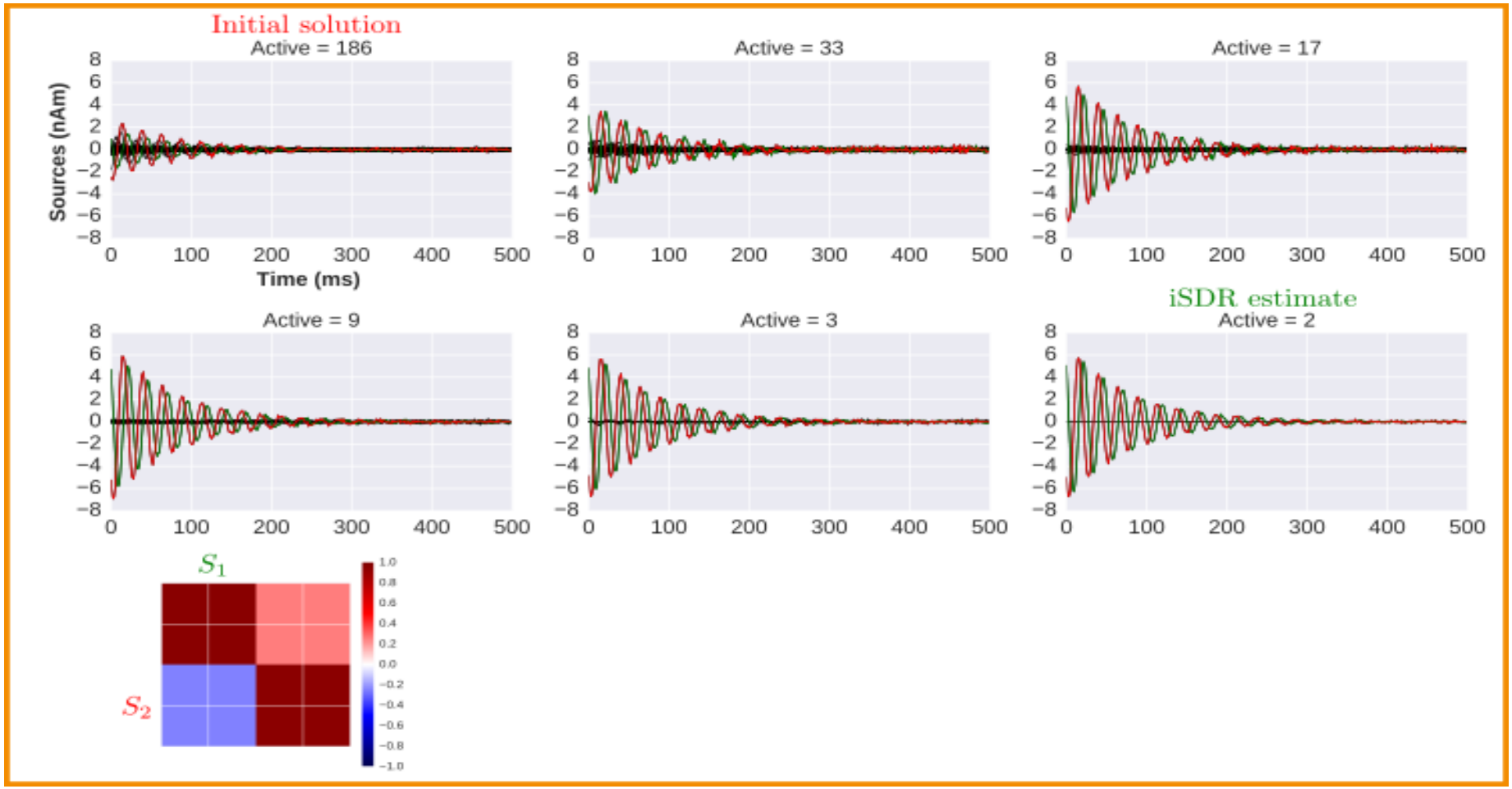

Figure 5.17: ***One result of simulated sources at SNR = 10 dB. We show the reconstructed sources and the number of active sources (sources with l_2-norm > 0) and the resulting MAR elements of only the detected active sources. The initial number of active sources obtained from MxNE is 186. It decreases to 2 sources in the seventh iteration. The green and red color represent, respectively, the time course of S1 and S2. We show the remaining sources in black. In the lower left corner, we show the estimated MAR for only nonzero sources at the last iteration.***

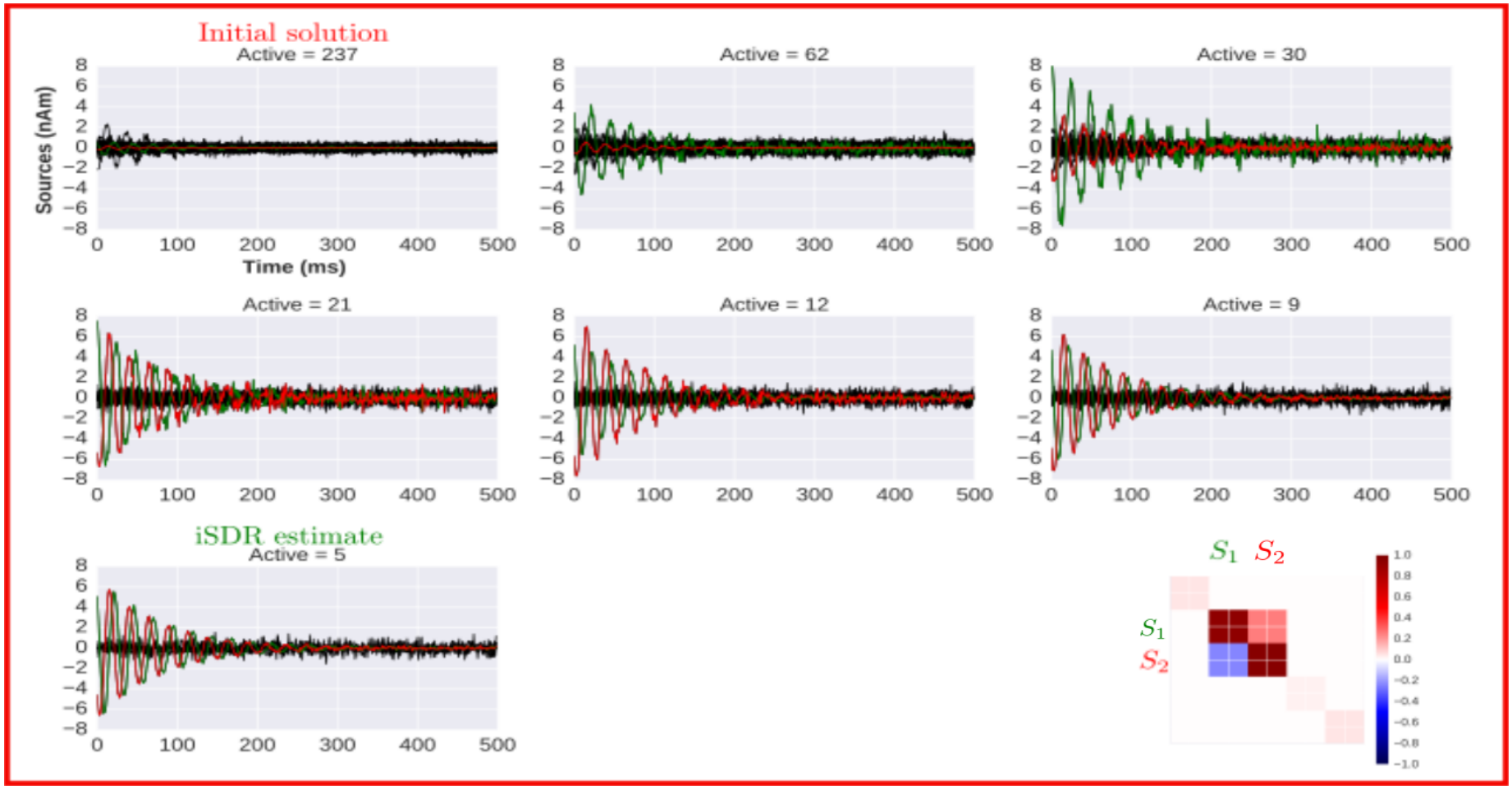

Figure 5.18: ***One result of simulated sources at SNR = 5 dB. We show the reconstructed sources and the number of active sources (sources with l_2-norm > 0) and the resulting MAR elements of only the detected active sources. The initial number of active sources obtained from MxNE is 261. It decreases to 5 sources in the 7^{th} iteration. The green and red color represent, respectively, the time course of S1 and S2. We show the remaining sources in black. In the lower left corner, we show the estimated MAR (5×5 matrix) for the 5 nonzero sources at the last iteration.***

The percentage of simulations in which iSDR did not converge to the right number of active sources for all simulations at the different noise levels is around 14% (the majority is at -5 dB). This is mainly due to initialization and noise.

In conclusion, iSDR could estimate accurately both the sources time courses and their effective connectivity when working in relatively high SNR. In low SNR, iSDR underestimates the effective relation between sources but detects the true active source set (see Figure 5.16 to 5.18). The big advantage of iSDR over MxNE and irMxNE is that the reconstruction of the effective network is possible while estimating the sources' magnitudes.

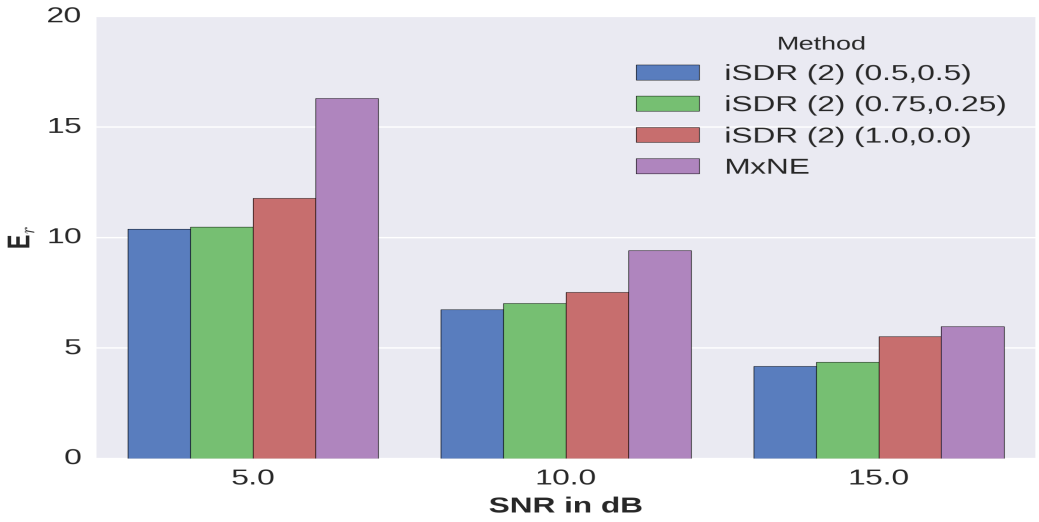

Figure 5.19: ***The mean of reconstruction error of mixed norm estimates and iSDR (with $p = 2$) for the synthetic simulation when considering MAR model of order 2 for different initialization of MAR matrices at three different noise levels.***

5.4.3.2 iSDR with a higher MAR model

The iSDR method solves a non convex problem. It depends strongly on the initial solution of the source activations (i.e. on λ) and on the initial value of autoregressive model (A). It was found that for MAR model of order 1 setting A, initially, to the identity matrix could give an accurate solution for relatively low SNR. The effect of the initial value of A for higher MAR models is investigated in this section.

When using a higher order MAR model, iSDR becomes time consuming. To test our algorithm for higher order, we use a random lead-field matrix whose elements are obtained from a normal distribution $\mathcal{N}(0, 1)$. Each column of the lead field matrix is normalized to 1. We consider 500 point-sources and 20 sensors. Each source was connected randomly to 4 other sources. We activate randomly 50 pairs of sources. For each of them, 100 simulations at different noise levels were generated using the following simple MAR model:

$$\begin{bmatrix} S_1 \\ S_2 \end{bmatrix}_t = \begin{bmatrix} 0.432 & 0.242 \\ -0.241 & 0.427 \end{bmatrix} \times \begin{bmatrix} S_1 \\ S_2 \end{bmatrix}_{t-1} + \begin{bmatrix} 0.476 & 0.122 \\ -0.124 & 0.466 \end{bmatrix} \times \begin{bmatrix} S_1 \\ S_2 \end{bmatrix}_{t-2}$$

with $J_0(S_1) = 6.15$, $J_0(S_2) = -3.64$, $J_1(S_1) = 5$ and $J_1(S_2) = -5$ nA.

Let A_1 and A_2 be the MAR model matrices so that $J_t = A_1 J_{t-1} + A_2 J_{t-2}$. We estimated the sources and their interactions by initializing A_2 and A_1 with different values to have an insight about the effect of the MAR's initialization on the resulting estimate. We use the following combinations: $A_2 = \alpha I$ and $A_1 = \beta I$ with $(\alpha, \beta) \in \{(1.0, 0.0), (0.75, 0.25), (0.5, 0.5)\}$. The number of iterations I and L were set, respectively, to 15 and 8×10^3 iterations, see Algorithm 3. The mean reconstruction error, computed as l_2-norm of the difference between ground truth and reconstructed sources, is shown in Figure 5.19. Only 3% of the iSDR runs fails to detect the true active source set. In Figure 5.20, we show the reconstructed initial values of S_1 and S_2 at different noise levels and initialization of the MAR matrices. The ground truth points, $(-3.64, -5.0)$ and $(6.15, 5)$, are shown in black. An example of the estimated time course for the different α and β values at SNR equal to 5 dB can be seen in Figure 5.21.

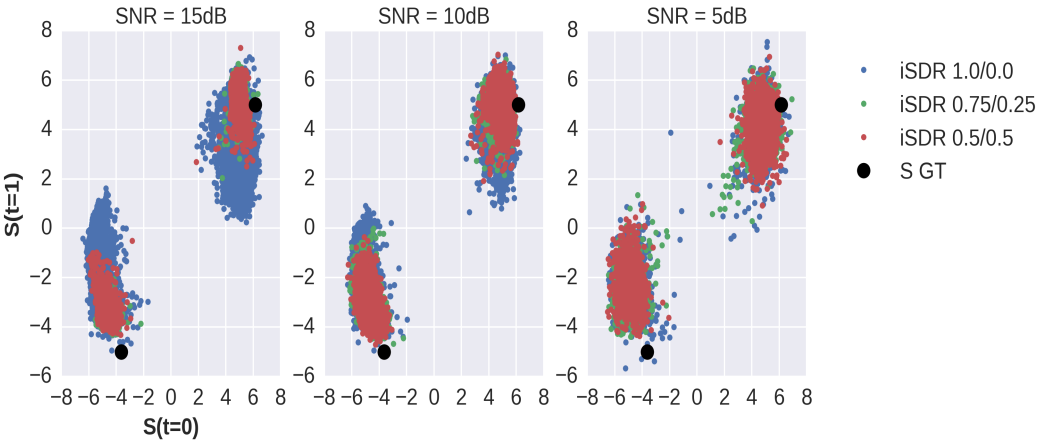

Figure 5.20: ***The values of the reconstructed initial source estimate of S_1 and S_2 (with $p = 2$) for the synthetic simulation when considering MAR model of order 2 at three different noise levels and initialization of iSDR. The ground truth values are shown in black.***

Figure 5.21 (a) (b) (c) represent, respectively, the reconstructed time courses by using iSDR with (α, β) equal to (1.0, 0.0), (0.75, 0.25) and (0.5, 0.5). $(\alpha, \beta) = (1, 0)$, iSDR fails to accurately reconstruct initial value of S_1 and S_2. This is mainly due to the initialization of the spatial correlation matrix of time-lag 2 i.e. A_2 to zero which favors the sources to have small dipole magnitudes (see Figure 5.21 (a)). With (α, β) = (0.5, 0.5), iSDR gives better initial values reconstruction. The source reconstruction is indeed affected by the choice of the initialization of A.

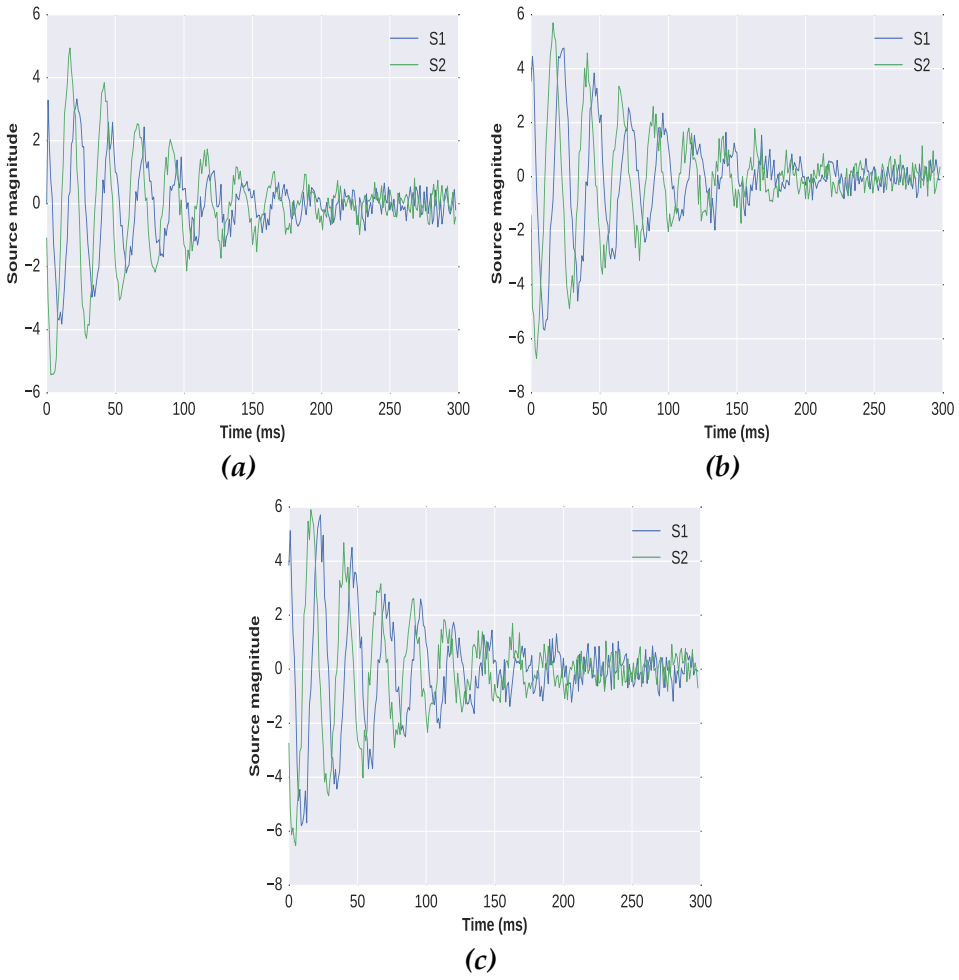

Figure 5.21: ***An example of the time course from iSDR by considering initial values (a) (α, β) = (1.0, 0.0) (b) (α, β) = (0.75, 0.25) and (c) (α, β) = (0.5, 0.5) at SNR equal to 5dB.***

In Figure 5.22, we show the estimated eigenvalues of the companion matrix Φ (see Equation 5.15), obtained from the estimated MAR model at different noise levels and initializations of the MAR matrices. All the estimated eigenvalues of the companion matrix have modulus less than one which means that the estimated MAR models are found to be stable (simulated MAR model is stable). The ground truth eigenvalues are in black and the estimated ones by the different initializations of A are shown in blue, green and blue. Panel correspond to results at the different noise levels (SNR values equal to 15, 10, and 5 dB).

In the three test initializations, iSDR could estimate very accurately the two eigenvalues in the positive plane. The eigenvalues in the negative plane are affected by the choice of the initialization of the A_i's matrices. The more accurate results are the ones correspond to (α, β) = (0.5, 0.5). But other initializations may provide more accurate results.

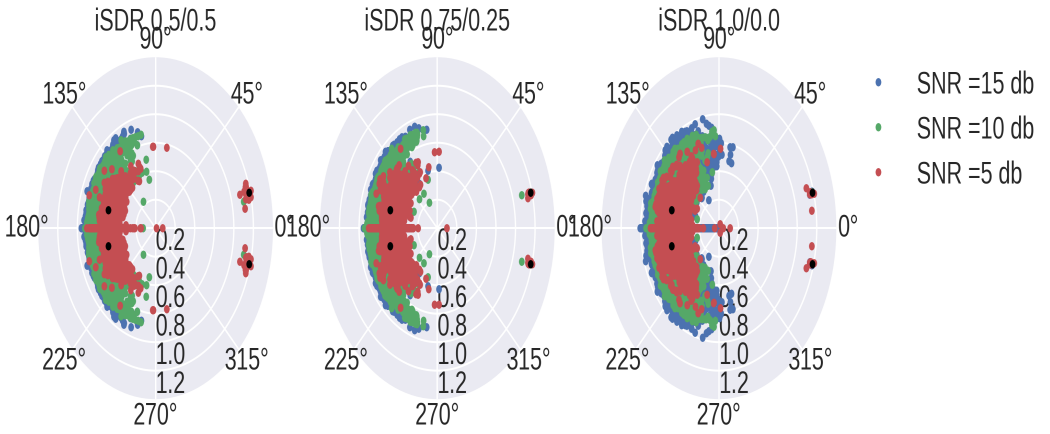

Figure 5.22: ***The values of the reconstructed eigenvalues of the MAR model from iSDR (with*** $p = 2$***) at three different noise levels and initialization of iSDR. The ground truth values are shown in black. From left to right: iSDR with*** $(\alpha, \beta) = (0.5, 0.5)$***,*** $(\alpha, \beta) = (0.75, 0.25)$***,*** $(\alpha, \beta) = (1.0, 0.0)$***. The estimated eigenvalues with positive real part are superposed with the ground truth.***

It is worth mentioning that the iSDR detects effective connectivity between "*connected*" regions if they are both active. The strength of the causality depends on the strength of both activations.

The initialization of A_2 to the identity matrix and $A_1 = 0$ gives good results but favors the reconstruction at time $t = 0$ to be zero because of the causality of the source signals. This is why including the measurements between t equal to 1 and p may increase the accuracy of the iSDR reconstruction.

5.4.3.3 Real data

Literature review

In Figure 5.23, we show the fMRI results from two different works that used the same data as the one we use in our work. Figure 5.23 (a), which is taken from (Wakeman et al., 2015), shows the results of group fMRI analysis, specifically voxels that show greater BOLD responses when using face stimuli compared to scrambled pictures, thresholded at p<0.001 uncorrected. The results are displayed on glass-brain. The group-analysis in this paper shows two distinct regions, fusiform and occipital areas in both hemispheres, plus a cluster in the right posterior, superior temporal cortex. There are other fMRI clusters found in anterior medial temporal lobes and orbitofrontal cortex. Figure 5.23 (b) shows voxels that show a greater BOLD response when using pictures of famous people compared to unfamiliar faces. It shows activation in bilateral temporal poles extending to inferior prefrontal cortex on the left and bilateral medial parietal cortex.

In Figure 5.23 (c), we show the group-averaged fMRI t-value maps with the contrast of faces stimulus against a baseline. This result is taken from (Fukushima et al., 2015). This result shows activation in ventral occipital gyrus (IOG) and fusiform area in both hemispheres like in 5.23 (a). It shows

also a small activation in parietal and frontal lobes. Because we use the measurement of famous subtracted to scrambled faces, we expect to find all of the regions, listed earlier, to be active.

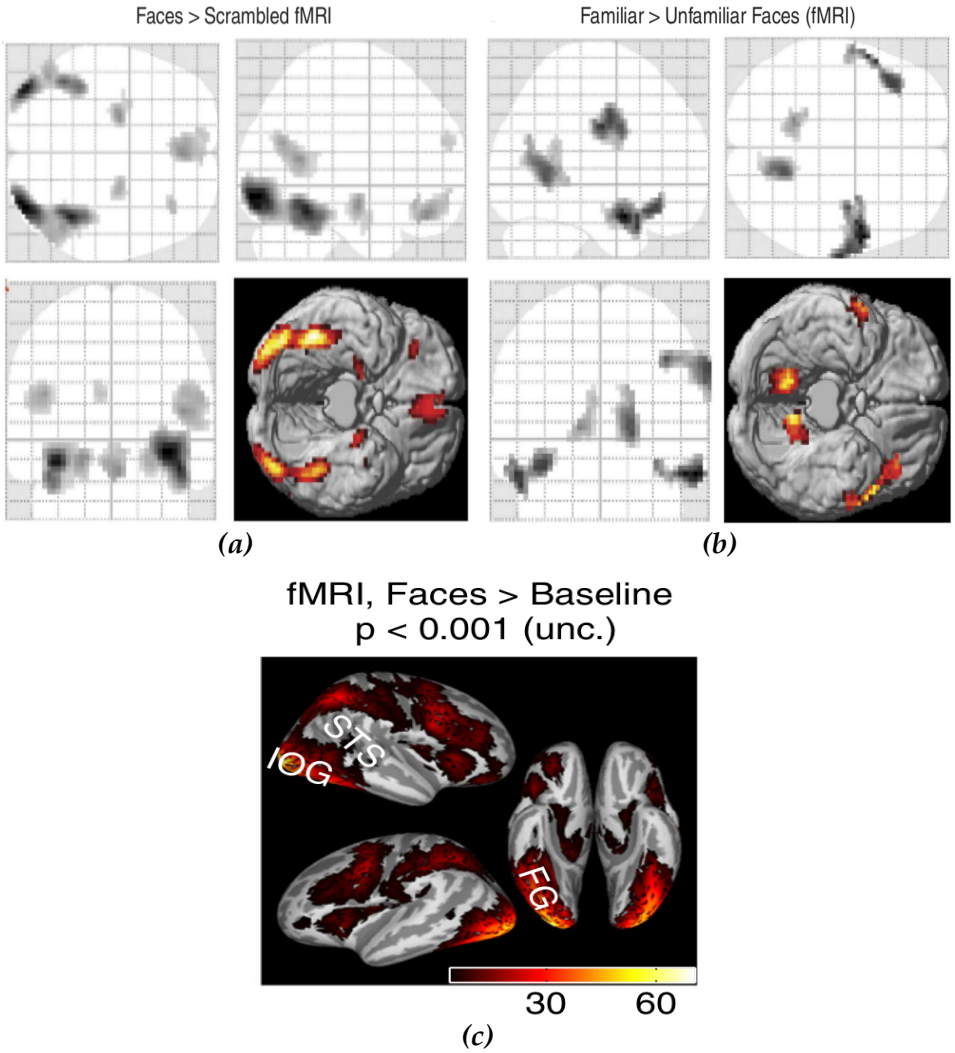

Figure 5.23: ***Sub-figure (a) and (b) show, respectively, where faces produced greater BOLD response than scrambled faces using a statistical test on fMRI data (p<0.001 uncorrected) and famous vs scrambled faces (Wakeman et al., 2015). In (c), we show the group-averaged fMRI t-value maps with a contrast of face stimulus conditions against the baseline (Fukushima et al., 2015).***

In (Bukowski et al., 2013), the authors show that subjects may have right or bilateral FF activation if they are right or left handed respectively. This may explain the results in Figure 5.23 in which, in average through the subjects, bilateral inferior activation was noticed. Unfortunately, the information weather subjects are left or right handed is not available.

In Figure 5.24, we show the result of the same subjects and MEG data from (Fukushima et al., 2015). They use a dynamic hierarchical variational Bayesian (dhVB) method to estimate the sources and their interactions.

Green arrows represent bidirectional interactions, while yellow arrows represent unidirectional interactions. This method fails to detect superior temporal regions which the authors claim to be hard to detect using the MEG data. Also, it failed to detect orbitofrontal activation as reported by the fMRI study in (Wakeman et al., 2015). The dhVB could mainly detect activations in the ventral temporal gyrus and some of the temporal poles.

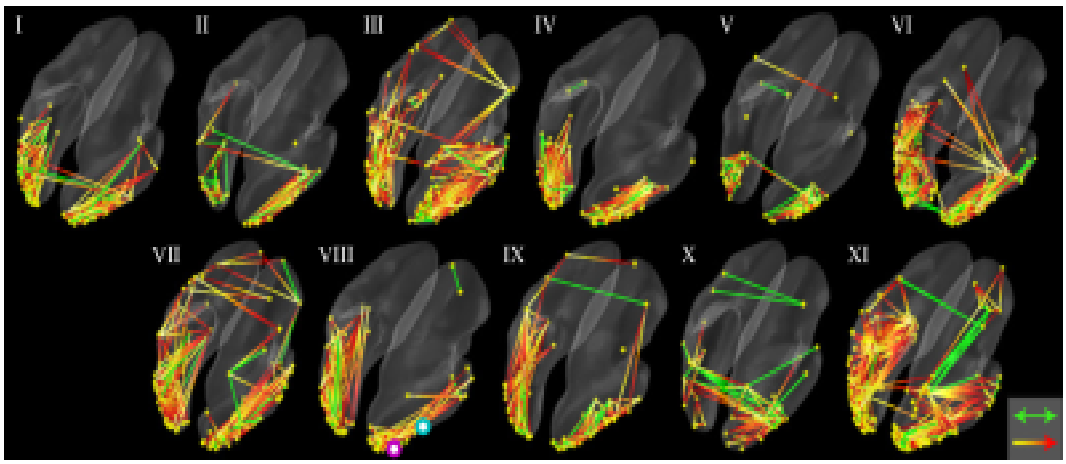

Figure 5.24: ***The effective network obtained from real data (Wakeman et al., 2015) using dhVB (Fukushima et al., 2015) for the 11 subjects.***

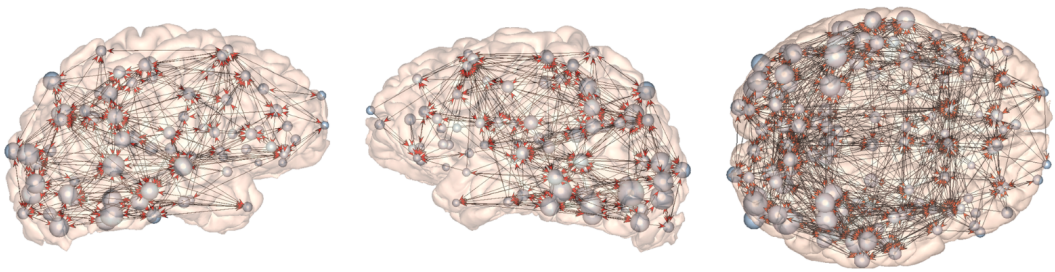

Figure 5.25: ***Different views of the functionally relevant structural network that predicts fMRI signal for face recognition task. Nodes reflect parcels and edges are anatomical connections that are significant predictors of fMRI data. The node's size are scaled with its task selectivity, large spheres represent parcels with higher face selectivity. (adopted from Osher et al., 2016)***

In Osher et al., 2016, the authors showed that the anatomical connectivity of cortical regions alone can predict fMRI responses to 4 visual categories (faces, objects, scenes, and bodies) in individual subjects. They used a linear model between the fMRI signals and brain structural connectivity. Their linear model is written as:

$$M = SCf\,, \tag{5.36}$$

where M is the fMRI signals at each voxel, SC is the cortical structural connectivity matrix between brain regions and f is a selective vector which

depends on the performed task. A linear regression model was used to estimate the selective vector f for each visual stimulus. In Figure 5.25, we show the result that they obtained for face stimulus. Each node represents a cortical patch and edges represent anatomical connections that were found to have a significant prediction of the fMRI data. The node's size reflects selectivity. Large spheres represent parcels with a significant contribution to fMRI data during face stimulus. Confirming what was found and listed earlier, the regions that have a significant contribution to the fMRI data during face stimulus are the ones located in the inferior occipital-temporal gyrus and superior temporal gyrus in both hemispheres. Also, regions in the lateral parietal lobe, in both hemispheres which were not detected in the two works mentioned earlier, are found to have relatively high contribution to fMRI signal prediction. Regions in the frontal and orbitofrontal are found to have a small contribution to the prediction of fMRI data.

5.4.3.4 iSDR results

We test iSDR algorithm with the same real data as in section 5.3.1.2. We consider MAR model of order 1 and 2. After parcellating the cortical surface and using the masks defined in section 5.4.1, we obtained on average, across subjects, 9.46% of possible nonzero elements in the MAR model.

MAR model of order 1

We now consider MAR model of order one and reconstruct the source activation of seven different participants that have a high number of anatomical connections detected by dMRI and probabilistic tractography. We noticed that by considering around 70 active regions, we could explain the MEG/EEG measurements across the different subjects (i.e. iSDR (p = 1) need more than 70 regions to explain EEG/MEG data for this specific mental task). To compare the results of iSDR and MxNE, we set the regularization parameter λ in such a way to obtain approximately the same number of active regions in both reconstructions while maintaining the data fit term (measurement residual) as low as possible. In Figure 5.26 and 5.27, we show the normalized by the highest source energy activations obtained by iSDR and MxNE of subject 1 and 2 for approximately the same number of regions after magnitude bias correction (see section 5.4.2).

Even though both reconstruction algorithms gave the same number of regions for subject 1 and only one region difference for subject 2, they detected some different regions (some of these differences are shown in circles in Figure 5.26 and 5.27). This is more pronounced in the parietal and frontal lobe. Both algorithms could detect regions in the ventral temporal and occipital gyrus. But they are found to be more active for iSDR. This is also true for regions in the temporal poles, orbitofrontal, and posterior superior temporal gyrus. For subject 2 and in contrast to MxNE, iSDR could detect a region close to the orbitofrontal and more regions in the left temporal lobe. This difference in the reconstructions between iSDR and MxNE shows a difference in the regions' selection between the two algorithms.

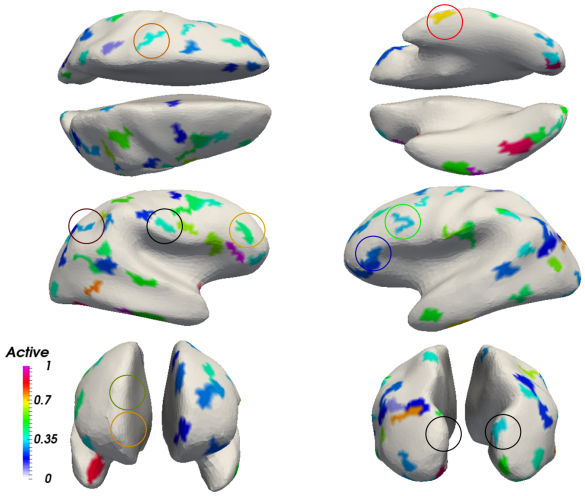

(a)

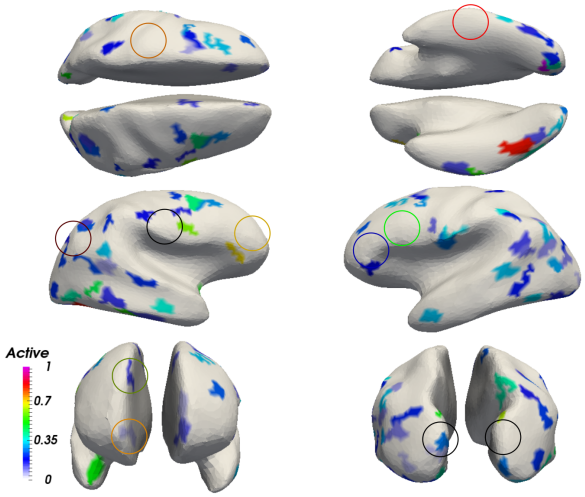

(b)

Figure 5.26: ***Activation strength, after bias correction, of the obtained regions using (a) iSDR with*** $p = 1$ ***and (b) MxNE for subject 1. There are 70 active regions in both reconstructions. Some of the noticeable differences between iSDR and MxNE reconstructions are shown in circles.***

The results of effective connectivity matrix for subject 1, 2, 3, 12, 13 and 15 are shown in Figure 5.28, 5.29, 5.30, 5.31, 5.32 and 5.33, respectively. Dots and edges represent, respectively, the center of active regions and uni/bidirectional interactions between the active regions.

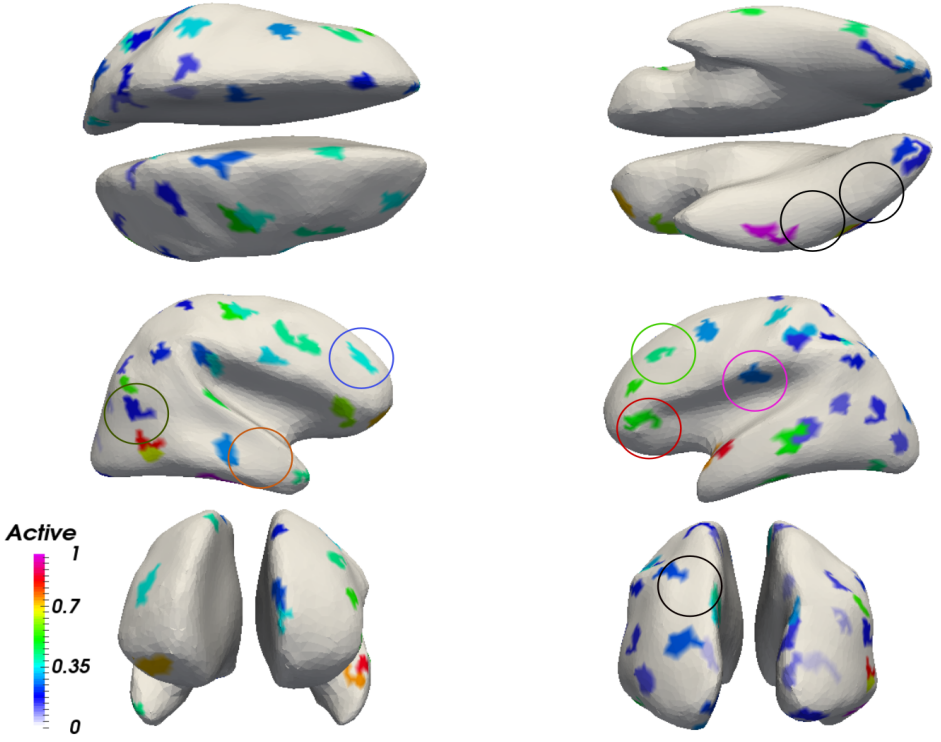

(a)

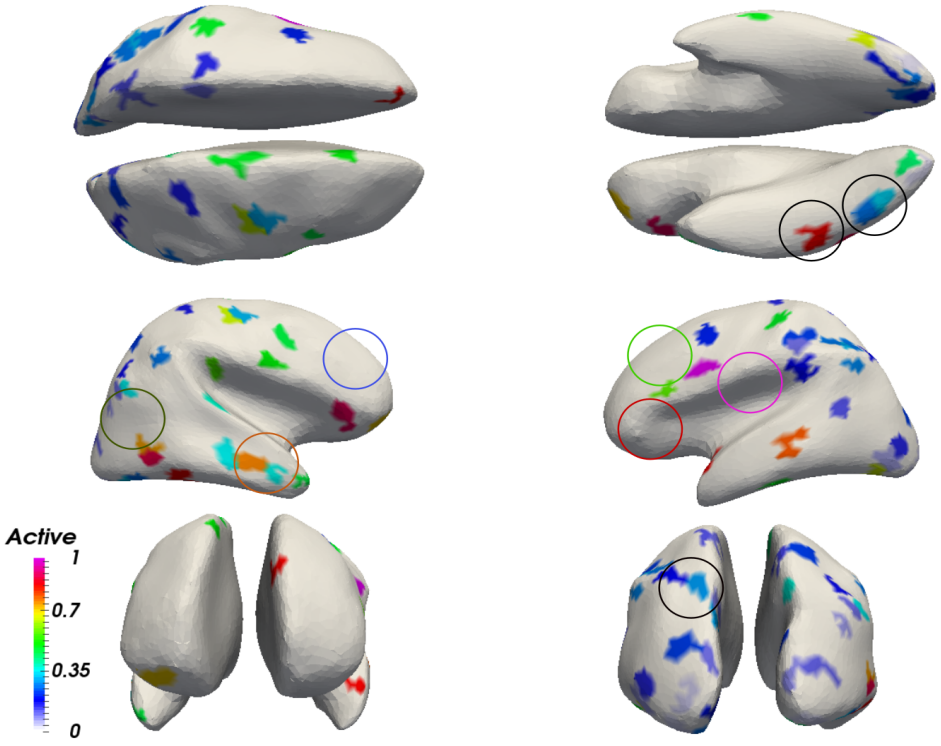

(b)

Figure 5.27: ***The activation strength, after bias correction, of the obtained regions using (a) iSDR with $p = 1$ and (b) MxNE for subject 2. 69 and 70 regions for iSDR and MxNE respectively. Some of the noticeable differences between iSDR and MxNE reconstructions are shown in circles.***

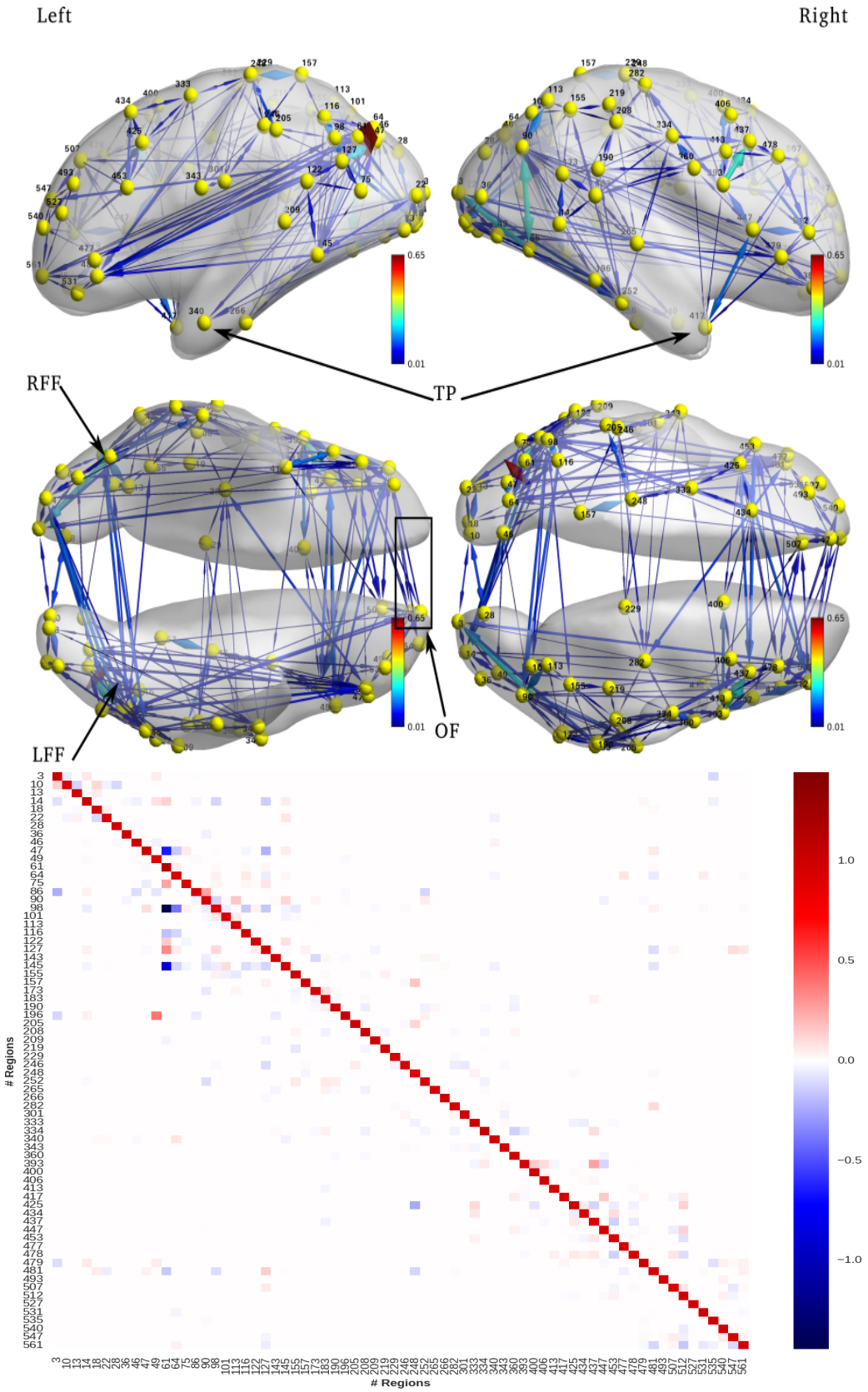

Figure 5.28: ***Effective network of subject 1 during face recognition and perception. Each node represents a parcel. The size of each uni/bi-directed edge represents the mean of the absolute value of the effective connectivity of one or both directions. 70 regions were found to be active.***

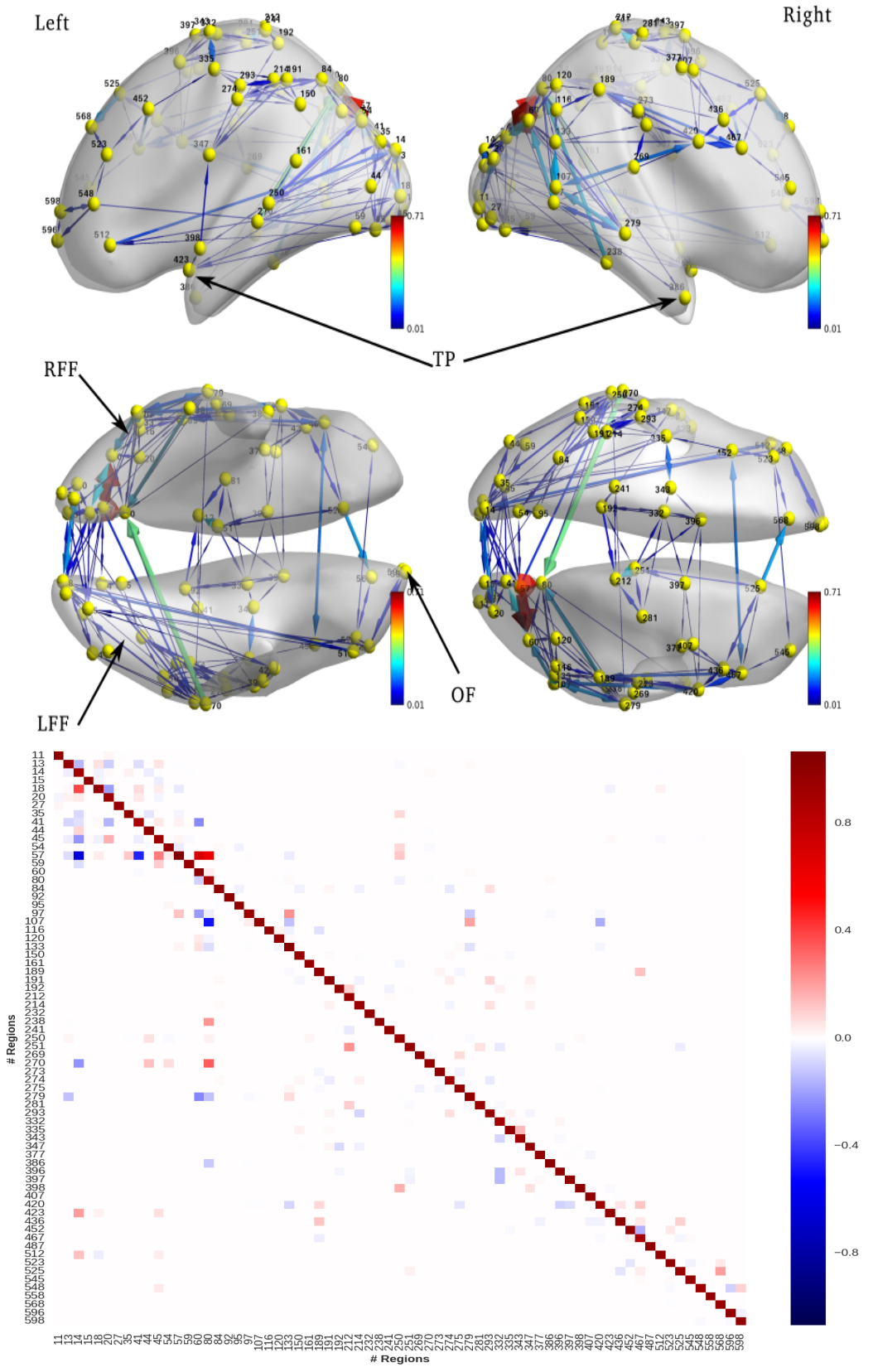

Figure 5.29: ***Effective network of subject 2 during face recognition and perception. Each node represents a parcel. The size of each directed edge represents the mean of the absolute value of the effective connectivity of both directions. 69 regions were found to be active after 7 iterations.***

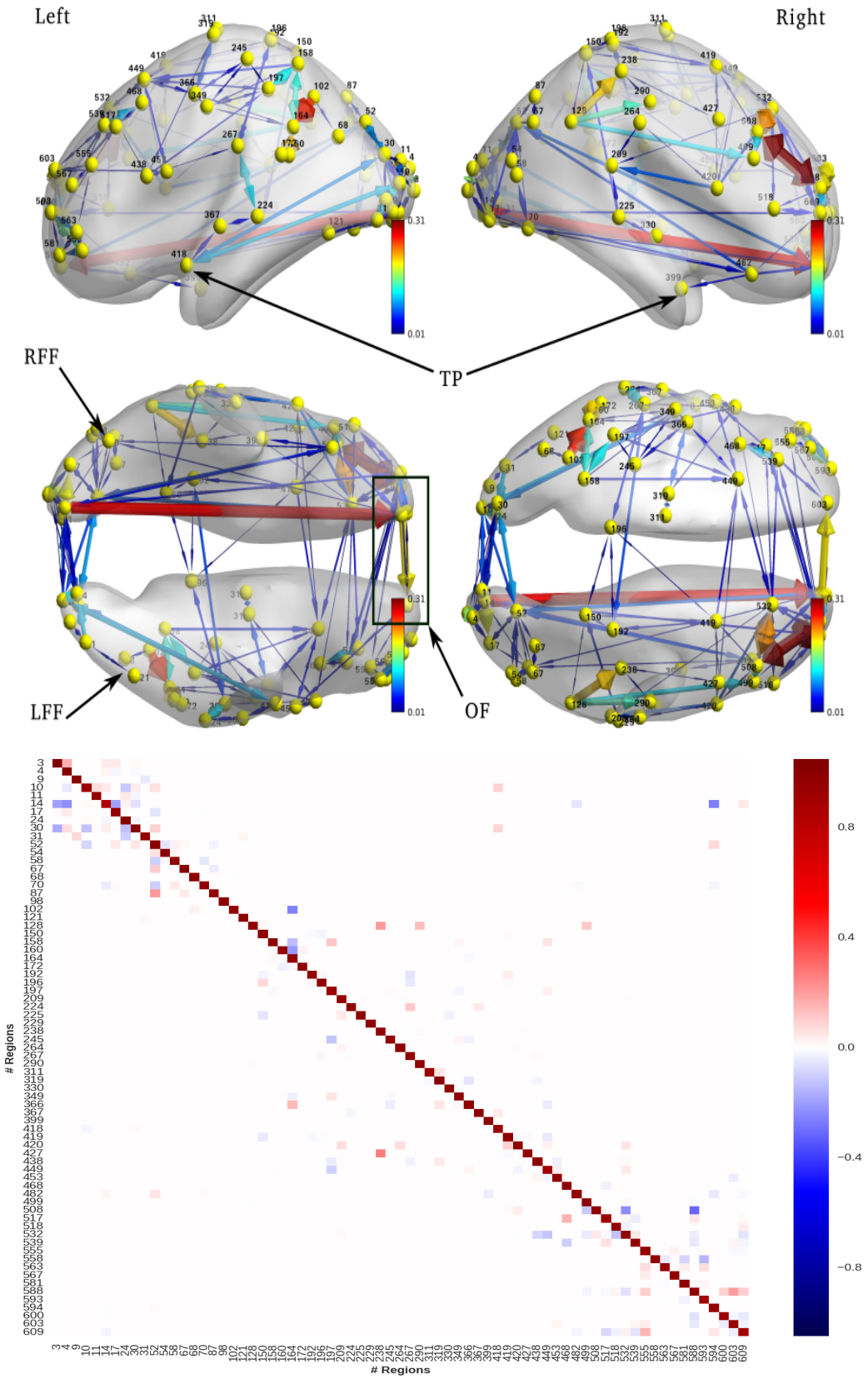

Figure 5.30: ***Effective network of subject 3 during face recognition and perception. Each node represents a parcel. The size of each directed edge represents the mean of the absolute value of the effective connectivity of both directions. 71 regions were found to be active after 5 iterations.***

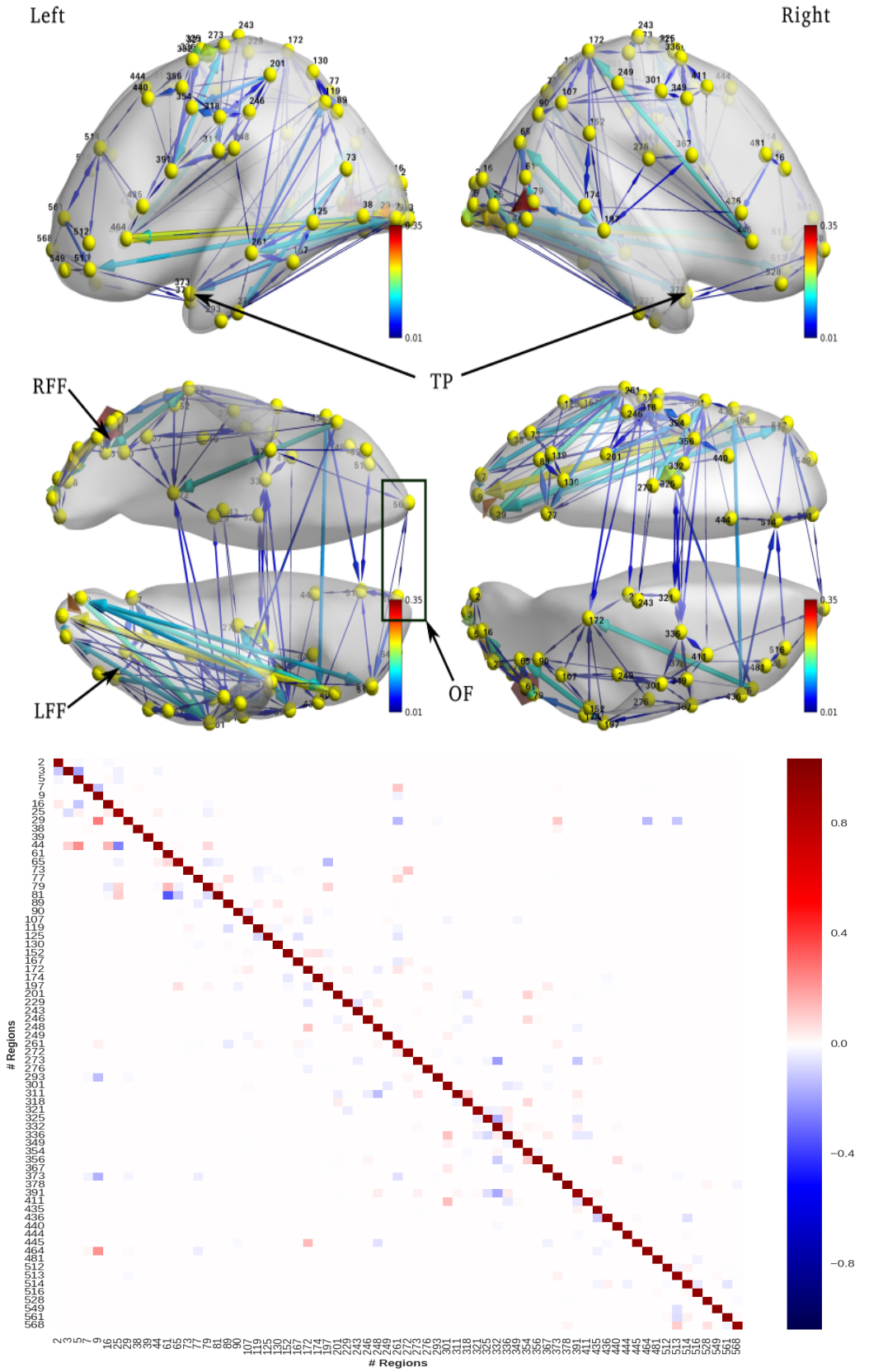

Figure 5.31: ***Effective network of subject 12 during face recognition and perception. Each node represents a parcel. The size of each directed edge represents the mean of the absolute value of the effective connectivity of both directions. 69 regions were found to be activated after 8 iterations.***

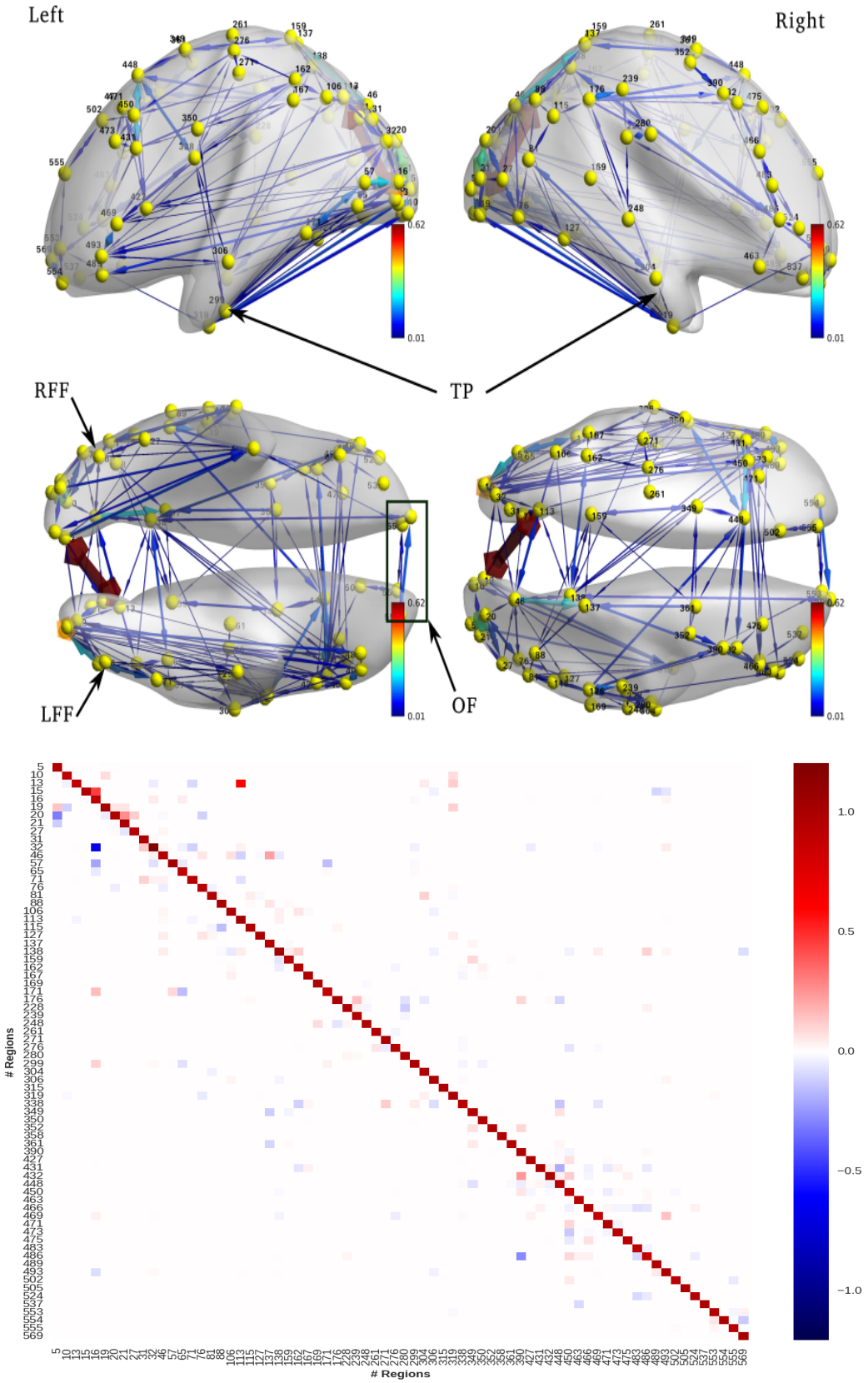

Figure 5.32: ***Effective network of subject 13 during face recognition and perception. Each node represents a parcel. The size of each directed edge represents the mean of the absolute value of the effective connectivity of both directions. 72 regions were found to be active after 4 iterations.***

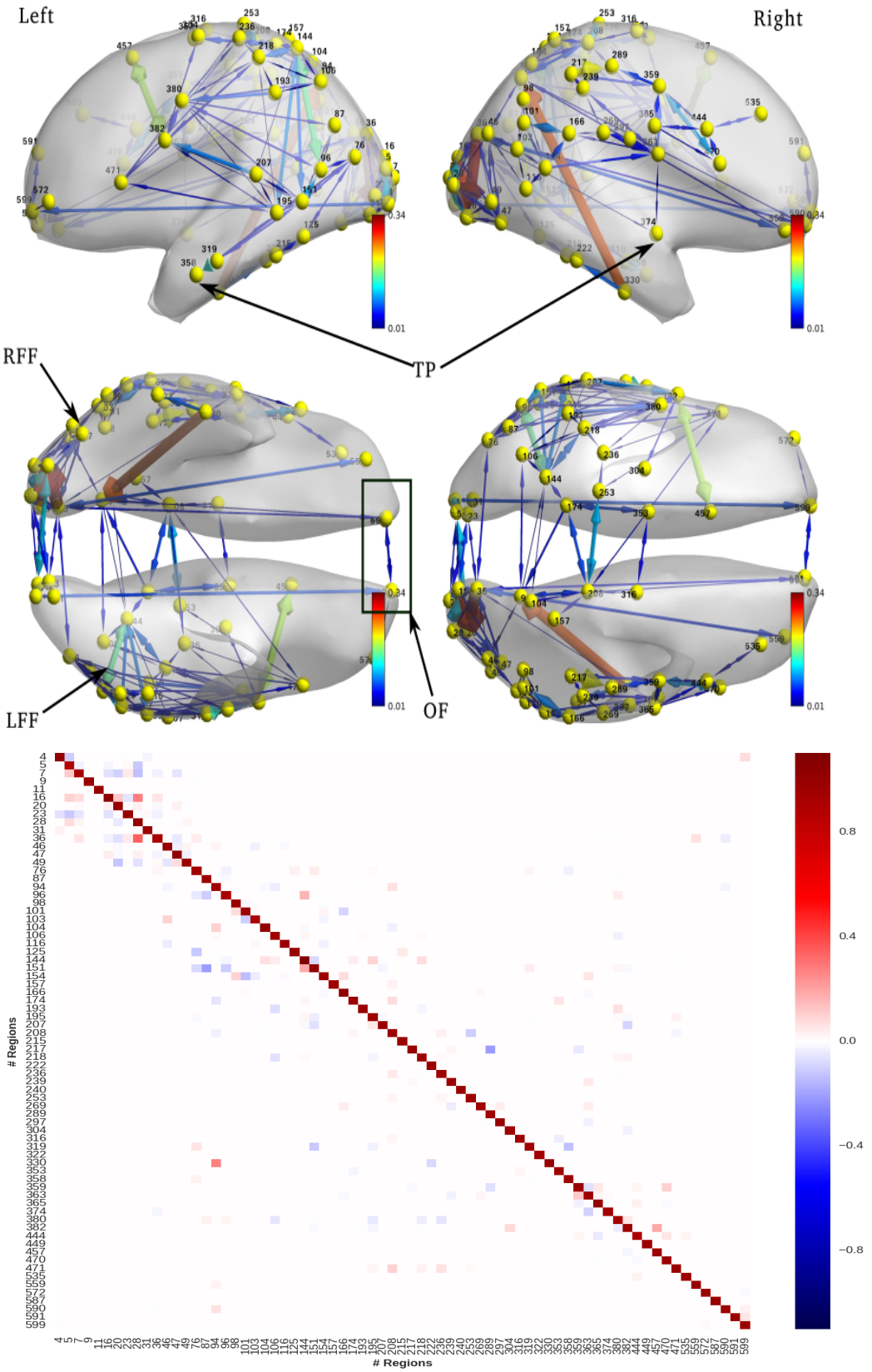

Figure 5.33: ***Effective network of subject 15 during face recognition and perception. Each node represents a parcel. The size of each directed edge represents the mean of the absolute value of the effective connectivity of both directions. 71 regions were found to be active after 4 iterations.***

It was observed that active regions, obtained with iSDR, coincide with those reported in other works. Less than 8 iterations were sufficient for iSDR to converge to a solution. It is hard to confirm whether the obtained interactions are correct or not.

By contrast to dhVB, iSDR could detect activations in the inferior, superior temporal gyrus and temporal poles for the different subjects. We found interaction between the frontal and the temporal poles, which are regions that are activated when recognizing familiar faces. Also, regions in medial parietal cortex are found to be active in all subjects. This coincides with what was reported in earlier studies (Wakeman et al., 2015). Subject 1 has the highest number of anatomical connections, this is why its effective network is the most complex among all subjects.

MAR model of order 2

MEG data

In Figure 5.34, we show the detected active regions when using iSDR of order 2 for Subject 1 shown on the inflated surface and example of time courses of three regions. These results are obtained from MEG data. The time course of a region in the orbitofrontal (OF), right fusiform area (RFF) and medial occipital (MO) are shown, respectively, in red, black and blue. The number of active regions is 55 regions (different λ) which are less than the size of active regions set of the same subject when using order 1. This is due to adding more degree of freedom to the model by adding another time lag which allows the model to improve the estimation of more complex time courses. This makes it possible to reduce the number of active regions while keeping data fit term low.

When comparing Figure 5.34 with 5.26 (a), we can see that iSDR ($p = 2$) detected fewer regions in the parietal, frontal and temporal lobes compared to the ones reconstructed by iSDR($p = 1$). But, it kept the regions in the temporal poles, orbitofrontal and in the inferior temporal-occipital gyrus.

In (Halgren et al., 2000), the authors show that MO has a negative peak ($\approx$ -5nA) just before 200 ms and a positive peak ($\approx$ 15nA) between 200 and 300 ms when using face stimuli. This coincides with our result (see the blue signal in the bottom of Figure 5.34). Several works suggested that the RFF is more engaged in face identification than the left fusiform gyrus and it has a peak of activation at around 170 ms after face stimuli (Hadjikhani et al., 2009; Ma et al., 2012). This is the case in our findings. The time course of RFF has a peak at 178 ms (for Subject 1). The time courses of RFF obtained by iSDR ($p = 2$) and sWMNE of Subject 1 have similar waveform, see Figure 5.6 (a) and bottom panel of 5.34 which may suggest that iSDR($p = 2$) could reconstruct the correct dynamics when performing a face recognition task.

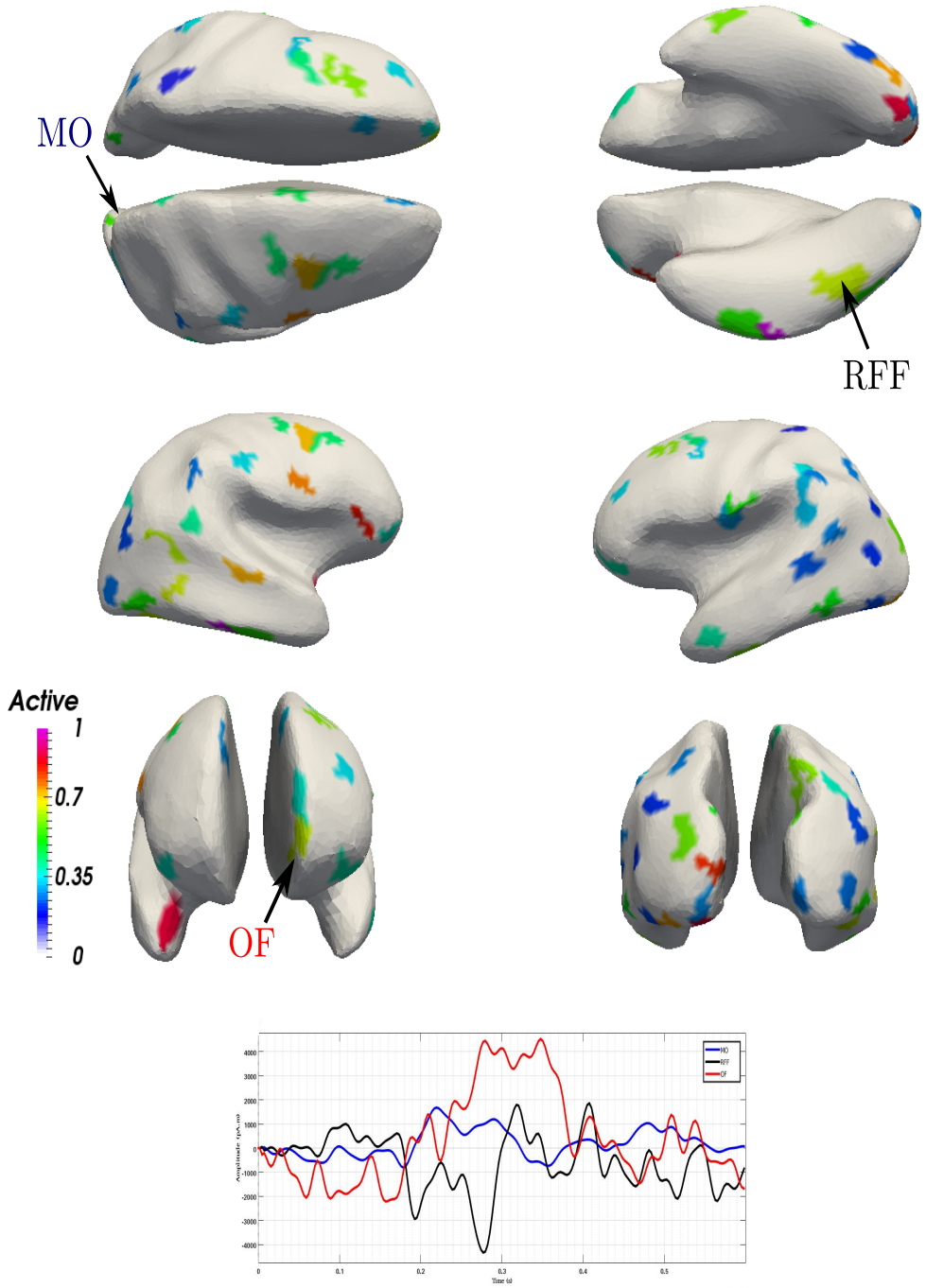

Figure 5.34: ***The active regions of participant 1 using iSDR of order 2 shown on the inflated surface. We show three-time courses of medial occipital (MO) (in blue), right fusiform area (RFF) (in black), and a region in the orbitofrontal area (OF) (in red).***

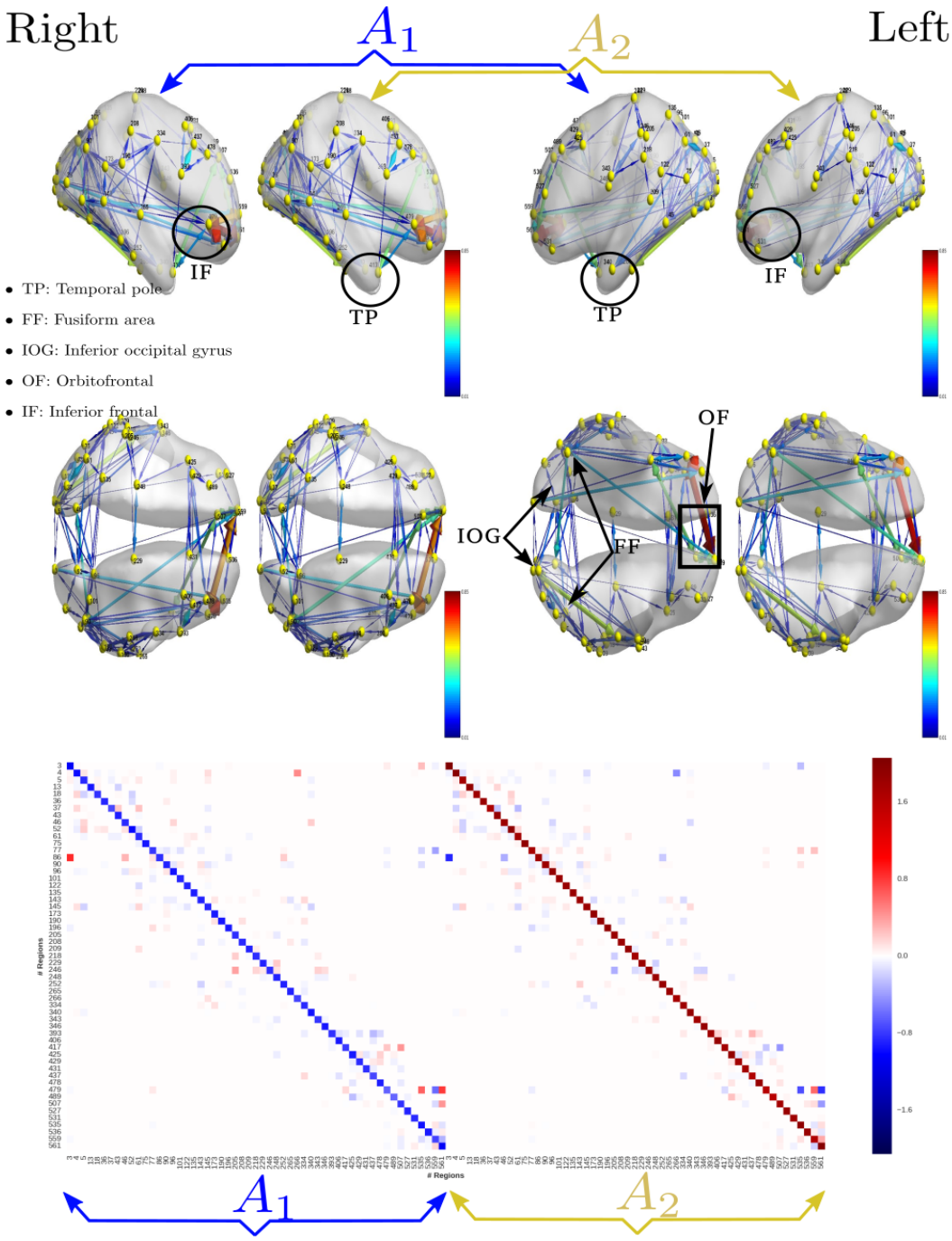

Figure 5.35: ***The effective connectivity between the different active regions (55 patches) of subject 1 obtained by iSDR with order 2 from MEG data. The highest eigenvalue of the companion matrix is 1 which means that there are nonstationary source signals.***

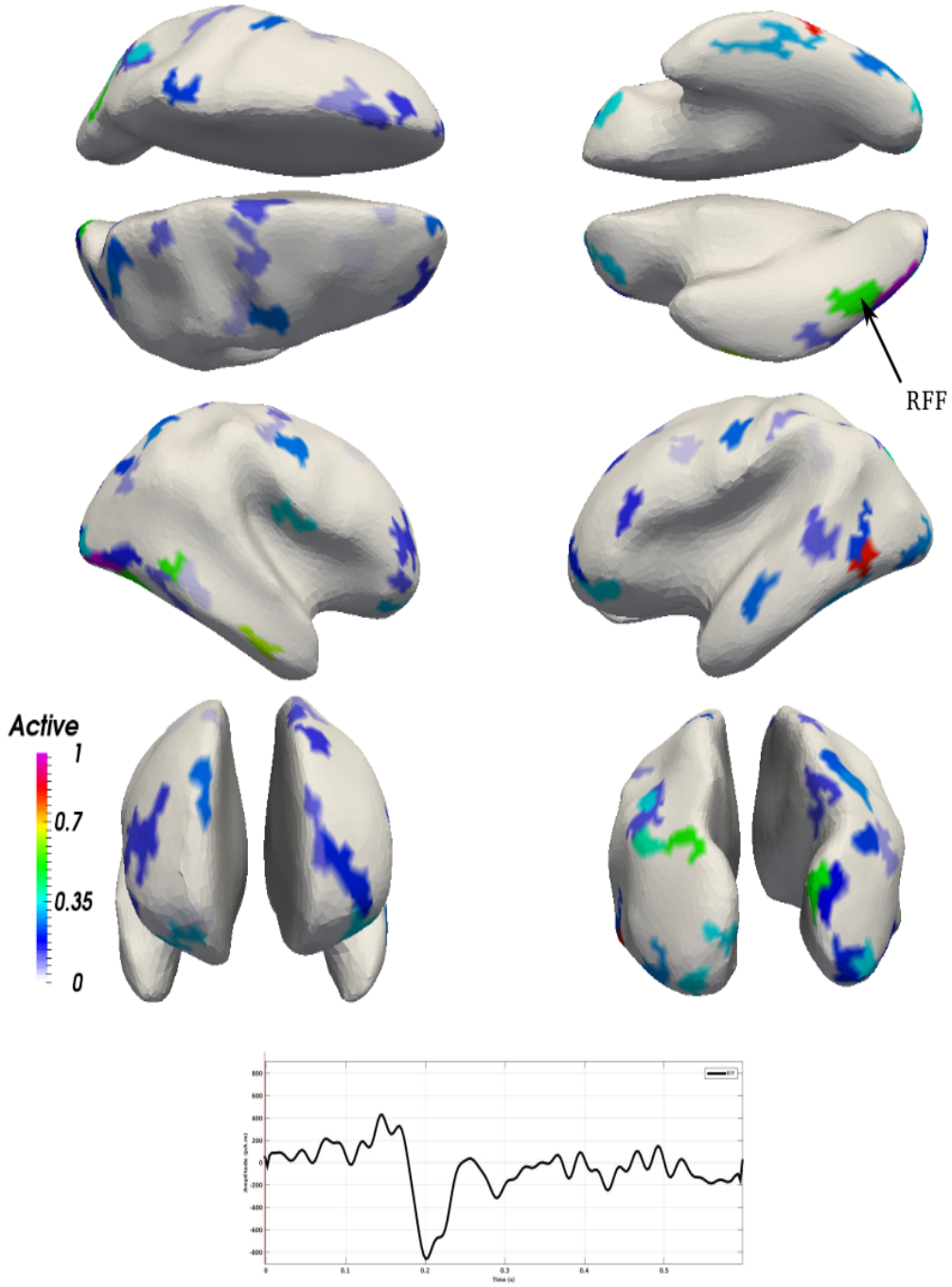

Figure 5.36: ***The active regions of participant 1 using iSDR of order 2 shown on the inflated surface obtained from EEG data. We observe a negative peak around 200 ms in RFF.***

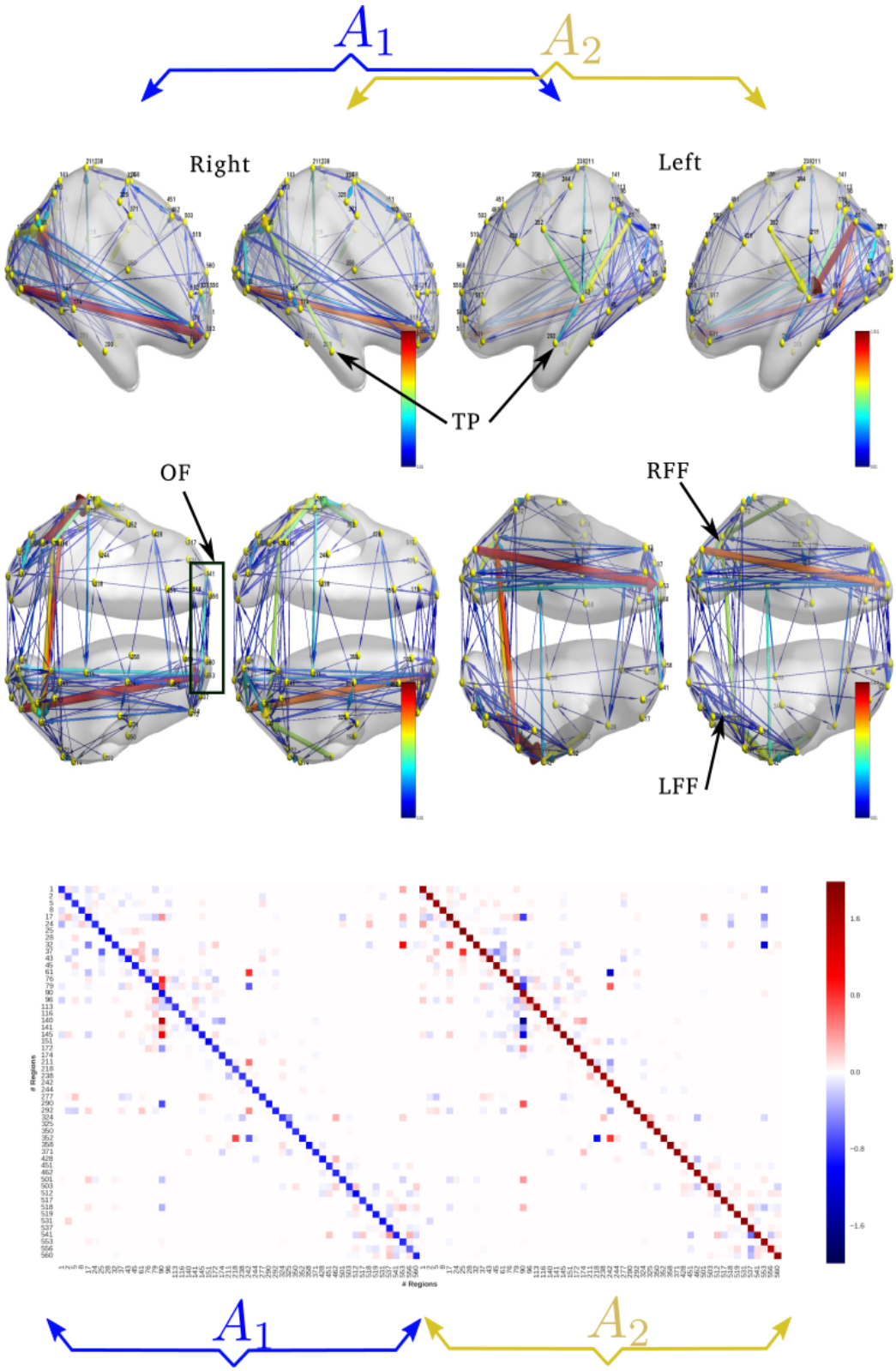

Figure 5.37: ***The effective connectivity between the different active regions (53 patches) of subject 1 obtained by iSDR with order 2 from EEG data. The highest eigenvalue of the companion matrix is 1 which means that there are nonstationary source signals.***

Figure 5.35 shows the effective connectivity network of Subject 1 obtained by iSDR ($p = 2$). High effective interactions are obtained between the RFF and right inferior frontal lobe (RIF), RFF with orbitofrontal (OF), RIF with OF, and between right/left inferior occipital gyrus (R/LIO). All are responsible of face perception and recognition. These interactions were also detected, with lower values, by iSDR ($p = 1$). In our work, we considered the possible nonzero elements in A_1 is the same as in A_2 which makes it highly probable if $A_1(i, j)$ is nonzero to have also a nonzero element in $A_2(i, j)$. The strength of the effective connectivity in both matrices depends on the source signals.

EEG data

Figure 5.36 shows the detected active regions using iSDR($p = 2$) from EEG data. Like with MEG data, iSDR could detect RFF and medial parietal activation. But it failed to detect orbitofrontal, temporal poles and right posterior superior temporal active regions mainly due to the poor spatial resolution of EEG. In the same figure, we show the time course of the RFF obtained from EEG. This region shows a significant activation at around 200 ms after the stimulus which coincides with what was obtained earlier from MEG by iSDR and sWMNE.

Figure 5.37 shows the effective connectivity between the active regions shown in Figure 5.36. The center of active regions in Figure 5.36 are shown in yellow dot in Figure 5.37. Effective connections that are found from both imaging modalities (EEG/MEG):

- High interaction between the right inferior temporal gyrus and right frontal lobe.
- Low interactions between regions in the medial occipital regions.
- High interactions between right and left parietal regions.
- Relatively high interactions between the left and right frontal lobe.
- High interactions between the inferior temporal gyrus and parietal lobe.

Unlike when using MEG, iSDR ($p = 2$) failed to detect interactions between the right temporal pole and the right frontal lobe when using EEG. This maybe because it did not detect active temporal pole, but it activated a closer region which did not have an anatomical pathway to the right frontal lobe.

We have found that six subjects show higher activation in the right FF. Only two subjects (3 and 12) show more activation in the left FF compared to the right FF. For visualization purposes, we show in Figure 5.38 (a) and (b) the temporal courses of a right and a left FF area reconstructed from MEG data and iSDR ($p = 2$). The curves are normalized by their l_2 norms for multi-subject comparison. The same thing is shown in Figure 5.38 (c) and (d) except we use EEG data and iSDR ($p = 2$). To validate this finding a large number of left and right-handed subjects must be used.

Differences between EEG and MEG

Figure 5.38 (e) represents the average over subjects of the temporal curves reconstructed from MEG and EEG for right and left FF activation. When averaging, the right FF reconstruction from MEG is consistent with the one obtained from EEG with a slight difference between 200 and 300 ms, see left panel of Figure 5.38 (e). A more noticeable difference is observed for left FF activation because the average was computed only with two subjects (3 and 12) which makes it more sensitive to reconstruction error.

Where does the difference between EEG and MEG reconstruction come from?

The first reason is the source dipole orientation. MEG is insensitive to radial dipoles whereas EEG is sensitive to both radial and tangential dipoles (see section 1.4.2.3). This may results to a difference in the source reconstructions. The same RFF/LFF regions were reconstructed using EEG or MEG in four different subjects. For the remaining subjects, EEG detected RFF/LFF region that are close to the ones reconstructed by MEG. As was stated earlier, different initialization values of A_i's and λ may result to different reconstructions hence different MAR models. In all real data reconstructions, we initialized (A_1, A_2) by $(0, I)$, but different λ values are needed for the two functional imaging modalities (EEG/MEG) because they do have different nature and different number of electrodes. Because a MAR model plays the role of a source filter, we expect to have differences in the temporal reconstruction when using EEG or MEG.

Summary

All subjects show higher activation in either a right of a left FF area, which is an area that intervenes in face recognition, between 170 and 200 ms after the stimuli. This coincide with what was reported in several studies.

It was observed that fewer regions were sufficient to explain EEG/MEG when using iSDR($p = 2$) compared to iSDR($p = 1$). This is due to using higher MAR model which allows iSDR to explain more complex time courses with fewer active regions. An example of MEG/EEG measurements and the explained data can be seen in Figure 5.39. Source debiasing was only applied to the MEG data because the number of reconstructed active regions with EEG data is close to the number of EEG electrodes (≈ 70) which was found to explain well the EEG data. As stated before in section 5.4.3.2, by initializing A_1 to zero, iSDR($p = 2$) favors the sources to have dipole magnitudes close to zero hence a bigger data fit between $0 < t < 2\delta$ (δ is sampling time). After $t > 2\delta$, iSDR($p = 2$) could explain, accurately, both EEG and MEG.

Applying our method to real EEG/MEG data collected during a face perception and recognition task, we obtained physiologically plausible estimates that were appropriately consistent among subjects.

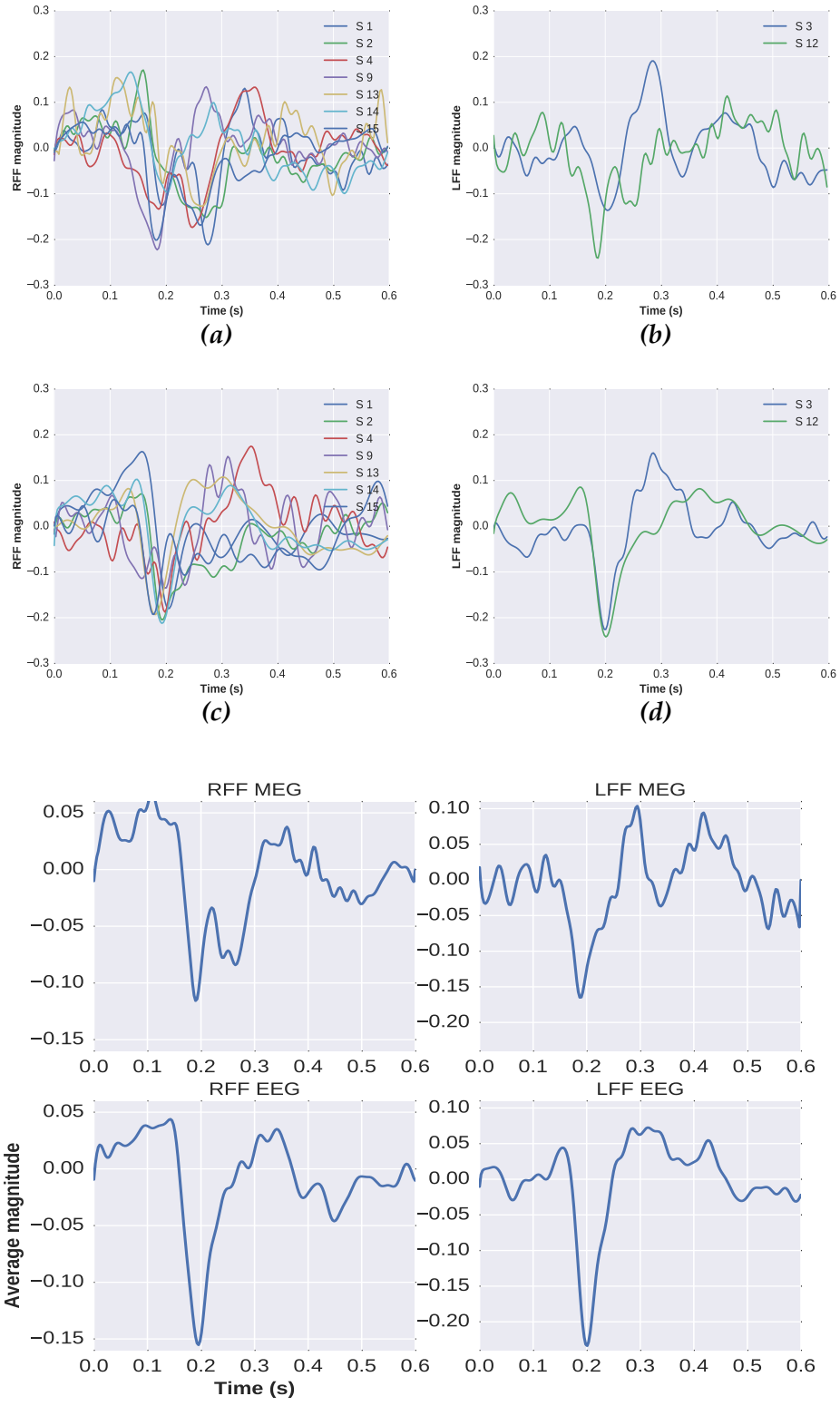

Figure 5.38: ***The temporal course obtained by iSDR ($p = 2$) from MEG of a right FF area (a) and a left FF (b). In (c) and (d), we show the temporal course of a right FF and left FF region respectively. Each curve is normalized with its l_2-norm for comparison between the 9 subjects. In (d), we show the average, over subjects, of temporal courses of the left and right FF.***

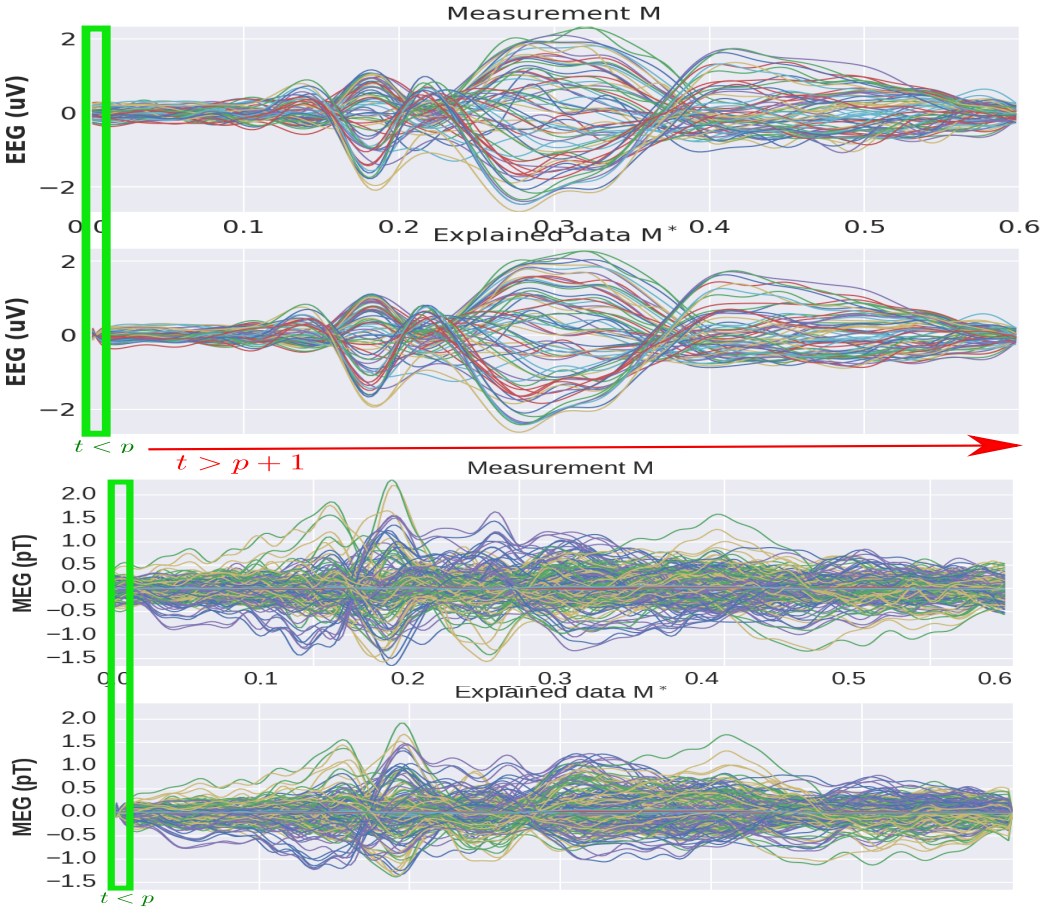

Figure 5.39: ***Acquired EEG and MEG data and the explained data, computed as $G_d J_v$, with iSDR(p = 2) of subject 15. We show the reconstructed MEG after magnitude debiasing. No magnitude debiasing is applied for reconstructed EEG. Our initialization favors small activations at the beginning, but could explain accurately the remaining time samples.***

5.5 Discussion

In this chapter, we have presented our two contributions to use the dMR information in the EEG/MEG inverse problem. The first (sWMNE) uses a spatial prior to recover some variation in source magnitudes inside each cortical region as a function of the structural inhomogeneity found in cortical regions. The second approach (iSDR) uses MAR model to constrain cortical activations. It assumes a stable MAR model with spatial sparsity in a time window.

sWMNE provides more accurate results, in terms of reconstruction accuracy and spatial focality, compared to MN reconstruction. sWMNE, on average, does not provide a significant improvement in terms of source reconstruction accuracy when compared to CP. But it is better in detecting the activation spatial extent as shown by synthetic and real data. Both methods are computationally expensive because of the need to invert a $N_s \times N_s$ matrix. In our experimental settings, the average execution time for a specific choice of the regularization parameters α and μ is around 2 min. Because the weighting matrix is singular, μ should be nonzero to have a computationally stable solution.

iSDR is a non-convex optimization problem. We assume a constant MAR model on the time window of analysis. iSDR is solved by iteratively solving a sequence of weighted MxNE problems, which allows for a fast algorithm and global convergence control at each iteration. iSDR uses a multivariate autoregressive model to constrain the sources' dynamics. iSDR and MxNE show different source estimates even with the same size of region active set. The investigation of the time window length (or the number of time samples) on the accuracy of the reconstruction should and will be investigated in future work. iSDR showed improvement in terms of reconstruction accuracy and source magnitude bias when compared to MxNE. The number of possible effective connections is controlled mainly by the number of anatomical connections detected by the probabilistic tractography applied to dMR images. We thresholded the structural connectivity matrix to distinguish between positive and false-positive connections. Possible false anatomical connections are obtained with low threshold values.

The previous assumption, which states that a source depends only on the anatomical connections, can suffer from the problem of undetected anatomical connections by probabilistic tractography. To overcome this, we added another assumption that sources interact with their neighbors even if they do not have any detectable anatomical connections by dMRI. This assumption is inspired by the fact that there are horizontal fibers, in the gray matter, that connect cortical regions (layer I of gray matter).

It is worth noting that iSDR framework accepts other possible information coming from other imaging modalities (e.g. fMRI) concerning possible effective connectivity between regions. This is done by adding another matrix to Equation 5.34 which contains the possible regions interactions from other imaging modality or prior. The MAR model can be sparser if we use the assumption made in Fukushima et al. (Fukushima et al., 2015), in which

they assumed that interactions between regions happen at only one-time lag. This time lag is defined by the length of the anatomical connections between regions. This will reduce considerably the number of MAR elements to be estimated but reduce the degree of freedom of the model which reduces the set of curves that can fit the source estimate. In our model, a pair of regions can interact at a maximum of p time lags. We observed that initializing the iSDR with the MxNE solution and identity matrix for MAR model of order 1 provides good results. For higher order, when initializing A_p by the identity and $A_i = 0$ for $i \in \{1, p-1\}$, iSDR favors the initial estimate values to be close to zero. But, the estimates of the remaining time samples are weakly affected by A_i's initialization. Other possible initializations showed possible improvements on the initial estimate.

We assumed in iSDR that the process of the multivariate autoregressive model is (non)stationary stable. This means that we did not deal with explosive processes. iSDR relies on the mixed norm estimate to estimate sources (S-step). The A-step then fits the MAR model to the signals that are supposed to be with finite variance.

Because the iSDR algorithm is non-convex, a special care must be given to the initial values of both λ (the first estimate of MxNE) and MAR model matrices. Finally, we obtained empirical evidence that iSDR outperforms MxNE in terms of active source set identification and source magnitude bias. It is true that the simulations were biased because they were generated from MAR models, but the bias was reduced by initializing the MAR model by diagonal matrices and activating regions that are, anatomically, connected to inactive regions. iSDR could, even in low SNR level, reconstruct the true active source set with high temporal course accuracies. When tested with real data, iSDR and sWMNE reconstruction algorithms showed plausible results that coincide with what were found in other work concerning face perception and recognition task.

The computation time for iSDR depends on the window size, the MAR model order and strongly on the regularization parameter. It is faster when λ is bigger because it needs less time to converge to the optimal solution. When using Intel(R) Core(TM) i7-3840QM CPU @ 2.80GHz, between 1-2 minutes was needed for one iSDR iteration. It is worth mentioning that less than 8 iterations were needed to stop iterating iSDR when using real data.

However, the present experiment only tested high-level visual categories and whether this assumption also holds for other tasks such as auditory, memory, or language remains untested. Future studies can use the present approach to test the connectivity-function relationship in other tasks.

5.6 Conclusion

In this work, we developed two algorithms to solve the EEG/MEG inverse problem. A spatial method that uses the homogeneity inside the cortical regions to constrain the sources activations. The second method uses anatomical connections, as detected by dMR images, and neighboring information to constrain the dynamics of the sources. To detect anatomical connections,

we have chosen a threshold to reduce possible false negative connections. Although more MAR coefficients should increase the false positive effective connectivity, this effect is partially negated by the sparse prior, mixed norm, applied to the regions intensities in iSDR. Nonlinear extension of the linear MAR source model to embrace a wide range of nonlinear dynamic phenomena should be investigated.

Few improvements can be considered to obtain more accurate reconstructions. The first one is including the first p measurements. Also, combining MEG and EEG data may result to better localization of brain activity. The last and not the least improvement can be by considering a sparser MAR model.

Chapter 6

General conclusion

Contents

6.1 Contributions 160
6.1.1 Cortical surface parcellation 160
6.1.2 Spatial regularization (sWMNE) 160
6.1.3 Spatiotemporal regularization (iSDR) 161
6.2 Other contributions 161
6.3 Perspectives 161

In this work, we focused on solving the EEG and MEG inverse problem by using and integrating information coming from another imaging modality, diffusion MRI, which has a very different nature. More precisely, dMRI information was used in three ways:

- to divide the cortical surface into functional regions with homogeneous structural connectivity.
- to build a weighting matrix, based on the inhomogeinity of the structural connectivity inside cortical regions, which is used in sWMNE solver.
- to constrain the source dynamics using a multivariate autoregressive model (iSDR).

In the next sections, we describe, briefly, the three contributions and some perspectives.

6.1 Contributions

6.1.1 Cortical surface parcellation

(Chapter 4.1) Few people tackle the problem of parcellating the whole brain into region due to the high dimensionality of the fingerprint (tractograms in our work). We used a bottom-up agglomerative approach based on the mutual nearest neighbor condition to obtain brain regions with the highest homogeneity according to a similarity measure. In our work, we investigated the effect five similarity measures on the resulting parcels. Two among them showed good results in terms of computation time and good contrast between the dispersion of the similarity values, computed between the connectivity profiles when targeting a small or a big number of regions . They are Cosine and Tanimoto measure. There MNN algorithm depends on one parameter. It was found that there is a linear relationship between this parameter and the resulting number of regions. Related publications are [4], [5], [8] and [9] in Appendix A.

6.1.2 Spatial regularization (sWMNE)

The regions obtained from the MNN parcellation are used to constrain spatially the sources according to the homogeneity of the regions. This is done by introducing a weighting matrix whose elements are obtained by computing the similarity measure value of each of the sources' pairs inside each region. The sWMNE showed more accurate results with compared to the MNE in terms of reconstruction accuracy and spatial focality. Although, sWMNE did not show, in average, a significant improvement with compared to PC, but it is better in detecting the spatial extent of the activation (see section 5.3). Related publications is [2] in Appendix A.

6.1.3 Spatiotemporal regularization (iSDR)

In this model, the sources inside each region of the MNN parcellation are assumed to have the same activation. We estimate the anatomical connections between the parcels by running probabilistic tractography on all the seeds of the cortical surface. We use a low threshold to decide to whether an anatomical connection is a "true" connection or a false positive one. Then, we constrain the source dynamics to follow a multivariate autoregressive model (MAR) of order p. The framework, iSDR, that we proposed is divided into two steps. The first one uses mixed norm to estimate the temporal evaluation of the sources. The framework can be seen as an extension of the MxNE method. The second step uses ordinary least square to fit the MAR model. Related publication is [1], [3] and [6] in Appendix A.

6.2 Other contributions

Some work is not listed in details in this manuscript. We have used cortical regions defined by three methods and maximum entropy on the mean (MEM) method (see section 2.3.3.3) to reconstruct cortical activation. The first parcellation algorithm uses *k-means* to parcellate the dMRI-based fingerprint. Multivariate source prelocalization (MSP) scores were used to functionally parcellate the cortical surface. We compared the MEM estimates using these two parcellations to the ones obtained with a random parcellation using synthetic data (see Figure 6.1). An interesting result is that random parcellations can provide better source reconstruction in terms of magnitude and spatial extent, when averaged, when compared to dMRI-based and functionally based parcellation. Finally, MEM with dMRI-based parcels was found to provide functionally plausible results when tested with real data. Related works are [5], [8] and [9] in Appendix A.

6.3 Perspectives

In our work, we used a probabilistic tractography, to estimate the degree of existence of anatomical connections between two brain voxels/regions, but this can result in false connections due to noise in dMR images, to false detection of the fiber directions and general assumptions made in tractography. This can result in possible false interactions between brain areas when using our EEG/MEG spatiotemporal algorithm iSDR. The use of microstructure landmarks, like axon diameter, could provide more reliable results and its use should be investigated in the iSDR framework. The axon diameter and anatomical pathway distance control the information speed. This results in different time-lags between regions which can be integrated in the iSDR algorithm.

We also defined the functional regions by using parcellation algorithm based on the mutual nearest neighbor condition. The validation of these regions using functional modalities are required to tune the MNN parameter.

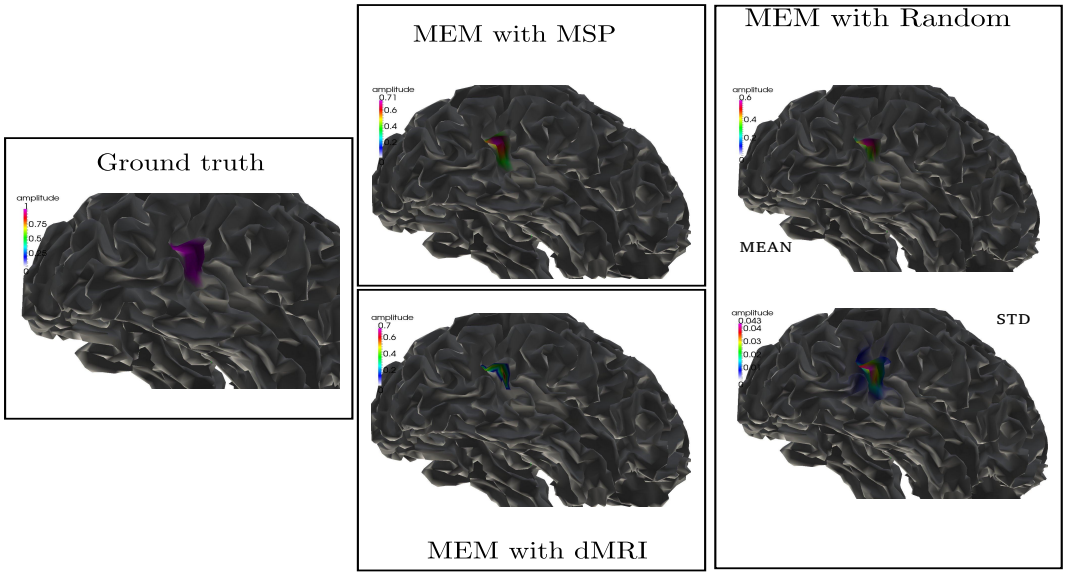

Figure 6.1: ***Source reconstruction of synthetic data using MEM solver with three parcellations (MSP, Ransom and dMRI-based parcellation)***

Multi-subject studies can be conducted to build structural atlas using MNN algorithm which will allows us to understand better the relation between the white matter pathways and the functional interactions of brain regions.

In iSDR, we did not investigate the best order MAR model (value of p) i.e. lag length selection. The MAR complexity depends on the number of time lags i.e. the value of p. Simple signals can be obtained with few time lags and more complex source signals are obtained by considering higher order MAR models. So the choice of the MAR model is critical. There is a compromise between the complexity of the MAR model and the number of MAR elements to be made. The number of MAR elements increases tremendously with more time lags or connectivity threshold. For example, if we have n parameters to be estimated when considering MAR model of order 1, we will have $p \times n$ elements to be estimated for MAR model of order p.

Model selection

Information criterion can be used to find the optimal time lag p. The three most common information criteria are Akaike (AIC) (Akaike, 1998), Schwarz-Bayesian (BIC) (Kass et al., 1995) and Hannan-Quinn (HQ) (Hannan et al., 1979). For the case of optimizing p, this gives:

$$AIC(p) = \log \det(\Sigma_p) + \frac{2}{T}K$$

$$HQ(p) = \log \det(\Sigma_p) + \frac{2\log \log T}{T}K$$

$$BIC(p) = \log \det(\Sigma_p) + \frac{\log T}{T}K$$

where $\Sigma_p = \frac{1}{T}\sum_{i=1}^{T} \omega_t \omega_t^T$ is the residual covariance matrix of MAR model

(or EEG/MEG residuals) of order p and K is the number of MAR elements to be estimated. It has been shown that AIC favors large order, while BIC chooses smallest order and HQ is in between (Lütkepohl, 2007). That is why, we suggest to use BIC.

In iSDR, we did not investigate the effect of window size, in which the sources' dynamics are assumed to be constant which probably depends on different factors like the mental or physical task and fatigue. Because we assume that the relation between brain regions is constant during each functional task. A change in the MAR model can be due to a change in the performed function. Using a sliding window to estimate the MAR model can be used to detect MAR model jumps.

Our iSDR framework also assumes a linear relation between the sources and their past values, which is a simple model for complex brain's regions interactions. For future work, we should investigate a possible integration of nonlinear dynamics in the iSDR framework.

Appendix A

Publication of the author

[1] **Brahim Belaoucha**, Théodore Papadopoulo. Large brain effective network from EEG/MEG data and dMR information. *7th International Workshop on Pattern Recognition in Neuroimaging (PRNI)*, 2017, Toronto, Canada.

[2] **Brahim Belaoucha**, Théodore Papadopoulo. Spatial regularization based on dMRI to solve EEG/MEG inverse problem. *The 39th Annual International Conference of the IEEE Engineering in Medicine and Biology Society*, 2017, Jeju, South Korea.

[3] **Brahim Belaoucha**, Mouloud Kachouane, Théodore Papadopoulo. Multivariate autoregressive model constrained by anatomical connectivity to reconstruct focal sources, *The 38th Annual International Conference of the IEEE Engineering in Medicine and Biology Society*, 2016, Orlando, USA.

[4] **Brahim Belaoucha**, Maureen Clerc, Théodore Papadopoulo. Cortical surface parcellation via dMRI using mutual nearest neighbor condition. *ISBI - 13th IEEE International Symposium on Biomedical Imaging*, April 2016, Prague, Czech Republic.

[5] **Brahim Belaoucha**, Jean-Marc Lina, Maureen Clerc, Théodore Papadopoulo. MEM-diffusion MRI framework to solve MEEG inverse problem. *European Signal Processing Conference (EUSIPCO 2015)*, 2015, Nice, France.

[6] **Brahim Belaoucha**, Théodore Papadopoulo. Iterative two-stage approach to estimate sources and their interactions. *20th International Conference on Biomagnetism*, 2016, Seoul, South Korea.

[7] **Brahim Belaoucha**, Théodore Papadopoulo. MEG/EEG reconstruction in the reduced source space. *International Conference on Basic and Clinical Multimodal Imaging*, 2015, Utrecht, Netherlands.

[8] **Brahim Belaoucha**, Anne-Charlotte Philippe, Maureen Clerc, Théodore Papadopoulo. Diffusion Magnetic Resonance information as a regularization term for MEG/EEG inverse problem, *19th International Conference On Biomagnetism*, 2014, Halifax, Canada.

[9] **Brahim Belaoucha**, Jean-Marc Lina, Maureen Clerc, Anne-Charlotte Philippe, Christophe Grova, Théodore Papadopoulo. Using diffusion MRI information in the Maximum Entropy on Mean framework to solve MEG/EEG inverse problem, *19th International Conference On Biomagnetism*, 2014, Halifax, Canada.

References

Aboitiz, Francisco, Arnold B. Scheibel, Robin S. Fisher, and Eran Zaidel (1992). "Fiber composition of the human corpus callosum". In: *Brain Research* 598.1–2, pp. 143 –153.

Aggarwal, Charu C., Alexander Hinneburg, and Daniel A. Keim (2001). "On the Surprising Behavior of Distance Metrics in High Dimensional Space". In: *Database Theory — ICDT 2001: 8th International Conference London, UK, January 4–6, 2001 Proceedings*. Ed. by Jan Van den Bussche and Victor Vianu. Berlin, Heidelberg: Springer Berlin Heidelberg, pp. 420–434.

Akaike, Hirotogu (1998). "Information Theory and an Extension of the Maximum Likelihood Principle". In: *Selected Papers of Hirotugu Akaike*. Ed. by Emanuel Parzen, Kunio Tanabe, and Genshiro Kitagawa. New York, NY: Springer New York, pp. 199–213.

Alexander, Daniel C. (2005). "Multiple-Fiber Reconstruction Algorithms for Diffusion MRI". In: *Annals of the New York Academy of Sciences* 1064.1, pp. 113–133.

Amblard, C., E. Lapalme, and J.-M. Lina (2004). "Biomagnetic source detection by maximum entropy and graphical models". In: *Biomedical Engineering, IEEE Transactions on* 51.3, pp. 427–442.

Anwander, A., M. Tittgemeyer, D.Y. von Cramon, A.D. Friederici, and T.R. Knösche (2007). "Connectivity-Based Parcellation of Broca's Area". In: *Cerebral Cortex* 17.4, pp. 816–825.

Arlot, Sylvain and Alain Celisse (2010). "A survey of cross-validation procedures for model selection". In: *Statist. Surv.* 4, pp. 40–79.

Arsigny, Vincent, Pierre Fillard, Xavier Pennec, and Nicholas Ayache (2006). "Log-Euclidean metrics for fast and simple calculus on diffusion tensors". In: *Magnetic Resonance in Medicine*.

Bajusz, Dávid, Anita Rácz, and Károly Héberger (2015). "Why is Tanimoto index an appropriate choice for fingerprint-based similarity calculations?" In: *Journal of Cheminformatics* 7.1, pp. 1–13.

Basser, Peter J., Jim Mattiello, and Denis Le Bihan (1994a). "Estimation of the effective self-diffusion tensor from the NMR spin echo". In: *Journal of Magnetic Resonance* B.103, pp. 247–254.

— (1994b). "MR Diffusion Tensor Spectroscopy and imaging". In: *Biophysical Journal* 66.1, 259âĂŞ267.

Basser, Peter J. and Derek K. Jones (2002). "Diffusion-tensor MRI: theory, experimental design and data analysis âĂŞ a technical review". In: *NMR in Biomedicine* 15.7-8, pp. 456–467.

Basser, P.J., S. Pajevic, C. Pierpaoli, J. Duda, and A. Aldroubi (2000). "In Vivo Fiber Tractography Using DT-MRI Data". In: *Magnetic Resonance in Medicine* 44, pp. 625–632.

Baumann, Nicole and Danielle Pham-Dinh (2001). "Biology of Oligodendrocyte and Myelin in the Mammalian Central Nervous System". In: *Physiological Reviews* 81.2, pp. 871–927.

Beck, Amir and Marc Teboulle (2009). "A Fast Iterative Shrinkage Thresholding Algorithm for Linear Inverse Problems". In: *SIAM Journal on Imaging Sciences* 2.1, pp. 183–202.

Beeck, Hans P Op de, Johannes Haushofer, and Nancy G Kanwisher (2008). "Interpreting fMRI data : maps, modules and dimensions". In: *Nature Reviews Neuroscience* 9.2, pp. 123–135.

Behrens, T. E. J., H. Johansen-Berg, S. Jbabdi, M.F.S. Rushworth, and M.W. Woolrich (2007). "Probabilistic diffusion tractography with multiple fibre orientations. What can we gain?" In: *NeuroImage* 34.1, pp. 144–155.

Behrens, T.E.J. et al. (2003). "Non-invasive mapping of connections between human thalamus and cortex using diffusion imaging". In: *Nature Neuroscience* 6.7, pp. 750–757.

Belaoucha, B., A.-C. Philippe, M. Clerc, and T. Papadopoulo (2014). "Diffusion Magnetic Resonance information as a regularization term for MEG/EEG inverse problem". In: *Proceedings of Biomag*. Halifax, Canada.

Belaoucha, B., J. M. Lina, M. Clerc, and T. Papadopoulo (2015a). "MEM-diffusion MRI framework to solve MEEG inverse problem". In: *Signal Processing Conference (EUSIPCO), 2015 23rd European*, pp. 1875–1879.

Belaoucha, B., M. Clerc, and T. Papadopoulo (2016). "Cortical surface parcellation via dMRI using mutual nearest neighbor condition". In: *2016 IEEE 13th International Symposium on Biomedical Imaging (ISBI)*, pp. 903–906.

Belaoucha, Brahim and Théodore Papadopoulo (2015b). "MEG/EEG reconstruction in the reduced source space". In: *BaCi*. Utrecht, Netherlands.

Bellec, P., V. Perlbarg, S. Jbabdi, M. Pélégrini-Issac, J. Anton, J. Doyon, and H. Benali (2006). "Identification of large-scale networks in the brain using fMRI". In: *NeuroImage* 29.4, pp. 1231–1243.

Binder, Jeffrey R., Julie A. Frost, Thomas A. Hammeke, Robert W. Cox, Stephen M. Rao, and Thomas Prieto (1997). "Human Brain Language Areas Identified by Functional Magnetic Resonance Imaging". In: *The Journal of Neuroscience* 17.1, pp. 353–362.

Blumensath, Thomas, Timothy E. J. Behrens, and Stephen M. Smith (2012). "Resting-State FMRI Single Subject Cortical Parcellation Based on Region Growing". In: *Medical Image Computing and Computer-Assisted Intervention – MICCAI 2012: 15th International Conference, Nice, France, October 1-5, 2012, Proceedings, Part II*. Ed. by Nicholas Ayache, Hervé Delingette, Polina Golland, and Kensaku Mori. Berlin, Heidelberg: Springer Berlin Heidelberg, pp. 188–195.

Bonmati, E., A. Bardera, I. Boada, M. Feixas, and M. Sbert (2015). "Hierarchical clustering based on the information bottleneck method using a control process". In: *Pattern Analysis and Applications* 18.3, pp. 619–637.

Boyd, S. and L. Vandenberghe (2004). *Convex Optimization*. Cambridge, U.K.: Cambridge Univ. Press.

Brodmann, K. (1909). *Vergleichende Lokalisationslehre der Grobhirnrinde*. J.A.Barth, Leipzig.

Bubeck, S., M. Meila, and U. von Luxburg (2012). "How the initialization affects the stability of the k-means algorithmâĹŮ". In: *ESAIM: PS* 16, pp. 436–452.

Bukowski, Henryk, Laurence Dricot, Bernard Hanseeuw, and Bruno Rossion (2013). "Cerebral lateralization of face-sensitive areas in left-handers: Only the {FFA} does not get it right". In: *Cortex* 49.9, pp. 2583 –2589.

Cha, Sung-Hyuk (2008). "Taxonomy of Nominal Type Histogram Distance Measures". In: *Proceedings of the American Conference on Applied Mathematics*. MATH'08. Cambridge, Massachusetts: World Scientific, Engineering Academy, and Society (WSEAS), pp. 325–330.

Chowdhury, Rasheda Arman, Jean Marc Lina, Eliane Kobayashi, and Christophe Grova (2013). "MEG Source Localization of Spatially Extended Generators of Epileptic Activity: Comparing Entropic and Hierarchical Bayesian Approaches". In: *PLoS ONE* 8.2, pp. 1–19.

Cottereau, Benoit (2008). "Modèles hiérarchiques en imagerie MEG/EEG : application á la création rapide de cartes rétinotopiques". Thése de doctorat dirigée par Baillet, Sylvain Physique Université de Paris-Sud. Faculté des Sciences d'Orsay (Essonne) 2008. PhD thesis, 1 vol. (207 p.)

Cottereau, Benoit R, Justin M Ales, and Anthony M Norcia (2012). "Increasing the accuracy of electromagnetic inverses using functional area source correlation constraints". In: *Human brain mapping* 33.11, pp. 2694–2713.

Dale, A.M., B. Fischl, and M.I. Sereno (1999). "Cortical surface-based analysis I: Segmentation and surface reconstruction". In: *NeuroImage* 9, pp. 179–194.

Dassios, G. and F. Kariotou (2003). "Magnetoencephalography in ellipsoidal geometry". In: *Journal of Mathematical Physics* 44, pp. 220–241.

Daubechies, I., R. DeVore, M. Fornasier, and S. Gunturk (2008). "Iteratively Re-weighted Least Squares minimization: Proof of faster than linear rate for sparse recovery". In: *2008 42nd Annual Conference on Information Sciences and Systems*, pp. 26–29.

Dendy, P. (2006). "Basics of PET imaging: Physics, Chemistry and Regulations. By Gopal B Saha, (Springer, NY)". In: *The British Journal of Radiology* 79.947, pp. 933–933.

Descoteaux, Maxime (2008). "High Angular Resolution Diffusion MRI: From Local Estimation to Segmentation and Tractography". PhD thesis. University of Nice Sophia Antipolis.

Desikan, Rahul S. et al. (2006). "An automated labeling system for subdividing the human cerebral cortex on MRI scans into gyral based regions of interest". In: *NeuroImage* 31.3, pp. 968–980.

Dice, Lee R. (1945). "Measures of the Amount of Ecologic Association Between Species". In: *Ecology* 26.3, pp. 297–302.

Efron, Bradley, Trevor Hastie, Iain Johnstone, and Robert Tibshirani (2004). "Least angle regression". In: *Ann. Statist.* 32.2, pp. 407–499.

Einstein, A. (1905). "Über die von der molekularkinetischen Theorie der Wärme geforderte Bewegung von in ruhenden Flüssigkeiten suspendierten Teilchen". In: *Annalen der Physik* 322.8, pp. 549–560.

— (1956). *Investigations on the Theory of the Brownian Movement*. Dover Pubns.

Faugeras, Olivier et al. (1999). *The Inverse EEG and MEG Problems : The Adjoint State Approach I: The Continuous Case*. Research Report RR-3673. Projet CERMICS. INRIA, p. 28.

Fillard, Pierre, Cyril Poupon, and Jean-François Mangin (2009). "A novel global tractography algorithm based on an adaptive spin glass model." In: *Medical image computing and computer-assisted intervention : MICCAI ... International Conference on Medical Image Computing and Computer-Assisted Intervention* 12.Pt 1, pp. 927–34.

Finger, Holger, Marlene Bönstrup, Bastian Cheng, Arnaud Messé, Claus Hilgetag, Götz Thomalla, Christian Gerloff, and Peter König (2016). "Modeling of Large-Scale Functional Brain Networks Based on Structural Connectivity from DTI: Comparison with EEG Derived Phase Coupling Networks and Evaluation of Alternative Methods along the Modeling Path". In: *PLOS Computational Biology* 12.8, pp. 1–28.

Fischl, Bruce et al. (2004). "Automatically Parcellating the Human Cerebral Cortex". In: *Cerebral Cortex* 14.1, pp. 11–22.

Fodor, J.A (1983). *The modularity of the mind*. Cambridge: MIT press.

Friedman, Jerome, Trevor Hastie, Holger Höfling, and Robert Tibshirani (2007). "Pathwise coordinate optimization". In: *Ann. Appl. Stat.* 1.2, pp. 302–332.

Fukushima, M., O. Yamashita, A. Kanemura, S. Ishii, M. Kawato, and M. a. Sato (2012). "A State-Space Modeling Approach for Localization of Focal Current Sources From MEG". In: *Biomedical Engineering, IEEE Transactions on* 59.6, pp. 1561–1571.

Fukushima, M., O. Yamashita, T. R. Knösche, and M. a. Sato (2013). "MEG source reconstruction constrained by diffusion MRI based whole brain dynamical model". In: *2013 IEEE 10th International Symposium on Biomedical Imaging*, pp. 1002–1005.

Fukushima, Makoto, Okito Yamashita, Thomas R. Knösche, and Masa-aki Sato (2015). "MEG source reconstruction based on identification of directed source interactions on whole-brain anatomical networks". In: *NeuroImage* 105, pp. 408 –427.

Gabriel, S., R. W. Lau, and C. Gabriel (1996). "The dielectric properties of biological tissues: II. Measurements in the frequency range 10 Hz to 20 GHz". In: *Physics in Medicine and Biology* 41.11, p. 2251.

Galán, Julia Guiomar Niso (2013). "Functional and effective connectivity in MEG: Application to the study of epilepsy". PhD thesis. Universidad Politècnica de Madrid.

Galka, Andreas, Okito Yamashita, Tohru Ozaki, Rolando Biscay, and Pedro Valdes-Sosa (2004). "A solution to the dynamical inverse problem of EEG generation using spatiotemporal Kalman filtering". In: *NeuroImage* 23.2, pp. 435–453.

Gavit, L., S. Baillet, J. F. Mangin, J. Pescatore, and L. Garnero (2001). "A multiresolution framework to MEG/EEG source imaging". In: *IEEE Transactions on Biomedical Engineering* 48.10, pp. 1080 –1087.

Geyer, Stefan, Giuseppe Luppino, and Stefano Rozzi (2012). "Chapter 27 - Motor Cortex". In: *The Human Nervous System (Third Edition)*. Ed. by Juergen K. Mai and George Paxinos. Third Edition. San Diego: Academic Press, pp. 1012 –1035.

Ghosh, A. (2011). "High Order Models in Diffusion MRI and Applications". PhD thesis. University of Nice-Sophia Antipolis.

Giraldo, E., A. J. den Dekker, and G. Castellanos-Dominguez (2010). "Estimation of dynamic neural activity using a Kalman filter approach based on physiological models". In: *2010 Annual International Conference of the IEEE Engineering in Medicine and Biology*, pp. 2914–2917.

Golub, Gene H., Michael Heath, and Grace Wahba (1979). "Generalized Cross-Validation as a Method for Choosing a Good Ridge Parameter". In: *Technometrics* 21.2, pp. 215–223.

Gorodnitsky, I.F., J.S. George, and B.D. Rao (1995). "Neuromagnetic source imaging with focuss: a recursive weighted minimum norm algorithm". In: *Electroencephalography and clinical Neurophysiology*.

Gramfort, A., D. Strohmeier, J. Haueisen, M.S. Hämäläinen, and M. Kowalski (2013). "Time-frequency mixed-norm estimates: Sparse M/EEG imaging with non-stationary source activations". In: *NeuroImage* 70, pp. 410–422.

Gramfort, Alexandre (2009). "Mapping, timing and tracking cortical activations with MEG and EEG: Methods and application to human vision". PhD thesis. Graduate School of Telecom ParisTech.

Gramfort, Alexandre, Théodore Papadopoulo, Emmanuel Olivi, and Maureen Clerc (2010). "OpenMEEG: opensource software for quasistatic bioelectromagnetics". In: *BioMedical Engineering OnLine* 9.1, pp. 1–20.

Gramfort, Alexandre, Matthieu Kowalski, and Matti Hämäläinen (2012). "Mixed-norm estimates for the M/EEG inverse problem using accelerated gradient methods". In: *Physics in Medicine and Biology* 57.7, pp. 1937–1961.

Gray, Henry. (1918). *Gray's Anatomy of the Human Body*. LEA and FEBIGER, 1918.

Gross, J., J. Kujala, M. Hamalainen, L. Timmermann, A. Schnitzler, and R. Salmelin (2001). "Dynamic imaging of coherent sources: Studying neural interactions in the human brain". In: *Proceedings of the National Academy of Sciences of the United States of America* 98.2, pp. 694–699.

Guo, Weihong, Qingguo Zeng, Yunmei Chen, and Yijun Liu (2006). "Using multiple tensor deflection to reconstruct white matter fiber traces with branching". In: *3rd IEEE International Symposium on Biomedical Imaging: Nano to Macro, 2006.* Pp. 69–72.

Hadjikhani, N., K. Kveraga, P. Naik, and S. P. Ahlfors (2009). "Early (N170) activation of face-specific cortex by face-like objects". In: *Neuroreport* 20.4, pp. 403–407.

Halgren, Eric, Tommi Raij, Ksenija Marinkovic, Veikko JousmÃd'ki, and Riitta Hari (2000). "Cognitive Response Profile of the Human Fusiform Face Area as Determined by MEG". In: *Cerebral Cortex* 10.1, p. 69.

Hämäläinen, Matti, Riitta Hari, Risto J. Ilmoniemi, Jukka Knuutila, and Olli V. Lounasmaa (1993a). "Magnetoencephalography—theory, instrumentation, and applications to noninvasive studies of the working human brain". In: *Rev. Mod. Phys.* 65 (2), pp. 413–497.

— (1993b). "Magnetoencephalography—theory, instrumentation, and applications to noninvasive studies of the working human brain". In: *Rev. Mod. Phys.* 65 (2), pp. 413–497.

Hämäläinen, Matti S. and Jukka Sarvas (1989). "Realistic Conductivity Geometry Model of the Human Head for Interpretation of Neuromagnetic Data". In: *IEEE Trans. Biomed. Eng.* 36.2, pp. 165–171.

Hammond, D. K., B. Scherrer, and A. Malony (2012). "Incorporating anatomical connectivity into EEG source estimation via sparse approximation with cortical graph wavelets". In: *2012 IEEE International Conference on Acoustics, Speech and Signal Processing (ICASSP)*, pp. 573–576.

Hammond, D. K., B. Scherrer, and S. K. Warfield (2013). "Cortical Graph Smoothing: A Novel Method for Exploiting DWI-Derived Anatomical Brain Connectivity to Improve EEG Source Estimation". In: *IEEE Transactions on Medical Imaging* 32.10, pp. 1952–1963.

Hannan, E. J. and B. G. Quinn (1979). "The Determination of the Order of an Autoregression". In: *Journal of the Royal Statistical Society. Series B (Methodological)* 41.2, pp. 190–195.

Hansen, P. C. (1992). "Analysis of Discrete Ill-Posed Problems by Means of the L-Curve". In: *SIAM Review* 34.4, pp. 561–580.

Haufe, S., R. Tomioka, G. Nolte, K. R. MÃijller, and M. Kawanabe (2010). "Modeling Sparse Connectivity Between Underlying Brain Sources for EEG/MEG". In: *IEEE Transactions on Biomedical Engineering* 57.8, pp. 1954–1963.

Henson, R.N., Y. Goshen-Gottstein, T. Ganel, L.J. Otten, A. Quayle, and M.D. Rugg (2003). "Electrophysiological and Haemodynamic Correlates of Face Perception, Recognition and Priming". In: *Cerebral Cortex* 13.7, pp. 793–805.

Hoenig, Klaus, Christiane K. Kuhl, and Lukas Scheef (2005). "Functional 3.0-T MR Assessment of Higher Cognitive Function: Are There Advantages over 1.5-T Imaging?" In: *Radiology* 234.3. PMID: 15650039, pp. 860–868.

Horowitz, Assaf, Daniel Barazany, Ido Tavor, Moran Bernstein, Galit Yovel, and Yaniv Assaf (2015). "In vivo correlation between axon diameter and conduction velocity in the human brain". In: *Brain Structure and Function* 220.3, pp. 1777–1788.

Hudspeth, A. J., J. E. Ruark, and J. P. Kelly (1976). "Cytoarchitectonic mapping by microdensitometry". In: *Proceedings of the National Academy of Sciences* 73.8, pp. 2928–2931.

Huppertz, H.-J., S. Hoegg, C. Sick, C.H. LÃijcking, J. Zentner, A. Schulze-Bonhage, and R. Kristeva-Feige (2001). "Cortical current density reconstruction of interictal epileptiform activity in temporal lobe epilepsy". In: *Clinical Neurophysiology* 112.9, pp. 1761 –1772.

Jbabdi, S., M.W. Woolrich, J.L.R. Andersson, and T.E.J. Behrens (2007). "A Bayesian framework for global tractography". In: *NeuroImage* 37.1, pp. 116–129.

Jbabdi, S., M.W. Woolrich, and T.E.J. Behrens (2009). "Multiple-subjects connectivity-based parcellation using hierarchical Dirichlet process mixture models". In: *NeuroImage* 44.2, pp. 373 –384.

Jeurissen, Ben, Alexander Leemans, Derek K. Jones, Jacques-Donald Tournier, and Jan Sijbers (2010). "Estimating the number of fiber orientations in diffusion MRI voxels: a constrained spherical deconvolution study". In: Stockholm, Sweden.

Johansen-Berg, H., T. E. J. Behrens, M. D. Robson, I. Drobnjak, M. F. S. Rushworth, J. M. Brady, S. M. Smith, D. J. Higham, and P. M. Matthews (2004). "Changes in connectivity profiles define functionally distinct regions in human medial frontal cortex". In: *Proceedings of the National Academy of Sciences of the United States of America* 101.36, pp. 13335 –13340.

Johansen-Berg, Heidi and Timothy E.J. Behrens, eds. (2009). *Diffusion MRI: From Quantitative Measurement to In vivo Neuroanatomy*. Elevier Academic Press.

Kandel, Eric, James Schwartz, and Thomas Jessell (2000). *Principles Of Neural Science*. 4th ed. McGraw-Hill Medical.

Kass, Robert E. and Adrian E. Raftery (1995). "Bayes Factors". In: *Journal of the American Statistical Association* 90.430, pp. 773–795.

Klein, Arno and Joy Hirsch (2005). "Mindboggle: a scatterbrained approach to automate brain labeling". In: *NeuroImage* 24.2, pp. 261–280.

Knösche, Thomas R., Alfred Anwander, Matthew Liptrot, and Tim B. Dyrby (2015). "Validation of tractography: Comparison with manganese tracing". In: *Human Brain Mapping* 36.10, pp. 4116–4134.

Knosche, T.R., M. Graser, and A. Anwander (2013). "Prior knowledge on cortex organization in the reconstruction of source current densities from {EEG}". In: *NeuroImage* 67, pp. 7–24.

Kreher, B. W., J. F. Schneider, I. Mader, E. Martin, J. Hennig, and K. A. Il'yasov (2005). "Multitensor approach for analysis and tracking of complex fiber configurations". In: *Magnetic Resonance in Medicine* 54.5, pp. 1216–1225.

Kreher, B. W., I. Mader, and V. G. Kiselev (2008). "Gibbs Tracking: A Novel Approach for the Reconstruction of Neuronal Pathways". In: *Magnetic Resonance in Medicine* 60.4, pp. 953–963.

Kristensen, Thomas G. and Christian N. S. Pedersen (2010). "Data Structures for Accelerating Tanimoto Queries on Real Valued Vectors". In: *Algorithms in Bioinformatics: 10th International Workshop, WABI 2010, Liverpool, UK, September 6-8, 2010. Proceedings*. Ed. by Vincent Moulton and Mona Singh. Berlin, Heidelberg: Springer Berlin Heidelberg, pp. 28–39.

Kuhn, H. W. and A. W. Tucker (1951). "Nonlinear Programming". In: *Proceedings of the Second Berkeley Symposium on Mathematical Statistics and Probability*. Berkeley, Calif.: University of California Press, pp. 481–492.

Kybic, J., M. Clerc, T. Abboud, O. Faugeras, R. Keriven, and T. Papadopoulo (2005). "A common formalism for the Integral formulations of the forward EEG problem". In: *IEEE Transactions on Medical Imaging* 24.1, pp. 12–28.

Lachaux, Jean-Philippe, Nathalie George, Catherine Tallon-Baudry, Jacques Martinerie, Laurent Hugueville, Lorella Minotti, Philippe Kahane, and Bernard Renault (2005). "The many faces of the gamma band response to complex visual stimuli". In: *NeuroImage* 25.2, pp. 491–501.

Lamus, Camilo, Matti S. Hämäläinen, Simona Temereanca, Emery N. Brown, and Patrick L. Purdon (2012). "A spatiotemporal dynamic distributed solution to the MEG inverse problem". In: *NeuroImage* 63.2, pp. 894–909.

Long, C. J., P. L. Purdon, S. Temereanca, N. U. Desai, M. Hamalainen, and E. N. Brown (2006). "Large Scale Kalman Filtering Solutions to the Electrophysiological Source Localization Problem- A MEG Case Study". In: *2006 Annual International Conference of the IEEE Engineering in Medicine and Biology*, pp. 4532–4535.

LopesÂădaÂăSilva, F. (2013). "EEG and MEG: Relevance to Neuroscience". In: *Neuron* 80.5, pp. 1112 –1128.

Lütkepohl, Helmut (2007). *New Introduction to Multiple Time Series Analysis*. Springer Publishing Company, Incorporated.

Ma, Yina and Shihui Han (2012). "Functional dissociation of the left and right fusiform gyrus in self-face recognition". In: *Human Brain Mapping* 33.10, pp. 2255–2267.

Mars, Rogier B. et al. (2011). "Diffusion-Weighted Imaging Tractography-Based Parcellation of the Human Parietal Cortex and Comparison with Human and Macaque Resting-State Functional Connectivity". In: *The Journal of Neuroscience* 31.11, pp. 4087 –4100.

Matsuura, K. and Y. Okabe (1995). "Selective minimum-norm solution of the biomagnetic inverse problem". In: *IEEE Transactions on Biomedical Engineering* 42.6, pp. 608–615.

Mattout, J., M. Pélégrini-Issac, L. Garnero, and H. Benali (2005). "Multivariate source prelocalization (MSP): Use of functionally informed basis functions for better conditioning the MEG inverse problem". In: *NeuroImage* 26.2, pp. 356 –373.

Meijs, J. W. H. and M. Peters (1987). "The EEG and MEG using a model of eccentric spheres to describe the head". In: *IEEE Transactions on Biomedical Engineering* 34, pp. 913–920.

Meijs, J. W. H., M. J. Peters, H. B. K. Boom, and F. H. Lopes da Silva (1988). "Relative influence of model assumptions and measurement procedures in the analysis of the MEG". In: *Medical and Biological Engineering and Computing* 26.2, pp. 136–142.

Michalareas, George, Jan-Mathijs Schoffelen, and Joachim Gross (2009). "Causality analysis between brain areas based on multivariate autoregressive models of MEG sensor data". In: *BMC Neuroscience* 10.1, P234.

Mohr, J. P., M. S. Pessin, S. Finkelstein, H. H. Funkebstein, G. W. Duncan, and K. R. Davis (1978). "Broca aphasia: Pathologic and clinical". In: *Neurology* 28.4, p. 311.

Mohr, JP. (1976). "Broca's area and Broca's aphasia". In: *Stud Neurolinguis* 1, pp. 201–236.

Moreau, J.J. (1965). "ProximitÃľ et dualitÃľ dans un espace hilbertien". fre. In: *Bulletin de la SociÃľtÃľ MathÃľmatique de France* 93, pp. 273–299.

Moreno-Dominguez, D. (2014). "Whole-brain cortical parcellation: A hierarchical method based on dMRI tractography". PhD thesis. Ilmenau University of Technology.

Mosher, J. C. and R. M. Leahy (1988). "Source localization using recursively applied and projected (RAP) MUSIC". In: *IEEE Transactions on Signal Processing* 47.2, pp. 332 –340.

Mosher, J. C., P. S. Lewis, and R. M. Leahy (1992). "Multiple dipole modeling and localization from spatio-temporal MEG data". In: *IEEE Transactions on Biomedical Engineering* 39.6, pp. 541–557.

Mosher, J. C. and R. M. Leahy (1999). "Source localization using recursively applied and projected (RAP) MUSIC". In: *IEEE Transactions on Signal Processing* 47.2, pp. 332–340.

Motyka, J., B. Dobrzanski, and S. Zawadzki (1951). *Wstepne badania nad lakami poludniowo-wschodniej Lubelszczyzny*. Lublin : Uniwersytet M. Curie-SkÅĆodowskiej.

Mukherjee, Sudipta (1956). *F# for Machine Learning Essentials*. Packt Publishing.

Murty, P. S. R., R. K. Kumar, and M. Sailaja (2016). "Exploring the Similarity/Dissimilarity measures for unsupervised IDS". In: pp. 220–224.

Nunez, P.L. (2005). *Electric fields of the brain: the neurophysics of EEG*. Oxford University Press.

O'Donnell, Lauren J. and Carl-Fredrik Westin (2011). "An Introduction to Diffusion Tensor Image Analysis". In: *Neurosurgery Clinics of North America* 22.2. Functional Imaging, pp. 185 –196.

Osher, David E., Rebecca R. Saxe, Kami Koldewyn, John D.E. Gabrieli, Nancy Kanwisher, and Zeynep M. Saygin (2016). "Structural Connectivity Fingerprints Predict Cortical Selectivity for Multiple Visual Categories across Cortex". In: *Cerebral Cortex* 26.4, p. 1668.

P. Yeh, T. Oakes and G. Riedy (2012). "Diffusion Tensor Imaging and Its Application to Traumatic Brain Injury: Basic Principles and Recent Advances". In: *Open Journal of Medical Imaging* 2.4, pp. 137–164.

Pascual-Marqui, R.D., C.M. Michel, and D. Lehmann (1994). "Low resolution electromagnetic tomography: a new method for localizing electrical activity in the brain". In: *International journal of psychophysiology* 18.1, pp. 49–65.

Passingham, R.E., K.E. Stephan, and R. Kotter (2002). "The anatomical basis of functional localization in the cortex". In: *Nature Reviews Neuroscience* 3.8, pp. 606–616.

Peled, Sharon, Ola Friman, Ferenc Jolesz, and Carl-Fredrik Westin (2006). "Geometrically constrained two-tensor model for crossing tracts in DWI". In: *Magnetic Resonance Imaging* 24, pp. 1263–1270.

Perrin, Muriel et al. (2008). "Connectivity-Based Parcellation of the Cortical Mantle Using q-Ball Diffusion Imaging". In: *International Journal of Biomedical Imaging* 2008, p. 368406.

Philippe, Anne-Charlotte (2013). "Régularisation du probléme inverse MEG par IRM de Diffusion". PhD thesis. Université Nice Sophia Antipolis.

Philippe, Anne-Charlotte, Maureen Clerc, Théodore Papadopoulo, and Rachid Deriche (2012). "Whole cortex parcellation combining analysis of MEG forward problem, structural connectivity and Brodmann atlas". In: *BIOMAG*. Paris, France.

— (2013). "Cortex Parcellation Via Diffusion Data As Prior Knowledge for the Meg Inverse Problem". In: *International Symposium on Biomedical Imaging: From Nano to Macro*. San Francisco, CA, USA.

Picard, Nathalie and Peter L. Strick (1996). "Motor Areas of the Medial Wall: A Review of Their Location and Functional Activation". In: *Cerebral Cortex* 6.3, pp. 342–353.

Pineda-Pardo, José Angel, Ricardo Bruna, Mark Woolrich, Alberto Marcos, Anna C. Nobre, Fernando Maestu, and Diego Vidaurre (2014). "Guiding functional connectivity estimation by structural connectivity in MEG: an application to discrimination of conditions of mild cognitive impairment". In: *NeuroImage* 101, pp. 765–777.

Project, The CGAL (2016). *CGAL User and Reference Manual*. 4.9. CGAL Editorial Board.

Ragazzini, J. R. and L. A. Zadeh (1952). "The analysis of sampled-data systems". In: *Electrical Engineering* 71.12, pp. 1102–1102.

Reisert, M., I. Mader, C. Anastasopoulos, M. Weigel, S. Schnell, and V. Kiselev (2011). "Global fiber reconstruction becomes practical". In: *NeuroImage* 54.2, pp. 955 –962.

Robinson, SE and J Vrba (1998). "Functional neuroimaging by synthetic aperture magnetometry SAM". In: pp. 1–4.

Roca, P. (2011). "Parcellisation du manteau cortical à partir du réseau de connectivité anatomique cartographié par imagerie de diffusion". PhD thesis. Université Paris Sud - Paris XI.

Rockafellar, R.T. (1970). *Convex analysis*. Princeton, N. J.: Princeton University Press.

Rogers, Kara, ed. (2010). *The Brain and the Nervous System*. Britannica Educational Publishing.

Ruchalski, Kathleen and Gasser M. Hathout (2012). "A Medley of Midbrain Maladies: A Brief Review of Midbrain Anatomy and Syndromology for Radiologists". In: *Radiology Research and Practice* 2012, p. 11.

Sanei, S. and J. A. Chambers (2007). *EEG signal processing*. John Wiley & Sons.

Santello, M. and A. Volterra (2009). "Synaptic modulation by astrocytes via Ca2+-dependent glutamate release". In: *Neuroscience* 158.1. Protein trafficking, targeting, and interaction at the glutamate synapse, pp. 253 –259.

Sardy, Sylvain, Andrew G. Bruce, and Paul Tseng (2000). "Block Coordinate Relaxation Methods for Nonparametric Wavelet Denoising". In: *Journal of Computational and Graphical Statistics* 9.2, pp. 361–379.

Schmitt, U., A. K. Louis, F. Darvas, H. Buchner, and M. Fuchs (2001). "Numerical aspects of spatio-temporal current density reconstruction from EEG-/MEG-data". In: *IEEE Transactions on Medical Imaging* 20.4, pp. 314–324.

Schmitt, U. and A. K. Louis (2002). "Efficient algorithms for the regularization of dynamic inverse problems: I. Theory". In: *Inverse Problems* 18.3, p. 645.

Schomer, D.L. and F.L. da Silva (2012). *Niedermeyer's Electroencephalography: Basic Principles, Clinical Applications, and Related Fields*. Wolters Kluwer Health.

Sekihara, Kensuke and Srikantan S. Nagarajan (2015). "Source-Space Connectivity Analysis Using Imaginary Coherence". In: *Electromagnetic Brain Imaging: A Bayesian Perspective*. Cham: Springer International Publishing, pp. 139–169.

Shirkhorshidi, Ali Seyed, Saeed Aghabozorgi, and Teh Ying Wah (2015). "A Comparison Study on Similarity and Dissimilarity Measures in Clustering Continuous Data". In: *PLoS ONE* 10.12, pp. 1–20.

Smith, Stephen M. et al. (2004). "Advances in functional and structural MR image analysis and implementation as FSL". In: *NeuroImage* 23, Supplement 1, S208 –S219.

Sporns, Olaf (2011). *Networks of the Brain*. MIT press.

Sporns, Olaf, Dante R. Chialvo, Marcus Kaiser, and Claus C. Hilgetag (2004). "Organization, development and function of complex brain networks". In: *Trends in Cognitive Sciences* 8.9, pp. 418–425.

Stejskal, E. O. and J. E. Tanner (1965). "Spin Diffusion Measurements: Spin Echoes in the Presence of a TimeâĂŘDependent Field Gradient". In: *The Journal of Chemical Physics* 42.1, pp. 288–292.

Strehl, Alexander, Er Strehl, Joydeep Ghosh, and Raymond Mooney (2000). "Impact of Similarity Measures on Web-page Clustering". In: *In Workshop on Artificial Intelligence for Web Search (AAAI 2000*. AAAI, pp. 58–64.

Strohmeier, D., Y. Bekhti, J. Haueisen, and A. Gramfort (2016). "The Iterative Reweighted Mixed-Norm Estimate for Spatio-Temporal MEG/EEG Source Reconstruction". In: *IEEE Transactions on Medical Imaging* 35.10, pp. 2218–2228.

Sutherling, W.W., Crandall P.H., Cahan L.D., and Barth D.S. (1988). "The magnetic field of epileptic spikes agrees with intracranial localizations in complex partial epilepsy". In: *Neurology* 38.5, pp. 778–786.

Tadel, François, Sylvain Baillet, John C. Mosher, Dimitrios Pantazis, and Richard M. Leahy (2011). "Brainstorm: A User-friendly Application for MEG/EEG Analysis". In: *Intell. Neuroscience* 2011, 8:1 –8:13.

Taulu, Samu and Matti Kajola (2005). "Presentation of electromagnetic multichannel data: The signal space separation method". In: *Journal of Applied Physics* 97.12.

Terada, Y. (2013). "Clustering for high-dimension, low-sample size data using distance vectors". In: *ArXiv e-prints*.

Thirion, Bertrand (2003). "fMRI data analysis : statistics, information and dynamics". Theses. Télécom ParisTech.

Thirion, Bertrand, Gael Varoquaux, Elvis Dohmatob, and Jean-Baptiste Poline (2014). "Which fMRI clustering gives good brain parcellations?" In: *Frontiers in Neuroscience* 8.167.

Tian, Tian Siva, Jianhua Z. Huang, Haipeng Shen, and Zhimin Li (2013). "EEG/MEG Source Reconstruction with Spatial-Temporal Two-Way Regularized Regression". In: *Neuroinformatics* 11.4, pp. 477–493.

Tikhonov, Andrey Nikolayevich (1943). "On the stability of inverse problems". In: *Dokl. Akad. Nauk SSSR* 39, pp. 195–198.

Todeschini, Roberto, Viviana Consonni, Hua Xiang, John Holliday, Massimo Buscema, and Peter Willett (2012). "Similarity Coefficients for Binary Chemoinformatics Data: Overview and Extended Comparison Using Simulated and Real Data Sets". In: *Journal of Chemical Information and Modeling* 52.11. PMID: 23078167, pp. 2884–2901.

Toga, Arthur W, Paul M Thompson, Susumu Mori, Katrin Amunts, and Karl Zilles (2006). "Towards multimodal atlases of the human brain". In: *Nature Reviews Neuroscience* 7.12, pp. 952 –966.

Tomassini, V., S. Jbabdi, J.C. Klein, T.E.J. Behrens, C. Pozzilli, P.M. Matthews, M.F.S. Rushworth, and H. Johansen-Berg (2007). "Diffusion-weighted imaging tractography-based parcellation of the human lateral premotor cortex identifies dorsal and ventral subregions with anatomical and functional specializations". In: *The Journal of Neuroscience* 27.38, pp. 10259–10269.

Tuch, David S., Timothy G. Reese, Mette R. Wiegell, Nikos Makris, John W. Belliveau, and Van J. Wedeen (2002). "High angular resolution diffusion imaging reveals intravoxel white matter fiber heterogeneity". In: *Magnetic Resonance in Medicine* 48.4, pp. 577–582.

Vallaghé, Sylvain (2008). "EEG and MEG forward modeling : computation and calibration". PhD thesis. Université de Nice-Sophia Antipolis.

Van Veen, B. D., W. Van Drongelen, M. Yuchtman, and A. Suzuki (1997). "Localization of brain electrical activity via linearly constrained minimum variance spatial filtering". In: *IEEE Transactions on Biomedical Engineering* 44.9, pp. 867–880.

Varoquaux, Gaël, Alexandre Gramfort, Fabian Pedregosa, Vincent Michel, and Bertrand Thirion (2011). "Multi-subject dictionary learning to segment an atlas of brain spontaneous activity". In: *Information Processing in Medical Imaging*. Vol. 6801. Gábor Székely, Horst Hahn. Kaufbeuren, Germany: Springer, pp. 562–573.

Von Luxburg, Ulrike (2007). "A Tutorial on Spectral Clustering". In: *CoRR* abs/0711.0189.

Wakeman, D. G. and Richard N. Henson (2015). "A multi-subject, multi-modal human neuroimaging dataset". In: *Scientific Data* 2.

Weisberg, Sanford (2005). *Applied linear regression*. 3rd ed. Wiley series in probability and statistics. Wiley-Interscience.

Weken, D. Van der, M. Nachtegael, and E. E. Kerre (2002). "An overview of similarity measures for images". In: *Acoustics, Speech, and Signal Processing (ICASSP), 2002 IEEE International Conference on*. Vol. 4, pp. IV–3317–IV–3320.

Winston, Gavin P (2012). "The physical and biological basis of quantitative parameters derived from diffusion MRI". In: *Quantitative Imaging in Medicine and Surgery* 2.4.

Wolters, C. H., L Grasedyck, and W Hackbusch (2004). "Efficient computation of lead field bases and influence matrix for the FEM-based EEG and MEG inverse problem". In: *Inverse Problems* 20.4, p. 1099.

Xekardaki, Aikaterini, Panteleimon Giannakopoulos, and Sven Haller (2011). "White Matter Changes in Bipolar Disorder, Alzheimer Disease, and Mild Cognitive Impairment: New Insights from DTI". In: *Journal of Aging Research* 2011.

Yvert, B., O. Bertrand, J.-F. Echallier, and J. Pernier (1995). "Improved forward EEG calculations using local mesh refinement of realistic head geometries". In: *Electroencephalography and Clinical Neurophysiology* 95, pp. 381–392.

Zhan, Wang and Yihong Yang (2006). "How accurately can the diffusion profiles indicate multiple fiber orientations? A study on general fiber crossings in diffusion MRI". In: *Journal of Magnetic Resonance* 183.2, pp. 193–202.